

Utah State University

DigitalCommons@USU

All Graduate Theses and Dissertations

Graduate Studies

12-2008

Extending F10.7's Time Resolution to Capture Solar Flare Phenomena

Ariel O. Acebal
Utah State University

Follow this and additional works at: <https://digitalcommons.usu.edu/etd>



Part of the [Physics Commons](#)

Recommended Citation

Acebal, Ariel O., "Extending F10.7's Time Resolution to Capture Solar Flare Phenomena" (2008). *All Graduate Theses and Dissertations*. 184.
<https://digitalcommons.usu.edu/etd/184>

This Dissertation is brought to you for free and open access by the Graduate Studies at DigitalCommons@USU. It has been accepted for inclusion in All Graduate Theses and Dissertations by an authorized administrator of DigitalCommons@USU. For more information, please contact digitalcommons@usu.edu.



12-1-2008

Extending F10.7's Time Resolution to Capture Solar Flare Phenomena

Ariel O. Acebal
Utah State University

Recommended Citation

Acebal, Ariel O., "Extending F10.7's Time Resolution to Capture Solar Flare Phenomena" (2008). *All Graduate Theses and Dissertations*. Paper 184.
<http://digitalcommons.usu.edu/etd/184>

This Dissertation is brought to you for free and open access by the Graduate Studies, School of at DigitalCommons@USU. It has been accepted for inclusion in All Graduate Theses and Dissertations by an authorized administrator of DigitalCommons@USU. For more information, please contact digitalcommons@usu.edu.

Take a 1 Minute Survey- <http://www.surveymonkey.com/s/BTVT6FR>



EXTENDING F10.7'S TIME RESOLUTION TO CAPTURE
SOLAR FLARE PHENOMENA

by

Ariel Acebal

A dissertation submitted in partial fulfillment
of the requirements for the degree

of

DOCTOR OF PHILOSOPHY

in

Physics

Approved:

Jan J. Sojka
Major Professor

Lie Zhu
Committee Member

Robert W. Schunk
Committee Member

Randy J. Jost
Committee Member

James T. Wheeler
Committee Member

Byron R. Burnham
Dean of Graduate Studies

UTAH STATE UNIVERSITY
Logan, Utah

2008

“The views expressed in this article are those of the author and do not reflect the official policy or position of the United States Air Force, Department of Defense, or the U.S. Government.”

ABSTRACT

Extending F10.7's Time Resolution to Capture Solar Flare Phenomena

by

Ariel O. Acebal, Doctor of Philosophy

Utah State University, 2008

Major Professor: Dr. Jan J. Sojka
Department: Physics

Solar ultraviolet (UV) radiation ionizes the neutral components in the atmosphere, which is partly responsible for the formation of the ionosphere, and contributes to heating of the atmosphere. Solar flares change the solar spectrum at times by several orders of magnitude. These changes modify the Earth's upper atmosphere, causing problems to communication systems and space operations, such as increased satellite drag. Unfortunately, solar UV measurements are limited since they can only be observed with space-based sensors. In order to work around this limitation, the solar radio emissions at a wavelength of 10.7 cm have been used as a proxy for the solar UV radiation. These measurements, known as the F10.7 index, are a snapshot of the solar activity at the time they are taken and do not capture the changes that occur throughout the day, such as flares. In order to capture this daily variation, we used 1-second cadence solar radio data and compared it to solar UV measurements taken once per orbit by the TIMED satellite. We found significant correlations between some radio frequencies and different UV wavelengths during quiet times. These correlations changed in terms of radio frequency and UV wavelength during solar flares.

(186 pages)

ACKNOWLEDGMENTS

There is no way I could have completed my Ph.D. at Utah State University without the help of many people. At the risk of sounding like an Oscar recipient, there are several people I need to thank for all their assistance.

First of all, I would have never made it to Utah State University without the sponsorship of the Air Force and the Air Force Institute of Technology. My time at Utah State University would not have been as productive and enjoyable without the help of Karalee, Shawna, Melanie, Sharon, and Shelley (who had to read this dissertation at least two times). My dissertation would not have been possible without the guidance and encouragement of Dr. Sojka. The idea we discussed while I was still working in Hawaii proved interesting, successful, and hopefully applicable to space weather operations. My committee's inputs and flexibility were excellent and greatly appreciated.

On a personal level, my parents made incredible sacrifices to give my sisters and me the opportunity to grow up and succeed in this great country. All I have been able to accomplish, I owe to the example they set for me. The patience my wife has for me, seemed to have no limit, although I often test it. Thank you for everything you do for us. Finally, to my kids, thanks for putting up with grumpy dad, making me laugh, reminding me daily what is important, and keeping my priorities straight.

Ariel Acebal

CONTENTS

	Page
ABSTRACT	iv
ACKNOWLEDGMENTS	iv
LIST OF TABLES	vii
LIST OF FIGURES	viii
CHAPTER	
1. INTRODUCTION.	1
1.1 Motivation	1
1.2 Method	3
2. RADIO PHYSICS.	4
2.1 The Sun	4
2.2 Solar Radio Spectrum	6
2.3 Bremsstrahlung	8
2.4 Magnetobremstrahlung	11
2.5 Plasma Emission	16
2.6 Electron Cyclotron Maser	18
2.7 Summary	21
3. THE RADIO SOLAR TELESCOPE NETWORK.	22
3.1 Brief History of USAF Solar Radio Observatories	22
3.2 Why Observe the Radio Sun?	23
3.3 A Simple Radio Telescope	25
3.4 The Radio Solar Telescope Network	27
3.5 A “Typical” Radio Day	34
3.6 Burst Morphology	39
3.7 RSTN Data	44
4. DAILY SOLAR PROXIES.	47
4.1 Introduction to Solar Activity Proxies	47
4.2 Observations of the Sun	49
4.3 Reported and Computed Daily RSTN Flux Densities	53
4.4 SEE Data	76
4.5 Correlations Between EUV, Radio Data, and Other Indices	78
5. SUB-DAILY PROXIES.	81
5.1 Solar Flares	81

5.2	Flare Characteristics	83
5.3	TIMED-SEE Orbits	93
5.4	SEE, GOES, SEM Orbit Correlations	96
5.5	RSTN, GOES, SEM Analysis	102
5.6	RSTN-SEE Analysis	115
6.	INTERPRETATION OF RESULTS.	125
6.1	Typical Flare	125
6.2	Flare 509111244	128
6.3	Flare 509071717	136
6.4	Summary	143
7.	CONCLUSIONS AND FUTURE WORK.	144
7.1	Conclusions	144
7.2	Future Work	146
	REFERENCES	148
	APPENDICES	
A.	RADIO EMISSIONS.	153
B.	ADDITIONAL DATA SOURCES.	160
C.	RANK CORRELATIONS.	166
D.	COPYRIGHT PERMISSIONS.	170

LIST OF TABLES

Table	Page
2.1 Magnetobremstrahlung emission characteristic	15
3.1 Actual frequencies monitored by the USAF's RSTN sites.....	24
4.1 Solar flares observed by GOES during July 19, 1995 to October 27, 2005	52
4.2 Rank correlation table for reported RSTN flux values	72
4.3 Correlations between computed daily flux densities	74
4.4 Correlations between computed and reported RSTN daily values	75
4.5 Correlations between computed RSTN daily values and F10 daily values.....	76
4.6 Correlations between binned TIMED-SEE data and RSTN data	79
5.1 Number of M-class flares observed in 2005 by GOES, SEM, and RSTN	84
5.2 Breakdown of M-class flares observed by GOES, SEM, and radio based on magnitude, latitude, and longitude.....	84
5.3 Number of flares per frequency that had the largest intensity and largest integrated values for the 103 M-class flares in 2005	87
5.4 GOES flares and SEE orbits.....	94
5.5 Number and type of orbits observed by RSTN observatories.....	110
5.6 Non-flare orbits in common between RSTN observatories	120
5.7 Flare orbits in common between RSTN observatories.....	121
6.1 Changes from pre-flare orbit for flare 509111244	135
6.2 Changes from pre-flare orbit for flare 509071717	142
B.1 Soft x-ray sensor characteristics.....	161
B.2 Available TIME-SEE data sets.....	163
C.1 Example of ranked data.....	167

LIST OF FIGURES

Figure	Page
1.1 Radio observations for September 9, 2005.....	2
2.1 Schematic cross sectional view of the sun	5
2.2 Solar temperature profile of the outer atmospheric regions	5
2.3 Binary coulomb collision	8
2.4 Path of an electron moving past an ion.....	9
2.5 Radiation pattern for a charged particle that experiences an acceleration perpendicular to its velocity	13
2.6 Radiation pattern along the charged particles trajectory.....	14
2.7 Radiation pattern of received pulses	15
2.8 Type III solar burst observed by the Air Force’s Sagamore Hill Observatory, MA.....	18
2.9 One-sided loss cone distribution contour.....	20
3.1 Location of current RSTN sites	23
3.2 Energy from the sun in the radio spectrum can be measured by ground sensors since it is not absorbed by the planet’s atmosphere..	24
3.3 Palehua’s 28-ft dish is used to monitor 245, 410, and 610 MHz radio emissions from the sun.....	28
3.4 Palehua’s 8-ft parabolic dish.....	29
3.5 3-ft parabolic dish antenna at Palehua Solar Observatory is used to monitor 15,400 MHz.....	29
3.6 Antenna control unit for the 28-ft dish.....	30
3.7 Raw data from Palehua Solar Observatory for September 7, 2005	35
3.8 Start of radio patrol at the Palehua Solar Observatory on September 7, 2005	35
3.9 At the end of the patrol day, the 3-ft and 8-ft “lose” the sun starting around 0400 UT	36
3.10 A complex burst observed at Palehua Solar Observatory	37

3.11	Noon calibration gap.....	37
3.12	Examples of radio frequency interference at the Palehua Solar Observatory	39
3.13	Impulsive bursts observed at the Learmonth Solar Observatory on September 9, 2005.....	41
3.14	Great Burst observed at Learmonth Solar Observatory on December 2, 2005.....	42
3.15	Great Complex bursts at Palehua Solar Observatory on September 7, 2005.....	42
3.16	A gradual rise and fall (GRF) burst observed by the Sagamore Hill Observatory on January 15, 2005 on 15,400 MHz	44
3.17	A noise storm is observed by the Sagamore Hill Observatory on February 11, 2005	45
4.1	Solar flares relative to the four solar rotations in 2005.....	50
4.2	Four solar rotations as measured by different solar indices in 2005	51
4.3	TIMED-SEE Data.....	52
4.4	RSTN 245 MHz during the four solar rotations	54
4.5	RSTN 410 MHz reported daily values compared to F10.7	55
4.6	RSTN 610 MHz reported daily values compared to F10.7	56
4.7	RSTN 1415 MHz reported daily values compared to F10.7.....	57
4.8	RSTN 2695 MHz reported daily values compared to F10.7.....	58
4.9	RSTN 4995 MHz reported daily values compared to F10.7.....	59
4.10	RSTN 8800 MHz reported daily values compared to F10.7.....	60
4.11	RSTN 15400 MHz reported daily values compared to F10.7	61
4.12	RSTN 245 MHz computed daily flux value	63
4.13	RSTN 410 MHz computed daily flux value	64
4.14	RSTN 610 MHz computed daily flux value	65
4.15	RSTN 1415 MHz computed daily flux value.....	66
4.16	RSTN 2695 MHz computed daily flux value.....	67

4.17 RSTN 4995 MHz computed daily flux value.....	68
4.18 RSTN 8800 MHz computed daily flux value.....	69
4.19 RSTN 15400 MHz computed daily flux value	70
4.20 TIMED-SEE daily value correlation results.....	77
4.21 Correlation results between all RSTN observatories and SEE wavelengths.....	79
4.22 Correlation results between SEE wavelengths and Palehua radio frequencies	80
5.1 Radio Flare 501090825	85
5.2 GOES Flare 501090825.....	86
5.3 Distribution of flares according to time from start to peak of flare	87
5.4 Distribution of flares according to time from peak to half power of flare	88
5.5 Distribution of flares according to peak intensity.....	88
5.6 Distribution of flares according to net increase	89
5.7 Distribution of flares according to front slope	89
5.8 Distribution of flares according to back slope	90
5.9 Distribution of flares observed in the western solar hemisphere	91
5.10 Distribution of flares observed in the western solar hemisphere	91
5.11 Distribution of flares observed in the western solar hemisphere	92
5.12 Distribution of flares observed in the northern solar hemisphere.....	93
5.13 Correlations between SEE wavelengths for non-flare orbits.....	94
5.14 Correlations between SEE wavelengths for flare orbits.....	95
5.15 Correlations between SEE wavelengths for large flare orbits	95
5.16 Time series of non-flare orbits for GOES, SEM, and SEE wave- length 5 from July 1 to December 31, 2005	97
5.17 Time series of non-flare orbits for GOES, SEM, and SEE wave- length 41 from July 1 to December 31, 2005.....	97

5.18	Time series of non-flare orbits for GOES, SEM, and SEE wavelength 96 from July 1 to December 31, 2005.....	98
5.19	Time series of non-flare orbits for GOES, SEM, and SEE wavelength 122 from July 1 to December 31, 2005	98
5.20	Time series of non-flare orbits for GOES, SEM, and SEE wavelength 150 from July 1 to December 31, 2005	99
5.21	Correlations between GOES, SEM, and SEE for non-flare orbits	99
5.22	Correlations between GOES, SEM, and SEE for flare orbits	100
5.23	Correlations between GOES, SEM, and SEE for large flare orbits.....	100
5.24	Differences between flare and non-flare orbit correlations	101
5.25	Differences between large flare and flare orbit correlations.....	101
5.26	Radio plot for Sagamore Hill observatory on July 1, 2005	104
5.27	Radio plot for San Vito observatory on July 4, 2005	104
5.28	Time series of non-flare orbits for Palehua's lower four frequencies from July 1 to December 31, 2005.....	106
5.29	Time series of non-flare orbits for Palehua's lower four frequencies from July 1 to December 31, 2005.....	106
5.30	Time series of non-flare orbits for Learmonth's upper four frequencies from July 1 to December 31, 2005.....	107
5.31	Time series of non-flare orbits for Learmonth's upper four frequencies from July 1 to December 31, 2005.....	107
5.32	Time series of non-flare orbits for San Vito's lower four frequencies from July 1 to December 31, 2005.....	108
5.33	Time series of non-flare orbits for San Vito's upper four frequencies from July 1 to December 31, 2005.....	108
5.34	Time series of non-flare orbits for Sagamore Hill's lower four frequencies from July 1 to December 31, 2005	109
5.35	Time series of non-flare orbits for Sagamore Hill's upper four frequencies from July 1 to December, 31 2005	109
5.36	Correlations between Palehua, GOES, and SEM for non-flaring orbits.....	111
5.37	Correlations between Learmonth, GOES, and SEM for non-flaring orbits	111

5.38	Correlations between San Vito, GOES, and SEM for non-flaring orbits	112
5.39	Correlations between Sagamore Hill, GOES, and SEM for non-flaring orbits	112
5.40	Correlations between Palehua, GOES, and SEM for flaring orbits.....	113
5.41	Correlations between Learmonth, GOES, and SEM for flaring orbits....	113
5.42	Correlations between San Vito, GOES, and SEM for flaring orbits	114
5.43	Correlations between Sagamore Hill, GOES, and SEM for flaring orbits.....	114
5.44	Correlations between Palehua, and SEE for non-flaring orbits.....	115
5.45	Correlations between Learmonth, and SEE for non-flaring orbits	116
5.46	Correlations between San Vito, and SEE for non-flaring orbits.....	116
5.47	Correlations between Sagamore Hill, and SEE for non-flaring orbits.....	117
5.48	Correlations between Palehua, and SEE for flaring orbits.....	117
5.49	Correlations between Learmonth, and SEE for flaring orbits.....	118
5.50	Correlations between San Vito, and SEE for flaring orbits	118
5.51	Correlations between Sagamore Hill, and SEE for flaring orbits.....	119
5.52	Correlations between observatories for non-flare orbits	120
5.53	Correlations between observatories for flare orbits	121
5.54	X-class flare 507141016 observed by GOES main channel.....	123
5.55	The X-class flare of Figure 5.54 observed by Learmonth	123
5.56	The X-class flare of Figure 5.54 observed by San Vito	124
5.57	The X-class flare of Figure 5.54 observed by Sagamore Hill	124
6.1	Standard model of a solar flare modified from <i>Benz</i> [2008]	126
6.2	Time evolution of a radio flare	126
6.3	Example of two different radio emission mechanisms.....	127
6.4	Location of active region AR808.....	128

6.5	Flare 509111244 as seen by GOES 12	129
6.6	Flare 509111244 as seen by RSTN	130
6.7	The first radio peak in Flare 509111244	131
6.8	The second radio peak in Flare 509111244	131
6.9	Flare 509111244 as observed by TIMED-SEE	133
6.10	Flare 509111244 as observed by TIMED-SEE (1 to 15 nm)	133
6.11	Flare 509111244 as observed by TIMED-SEE (16 to 60 nm)	134
6.12	Flare 509111244 as observed by TIMED-SEE (61 to 120 nm)	134
6.13	Location of active region AR808 on September 9, 2005	136
6.14	Flare 509071717 as observed by GOES	137
6.15	Flare 509071717 as seen by RSTN	137
6.16	The first radio peak in Flare 509071717	139
6.17	The second radio peak in Flare 509071717	139
6.18	Flare 509071717 as observed by TIMED-SEE	140
6.19	Flare 509071717 as observed by TIMED-SEE (1-15 nm)	140
6.20	Flare 509071717 as observed by TIMED-SEE (16-60 nm)	141
6.21	Flare 509071717 as observed by TIMED-SEE (61-120 nm)	141
A.1	Typical radio burst spectrum	153
A.2	Plot of RFI commonly measured by RSTN's SRS	155
A.3	Type II radio sweep observed by the Learmonth Solar Observatory	155
A.4	Type III radio sweep observed by the Palehua Solar Observatory	157
A.5	Type IV radio sweep observed by the San Vito Solar Observatory	157
B.1	GOES measurements on July 7, 2005	162
B.2	SEE measurements on July 7, 2005	164
B.3	SEM measurements on July 7, 2005	165

D.1	Copyright permission submitted to the Annual Reviews of Astronomy and Astrophysics Journal	170
D.2	Copyright permission received from the Chinese Astronomy and Astrophysics Journal	171

CHAPTER 1

INTRODUCTION

1.1 Motivation

The total solar irradiance measured above Earth's atmosphere is around 1300 watts m^{-2} . Approximately 92% of this radiation is in the visible to infrared spectrum. This portion of the solar spectrum varies by less than a percent throughout the 11-year solar cycle. The remaining 8% of the solar irradiance comes from the UV and shorter wavelengths spectrum, and also the radio spectrum. While these wavelength ranges contribute a much smaller portion of the total solar irradiance, their variability is much larger and ranges over different time scales. This variation ranges from a few percents to several orders of magnitude depending on the wavelength and the time scale in question. The time scales range from the 11-year solar cycle, to the 27-day rotation, and down to the short-term variation from solar flares.

Solar UV radiation below 200 nm is the primary source for heating the thermosphere, creating the ionosphere, and driving diurnal cycles of winds and chemistry [Woods *et al.*, 1998]. Variations in this energy range change the energy, dynamics, and chemistry of the atmosphere. Unfortunately, solar UV radiation is completely absorbed by the thermosphere. This limits the observations of solar UV radiation since it can only be observed with space-based sensors. In order to work around this limitation, scientists have looked for different proxies for solar UV radiation. One of these proxies is the solar radio emissions at a wavelength of 10.7 centimeters, which can be measured by ground-based instruments. These radio measurements are called the F10.7 index and do not necessarily have a cause and effect relationship with solar UV radiation. However, both of these emissions originate in the same region of the solar atmosphere and thus, were shown to correlate with each other [Hedin, 1984].

The availability and long records of F10.7 measurements have made it a common proxy for solar UV radiation. Many space physics models including the Ionosphere Forecast Model (IFM), the Parameterized Real-Time Ionospheric Specification Model (PRISM), the Time Dependent Ionospheric Model (TDIM), and the Global Assimilation of Ionospheric Measurements (GAIM) use the F10.7 as the solar UV input.

The F10.7 index is a snapshot of the solar activity at the time the radio measurement is taken. During solar minimum and quite times, the measurement is representative of the daily variation of the sun [*Tapping and Charrois, 1994*]. However, during periods of increased solar activity, a daily index cannot accurately express the solar variation taking place throughout a day (Figure 1.1). Furthermore, impacts of solar flares are removed from the reported F10.7 values [*Tapping and Charrois, 1994*].

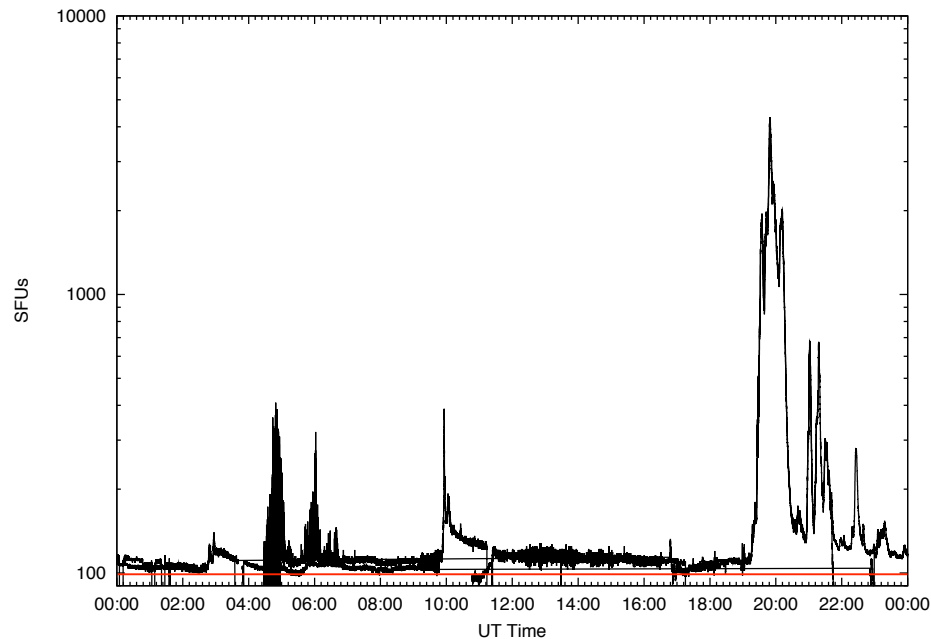


Figure 1.1: Radio observations for September 9, 2005. The red line is the F10.7 cm (2800 MHz) value. The black lines are the observations from the RSTN observatories measured at $\lambda = 11.1$ cm (2695 MHz).

1.2 Method

Over the years, many studies have been carried out to examine the correlation between radio and UV radiation. Some of these studies include *Bossy* [1983], *Hedin* [1984], *Floyd et al.* [2002], *Schamhl and Kundu* [1995], *Kane* [2002], and *Floyd et al.* [2005]. They have shown good correlations between radio and UV in yearly, monthly, and even daily scales.

The goal of this dissertation is to look for correlations between solar radio and UV radiation for time scales smaller than a day. To accomplish this task, one-second time resolution data from the Air Forces Radio Solar Telescope Network (RSTN) will be analyzed and compared against UV data from the Solar EUV Experiment (SEE) flying on the TIMED satellite.

Chapter 2 of this dissertation discusses the physics of solar radio emissions including the different mechanisms responsible for the solar radio spectrum. Chapter 3 is a detailed look at the RSTN data set. Chapters 4 and 5 show the results of the dissertation. Chapter 4 reviews the solar proxies and shows how RSTN data could be used as an additional daily proxy by first showing agreement between F10.7 measurements and RSTN data and then showing correlations between radio and UV data. In Chapter 5, the time resolution is decreased in order to incorporate the effects of solar flares. The purpose of this chapter is to determine if solar radio data can be used to determine the solar EUV output that occurs throughout a day and during flares. Finally, chapter 6 discusses the results of Chapters 4 and 5.

CHAPTER 2

RADIO PHYSICS

2.1 The Sun

The sun is an average star with a radius of 6.9×10^5 km, mass of 2×10^{30} kg, and it is about 150 million kilometers from Earth. It is primarily composed of hydrogen and helium, but has traces of many other elements. At the core of the sun, nuclear fusion of hydrogen into helium releases energy that will be transported through to the surface by conduction, radiation (radiation zone), and convection (convection zone) to fuel the entire solar system (Figure 2.1).

Directly above the convection zone is the photosphere. This is the region responsible for the visible wavelengths produced by the sun. The photosphere is usually considered the solar surface and has a density around 10^{14} particles per cm^3 . It is a fairly smooth surface that darkens at the limbs and may have other dark features, which are active regions or sunspots. The temperature at the base of the photosphere is around 6,000 K and decreases to 4,500 K at the top of the 500 km layer. This temperature minimum serves to mark the base of the next layer, the chromosphere. The chromosphere is about 1,500 km deep and has a density of 10^{10} particles per cm^3 at the top of the layer. The temperature increases with altitude to around 25,000 K. This marks the boundary to the next region, the transition zone. The transition zone is relatively shallow but the temperature increases several orders of magnitude to around a million degrees. Above the transition zone is the corona, the outer atmosphere of the sun. The corona is fully ionized and has a density around 10^5 particles per cm^3 and the temperatures exceed two million degrees (Figure 2.2).

The spectrum of the Sun resembles that of a black body at a temperature of 5,800 K. A black body at this temperature emits primarily in the visible and infrared

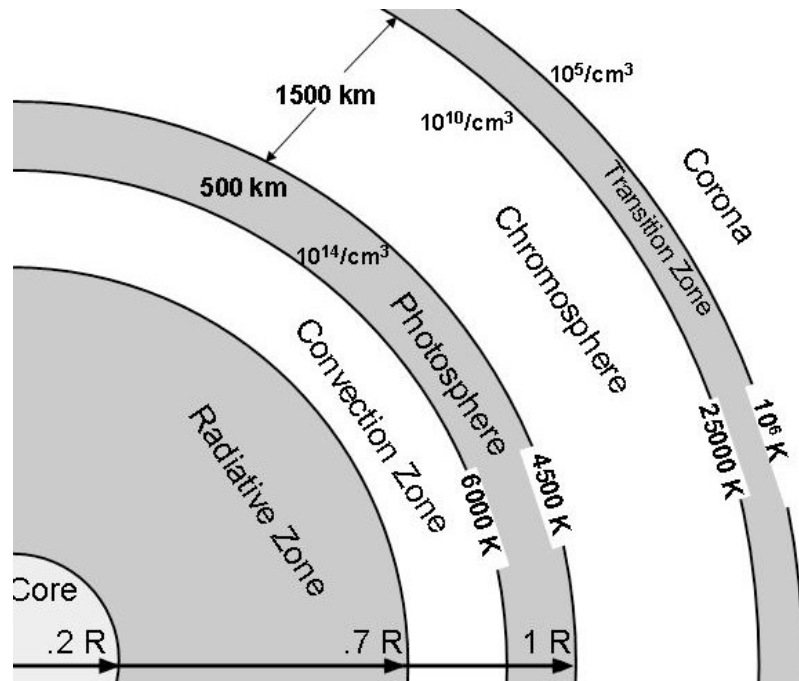


Figure 2.1: Schematic cross sectional view of the sun.

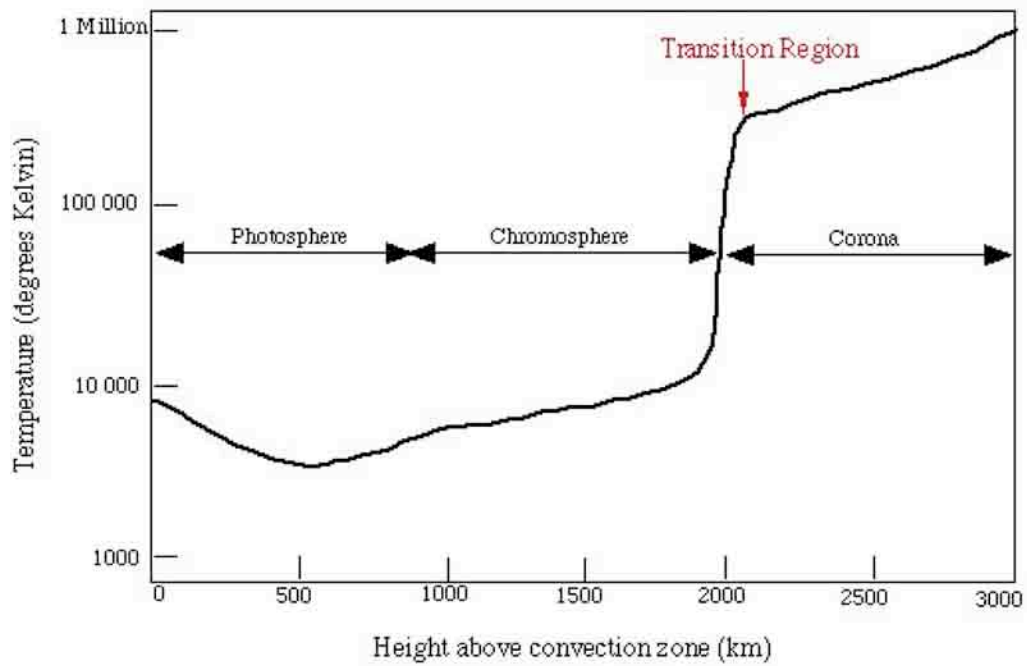


Figure 2.2: Solar temperature profile of the outer atmospheric regions.

wavelength range. This is evident in the solar energy received at the top of Earth's atmosphere. This energy is called the solar constant and is around 1360 W m^{-2} . Most of this energy is the infrared and visible range, while less than 0.1% falls in the range of x-rays, EUV, and radio. Despite the name, the solar constant is not constant. The variations are small for large time scales, but could be very large in short time scales. Also, not all wavelength ranges change in similar fashion. The visible and infrared range show little variation regardless of time scale. On the other hand, the x-ray and radio ranges show significant variation in all time scales. The 11-year solar sun spot cycle is one of the large time scale variations. These variations are very small and gradual, but last for a long time. On a smaller time scale, the 27-day solar rotation period also changes the solar constant. These changes are more rapid, but not as long lasting and are associated with the emergence, evolution, and disappearance of active regions. Finally, solar flares are another way to change the solar constant. Flares are violent events in the solar atmosphere that are associated with very large energy releases (up to 10^{25} J). These changes are very rapid, very large, but of relatively short duration. Depending on the frequency being observed, and mechanism responsible for the radio emissions, the radio emissions can take place along the entire altitude profile of a flare. This ranges from the corona down to the photosphere (Figure 2.1) [*Bastian et al.*, 1998].

2.2 Solar Radio Spectrum

The solar radio spectrum spans six orders of magnitude and varies according to the three time scales previously discussed. There are three types of solar radio emissions: quiet sun, the slowly varying component, and bursts. The background or quiet sun component varies in intensity over a time scale of years and originates all over the solar disk. The difference between solar maximum and solar minimum could

be as high as 300% at 2695 MHz. The slowly varying component is mainly due to enhanced thermal radiation from active regions. This component varies in a monthly time scale as new regions are formed and eventually disintegrate. The variation for this component could be as high as 25% change during solar minimum to 50% during solar maximum. The burst component is associated with flares. These bursts are usually located within active regions and could last a few minutes to several hours depending on the size of the flare. The changes observed in the radio spectrum depends on the frequency observed and the size of the flare and could be as large as a two order of magnitude increase.

Solar radio emissions can be divided into two broad categories depending on how the electrons behave: incoherent or coherent processes. The incoherent processes are bremsstrahlung and magnetobremsstrahlung emissions. The coherent processes are plasma and electron cyclotron maser emissions. In the incoherent processes, each particle emits radiation independently of the others. The sum of all these radiations is an emission that can only change if there is a change in the conditions of the medium. As a result, the brightness temperature cannot exceed the source temperature. On the other hand, in coherent mechanisms, the emitting particles behave as a whole and there exists a phase relation. In these mechanisms, the brightness temperature can exceed the mean particle energy. Coherent mechanisms are attributed to kinetic instabilities from unstable particle distributions. There are two major categories of unstable particle distributions: positive slopes in a parallel direction to the magnetic field, $\partial f / \partial v_{\parallel} > 0$, called beams, and positive slopes in a perpendicular direction to the magnetic field, $\partial f / \partial v_{\perp} > 0$, called losscones.

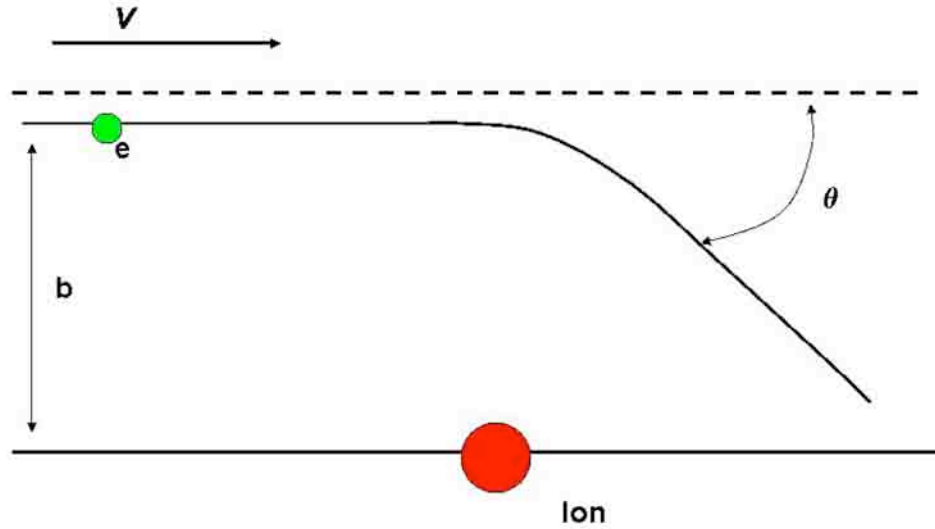


Figure 2.3: Binary coulomb collision.

2.3 Bremsstrahlung

The first mechanism to be discussed is free-free bremsstrahlung emissions. Free-free bremsstrahlung emissions are due to the acceleration of an electron in a Coulomb field of an ion (not considering other interactions). For example, a binary collision between electron with velocity v and ion of charge Z_i is shown in Figure 2.3. The effect of the collision between the electron and the ion is that the incoming electron is deflected by an amount which depends on the impact parameter b . In the generation of the solar radio spectrum, the distant encounters are more important and frequent than close encounters [Raulin and Pacini, 2005]. In this situation, the emission from one incoming electron can be calculated using the small angle approximation. The first step is to compute the motion along a straight line (Figure 2.4).

The force on the electron is

$$F = m\ddot{x} = \frac{Ze^2}{R^2} = \frac{Ze^2}{b^2 + v^2t^2}. \quad (2.1)$$

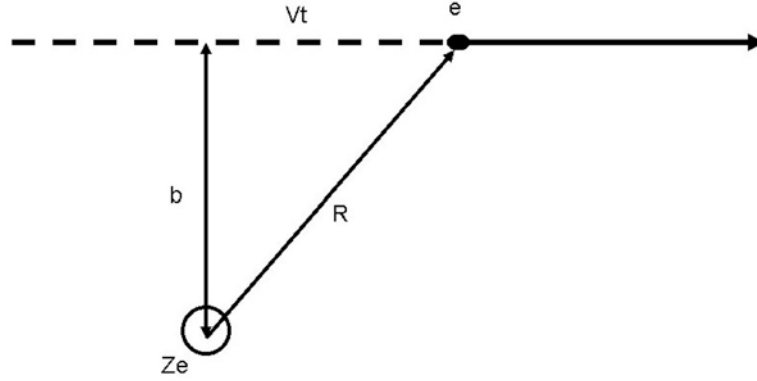


Figure 2.4: Path of an electron moving past an ion.

The acceleration is

$$\ddot{x} = \frac{Ze^2}{(b^2 + v^2t^2) m_e}. \quad (2.2)$$

The magnitude of the electric field for a dipole is given by

$$E(t) = \frac{e\ddot{x}\text{Sin}\theta}{c^2R} = \frac{Ze^3\text{Sin}\theta}{(b^2 + v^2t^2) m_e Rc^2} \quad (2.3)$$

Taking the Fourier transform yields,

$$E(\omega) = \frac{Ze^3\text{Sin}\theta}{m_e Rc^2} \left(\frac{\pi}{bv}\right) \text{Exp}\left(\frac{-\omega b}{v}\right). \quad (2.4)$$

The energy per unit area per unit frequency is

$$\frac{dW}{dAd\omega} = c |E(\omega)|^2, \quad (2.5)$$

which results in

$$\frac{dW}{d\omega} = \frac{Z^2 e^6 \text{Sin}^2\theta}{m_e^2 C^3} \left(\frac{\pi}{bv}\right)^2 \text{Exp}\left(\frac{-2\omega b}{v}\right) d\Omega \quad (2.6)$$

since $dA = R^2 d\Omega$. The next step is to integrate over the solid angle (from 0 to π),

$$\frac{dW}{d\omega} = \frac{8}{3\pi} \left(\frac{Z^2 e^6}{m_e^2 c^3} \right) \left(\frac{1}{bv} \right)^2 \text{Exp} \left(\frac{-2\omega b}{v} \right). \quad (2.7)$$

Therefore, the emission from a single collision is

$$\frac{dW}{d\omega} = \begin{cases} \frac{8}{3\pi} \left(\frac{Z^2 e^6}{m_e^2 c^3} \right) \left(\frac{1}{bv} \right)^2 & \text{for } b \ll v/\omega \\ 0 & \text{for } b \gg v/\omega \end{cases}. \quad (2.8)$$

The total emission per unit time per unit volume per unit frequency range for a medium with ion density n_i , electron density n_e with electron velocity v is

$$\frac{dW}{d\omega dV dt} = n_e n_i 2\pi v \int_{b_{\min}}^{\infty} \frac{dW(b)b}{d\omega} db, \quad (2.9)$$

since the flux of electrons with velocity v incident on an ion is simply $n_e v$, and the area about an ion is $2\pi b db$. Substituting equation 2.8 into 2.9 results in

$$\frac{dW}{d\omega dV dt} = \frac{16e^6}{3c^3 m^2 v} n_e n_i Z^2 \int_{b_{\min}}^{b_{\max}} \frac{db}{b} = \frac{16e^6}{3c^3 m^2 v} n_e n_i Z^2 \ln \left(\frac{b_{\max}}{b_{\min}} \right) \quad (2.10)$$

Since b_{\max} and b_{\min} appear in the logarithm, the precise values are not necessary. Usually b_{\max} is chosen so that the small angle approximation still holds, $b_{\max} = \frac{v}{\omega}$ [Rybicki and Lightman, 1979]. The choice for b_{\min} depends on whether one chooses the straight line approximation or a particle approach. In the straight line approximation, $b_{\min} = \frac{4Ze^2}{\pi m v^2}$, while in the particle approximation, $b_{\min} = \frac{\hbar}{mv}$ [Rybicki and Lightman, 1979]. Regardless of the choice of b_{\max} and b_{\min} , equation 2.10 is an approximate answer. A more precise answer requires equation 2.10 to be corrected

by the Gaunt factor yielding,

$$\frac{dW}{d\omega dV dt} = \frac{16e^6}{3^{3/2}c^3m^2v} n_e n_i Z^2 g_{ff}(v, \omega), \quad (2.11)$$

where

$$g_{ff}(v, \omega) = \frac{\sqrt{3}}{\pi} \ln \left(\frac{b_{max}}{b_{min}} \right). \quad (2.12)$$

Finally, to obtain the emissivity for the free-free bremsstrahlung process, equation 2.11 needs to be integrated over a distribution function. For the solar plasma, the distribution function used is the Maxwellian distribution function. The result is

$$\eta_\nu = \frac{2^5 \pi e^6}{3m_e c^3} \left(\frac{2\pi}{3m_e k_B} \right)^{1/2} n_e^2 T^{-1/2} g_{ff}(v, \omega) e^{-\frac{h\nu}{kT}}. \quad (2.13)$$

Equation 2.13 shows that for free-free bremsstrahlung emissions, the radiated power is proportional to the square of the ambient density and inversely proportional to the square root of the plasma temperature. Thus, this mechanism is effective in high density, low temperature areas, and is a dominant mechanism for the quiet sun, coronal holes, and sometimes active regions.

2.4 Magnetobremstrahlung

The next type of emission is magnetobremstrahlung radiation. Whenever there is a magnetic field present, a charged particle will spiral along the magnetic field lines due to the Lorentz force. This gyration causes a constant acceleration which leads to the emission of electromagnetic radiation. This is magnetobremstrahlung radiation. In this case, the Larmor formula is used to compute the power radiated by a single accelerated charged particle in the direction relative to the acceleration

vector [*Rybicki and Lightman, 1979*],

$$P = \frac{2q^2\dot{v}^2}{3c^3}. \quad (2.14)$$

This formula indicates several interesting aspects of magnetobremstrahlung radiation: (i) the total power emitted is proportional to the square of the charge and the square of the acceleration, (ii) no power is emitted in the direction of the acceleration, (iii) maximum power is emitted in a direction perpendicular to the acceleration, and (iv) the radiation from protons is insignificant compared to the radiation from electrons [*Raulin and Pacini, 2005; Rybicki and Lightman, 1979*]. To determine the radiation emitted by relativistic particles, it is necessary to do a Lorentz transform of equation 2.14 resulting in

$$P = \frac{2q^2}{3c^3}\gamma^4 (a_{\perp}^2 + \gamma^2 a_{\parallel}^2) \quad (2.15)$$

where γ is the Lorentz factor and is defined as $\gamma \equiv \left(1 - \frac{v^2}{c^2}\right)^{-\frac{1}{2}}$. In a uniform magnetic field, the motion of a charged particle is given by

$$\frac{d(\gamma m \vec{v})}{dt} = \frac{q}{c} \vec{v} \times \vec{B} \quad (2.16)$$

and

$$\frac{d(\gamma m c^2)}{dt} = q \vec{v} \cdot \vec{E} = 0. \quad (2.17)$$

Equation 2.17 implies that γ is a constant, so equation 2.16 can be rewritten as

$$m\gamma \frac{d\vec{v}}{dt} = \frac{q}{c} \vec{v} \times \vec{B}, \quad (2.18)$$

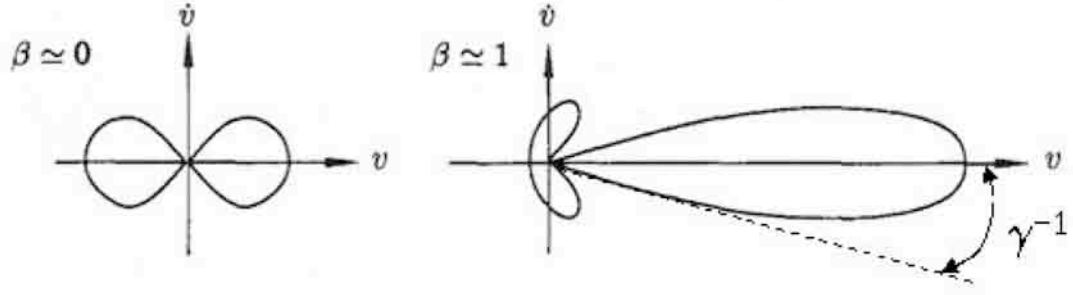


Figure 2.5: Radiation pattern for a charged particle that experiences an acceleration perpendicular to its velocity.

which when separated into components yields $\frac{dv_{\parallel}}{dt} = 0$ or $a_{\parallel} = 0$ and $\frac{dv_{\perp}}{dt} = \frac{q}{\gamma mc} \vec{v}_{\perp} \times \vec{B}$ or $a_{\perp} = \frac{qB}{\gamma mc} v_{\perp} \sin \alpha = v_{\perp} \omega_B \sin \alpha$ where α is the angle between \vec{v} and \vec{B} . The emitted power then is

$$P = \frac{2}{3} \frac{e^2}{c^3} \frac{v_{\perp}^2 e^2 B^2 \gamma^2}{m_e^2 c^2}. \quad (2.19)$$

In the electron reference frame, the power emitted is dipolar and in the rest frame, the power is beamed along the direction of \vec{v} as shown in Figure 2.5. In the electron frame, the beam passes the observer during time,

$$\Delta t = \frac{\Delta \theta}{\omega_B} \quad (2.20)$$

where $\Delta \theta = \frac{2}{\gamma}$ (see Figure 2.6) and $\omega_B = \frac{qB}{\gamma mc}$. Combining these equations gives

$$\Delta t = \frac{2mc}{qB} = \frac{2}{\omega_L}. \quad (2.21)$$

Another point to consider is that the Doppler effect shortens the duration of the pulse, i.e., the charged particle is closer to the observer at the end of the beam

by a factor of $1 - \frac{v}{c}$,

$$\tau = \left(1 - \frac{v}{c}\right) \Delta t = \frac{2}{\omega_L} \left(1 - \frac{v}{c}\right) = \frac{2}{\omega_L} (1 - \beta), \quad (2.22)$$

where τ is the observed pulse width. For $\gamma \gg 1, \beta = \frac{v}{c} \approx 1$ therefore,

$$\frac{1}{\gamma^2} = 1 - \frac{v^2}{c^2} = \left(1 + \frac{v}{c}\right) \left(1 - \frac{v}{c}\right) \approx 2(1 - \beta). \quad (2.23)$$

Substituting this result into equation 2.22, results in

$$\tau = \frac{1}{\omega_L \gamma^2}. \quad (2.24)$$

Thus, the width of the observed pulses is smaller than the gyration frequency by a factor of γ^2 . In the time domain, the τ wide pulses are separated by $\frac{2\pi\gamma^2 m_e c}{eB}$ and have a frequency of $\frac{eB}{2\pi\gamma^2 m_e c}$ (Figure 2.7). In the frequency domain, the electron emissions change according to the Lorentz factor. This is summarized on Table 2.1.

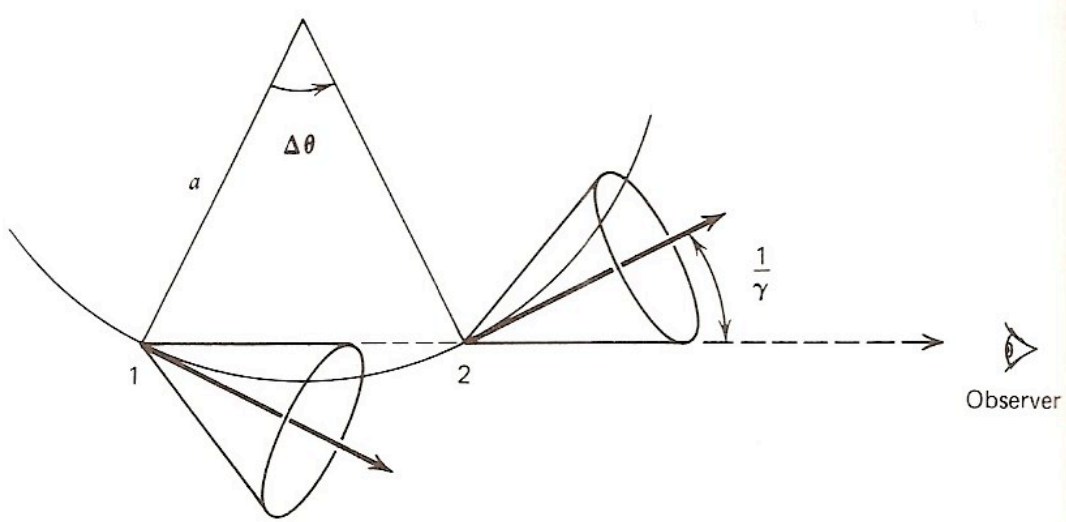


Figure 2.6: Radiation pattern along the charged particles trajectory.

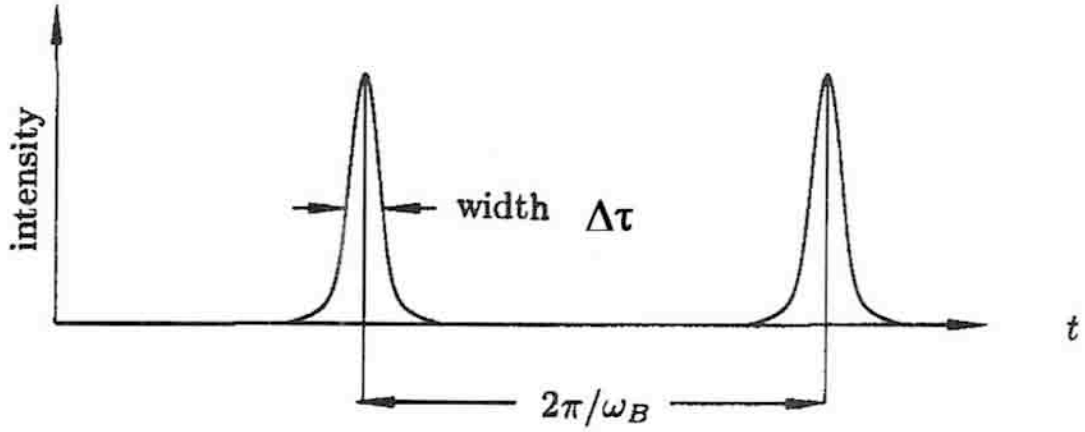


Figure 2.7: Radiation pattern of received pulses.

Table 2.1: Magnetobremstrahlung emission characteristics.

Name	Energy	Lorentz Factor	Harmonics
Gyroresonance or cyclotron	High energy thermal	$\gamma = 1$	1-5
Gyro synchrotron	Mild relativistic	$\gamma < 2$ or 3	10-100
Synchrotron	Highly relativistic	$\gamma \gg 1$	γ^3

Computations of magnetobremstrahlung emissions for a collection of electrons are complex since they require knowledge of pitch angle and velocity distributions of the particles, and magnetic field structures. Several sources deal with this matter in great detail, including emissivity calculations including *Dulk* [1985], *Lee and Gary* [2000], and *Pacholczyk* [1970]. This continues to be an active area of research to determine appropriate distribution function for any given situation. However, two of the most common distribution functions used for these computations are maxwellian and power-law distribution functions. The maxwellian treatment is used for discrete and low harmonic numbers of ω_B . In this case, the emissivity is a function of plasma density n_e , the magnetic field strength, and direction relative to the observer. The power law treatment is used to study the emissions from flare accelerated particles. In this case, the emissivity is a function of electron density with a particular energy

level, the magnetic field strength, and direction to observer [Raulin and Pacini, 2005]. This mechanism is effective in active regions and in solar flares. As a result, these emissions can be found throughout the outer solar regions shown in Figure 2.1.

2.5 Plasma Emission

The next type of radio emission is the plasma emission. This is a multi-step process involving the non-linear conversion of electron energy to plasma waves. The first step is the production of Langmuir wave. This depends on a source of free energy in the form of a non-equilibrium velocity distribution. According to Dulk [1985], the only accepted form of anisotropy that can lead to the production of Langmuir waves is the “bump in the tail” or “two-stream” instability. One way of creating this instability is for fast electrons to outpace slow ones creating an area of positive slope in the distribution function, $\partial f / \partial v_{\parallel} > 0$. Since the fast electrons outpace the slow ones, at some distance from the acceleration site the fast electrons arrive first. Thus, there are more particles with velocity greater than the phase velocity. This results in growth of the turbulence and reduction in beam velocity. Energy is then transferred from particle beam to wave. Another way to create the “bump in the tail” is through the depletion of slower electrons by collisions with the background plasma.

When the plasma frequency (ω_p) is greater than the cyclotron frequency (Ω_e), a Langmuir wave can resonantly interact with the electrons and become amplified. The growth of this wave continues until one of three conditions is met:

1. the stream changes characteristics that destroys resonance,
2. the waves are scattered off of ions, lower frequency waves, or inhomogeneous densities at angles that destroy resonance, or
3. waves react with streaming electrons in such a way that they remove the positive slope.

In order for radio waves to be detected, the Langmuir waves have to be converted to electromagnetic waves. This can be achieved by the interaction of the Langmuir wave and another small wave, leading to the fundamental plasma frequency. *Dulk* [1985] suggests three possible mechanisms: scattering by the electric fields associated with the thermal ions, scattering by low frequency waves (ion-sound or lower hybrid), or direct conversion in the presence of sharp density gradients. The creation of the second harmonic radiation is believed to be caused by the coalescence of two Langmuir waves to produce an electromagnetic wave.

According to *Aschwanden* [2004], the theory of plasma emission predicts certain conditions:

1. the propagation beams have mildly relativistic speeds which implies specific frequency-time drift rates,
2. the plasma frequency range is a function of the local electron density,
3. plasma emission produces higher brightness temperatures than incoherent processes, and
4. these emissions require flares to accelerate the electrons, so plasma emissions should be correlated with flare activity.

One observable solar phenomenon attributed to plasma emissions is the metric Type-III radio burst (Figure 2.8). The Type-III burst has a very fast frequency drift rate, which depends only on the local electron density. As the disturbance moves up in the solar corona 2.1, it encounters decreasing densities. The Type-III burst drifts from high to low frequencies. Additionally, most Type-III bursts are associated with an increase on the x-ray band. Additional details on Type III bursts can be found in Appendix A.

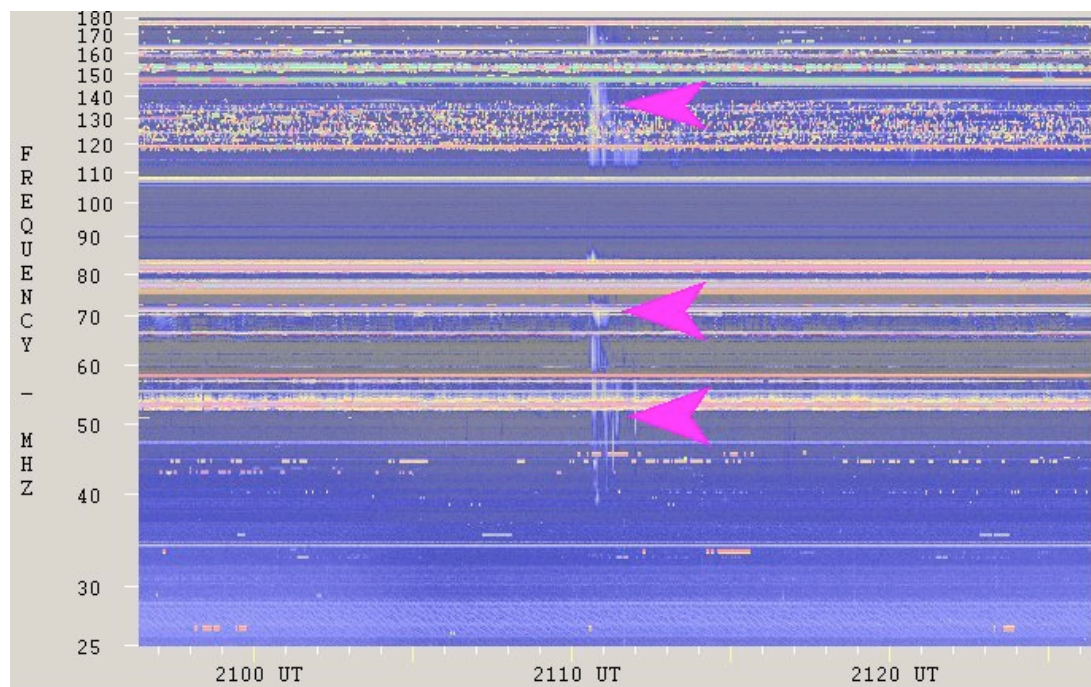


Figure 2.8: Type III solar burst observed by the Air Force’s Sagamore Hill Observatory, MA. The burst can be seen as a vertical sweep around 2112 UT.

2.6 Electron Cyclotron Maser

The last emission mechanism to be discussed is the electron cyclotron maser or ECM. Before discussing the details of this mechanism, it is necessary to examine the name of the mechanism in greater detail. The term maser is a predecessor of laser, and is the acronym for microwave amplification by stimulated emission of radiation. This often leads to an inaccurate view of the mechanism. *Treumann* [2006] states that the name was chosen because the ECM “resembles the well-known molecular maser or laser where population inversion leads to the stimulated emission of coherent radiation of high yield.” Unfortunately, the comparison is not accurate and the name is misleading since “neither quantum effects, nor energy levels, nor elementary population inversions are involved and no electrons jump coherently down from an excited energy level onto some lower level.” So what is the electron cyclotron maser? The

ECM is a plasma instability caused by the resonance between electromagnetic waves and plasma electrons in the presence of an externally generated magnetic field [*Conway and MacKinnon, 1998*]. The resonance only leads to the instability if the velocity distribution of the electrons has a particular kind of anisotropy. The most common type of anisotropy associated with ECM is the loss cone distribution. This type of distribution is found when electrons are energized in magnetic flux tubes that have converging legs whose footpoints are in high density regions and electrons with a particular pitch angle escape the flux tube [*Dulk, 1985*]. In the first step of the sequence of events for ECM, the electrons in the flux tube are accelerated or heated due to magnetic reconnection. Then, as the electrons spiral down to the mirror points of the flux tube, electrons with pitch angles smaller than some critical pitch angle value are lost; the other electrons are reflected back up into the flux tube. This results in an anisotropic distribution (i.e., loss-cone distribution) where there are fewer electrons with small, upgoing pitch angles (Figure 2.9).

The loss-cone anisotropy is the source of free energy. If a wave forces an electron to move from point 1 (higher energy) to point 2 (lower energy) in Figure 2.9, the released energy is given up to the wave. The wave then acts to organize the phase of the cyclotron motion in such a way that the electrons radiate in phase with the original wave. This is the similarity that the ECM has with masers or lasers. The “organization” is caused by a process known as relativistic phase bunching [*Treumann, 2006*]. Electrons moving along a strong magnetic field in the presence of a right-hand polarized electromagnetic wave are accelerated or decelerated by the transverse electric field. Acceleration depends on the rotation of the electron relative to the electromagnetic wave:

1. slower electrons will be accelerated,

2. faster electrons will be decelerated.

The bunching is due to the relativistic mass dependence of the electrons. This results in all electrons having the same phase angle as the wave. This is similar to the quantum coherency of regular masers. The electrons will then move together as a single macro particle. The radiation released by this macro particle is stimulated radiation since it's stimulated by an electromagnetic wave, which causes the electrons to be in phase and satisfy the resonance condition [Treumann, 2006]. The resonance condition that must be satisfied in order for gyroresonance emissions to occur is

$$\omega - \frac{s\Omega_e}{\gamma} - k_{\parallel}v_{\parallel} = 0 \quad (2.25)$$

where s is the harmonic number. For relativistic particles, equation 2.25 defines an ellipse with the major axis on the v_{\perp} -axis. For non-relativistic particles, the ellipse becomes a line and extreme anisotropies are required for growth. For mildly relativistic particles (500 keV), the equation becomes a semi-circle like the one shown

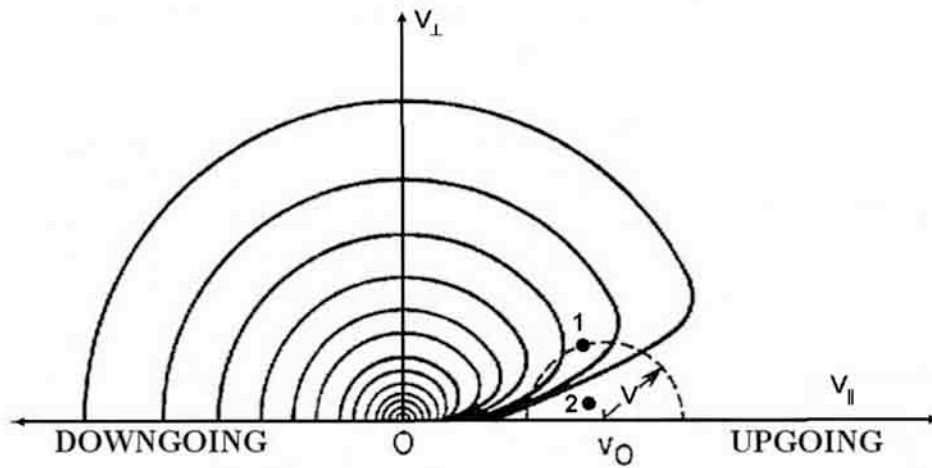


Figure 2.9: One-sided loss cone distribution contour. Modified from *Dulk* [1985].

in Figure 2.9. One type of observable ECM emissions are narrowband spikes [*Bastian et al.*, 1998]. These bursts were discovered in the early 1960s at around 300 MHz. They last less than 0.1 seconds and $\Delta v/v$ is less than a few percent. These emissions are related to flares and Type-III bursts and are observed in the corona (Figure 2.1).

2.7 Summary

The four mechanisms previously described make it easier to determine the source of the emission. Free-free bremsstrahlung is the dominant mechanism in the quiet sun regions, coronal holes, and sometimes in active regions. It dominates over other mechanisms in areas of high density or cooler regions, and at lower frequencies. Gyroemission is more dominant in the presence of strong magnetic fields and therefore dominates in active regions. Coherent emissions require anisotropic particle distributions, either through velocity dispersion or magnetic mirroring. Both of these conditions are usually caused by flares. Thus, plasma and electron cyclotron maser emissions are usually associated with flare activity [*Aschwanden*, 2004].

CHAPTER 3

THE RADIO SOLAR TELESCOPE NETWORK

The United States Air Force (USAF) currently operates four solar radio observatories spanned across the globe. The observatories monitor eight discrete frequencies and two frequency ranges 24 hours a day, 365 days a year using a 1-second time resolution. This chapter first looks at the history of these observatories, then it explains the generic concept of radio radio observations, followed by a detailed look at the instruments used by the USAF sites, examines a typical radio day at one of the observatories, discusses the burst classification system used by the USAF, and concludes with a look at the data generated by these sites.

3.1 Brief History of USAF Solar Radio Observatories

In the early 1960s, the National Aeronautics and Space Administration (NASA) together with the USAF and the National Oceanographic and Atmospheric Administration (NOAA) realized there was a need for a network of stations to observe the sun in optical and a wide range of radio wavelengths [Golightly, 2004]. The role within the Air Force fell to the Air Weather Service [Markus *et al.*, 1987]. Air Weather Service issued the first solar forecast in 1962 and established the Solar Forecast Center in Colorado Springs, Colorado soon after [English *et al.*, 1973; Markus *et al.*, 1987]. Part of the mission of the Solar Forecast Center was to monitor the sun 24 hours a day. This was achieved through the Solar Observing and Forecasting Network (SOFNET). The SOFNET included optical and radio observatories in Sacramento Peak, New Mexico; Sagamore Hill, Massachusetts; South Point, Hawaii; Athens, Greece; Manila, Philippines; Teheran, Iran; and Los Angeles, California. The first day of continuous operations was September 1, 1965 [Markus *et al.*, 1987]. Fast forwarding in time, through many political and operational changes, the USAF



Figure 3.1: Location of current RSTN sites.

now operates the Solar Electro-Optical Network (SEON). This network consists of five solar observatories. The optical observatories form the Solar Optical Observing Network and are located in Learmonth, Australia; San Vito, Italy; and Holloman Air Force Base, New Mexico. The radio observatories form the Radio Solar Telescope Network and are located in Palehua, Hawaii; Learmonth, Australia; San Vito, Italy; and Sagamore Hill, Massachusetts (see Figure 3.1).

The Sagamore Hill Observatory is the oldest one of the four radio sites. When it started operations, the observatory monitored five frequencies: 606, 1415, 2695, 4995, and 8800 MHz. In 1968, it started monitoring 15,400 MHz, followed by 245 MHz in 1969, and 410 MHz in 1971. Today, all four radio observatories monitor frequencies near the eight original frequencies (Table 3.1).

3.2 Why Observe the Radio Sun?

Before exploring the RSTN instruments and data, it is necessary to examine why solar radio data is observed in the first place and how this is accomplished. As

Table 3.1: Actual frequencies monitored by the USAF's RSTN sites.

Frequency	Palehua	Learmonth	San Vito	Sagamore Hill
245 MHz	247.71	245.97	245.47	245.00
410 MHz	400.04	410.92	390.47	410.00
610 MHz	609.71	609.33	617.79	609.00
1415 MHz	1416.16	1417.49	1415.61	1417.00
2695 MHz	2696.30	2695.95	2695.40	2696.00
4995 MHz	4965.60	4965.45	5020.56	4995.00
8800 MHz	8828.27	8827.46	8828.15	8827.00
15400 MHz	15372.06	15381.10	15429.47	15380.00

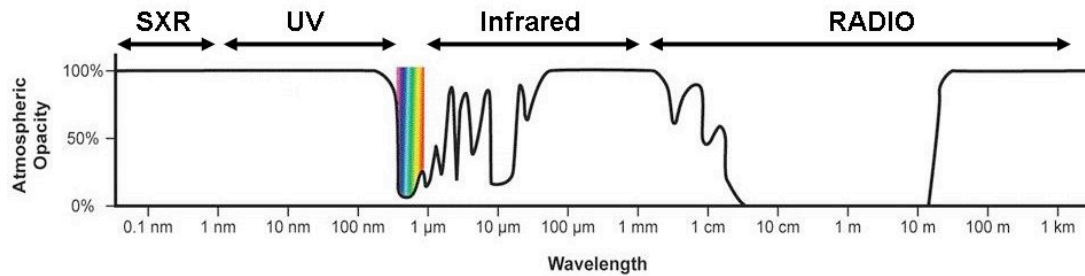


Figure 3.2: Energy from the sun in the radio spectrum can be measured by ground sensors since it is not absorbed by the planet's atmosphere.

already mentioned in the previous chapter, the sun emits energy through the electromagnetic spectrum. This energy travels through space and eventually arrives at Earth. Some of this energy interacts with the planet's atmosphere. For example, the energy in the x-ray band ionizes the neutral components in the atmosphere creating the D layer in the ionosphere, the energy in the UV band heats the stratosphere and mesosphere, and the EUV band is the major source of ionization in the E and F layers of the ionosphere. Any accurate measurement of these wavelengths has to be carried out by space-based sensors well above the earth's atmosphere. However, most radio energy is not absorbed by Earth's atmosphere and can be measured by ground sensors (Figure 3.2). This leads to simpler and less expensive instruments.

3.3 A Simple Radio Telescope

The simplest kind of radio telescope consists of an antenna connected by transmission lines to a receiver. The receiver amplifies the input from the antenna and sends it to a computer where the data can be analyzed and stored. The antenna is usually a parabolic reflector that concentrates the energy on a small receiving element placed on the antenna's focal point. These antennas usually have high directivity, meaning that they are most effective when they are pointed at the source, the sun in this case. The antenna needs to move in order to track the sun as it moves across the sky. This places a limitation on the practical size of antennas that can be used to observe the sun with a simple telescope. The size of the antenna depends on the resolution required of the telescope. When it comes to resolution, radio and optical telescopes are similar; the resolution depends on the ratio of the wavelength of light (radio) to the diameter of the lens (antenna)

$$\phi = \frac{\lambda}{D} \tag{3.1}$$

where ϕ is the angular resolution in radians, λ is the wavelength, and D is the diameter of the lens or antenna. When viewed from Earth, the sun has an angular resolution of $1/2^\circ$. To resolve the entire solar disc at a frequency of 245 MHz ($\lambda=1.2$ meters) the diameter of the parabolic dish would have to be 130 meters. This would not be practical or cost effective. There are various methods to get around this problem. If the resolution cannot be changed, then one can use a more complex instrument, such as an interferometer. These instruments are commonly used to map solar features which require higher resolution. If the main interest is to measure the emissions from the entire solar disk, then a smaller dish can be used as long as the antenna's beamwidth is increased. These emissions mentioned in the last example

are called the spectral flux density. The spectral flux density is what is received and measured by the radio telescope. According to *Kraus* [1966], the spectral flux density is the source intensity integrated over the solid angle subtended by the emitting source,

$$s_\nu = \int I_\nu d\Omega \quad (3.2)$$

where I_ν is the intensity of the source, and $d\Omega$ is the element of solid angle.

The units for flux density are watts per square meter per Hz or a jansky. The intensity of solar radio observations is very small, usually around $10^{-22} \text{ w m}^{-2} \text{ Hz}^{-1}$. This value is called a solar flux unit or SFU and is used to report solar radio emission values. The intensity in equation 3.2 for a blackbody is given by Planck's law,

$$I_\nu = \frac{2h\nu^3}{c^2} \frac{1}{e^{\frac{h\nu}{k_B T}} - 1} \quad (3.3)$$

where ν is the frequency,

T is the blackbody temperature in K,

k_B is Boltzmann's constant,

c is the speed of light, and

h is Planck's constant.

In the radio wavelength band, $h\nu \ll k_B T$, doing a series expansion, $e^x = 1 + x + \frac{x^2}{2!} + \frac{x^3}{3!} + \dots$ and $x \ll 1$, $e^x \approx 1 + x$, resulting in

$$e^{\frac{h\nu}{k_B T}} - 1 = 1 + \frac{h\nu}{k_B T} - 1 = \frac{h\nu}{k_B T}. \quad (3.4)$$

Thus, equation 3.3 simplifies to

$$I_\nu = \frac{2h\nu^3}{c^2} \frac{k_B T}{h\nu} = \frac{2\nu^2}{c^2} k_B T = \frac{2k_B T}{\lambda^2}, \quad (3.5)$$

which is the Rayleigh-Jeans Radiation Law. Assuming that the temperature is constant over the source, equation 3.2 becomes

$$S = \frac{2k_B T \Omega_e}{\lambda^2}. \quad (3.6)$$

In theory, the T in equation 3.6 is the effective temperature. This is the temperature that an object must have to generate the flux received at a certain frequency. In reality the temperature T in equation 3.6 is more than just the effective temperature. The signal that eventually arrives at the radio receiver will have the signal from the sun, as well as noise from the galactic and atmospheric background, ground radiation, noise from antenna feed losses, and injected noise from the receiver [*Tapping and Charrois*, 1994]. This combined noise is smaller than the signal received from the sun. Therefore, it is not necessarily a problem. However, since it does contribute to the overall signal, the noise contribution must be removed or must remain constant. In the case of the RSTN data, the noise contribution is treated as a constant that offsets the baseline. The temperature and humidity in the rooms housing the radiometers are constantly monitored and maintained at specific values. If these values are exceeded, the equipment is shutdown until the temperature and humidity return to acceptable values. *Kraus* [1966] provides additional details on antenna temperature, noise, and noise temperature.

3.4 The Radio Solar Telescope Network

The equipment used by the USAF to measure solar radio emissions is called the Radio Interference Measuring Sets (RIMS). The RIMS consists of three subsystems made up of parabolic reflectors (or “dishes”), antenna feed systems, tracking mechanisms, transmission lines, radiometer receivers, and computer systems. The



Figure 3.3: Palehua’s 28-ft dish is used to monitor 245, 410, and 610 MHz radio emissions from the sun. This picture shows the old tracking mechanism, that was replaced in late 2007.

first system consists of a 28-ft parabolic dish antenna with a log-periodic feed tuned to measure 245, 410, and 610 MHz (Figure 3.3). The antenna for the second system is an 8-ft parabolic dish with a multiple-element feed to measure 1415, 2695, 4995, and 8800 MHz (Figure 3.4). The last system’s antenna is a 3-ft parabolic dish with a waveguide fed diagonal horn for monitoring 15400 MHz (Figure 3.5).

3.4.1 Antennas

The antennas are mounted equatorially so the axis of rotation is aligned toward the celestial (north or south) pole. The angle from the plane perpendicular to this axis of rotation is called the declination angle (the North Star, Polaris, is at North 90 degrees declination.). The second reference needed to fix an object’s location in space is the Local Hour Angle (LHA), which is measured along the perpendicular



Figure 3.4: Palehua's 8-ft parabolic dish. This dish is used to monitor 1415, 2695, 4995, and 8800 MHz emissions from the sun.



Figure 3.5: 3-ft parabolic dish antenna at Palehua Solar Observatory is used to monitor 15,400 MHz. The antenna is mounted on top of the tracking mechanism.



Figure 3.6: Antenna control unit for the 28-ft dish.

plane (celestial equator) in hours and minutes. A full circle corresponds to 24 hours. Relative to an observer on the earth, the sun and distant celestial objects move one hour in LHA to the west per hour of time. During normal operations, the antenna follows the apparent solar movement on only one axis (LHA) automatically. However, the declination of the sun is constantly changing. When this happens, the signal strength begins to drop as the sun moves out of the field of view of the antenna. To compensate for this, the analyst must manually move the antenna to regain the strongest signal possible. This is done throughout the day, but more often during sunrise and sunset. All antenna movement, whether automated or manual, is achieved through two sets of synchronous motors installed in the antennas and in the antenna control units. The control units enable the display dials to indicate the precise orientation of the antenna in LHA and declination angle. Through the antenna control units, the duty analysts can move each antenna as needed (Figure 3.6).

To transfer the energy from the feed to the receiver system, special transmis-

sion lines are used: pressurized, shielded coaxial cables are used for frequencies lower than 8800 MHz, and waveguides for 8800 MHz and higher frequencies.

3.4.2 Radiometers

The sun is a strong source of radio energy emission. However, the solar radio power received at earth is very small compared to that received from terrestrial sources, such as radio and television stations. Therefore, the receivers (radiometers) used to detect and measure solar radio emissions must be very sensitive, with minimal internal sources of sensitivity (or gain) variability.

The radiometers used in the RIMS telescopes are designed to minimize equipment gain changes. The room housing the radiometers is climate controlled to reduce environmental impacts on the radio which could cause large gains on the signals. The sensitivity of the radiometer can be varied through the use of several gain channels for each discrete frequency, so that a wide dynamic range of solar emissions can be recorded. After the broadband radio frequency (RF) signals are received by the antenna, the antenna feed converts the radio energy from the desired frequency range into an electrical signal, which is fed through a waveguide or coaxial cable to the radiometer. Once at the radiometer, the signal is modulated to a reference signal generated by the radiometer's amplifier. The modulated signal then goes through a crystal mixer. The output from the mixer is then routed to a primary amplifier (a secondary amplifier is used for solar signals that exceed the capacity of the primary amplifier). The output from the amplifier is a DC voltage proportional to the sun's signal. This voltage is sent to the computer where the signal is converted to solar flux unit and analyzed. The Windows-based computer has a National Instruments IEEE-488.2 PCI interface card to connect to the radiometers.

3.4.3 Calibrations

Radio telescopes must be calibrated to compensate for internal equipment variations in the antennas, cabling, and radiometers in order to accurately measure solar emissions. To calibrate the radiometer, a calibration signal can also be fed into a radiometer through a directional coupler. The calibration signal is produced by a solid-state device (commonly called a noise tube (NT), even though it is no longer physically a “tube”). When energized, it generates RF noise at a known and constant output. The NT signal, or some other calibrated synthetic signal, is necessary to accurately calibrate a radiometer and compensate for long-term gain instability. There are daily, absolute, and linearity calibrations performed on the systems.

Daily system calibrations are used to establish the solar flux unit (SFU) per volt conversion factors and baselines for the computer each day. The daily calibration is typically performed before sunrise and at local noon. The first step in the daily calibration is to move the antenna two hours west (ahead) of the sun. Doing this allows the system to get a “cold sky” reading. The next step is to turn on a calibration signal. These two steps establish two voltage reference points:

1. a “sky” baseline voltage, and
2. a voltage increase from the known calibration source.

The sky baseline voltage represents zero solar flux units above system noise, and all received signals are then referenced to this voltage. Then, the antenna is repositioned so that the sun will drift into view as it moves across the sky. As the sun enters the field of view of the antenna, the baseline of a particular frequency will start to increase until it peaks. Once the antenna peaks, the analyst will re-engage the antenna’s tracking mechanism so it will continue to follow the sun. The peak value

measured will be the “draft” daily flux value. All eight values (one “draft” daily flux value for each frequency) are then quality controlled by the analyst to make sure they are realistic values. Since the quiet sun and the slowly varying component are not expected to change significantly from day to day, the analyst compares the values from his observatory’s calibrations to the calibrations performed during the last 24 hours by the other three observatories. Any frequency that differs by more than 10% from the average of the other three observatories’ calibrations is subject to further calibration. If the value exceeds the 10% threshold when compared to the other observatories after a second attempt at calibration, the value is considered “uncertain.” The values for all eight frequencies are then assigned a quality of observation code. All values that fall within the 10% parameter are coded as “good.” All “uncertain” values are coded as uncertain due to weather, local radio interference, flare in progress, or unknown reasons. These measurements are then reported as the daily flux values for that observatory’s frequency to the Air Force Weather Agency at Offutt Air Force Base, Nebraska. From there, the values are transmitted to other users, one of them being the Space Weather Prediction Center (formerly known as the Space Environment Center (SEC)) at Boulder, Colorado. The Space Weather Prediction Center decodes the messages from the observatories and sends the data to National Geophysical Data Center (NGDC) for archiving. Unfortunately, somewhere along the way, the code describing the accuracy of the data is lost and only the SFU reading for the daily value is stored in the database. This is a potential problem for anyone using the daily values since the records will include erroneous values.

The noise tube (NT) value is used during daily system calibrations, and its accuracy is essential for consistent burst and daily flux value data throughout the network. A new NT value (in SFU) is calculated after a correction factor is derived

from comparing several days worth of data from the entire network, to the daily flux value of the observatory doing the calibration. The Absolute NT Calibration requires continuously quiet solar conditions (same sun). Typically, absolute calibrations will be performed during, or shortly after, solar minimum.

Linearity calibrations are performed to correct for inherent deficiencies found in the radiometers. Normally, all solar activity is converted to a DC voltage by the primary amplifier. Large bursts which exceed the range of the primary amplifier are handled by the secondary amplifier. This calibration matches DC voltages to SFUs between the radiometer and the software used to display and analyze the data. It also determines the range of the primary amplifier and the SFU value beyond which the response of the radiometer is non-linear.

3.5 A “Typical” Radio Day

Figure 3.7 shows the raw data for all eight discrete RIMS frequencies from the Palehua Solar Observatory. At local sunrise (~ 1600 UT) the signal appears much weaker and eventually increases to a steady baseline. At sunset (~ 0400 UT) the signals appear to gradually get weaker and eventually completely drop off. There are two main reasons for this:

1. the radio sun has different diameters (higher frequency, smaller diameter) so the lower frequencies (emitted from higher up on the sun’s atmosphere) are picked up earlier (and monitored longer) by the radio telescope
[Das et al., 2000],
2. the antenna tracking system does not account for the sun’s declination angle and therefore is “off” track.

Figures 3.8 and 3.9 show sunrise and sunset in more detail.

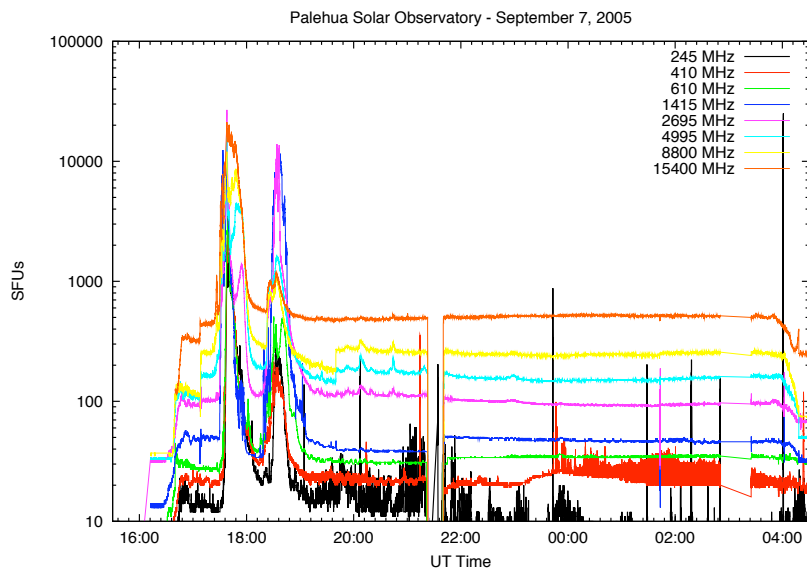


Figure 3.7: Raw data from Palehua Solar Observatory for September 7, 2005.

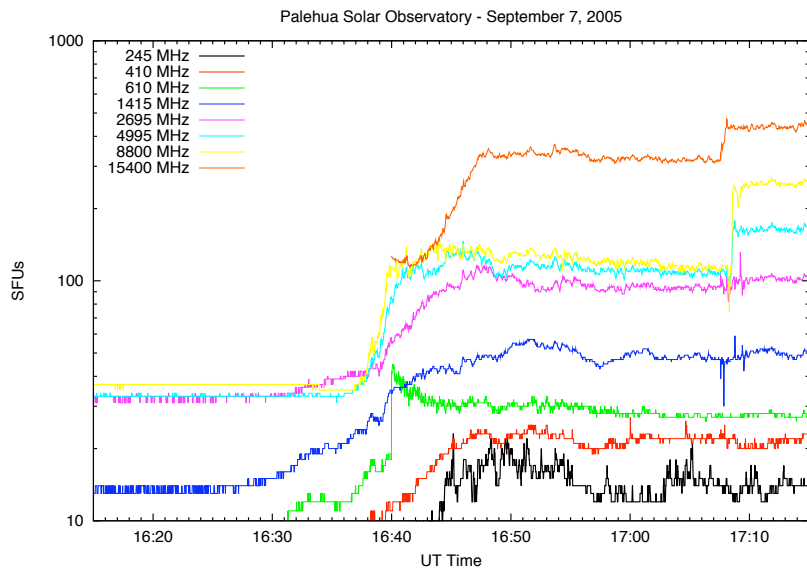


Figure 3.8: Start of radio patrol at the Palehua Solar Observatory on September 7, 2005. The 28-ft antenna (245, 410, and 610 MHz) was "peaked" around 1703 UT. This is necessary to account for the sun's declination. The 3-ft antenna (15400 MHz) was peaked around 1707 UT and the 8-ft antenna (1415, 2695, 4995, and 8800 MHz) was peaked at 1708 UT.

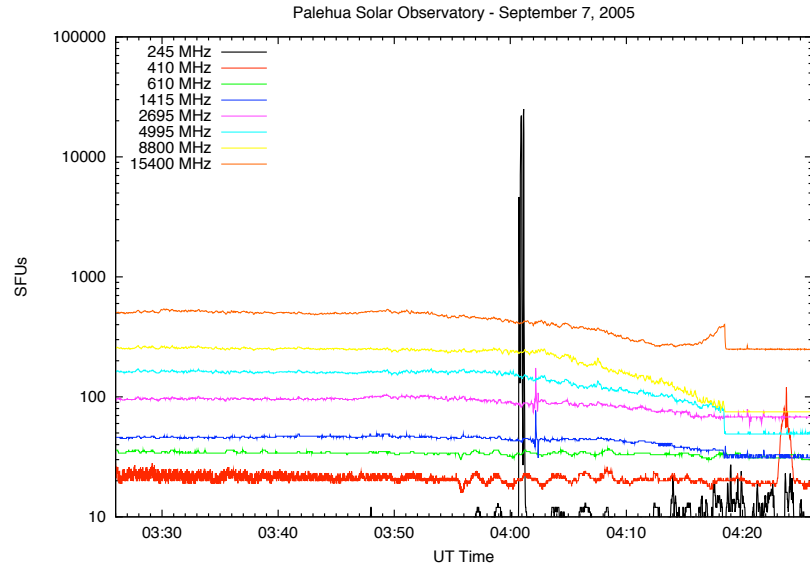


Figure 3.9: At the end of the patrol day, the 3-ft (15400 MHz) and 8-ft (1415, 2695, 4995, and 8800 MHz) “lose” the sun starting around 0400 UT. This is due to the antenna’s tracking mechanism.

On this same day, a flare was observed around 1725 UT (Figure 3.10). This particular flare was observed in all eight discrete frequencies and had two peaks, and lasted around two hours (radio burst classification will be discussed later in this chapter).

Around 2130 UT there is a data gap that lasts around 20 minutes (Figure 3.11). This gap is due to the daily noon calibration of the equipment discussed in the previous section. After this calibration is performed, each observatory transmits the daily flux value for each frequency. This value is then archived at NGDC and is available on-line.

The last set of features from Figure 3.7 that needs to be explained is radio frequency interference (RFI). With the advances in communications technology, the electromagnetic spectrum has become very crowded. The radio frequencies used by USAF’s RSTN are designated and reserved for radio astronomy. Unfortunately,

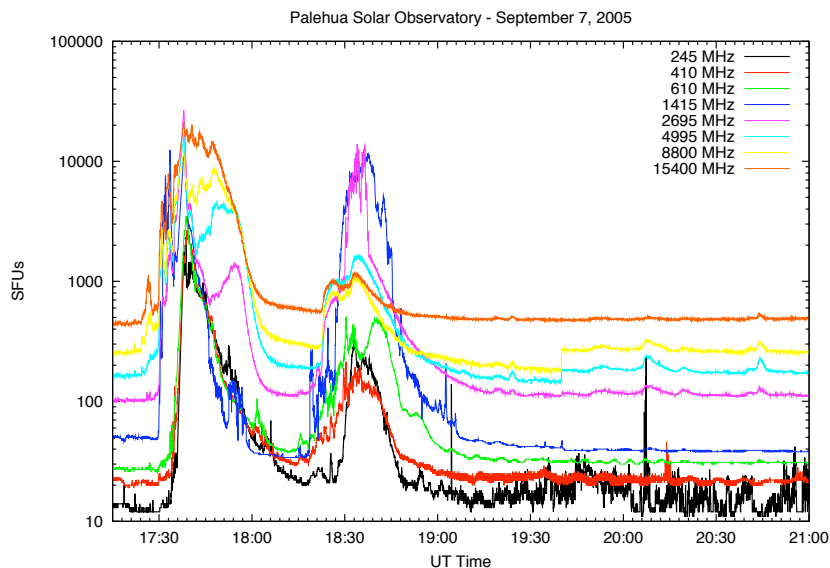


Figure 3.10: A complex burst observed at Palehua Solar Observatory. This was associated with an X 17.0 flare observed by GOES 10.

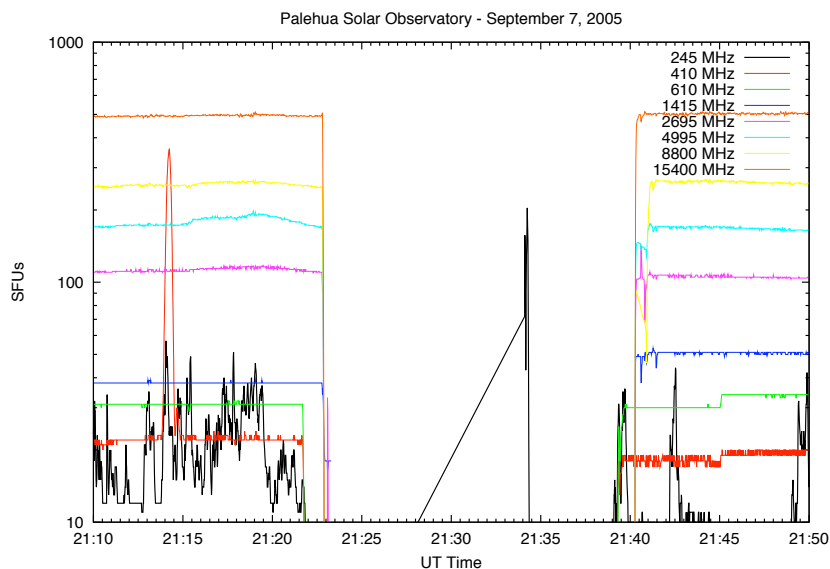


Figure 3.11: The noon calibration shows up as a data gap in this plot. During this time, data is collected by the radiometers but it is not analyzed in the same way as during other times of the day. The result of this calibration is a new baseline for each frequency as well as the daily flux value for each frequency.

that has not prevented some encroachment into these frequencies by others users. Some of this RFI comes from radars, television stations, citizens band radio, aircraft communications with the air traffic control tower, or shipboard systems. There are also naturally occurring RFI, such as lightning discharges. Some observatories have very localized RFI. For example, lawnmowers used by Palehua Solar Observatory's personnel caused RFI on 245 MHz. Distinguishing RFI from solar activity can be difficult. The observatories use the following guidelines to help distinguish between RFI and solar activity.

1. Know the local area, what systems are around the observatory, and their operation patterns.
2. Analyze the burst. RFI is usually narrow band and much more impulsive than the most impulsive solar radio bursts.
3. Look for similar activity on adjacent frequencies. Most RFI does not correlate on multiple frequencies.
4. Monitor local weather conditions.
5. Correlate signature with other observatories.

Some examples of RFI at the Palehua Solar Observatory are shown in Figure 3.12. As already mentioned, one way to distinguish RFI from solar activity is to know the local area. Palehua is located on the west coast of the island of Oahu, Hawaii. A few miles south of the observatory is the approach pattern for the Honolulu International Airport. The individual spikes on 245 MHz seen throughout the day are more than likely due to airplane to air control tower communications. Notice that these spikes are not seen on 410 or 610 MHz. This is because RFI is usually narrow-banded while solar activity is commonly seen on more than one adjacent frequency. Another RFI feature is seen from 0000 UT to around 0200 UT on 410 MHz.

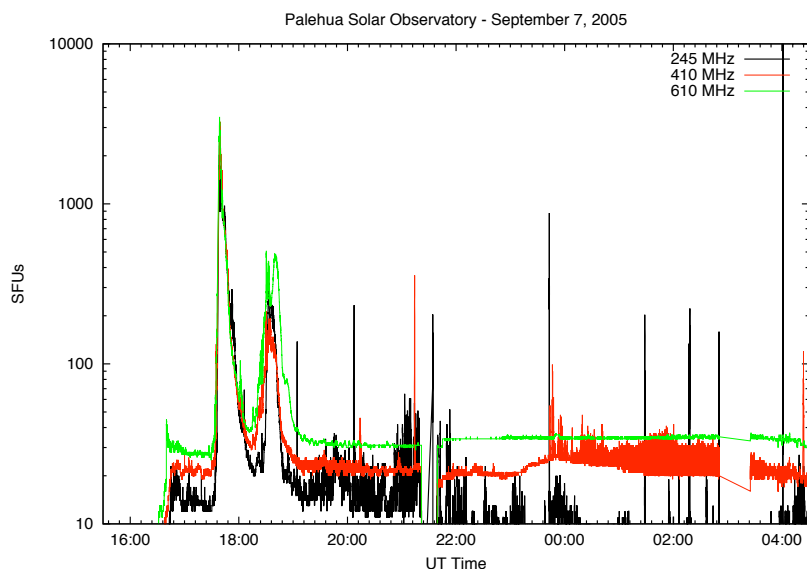


Figure 3.12: Examples of radio frequency interference at the Palehua Solar Observatory.

This was identified as activity from a US Army training range also located on the west coast of Oahu. This range usually conducted training exercises in the afternoon. Again, notice that this feature, unlike the flare, is not seen on 245 or 610 MHz.

There is one final feature in Figure 3.12 that bears mentioning. Around 0300 UT there is a data drop-out on the three lower frequencies (28-ft dish). Due to the size of the dish and the nature of the tracking mechanism, high winds force the observatories to take precautions to prevent damage to the equipment. When the critical wind speed is first observed, the 28-ft dish is stowed in a horizontal position, making the dish look like a gigantic bird bath. While in stowed position, data is not collected.

3.6 Burst Morphology

The RSTN frequencies cover the centimeter wavelength range (15400, 8800, 4995, and 2695 MHz), the decimeter wavelength range (1415, 610, and 410 MHz)

and the meter wavelength range (245 MHz). Many studies and books have been written about solar radio observations. Both Covington and Tanaka developed classification systems for discrete bursts [Coffey and McKinnon, 1987]. Kundu [1965] devotes several chapters to centimeter, decimeter, and meter wavelength bursts in his book. Additionally, papers by Güdel and Benz [1988] and Isliker and Benz [1994] are samples of descriptive spectral classification systems for radio bursts in the 1-3 GHz range. Appendix A provides an overview of the standard classification system for radio bursts. To ensure consistency among the RSTN observatories, the USAF developed a morphological classification system for the bursts it measures. This system is simpler version of the classification system developed by H. Tanaka for the Solar Geophysical Data reports [Coffey and McKinnon, 1987]. Although the RSTN frequencies span three “wavelength regions,” for practical purposes they can be grouped together when it comes to descriptive classification. The same type bursts seen on the centimeter are seen on the decimeter wavelength range. One difference is that on the decimeter range, sometimes there are more short period fluctuations [Kundu, 1965]. In general, the discrete bursts measured by the RSTN sites vary considerably in duration (from a fraction of a minute to over an hour), intensity (from a few SFUs to a quarter million SFUs), and profile (from simple to complex). For simplicity and consistency among the reporting sites, these bursts are grouped in three broad classes: Impulsive, Gradual Rise and Fall (GRF), and Noise Storm.

3.6.1 Impulsive Bursts

The impulsive bursts are divided into four types according to intensity and profile:

1. “Impulsive” = Intensity less than 500 SFUs; only one peak within 2 minutes (Figure 3.13).

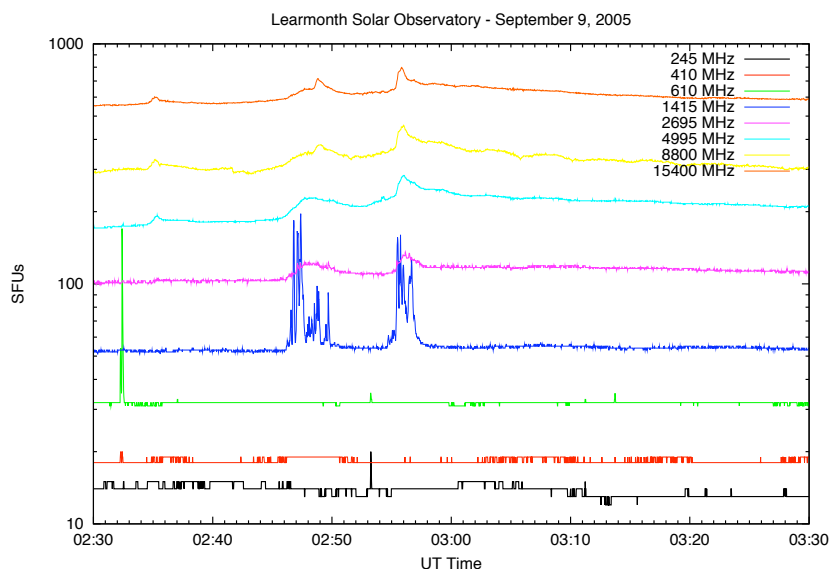


Figure 3.13: Impulsive bursts observed at the Learmonth Solar Observatory on September 9, 2005. There is RFI around 0232 UT on 610 MHz, and a complex burst on 1415 MHz around 0245 UT.

2. “Complex” = Intensity less than 500 SFUs; one or more secondary peaks.
3. “Great Burst” = Intensity 500 SFUs or greater; only one peak within 2 minutes (Figure 3.14).
4. “Complex Great” = Intensity 500 SFUs or greater; one or more secondary peaks (Figure 3.15).

Impulsive bursts are normally associated with the sudden flash phase of a flare and generally arise from the low corona in the close magnetic field lines of active regions [Dulk, 1985]. There is strong evidence that the radio energy is produced by flare-accelerated electrons spiraling about magnetic field lines in a field of several thousand gauss [Dulk, 1985]. This non-thermal mechanism can produce very intense, but generally brief, releases of radio energy. “Complex” bursts have a primary peak and one or more secondary peak(s). Complex bursts will typically be associated with the larger flares. The rise to maximum intensity normally occurs in about a minute

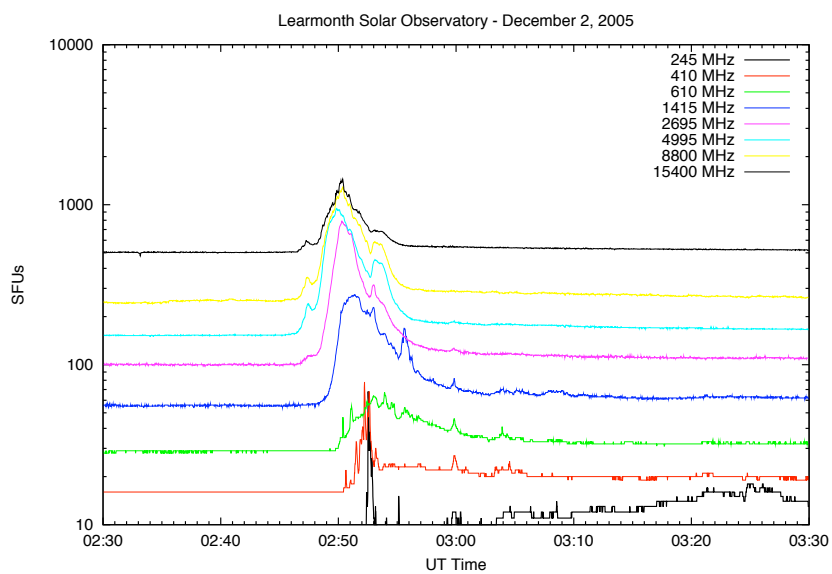


Figure 3.14: Great Burst observed at Learmonth Solar Observatory on December 2, 2005.

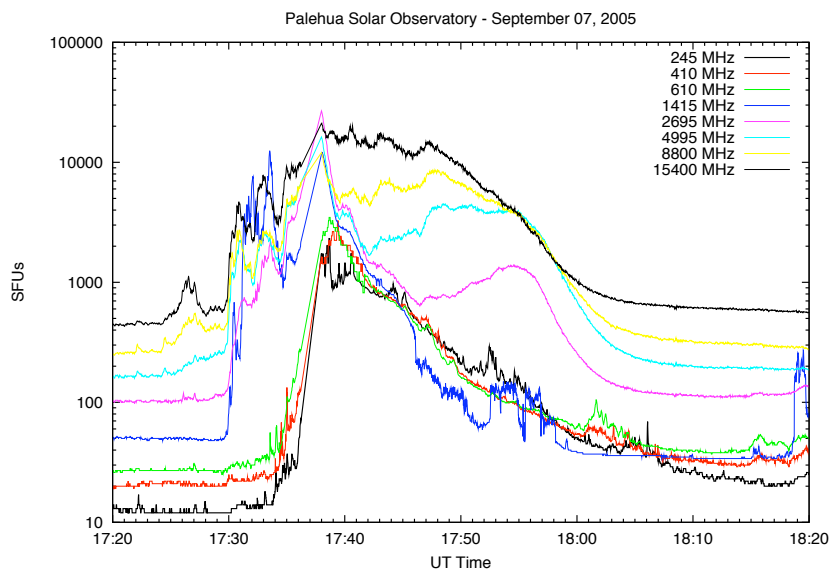


Figure 3.15: Great Complex bursts at Palehua Solar Observatory on September 7, 2005.

or less, and peaks at different frequencies almost simultaneously. The decay to pre-flare intensity is more gradual than the rise, and may take a few tens of minutes, or even hours. Complex bursts tend to have longer durations and be more intense than simple profile bursts.

3.6.2 Gradual Rise and Fall

Gradual rise and fall (GRF) bursts involve thermal mechanisms and is the reason why GRFs tend not to be very intense, but can last for hours [Kaufmann, 1971]. During a GRF burst, magnetic fields in an active region distort and in doing so, they compress and heat charged particles. These particles increase their thermal radio output (the gradual rise). As the magnetic fields later relax and release the compressed particles, the thermal output declines (the gradual fall) [Kundu, 1965]. Thus a GRF differs from the Slowly Varying Component (SVC) mentioned in Chapter 2 only in its shorter time scale (a few tens of minutes to several hours for a GRF, compared to days to weeks for the SVC). GRF bursts rise at a slow (non-impulsive) rate, then decline slowly to the normal quiet sun (baseline) level. Their profiles are generally very smooth and often occur on several adjacent frequencies simultaneously (Figure 3.16).

3.6.3 Noise Storms

Noise storms originate in the upper portions of the solar atmosphere, in regions that are associated with active regions [Kundu, 1965]. Noise storms can last from several hours to several days and are usually observed in the 50 to 300 MHz range [Dulk, 1985]. The intensity of the enhanced noise storm continuous emission can occasionally be many times the normal background (or baseline) on a discrete frequency (Figure 3.17). On discrete frequency RIMS radiometers, noise storms are

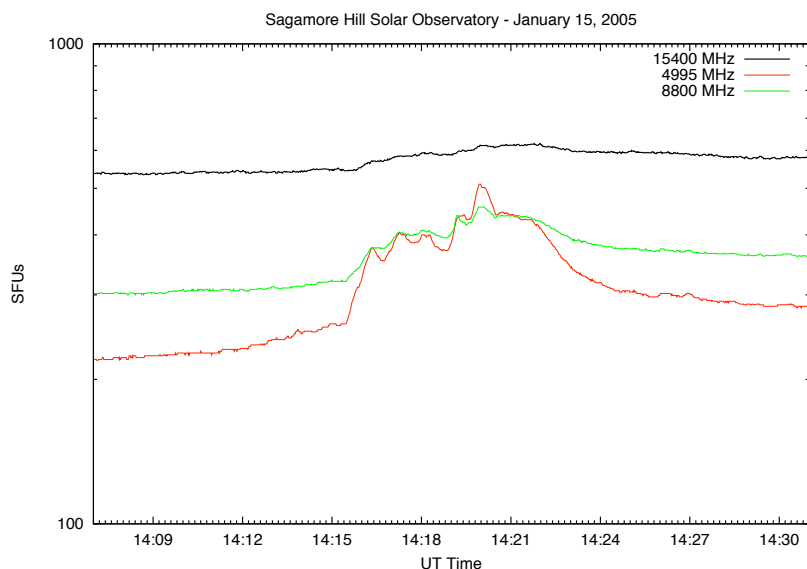


Figure 3.16: A gradual rise and fall (GRF) burst observed by the Sagamore Hill Observatory on January 15, 2005 on 15,400 MHz.

detected at 245 and sometimes on 410 MHz. Noise storms normally have two components:

1. a slowly varying, enhanced continuous emission over and above the usual quiet sun baseline for a frequency,
2. an irregular series of numerous, closely spaced, spiked peaks.

Noise storm peaks are measured relative to the pre-storm baseline, so that they will include both the enhanced continuous emission and the spiked components.

3.7 RSTN Data

The sites are operated and calibrated to support military operations. The main purpose for the data generated by these sites is also for military operations. This could cause a conflict when using the data for research purposes. For example, calibration is not completely performed in the way suggested by the experts in the radio community [*Tanaka et al.*, 1973]. Additionally, not all bursts are reported.

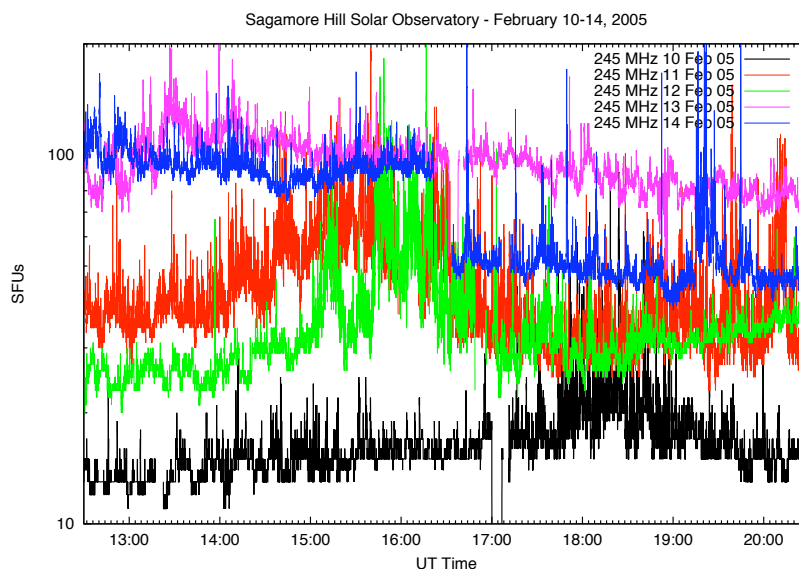


Figure 3.17: A noise storm is observed by the Sagamore Hill Observatory on February 11, 2005. The normal baseline for 245 MHz is shown for February 10, 2005. The noise storm started sometime on February 11, 2005 and lasted several days.

Bursts must exceed 50 SFU before they are reported by a site. Furthermore, the raw data is not available in real-time for research. Each observatory archives its data daily. At the end of the month, the entire previous month's data is sent to NGDC for archiving. Solar activity and daily flux values are transmitted real-time to the Space Weather Branch at the Air Force Weather Agency, Offutt Air Force Base, Nebraska. From there, the data is shared real-time with the Space Weather Prediction Center. The Space Weather Prediction Center then makes the data available through their website and by other means. On the positive side, the burst activity undergoes multiple quality control steps. Each observatory examines their transmitted messages to ensure proper coding and dissemination. Also, each observatory compares their products with the other three observatories. Any discrepancy is discussed among the sites and with the Space Weather Branch. Each observatory performs their own maintenance on a regularly scheduled basis. In addition to this maintenance, a

traveling team of expert maintainers based at the Palehua Solar Observatory travels to each site twice a year for more in-depth maintenance.

CHAPTER 4

DAILY SOLAR PROXIES

The F10.7 index is often used as a proxy for solar UV and EUV radiation. This chapter reviews the solar proxies and shows how RSTN data could be used as an additional daily proxy by first showing agreement between F10.7 measurements and RSTN data and then showing correlations between radio and UV data.

4.1 Introduction to Solar Activity Proxies

Solar ultraviolet radiation (UV) affects the earth's atmosphere. The solar EUV flux ($\lambda \sim 10\text{-}120$ nm) originates between the transition region and the solar corona, while UV ($\lambda \sim 120\text{-}400$ nm) comes from the transition region, the chromosphere, and upper photosphere [Floyd *et al.*, 2005]. Both of these energy ranges are the primary cause of ion production in the ionosphere and also partially responsible for heating of the thermosphere [Kane, 2002]. For these reasons, solar EUV emissions cannot be measured by ground instruments and can only be measured by space-based sensors. The space-based sensors are expensive and the sensitivity of the instruments degrades as a result of the exposure to the UV and EUV radiation [Floyd *et al.*, 2005]. As a result, EUV measuring instruments are not always available. This causes large gaps in the measuring of EUV, including the "EUV hole" from 1981 to the mid 1990s [Tobiska, 1996]. Since this data is not always available, many scientists have tried to establish a correlation between solar proxies and solar EUV activity. For over 100 years, the Wolf or Zurich sunspot number has been used as an index of solar activity. The sunspot number is a combination of the number of sunspot groups and the number of individual spots within a group [Covington, 1969]. Additionally, there is a correction factor to account for variations between observatories making these measurements. This index, with slight variations depending on who is

computing, goes back to 1755, the minimum of solar cycle 1. In 1947, the National Research Council of Canada began taking daily flux density measurements of the sun at 2800 MHz ($\lambda = 10.7$ cm). These measurements were made at the Algonquin Radio Observatory near Ottawa, Canada until May 31, 1991. The observing program was then moved to the Dominion Radio Astrophysical Observatory, near Penticton, British Columbia where it continues to operate today. The procedures for measuring this flux density are similar to the ones discussed in Chapter 3 for the RSTN sites. Detailed discussion of the observing technique and the calibration of the equipment can be found in articles written by *Tapping and Charrois* [1994] and *Tanaka et al.* [1973]. This measurement is not an average of the sun's daily variation, but a snapshot of the sun at the time the measurement is taken. The 10.7 cm flux density measurement is commonly referred to as the $F_{10.7}$ or F10 and is a combination of solar components. The quiet sun is always present as well as contributions from the slowly varying component and bursts from flares. Corrections are made to the flux value to remove any burst activity [*Tapping and Charrois, 1994*]. The units for this daily index are the same units used by the RSTN observatories, i.e., solar flux units.

The correlation between sunspot and solar radio emissions in the centimeter wavelength range was discovered independently by Covington and Lehany. It was not long before the F10 became a proxy for solar activity. Later research showed that the F10 could be used to model UV and EUV [*Bossy, 1983*]. As a result, space physics models routinely use the F10 index as the proxy for solar activity. Since this index is a daily value, models either update the solar input once a day, or use a linear interpolation between days to adjust the indices throughout the model run.

4.2 Observations of the Sun

Between 19 July 2005 and 27 October 2005, there were four solar rotations. Although the term solar rotation seems very straightforward, it could have different meaning depending on which solar parameter is being observed. On average, the sun rotates on its own axis every 27 days at the equator. This number is slightly lower at the poles. For the purposes of this discussion, solar rotation starts with a minimum in the F10.7 index and ends with the next observed minimum (which is the start of the next rotation) as shown in Figures 4.1 and 4.2. The first rotation started out with no visible sun spots on the solar disk until 23 July. This region grew quickly and started producing flares by 27 July. During this rotation there were a total of 21 C-class flares, 7 M-class flares, and 1 X-class flare as measured by GOES (see Appendix B for a description of GOES data). The second rotation also started out with very low activity. However, activity increased as one of the solar regions grew in size and complexity around 23 August. This rotation had 17 C-class flares and 5 M-class flares. The third rotation was the most active of the four rotations included in this study. Again, this rotation started with low activity, but there were indications that an active region was due to rotate back into view. This complex region rotated into view on 7 September. The third rotation had a total of 84 C-class flares, 26 M-class flares, and 10 X-class flares. The fourth rotation had very little activity and concluded with no visible sun spots on the disk and only 3 C-class flares. Table 4.1 shows the break down of the flares according to each rotation and Figure 4.1 shows when the flares occurred in relation to the solar rotations. Figure 4.2 shows this time period as observed with various daily solar indices. While all data sets clearly show the four rotations, variations among them are clearly seen. For example, the number of sun spots as reported by SEC peaked during the first rotation (Figure 4.2) while the

sun spot area and GOES x-ray background peaked on the third rotation. Figure 4.3 shows the TIMED-SEE daily measurements for the same time period. This data set also shows the four rotations and it also shows variability among the rotations. The smaller wavelengths show more variability.

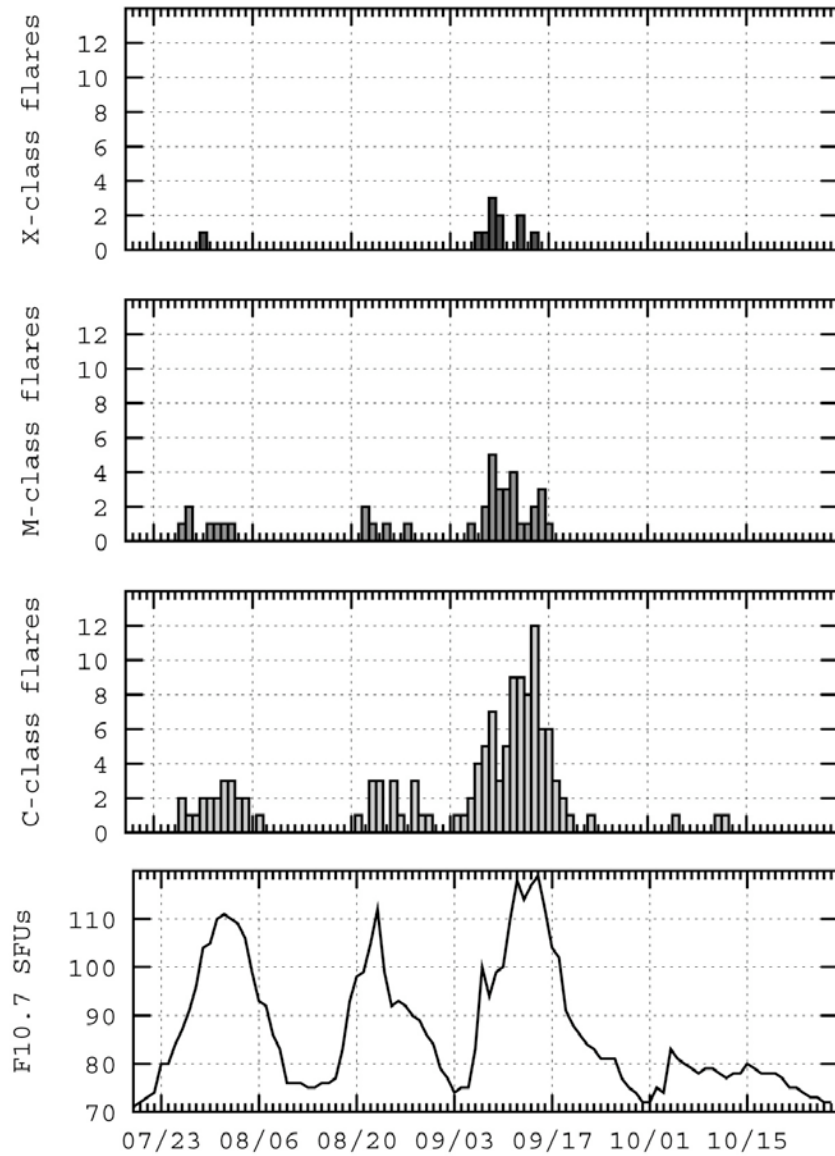


Figure 4.1: Solar flares relative to the four solar rotations in 2005.

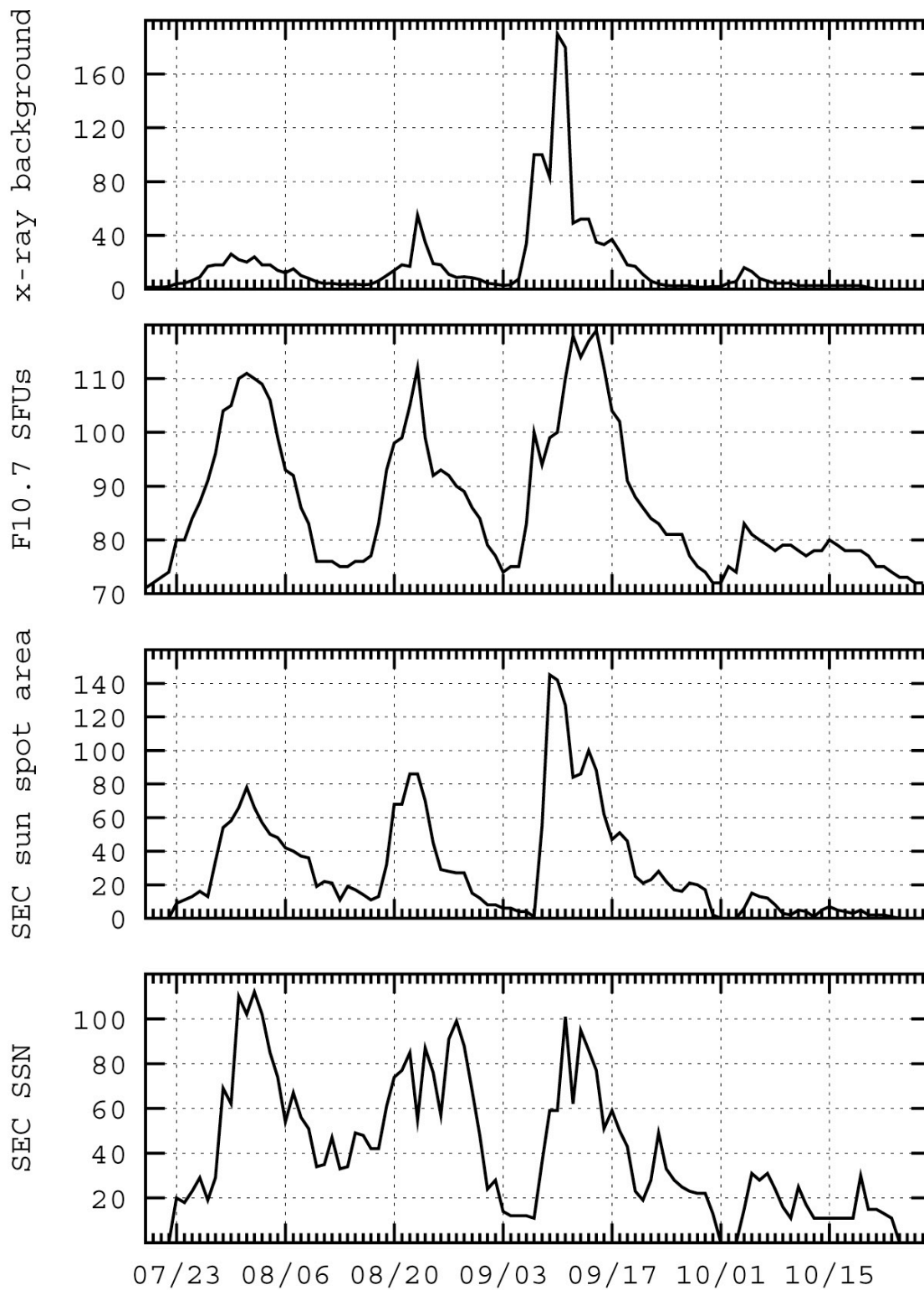


Figure 4.2: Four solar rotations as measured by different solar indices in 2005.

Table 4.1: Solar flares observed by GOES during July 19, 1995 to October 27, 2005.

Rotation	C-class	M-class	X-class
1	21	7	1
2	17	5	0
3	84	26	10
4	3	0	0

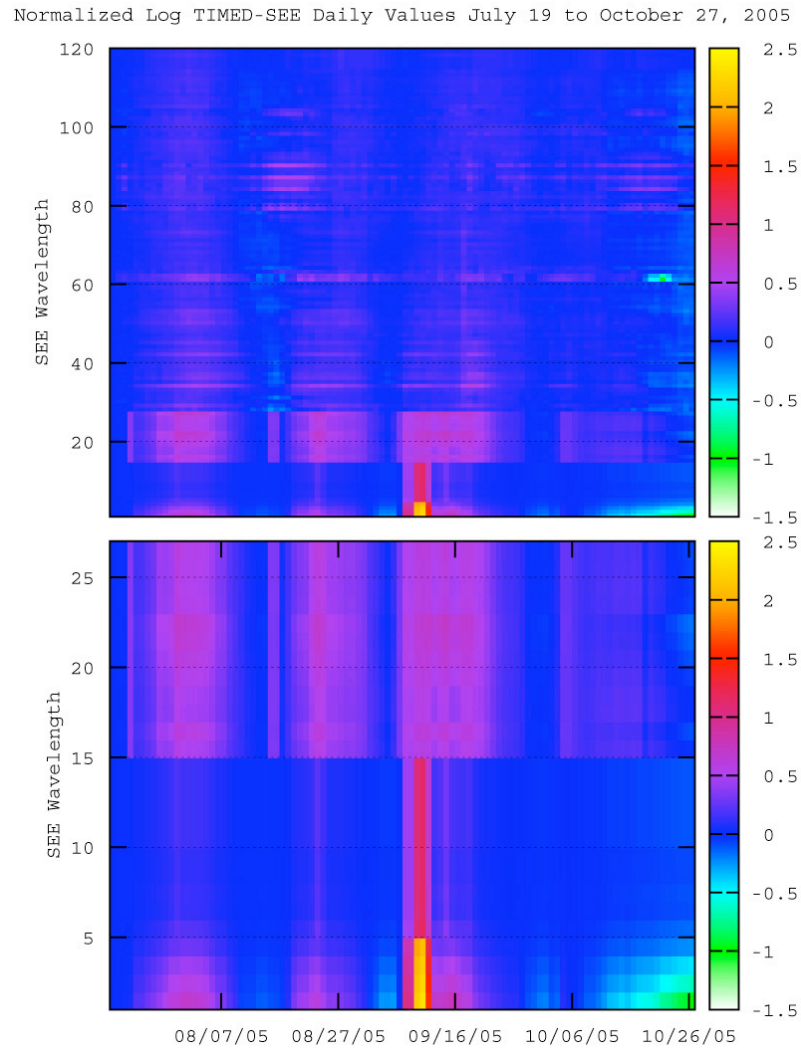


Figure 4.3: TIMED-SEE Data. The first three solar rotations are clearly seen by the increased activity. The fourth rotation (around 10/26/05) does not show as much activity.

4.3 Reported and Computed Daily RSTN Flux Densities

As discussed in Chapter 3, the RSTN sites calibrate their radios daily during their local noon. Part of this calibration includes measuring the daily flux density for each frequency. This value eventually becomes part of the database in NGDC. Unfortunately, the data quality code associated with each measurement is not part of the database. As a result, values that are suspect or incorrect are included in the data. Before exploring any relation between RSTN radio and EUV data, it is necessary to validate the RSTN data. The easiest way to understand this is to compare it to the radio standard, the F10 index.

Figures 4.4 through 4.11 show the reported RSTN daily flux values compared to F10.7. In all frequencies except 15400 MHz, the four solar rotations are clearly visible. Another feature that is present in all eight frequencies is missing data (e.g. Palehua and Learmonth's 245 MHz on August 20, Figure 4.4). There are several reasons for this feature. If there is a flare or noise storm in progress, the noon calibration is supposed to be delayed or not performed. In such instances, there would not be a daily flux value reported for the frequency that was not calibrated. Maintenance issues or equipment problems would also keep an analyst from performing the noon calibration with similar results. Another issue present in almost all the frequencies is contamination of the daily flux value with flare emissions. Probable contamination of the daily flux value due to a flare is seen on Sagamore Hill's 2695 and 4995 MHz plot on August 22 (Figures 4.8 and 4.9). If the flare was in progress before the calibration was started, the calibration should not have been performed at that time. On the other hand, if the flare started after the calibration was in progress, the daily flux value should (and probably was) coded as a bad value during the station's quality control. However, since the data code is not stored in the NGDC database, the exact

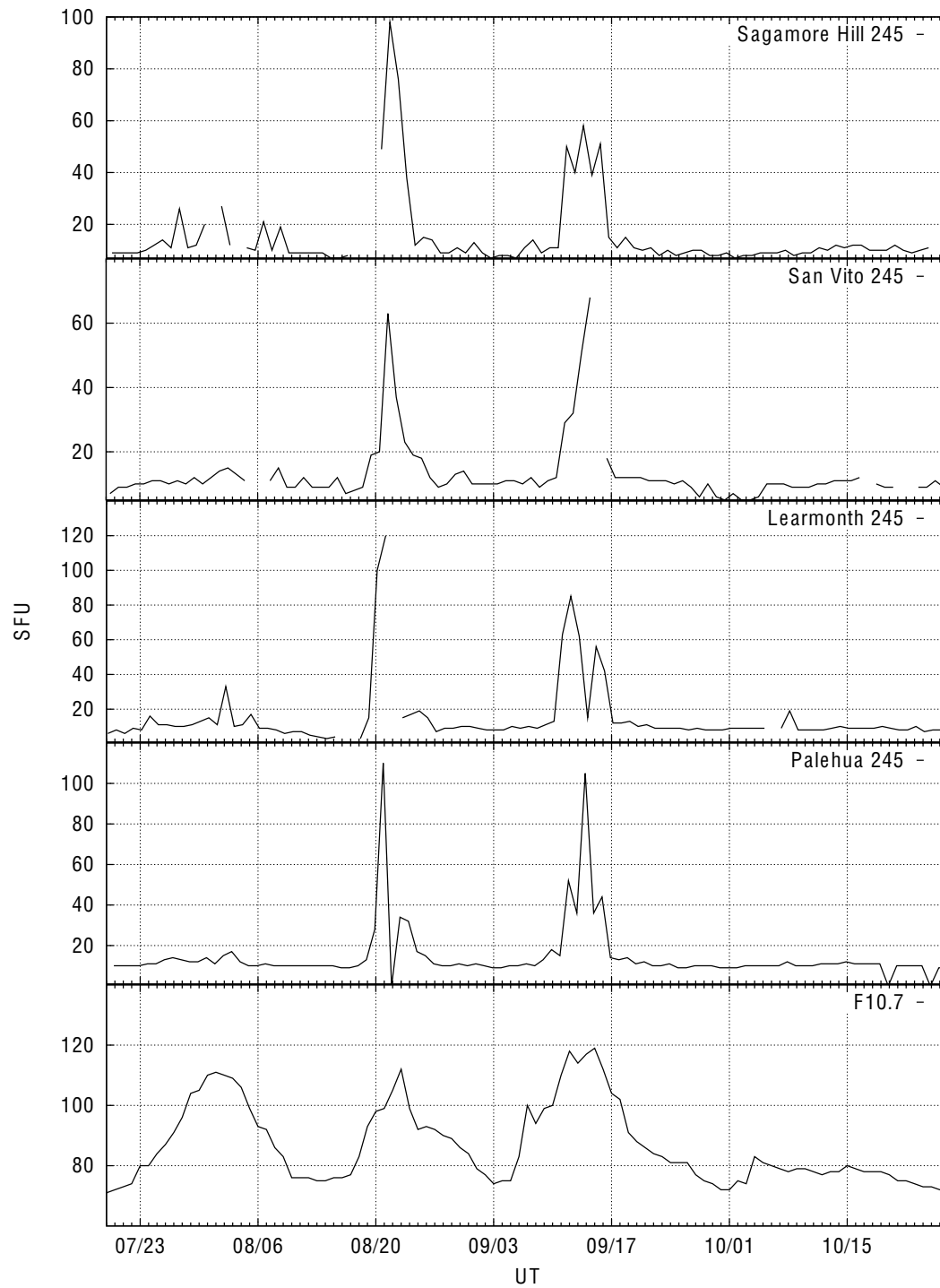


Figure 4.4: RSTN 245 MHz during the four solar rotations.

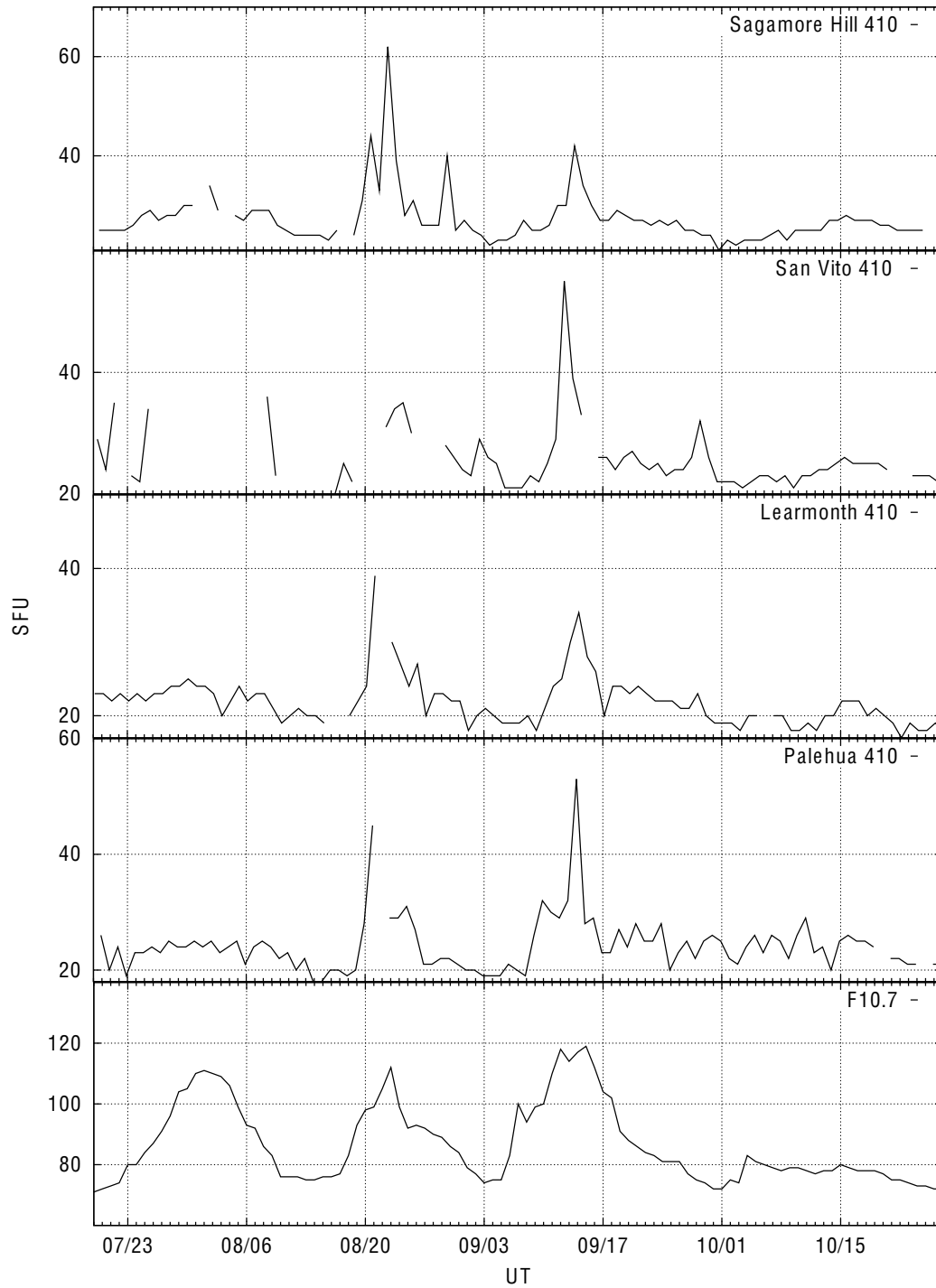


Figure 4.5: RSTN 410 MHz reported daily values compared to F10.7.

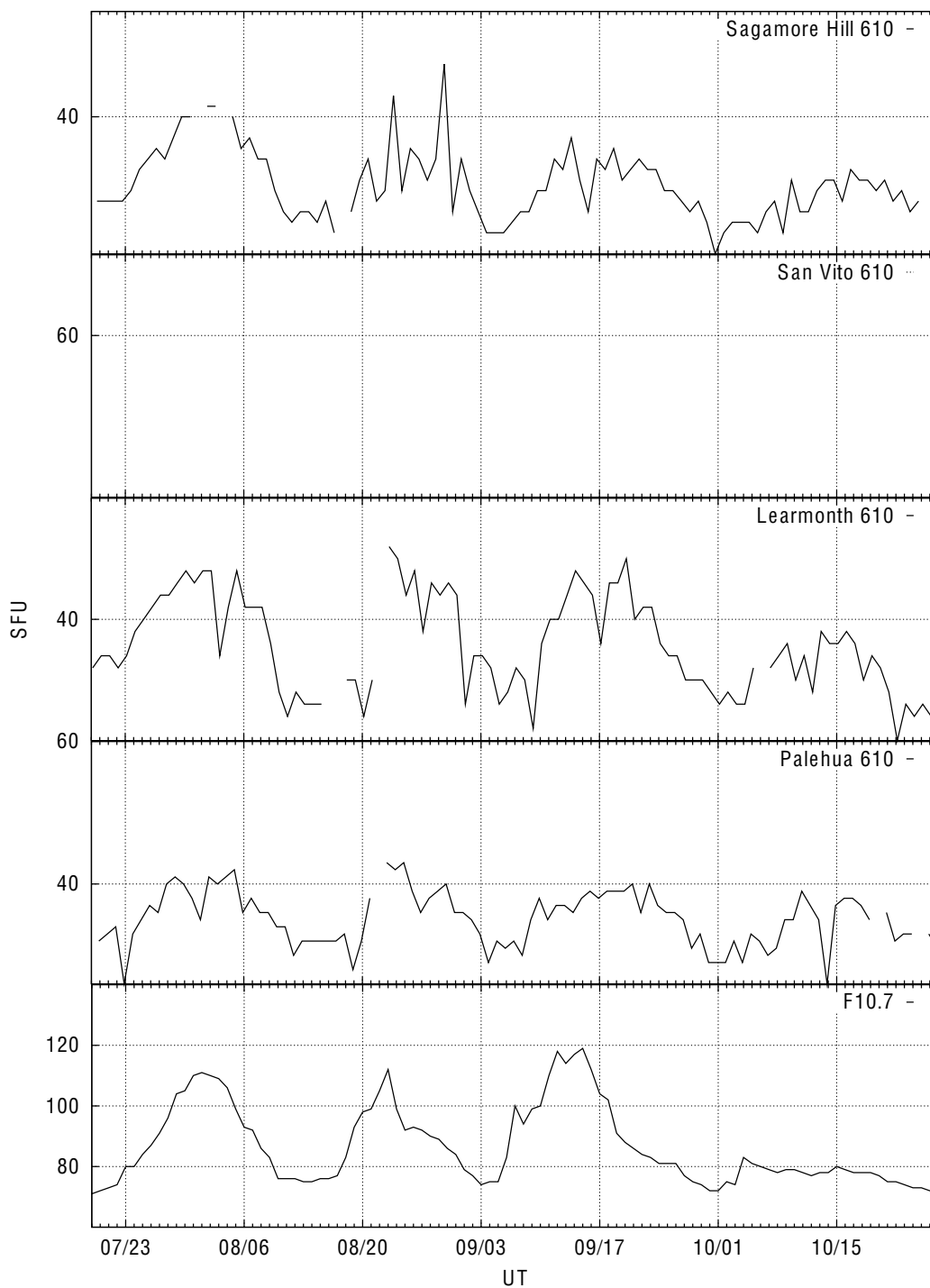


Figure 4.6: RSTN 610 MHz reported daily values compared to F10.7. San Vito has RFI issues at 610 MHz and does not report a daily flux value for this frequency.

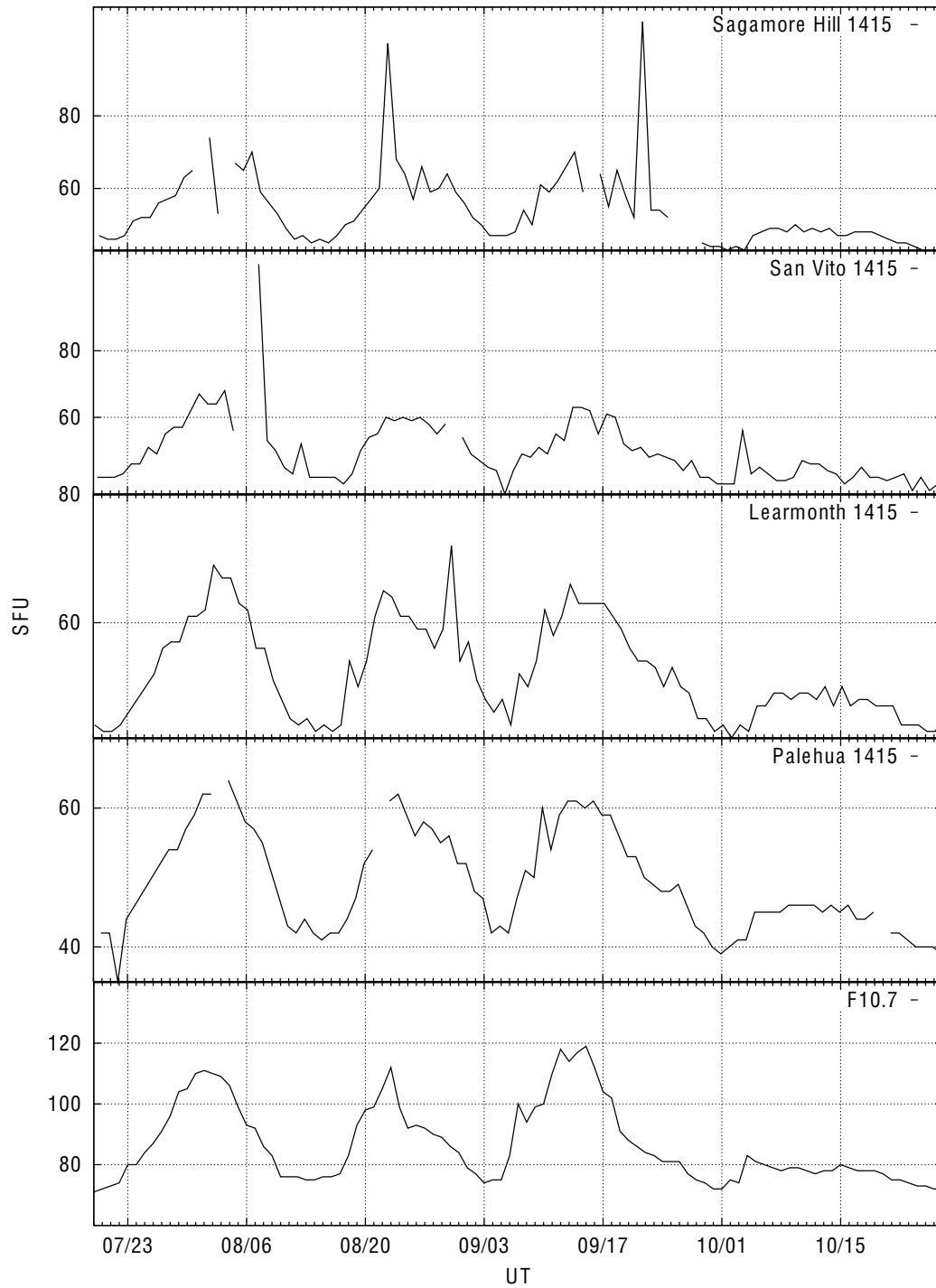


Figure 4.7: RSTN 1415 MHz reported daily values compared to F10.7.

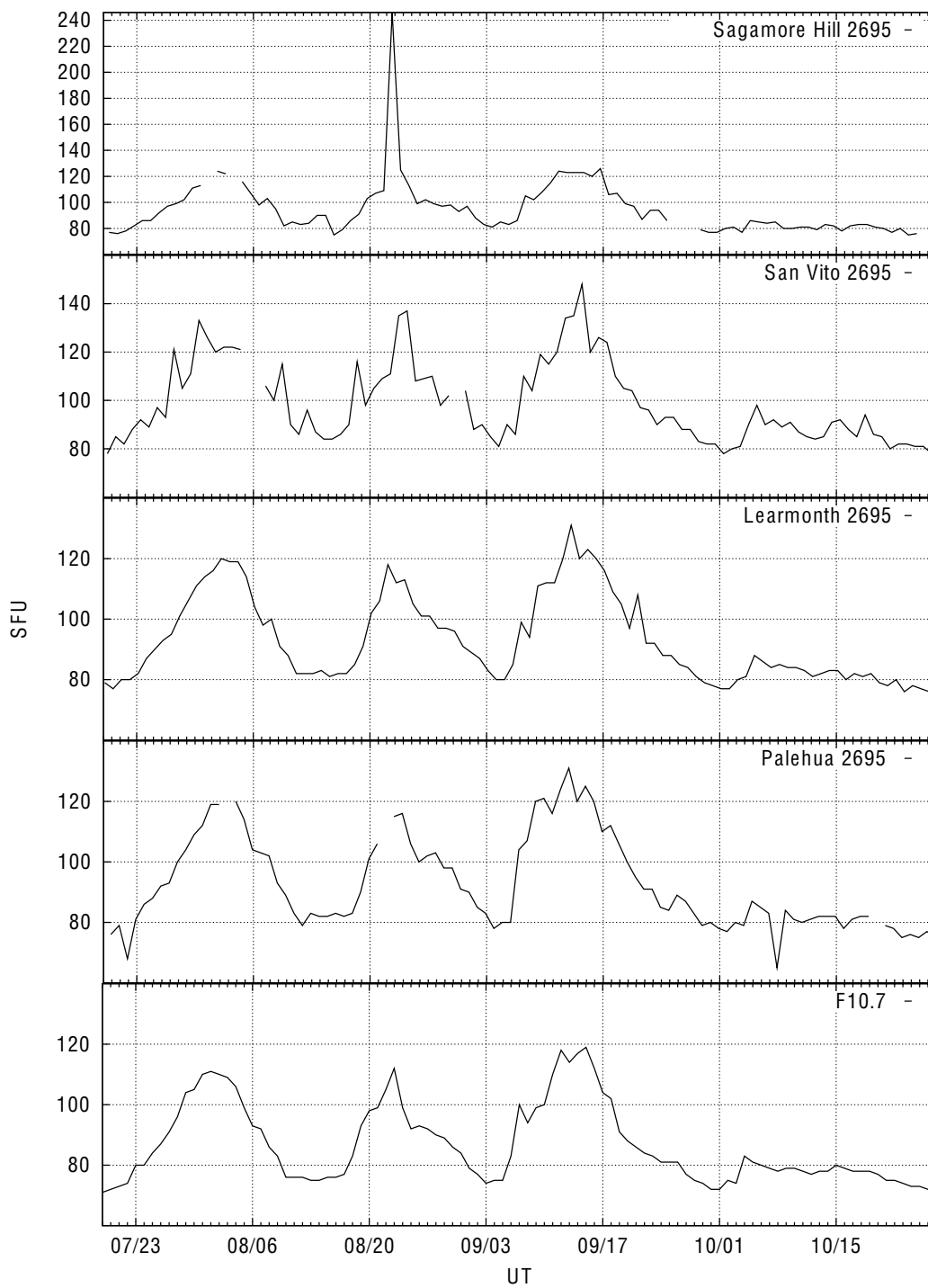


Figure 4.8: RSTN 2695 MHz reported daily values compared to F10.7.

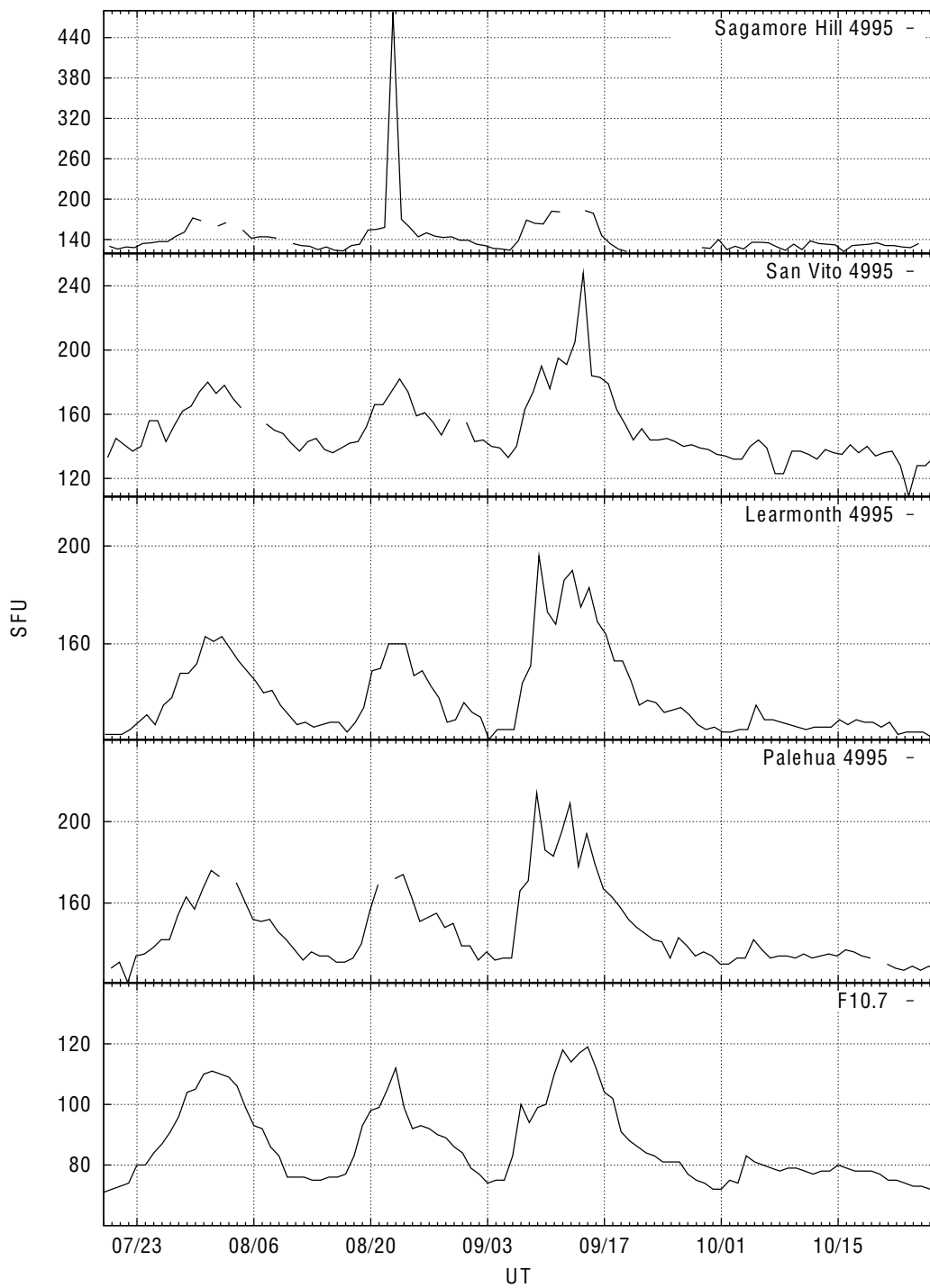


Figure 4.9: RSTN 4995 MHz reported daily values compared to F10.7.

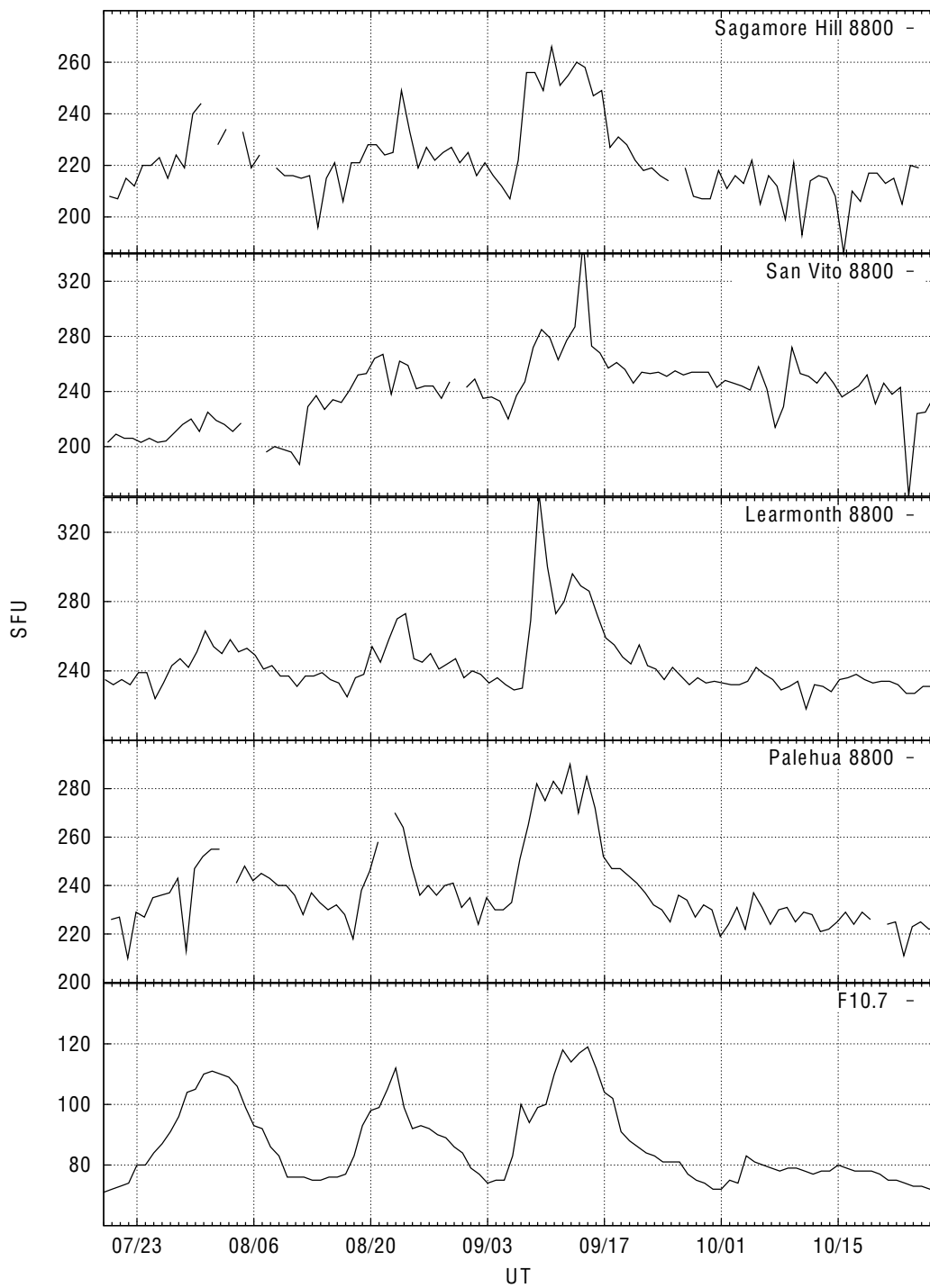


Figure 4.10: RSTN 8800 MHz reported daily values compared to F10.7.

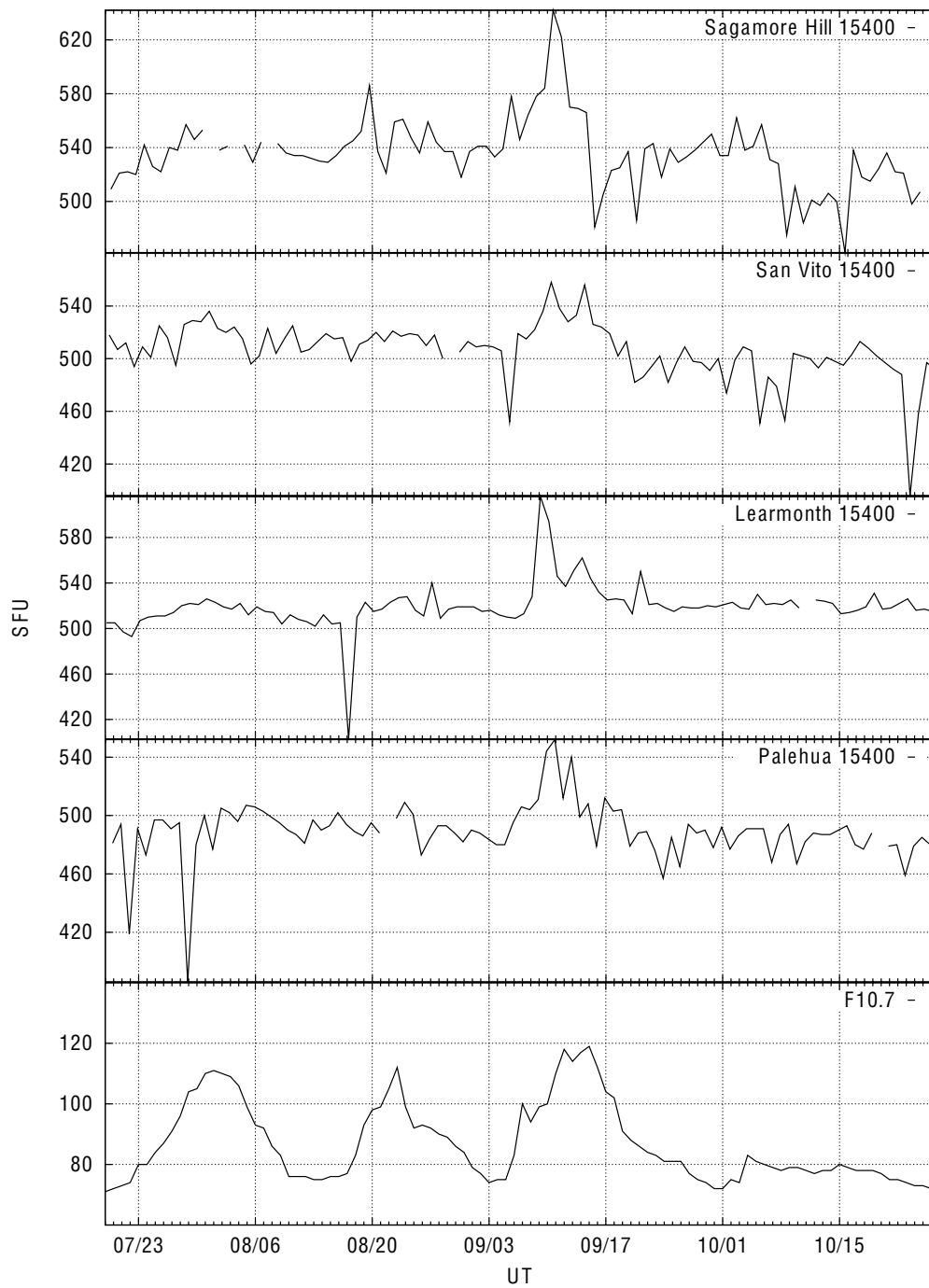


Figure 4.11: RSTN 15400 MHz reported daily values compared to F10.7.

reason for the enhanced value is not known unless the data is reanalyzed.

Several different approaches were taken to resolve the issues of elevated and missing values. As mentioned by *Tapping and Charrois* [1994], the daily flux density measurement is not an average of the sun's daily activity. Rather, it is a snapshot taken at a particular time, which "significantly undersamples the variability of the Sun's emission." Using these comments, the first attempt was to simply take the average for each observatory's frequency and use that value as the "new" daily flux density value. This approach is simple to implement and calculate. However, there are several problems with it. First, flare activity would still be included, thus increasing the baseline. Similarly, RFI would also enhance the baseline. On the other hand, any period when the radiometer is not collecting data would decrease the baselines (e.g., during calibrations, high wind antenna stow conditions, tracking problems). Another approach was to inspect each frequency and remove any of those activities previously mentioned yielding a "computed" daily flux value. This approach was implemented using the following steps.

1. Each observatory and each frequency was analyzed independently from the others.
2. The reported daily flux density values for ten years were used to compute an average, as well as yearly high and low values.
3. These values were used to determine a lower and upper bound such that the majority of the reported values fell within the two values.
4. Any measured data point that fell outside this window was not used to compute the flux density value.

The results of this approach are plotted in Figures 4.12 through 4.19 and are indicated by the red trace.

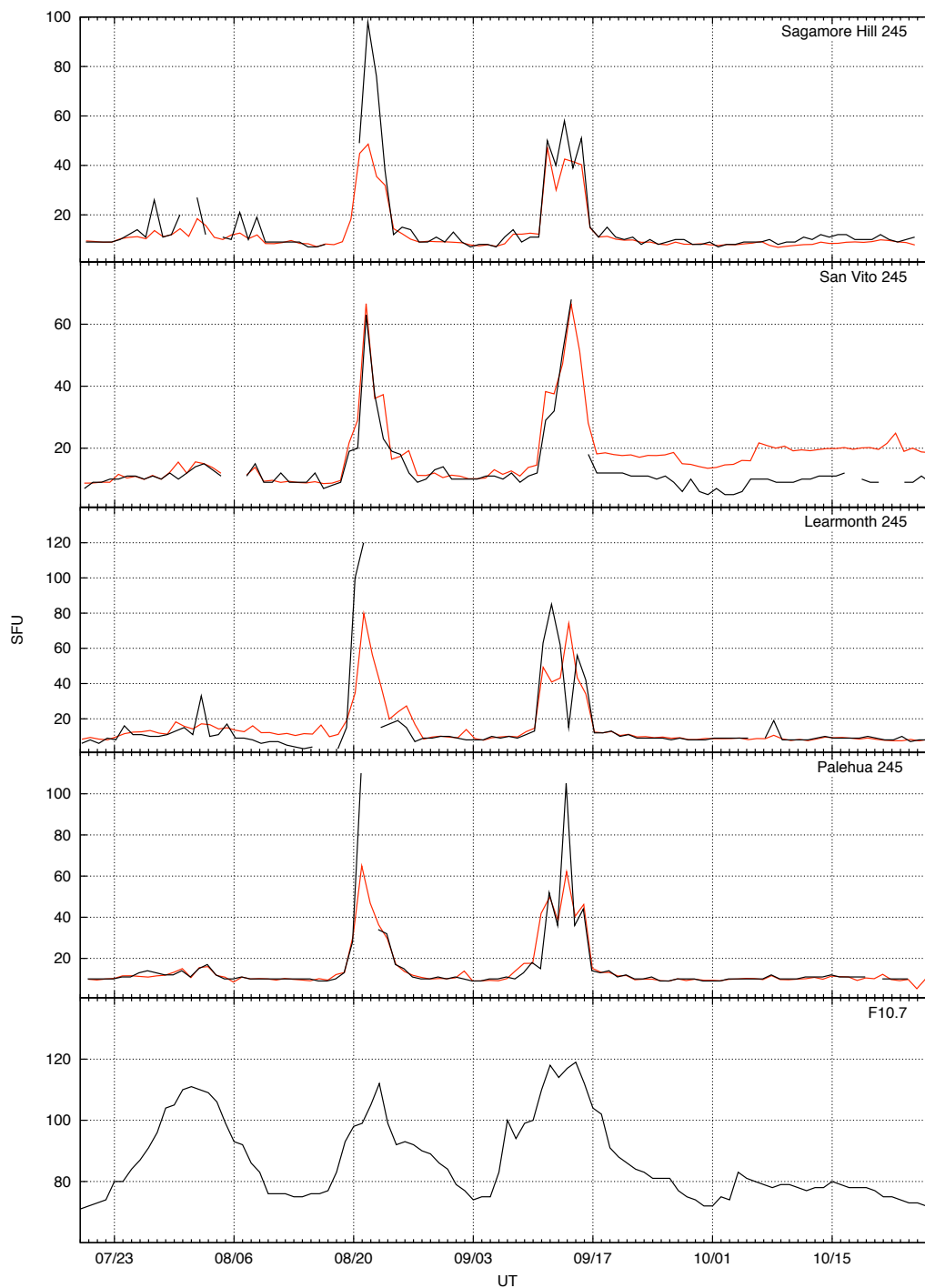


Figure 4.12: RSTN 245 MHz computed versus reported daily flux values. The red trace is the computed daily flux value. The black trace is the reported value.

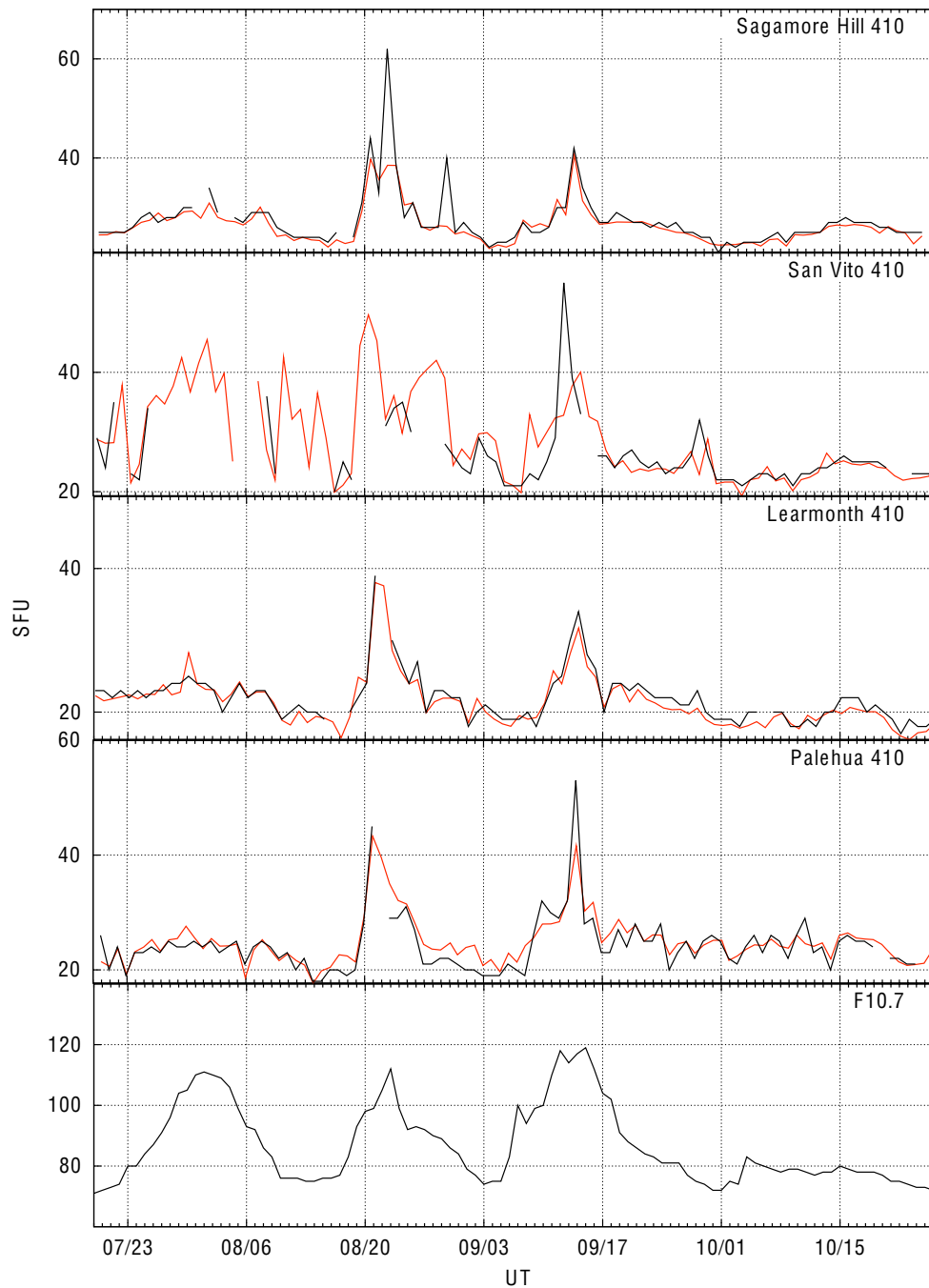


Figure 4.13: RSTN 410 MHz computed versus reported daily flux values. The red trace is the computed daily flux value. The black trace is the reported value.

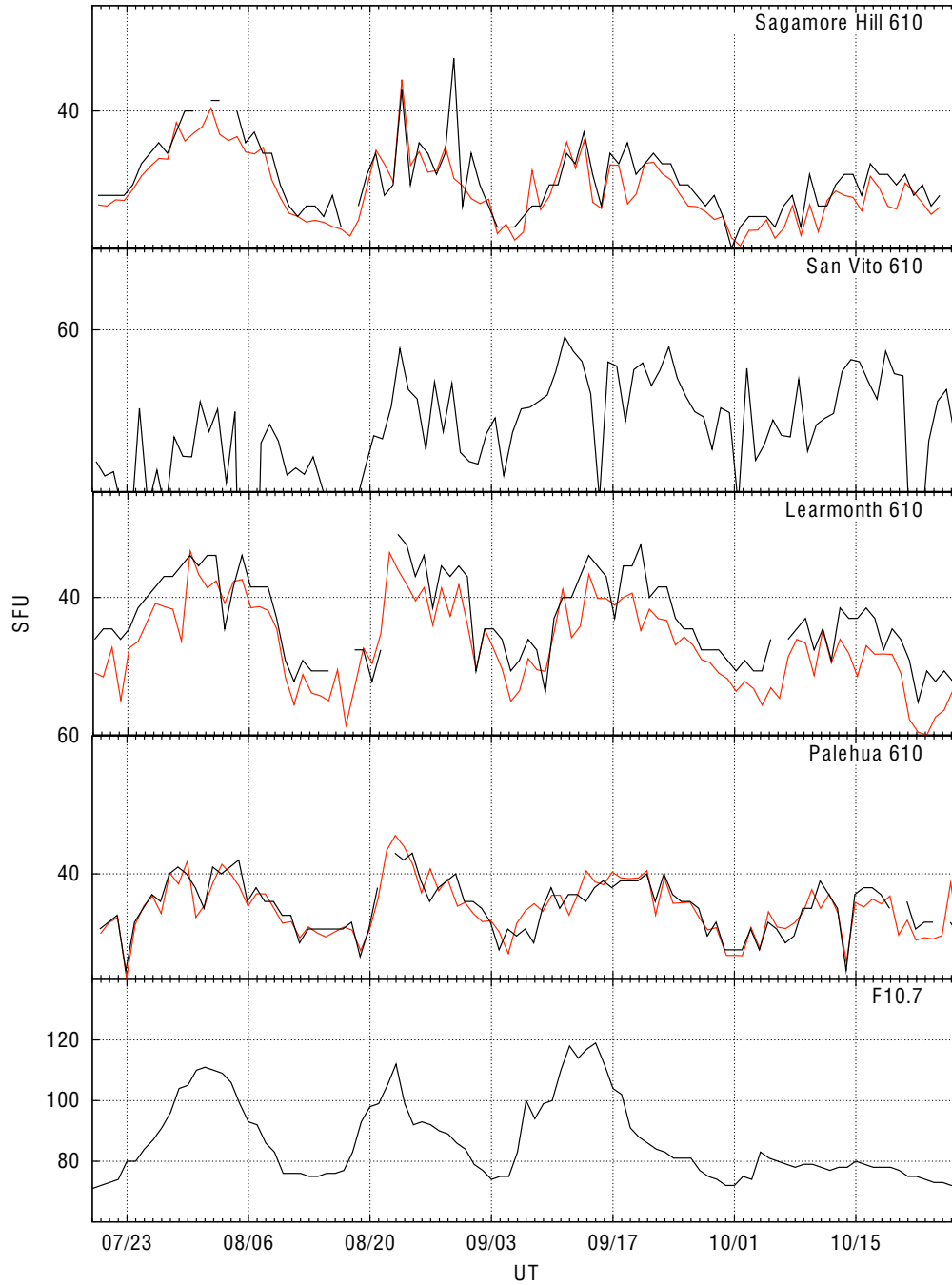


Figure 4.14: RSTN 610 MHz computed versus reported daily flux values. The red trace is the computed daily flux value. The black trace is the reported value.

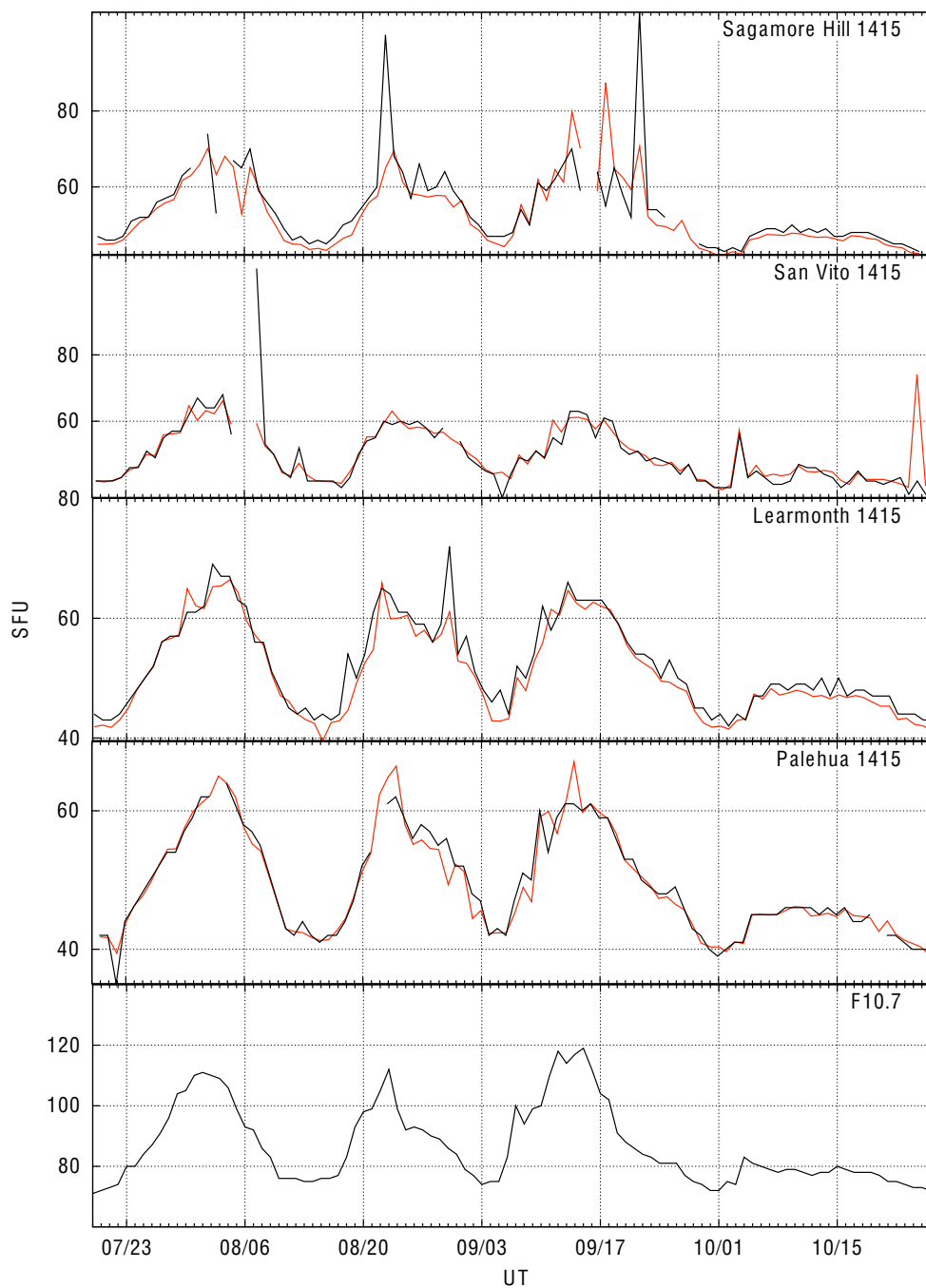


Figure 4.15: RSTN 1415 MHz computed versus reported daily flux values. The red trace is the computed daily flux value. The black trace is the reported value.

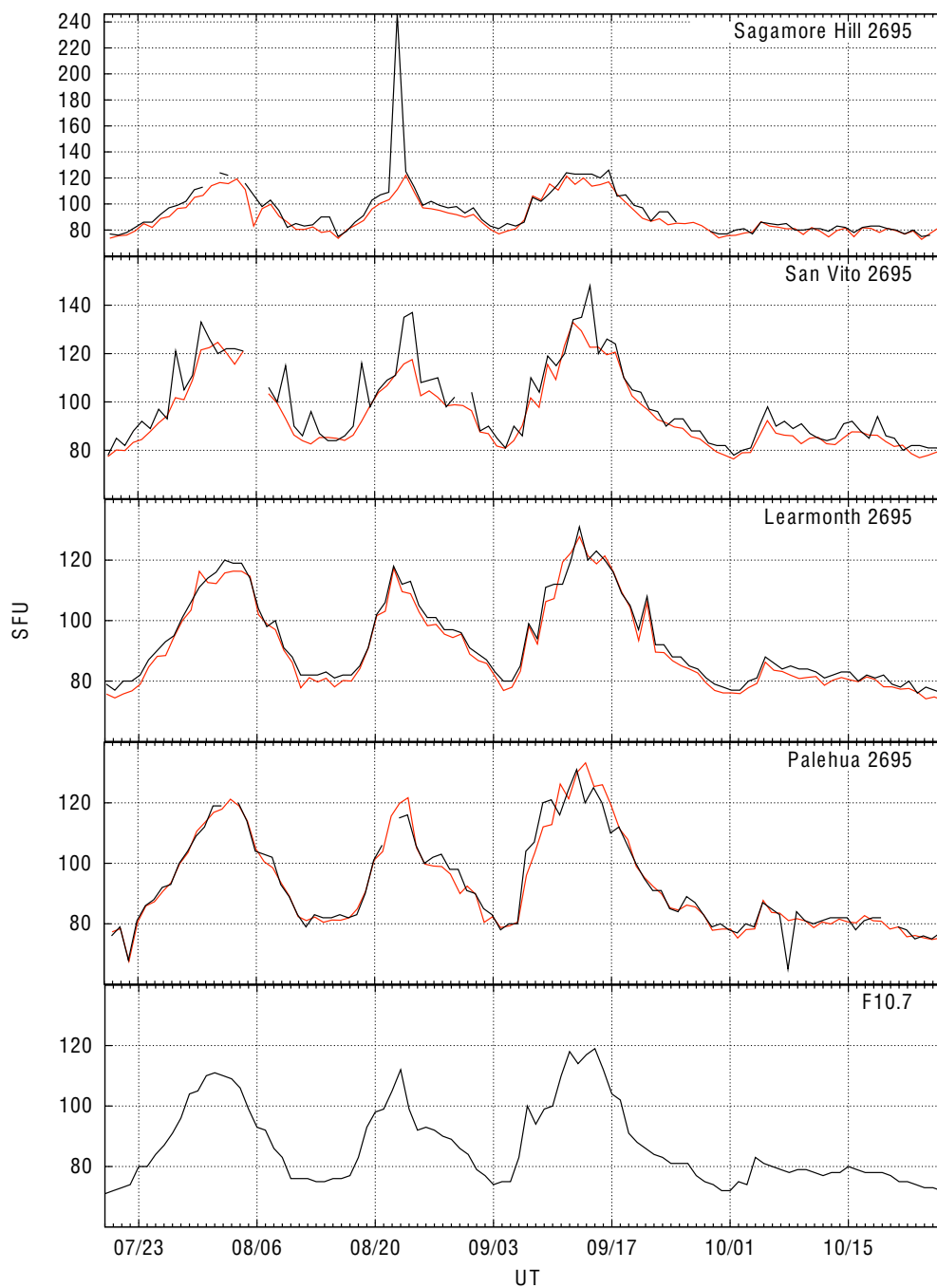


Figure 4.16: RSTN 2695 MHz computed versus reported daily flux values. The red trace is the computed daily flux value. The black trace is the reported value.

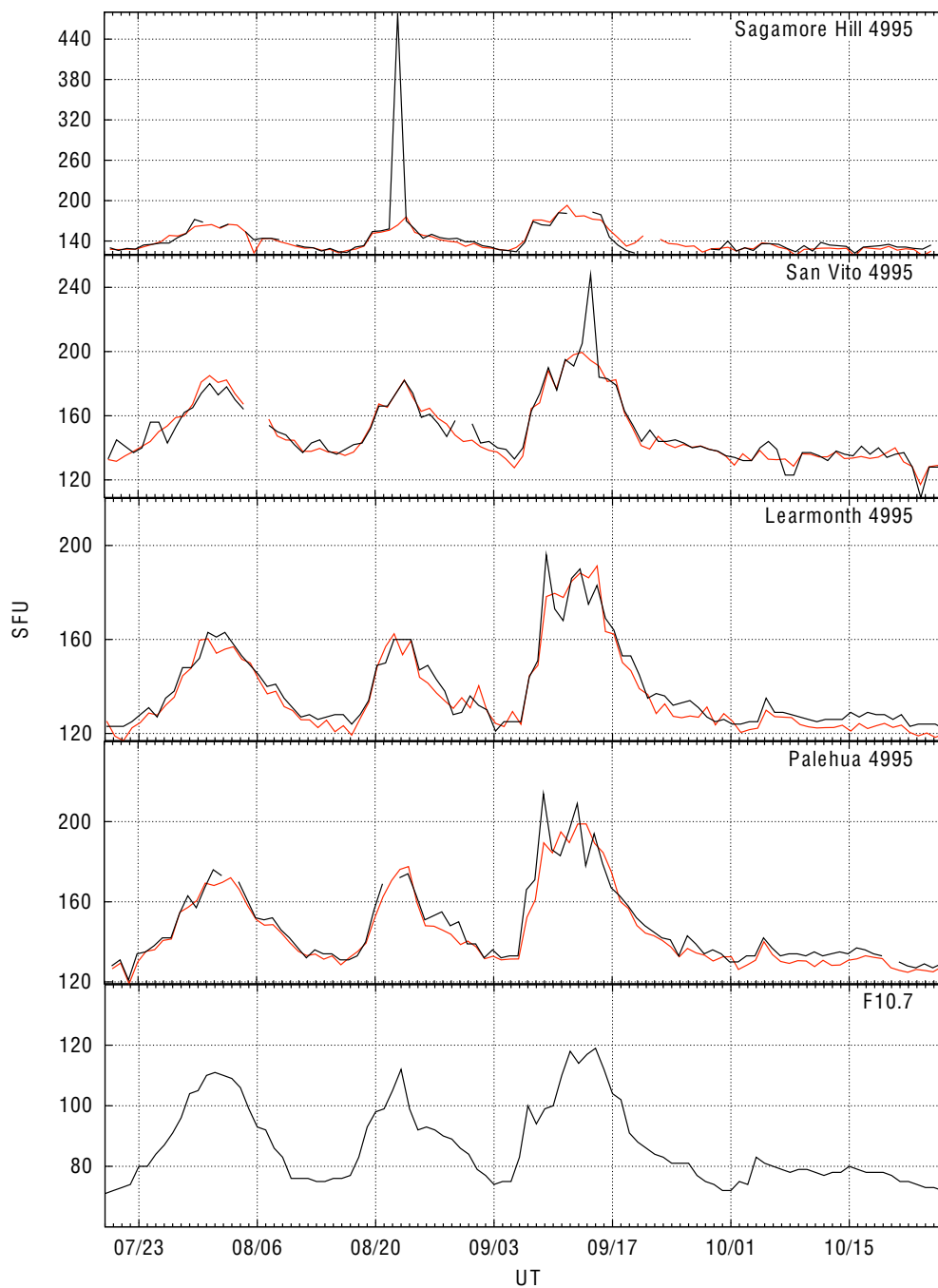


Figure 4.17: RSTN 4995 MHz computed versus reported daily flux values. The red trace is the computed daily flux value. The black trace is the reported value.

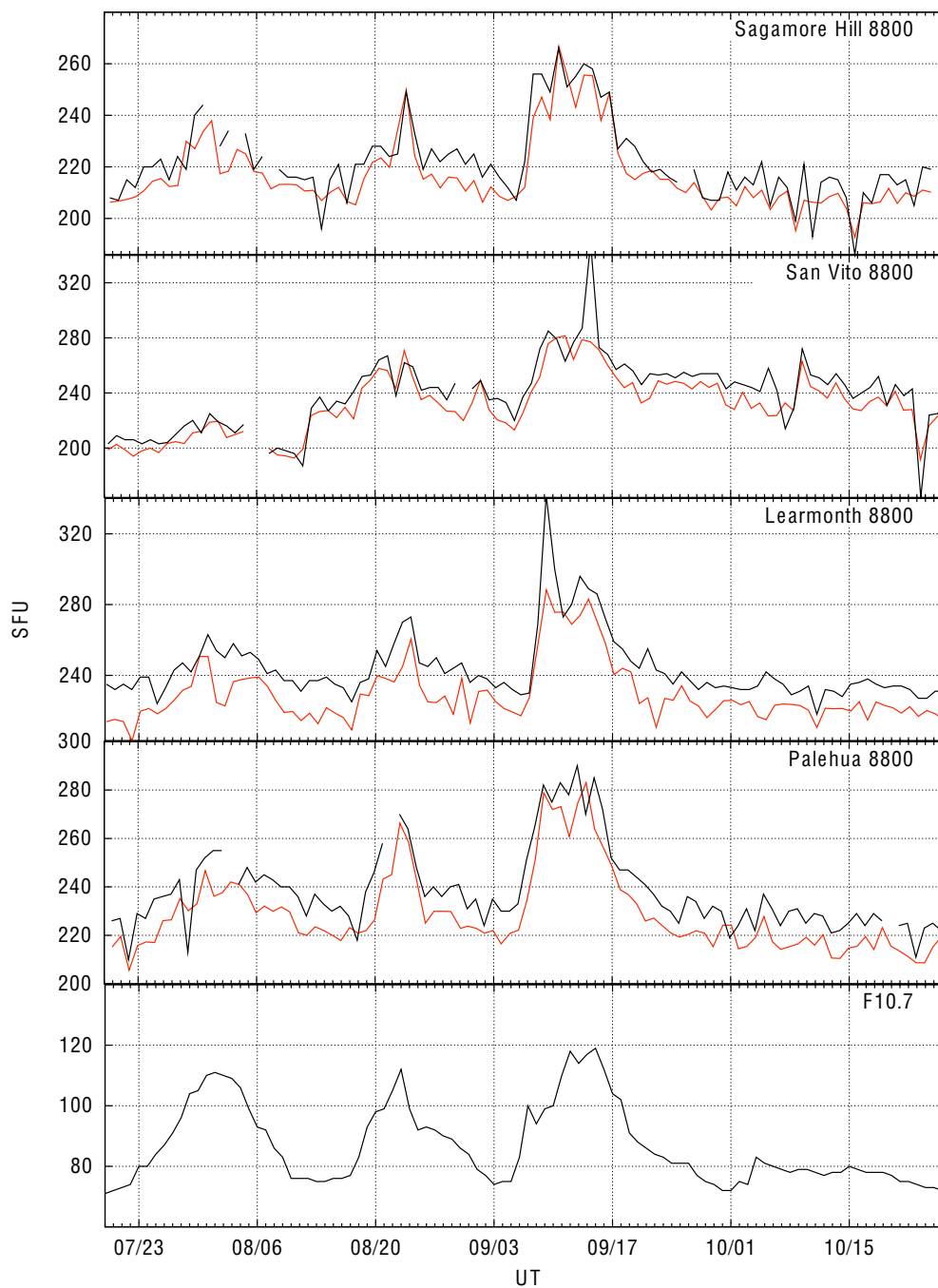


Figure 4.18: RSTN 8800 MHz computed versus reported daily flux values. The red trace is the computed daily flux value. The black trace is the reported value.

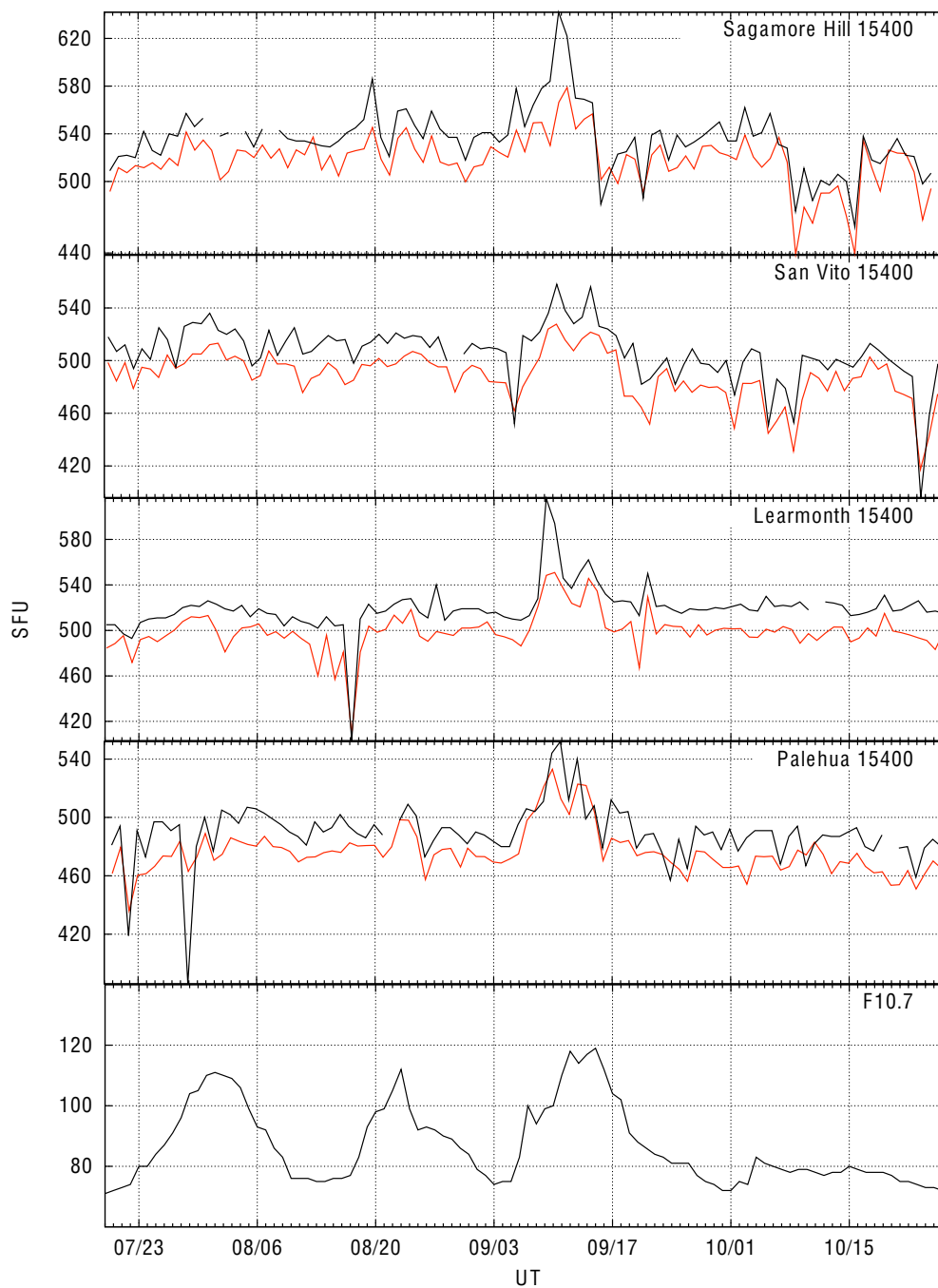


Figure 4.19: RSTN 15400 MHz computed versus reported daily flux values. The red trace is the computed daily flux value. The black trace is the reported value.

The next step in determining how well the RSTN daily values (computed and reported) compare to the F10.7 index was to determine if any correlations existed between the different data sets. The most often used statistic to test for correlation is the Pearson correlation coefficient. However, this statistic assumes that the distributions are normal and is better suited for linear relations [Wilks, 1995]. A better statistic is the Spearman correlation coefficient, ρ (described in detail in Appendix C). This method does not assume a normal distribution and determines the correlation by first ranking the data points and then determining the correlation of the ranking of the data. Only correlation coefficients greater than 0.70 were considered significant as this value implies a 50% explained variance. The null hypothesis for each case (and for each correlation) established that the data measurements, X and Y, were independent of the other. The alternative hypothesis determined that X and Y were positively associated. In each case, the null hypothesis was rejected with a 99% confidence level. In other words, the correlations measured would happen by chance less than 1% of the time.

The first correlation study was conducted using the reported daily flux values for the RSTN observatories. These results shown in Table 4.2 and the results are color-coded. Green represents a correlation coefficient between 0.90 and 1.00, yellow is between 0.80 and 0.90, and orange is between 0.70 and 0.80. The codes represent the reported value “R”, the observatory (“A” Learmonth, “P” Palehua, “K” Sagamore Hill, and “L” San Vito) and the frequency (1-245 MHz, 2-410 MHz, etc.). Due to severe RFI problems, San Vito does not report a daily value for 610 MHz, thus the correlations for San Vito’s third frequency are zero. These results indicate good correlations in the middle frequencies (1415 through 8800 MHz). Correlations on the lower three frequencies were not as good for several reasons. These frequencies

Table 4.2: Rank correlation table for reported RSTN flux values.

RA1-RA1	1.00	RP1-RA1	0.68	RK1-RA1	0.66	RL1-RA1	0.66
RA1-RP1	0.68	RP1-RP1	1.00	RK1-RP1	0.77	RL1-RP1	0.63
RA1-RK1	0.66	RP1-RK1	0.77	RK1-RK1	1.00	RL1-RK1	0.67
RA1-RL1	0.66	RP1-RL1	0.63	RK1-RL1	0.67	RL1-RL1	1.00
RA2-RA2	1.00	RP2-RA2	0.41	RK1-RA2	0.57	RL2-RA2	0.74
RA2-RP2	0.41	RP2-RP2	1.00	RK2-RP2	0.52	RL2-RP2	0.40
RA2-RK2	0.74	RP2-RK2	0.52	RK2-RK2	1.00	RL2-RK2	0.61
RA2-RL2	0.74	RP2-RL2	0.40	RK2-RL2	0.61	RL2-RL2	1.00
RA3-RA3	1.00	RP3-RA3	0.71	RK1-RA3	0.53	RL3-RA3	0.00
RA3-RP3	0.71	RP3-RP3	1.00	RK3-RP3	0.74	RL3-RP3	0.00
RA3-RK3	0.73	RP3-RK3	0.74	RK3-RK3	1.00	RL3-RK3	0.00
RA3-RL3	0.00	RP3-RL3	0.00	RK3-RL3	0.00	RL3-RL3	0.00
RA4-RA4	1.00	RP4-RA4	0.93	RK1-RA4	0.63	RL4-RA4	0.85
RA4-RP4	0.93	RP4-RP4	1.00	RK4-RP4	0.96	RL4-RP4	0.88
RA4-RK4	0.90	RP4-RK4	0.96	RK4-RK4	1.00	RL4-RK4	0.84
RA4-RL4	0.85	RP4-RL4	0.88	RK4-RL4	0.84	RL4-RL4	1.00
RA5-RA5	1.00	RP5-RA5	0.93	RK1-RA5	0.62	RL5-RA5	0.92
RA5-RP5	0.93	RP5-RP5	1.00	RK5-RP5	0.93	RL5-RP5	0.90
RA5-RK5	0.93	RP5-RK5	0.93	RK5-RK5	1.00	RL5-RK5	0.89
RA5-RL5	0.92	RP5-RL5	0.90	RK5-RL5	0.89	RL5-RL5	1.00
RA6-RA6	1.00	RP6-RA6	0.88	RK1-RA6	0.60	RL6-RA6	0.87
RA6-RP6	0.88	RP6-RP6	1.00	RK6-RP6	0.77	RL6-RP6	0.88
RA6-RK6	0.73	RP6-RK6	0.77	RK6-RK6	1.00	RL6-RK6	0.74
RA6-RL6	0.87	RP6-RL6	0.88	RK6-RL6	0.74	RL6-RL6	1.00
RA7-RA7	1.00	RP7-RA7	0.73	RK1-RA7	0.46	RL7-RA7	0.36
RA7-RP7	0.73	RP7-RP7	1.00	RK7-RP7	0.75	RL7-RP7	0.29
RA7-RK7	0.64	RP7-RK7	0.75	RK7-RK7	1.00	RL7-RK7	0.32
RA7-RL7	0.36	RP7-RL7	0.29	RK7-RL7	0.32	RL7-RL7	1.00
RA8-RA8	1.00	RP8-RA8	0.16	RK1-RA8	0.33	RL8-RA8	0.17
RA8-RP8	0.16	RP8-RP8	1.00	RK8-RP8	0.39	RL8-RP8	0.41
RA8-RK8	0.19	RP8-RK8	0.39	RK8-RK8	1.00	RL8-RK8	0.40
RA8-RL8	0.17	RP8-RL8	0.41	RK8-RL8	0.40	RL8-RL8	1.00

originate higher up in the corona than the previous three frequencies. The lower correlation could represent more dynamic radio activity which is only captured by each individual observatory. Furthermore, these lower frequencies showed more RFI

during this time period than the other five frequencies (particularly for San Vito). Lastly, the flux values for these frequencies are very low. Slight changes in the measured value are normal, but would change how the values are ranked which could lead to low rank correlation values. The last frequency, 15400 MHz, shows no correlation among the observatories. There are two possible explanations. The first one involves the equipment. The smaller antenna used for these measurements requires a more precise tracking of the sun in order to receive the radio signal. Slight deviations in the tracking could account for a different measurement. Another possibility is atmospheric attenuation. This frequency is susceptible to attenuation in the presence of moisture. A more detailed study of these observations in conjunction with synoptic weather observations would be required to confirm this hypothesis.

A similar correlation study was carried out using the computed daily flux values rather than the reported values. The method used to compute the daily values was described earlier in this chapter. This method eliminates most of the flare effects on the daily values and has two other advantages over the reported daily value. As noted by *Kane* [2002], many of the daily values for solar indices are not always available. This is true of the RSTN data. By computing a daily value from the available 1-second observations, data gaps is eliminated. Another advantage is the accuracy of the daily value. RSTN observatories transmit their daily values along with a data quality code. This data quality code describes the daily value as either good or questionable based on instrument problems, environmental problems, solar flare in progress, or data not available. Unfortunately, this quality code is not archived at NGDC. As a result, “bad” daily values are archived along with the “good” values. The results of this study are listed in Table 4.3. The colors and codes are similar to the ones used on the previous table. The “C” represents the computed value.

Table 4.3: Correlations between computed daily flux densities.

CA1-CA1	1.00	CP1-CA1	0.61	CK1-CA1	0.69	CL1-CA1	0.05
CA1-CP1	0.61	CP1-CP1	1.00	CK1-CP1	0.74	CL1-CP1	0.27
CA1-CK1	0.69	CP1-CK1	0.74	CK1-CK1	1.00	CL1-CK1	0.26
CA1-CL1	0.05	CP1-CL1	0.27	CK1-CL1	0.26	CL1-CL1	1.00
CA2-CA2	1.00	CP2-CA2	0.53	CK1-CA2	0.76	CL2-CA2	0.67
CA2-CP2	0.53	CP2-CP2	1.00	CK2-CP2	0.69	CL2-CP2	0.34
CA2-CK2	0.82	CP2-CK2	0.69	CK2-CK2	1.00	CL2-CK2	0.60
CA2-CL2	0.67	CP2-CL2	0.34	CK2-CL2	0.60	CL2-CL2	1.00
CA3-CA3	1.00	CP3-CA3	0.72	CK1-CA3	0.60	CL3-CA3	0.25
CA3-CP3	0.72	CP3-CP3	1.00	CK3-CP3	0.69	CL3-CP3	0.37
CA3-CK3	0.76	CP3-CK3	0.69	CK3-CK3	1.00	CL3-CK3	0.21
CA3-CL3	0.25	CP3-CL3	0.37	CK3-CL3	0.21	CL3-CL3	1.00
CA4-CA4	1.00	CP4-CA4	0.94	CK1-CA4	0.70	CL4-CA4	0.82
CA4-CP4	0.94	CP4-CP4	1.00	CK4-CP4	0.95	CL4-CP4	0.78
CA4-CK4	0.94	CP4-CK4	0.95	CK4-CK4	1.00	CL4-CK4	0.80
CA4-CL4	0.82	CP4-CL4	0.78	CK4-CL4	0.80	CL4-CL4	1.00
CA5-CA5	1.00	CP5-CA5	0.95	CK1-CA5	0.73	CL5-CA5	0.94
CA5-CP5	0.95	CP5-CP5	1.00	CK5-CP5	0.95	CL5-CP5	0.93
CA5-CK5	0.92	CP5-CK5	0.95	CK5-CK5	1.00	CL5-CK5	0.91
CA5-CL5	0.94	CP5-CL5	0.93	CK5-CL5	0.91	CL5-CL5	1.00
CA6-CA6	1.00	CP6-CA6	0.89	CK1-CA6	0.74	CL6-CA6	0.88
CA6-CP6	0.89	CP6-CP6	1.00	CK6-CP6	0.89	CL6-CP6	0.91
CA6-CK6	0.85	CP6-CK6	0.89	CK6-CK6	1.00	CL6-CK6	0.88
CA6-CL6	0.88	CP6-CL6	0.91	CK6-CL6	0.88	CL6-CL6	1.00
CA7-CA7	1.00	CP7-CA7	0.67	CK1-CA7	0.60	CL7-CA7	0.49
CA7-CP7	0.67	CP7-CP7	1.00	CK7-CP7	0.82	CL7-CP7	0.31
CA7-CK7	0.70	CP7-CK7	0.82	CK7-CK7	1.00	CL7-CK7	0.27
CA7-CL7	0.49	CP7-CL7	0.31	CK7-CL7	0.27	CL7-CL7	1.00
CA8-CA8	1.00	CP8-CA8	0.20	CK1-CA8	0.41	CL8-CA8	0.34
CA8-CP8	0.20	CP8-CP8	1.00	CK8-CP8	0.32	CL8-CP8	0.41
CA8-CK8	0.40	CP8-CK8	0.32	CK8-CK8	1.00	CL8-CK8	0.27
CA8-CL8	0.34	CP8-CL8	0.41	CK8-CL8	0.27	CL8-CL8	1.00

A comparison of Tables 4.2 and 4.3 shows statistically insignificant differences in correlation coefficients between computed and reported values. Additionally, Table 4.4 shows the correlation coefficients between reported and computed RSTN

Table 4.4: Correlations between computed and reported RSTN daily values.

Station	245 MHZ	410 MHZ	610 MHZ	1415 MHZ	2695 MHZ	4995 MHZ	8800 MHZ	15400 MHZ
Palehua	0.91	0.90	0.89	0.98	0.98	0.97	0.95	0.87
Learmonth	0.77	0.95	0.90	0.96	0.99	0.97	0.92	0.87
San Vito	0.90	0.45	0.00	0.78	0.95	0.94	0.92	0.90
Sagamore Hill	0.93	0.86	0.87	0.90	0.77	0.61	0.95	0.87

values. Ideally, this table would show high correlation coefficient values for each frequency and each observatory. However, this is not the case. All observatories had relatively low correlation values for 15400 MHz. This frequency requires precise tracking of the sun to obtain the strongest signal. Any tracking problems would significantly decrease the measured signal and possibly contribute to lower correlation values. Furthermore, the signal for this frequency is affected by rain, again possibly contributing to lower correlation values. The low correlation values for San Vito's lower frequencies are probably due to RFI which is often present on these frequencies. Sagamore Hill's 2695 and 4995 MHz show the lowest correlation values in this table. The reason for these low values is that the reported values for these frequencies contained measurements taken during solar flares. Once these values were removed from the dataset, the correlation coefficient for both of these frequencies increased to 0.97. The net result from these radio correlation studies is that the computed values are similar to and could be used in place of the reported values. Considering the advantage of the computed values already mentioned, the remaining correlations were conducted using the computed daily values.

A fourth set of radio correlation computations were performed using the daily computed RSTN values and the reported F10 index (Table 4.5). These results show high correlations for the middle frequencies, particularly 2695 MHz. These results

Table 4.5: Correlations between computed RSTN daily values and F10 daily values. “C” represents the computed values, “A” stands for Learmonth, “P” is Palehua, “K” is Sagamore Hill, and “L” is San Vito. The numbers 1 through 8 represent the eight discrete RSTN frequencies.

CA1	0.78	CP1	0.75	CK1	0.78	CL1	0.30
CA2	0.73	CP2	0.67	CK2	0.81	CL2	0.51
CA3	0.78	CP3	0.77	CK3	0.74	CL3	0.27
CA4	0.92	CP4	0.97	CK4	0.94	CL4	0.77
CA5	0.96	CP5	0.96	CK5	0.95	CL5	0.94
CA6	0.88	CP6	0.92	CK6	0.87	CL6	0.89
CA7	0.72	CP7	0.84	CK7	0.83	CL7	0.36
CA8	0.50	CP8	0.60	CK8	0.31	CL8	0.65

were expected considering how close the middle RSTN frequencies are to F10. The importance of these results is that RSTN frequency 5, 2695 MHz could be used by models instead of the daily F10. At first this may seem unimportant since it is essentially replacing one proxy with another. However, since there are four RSTN observatories, the solar input to models could be updated four times a day rather than the current one-time-a-day update (or the linear approach).

4.4 SEE Data

As described in Appendix B, the TIMED-SEE data consists of flux measurements from emission lines from 1 nm to 194 nm with 1 nm bins centered every 0.5 nm. Each SEE bin is made up of contributions from different emission lines. For example, bin 2.5 has contributions from the following emission lines: O VII (2.16 nm), O VII (2.18 nm), O VII (2.21 nm), C VI (2.847 nm), N VI (2.879 nm) and N VI (2.952 nm). For practicality reasons, when the bins are referenced in this dissertation, they are rounded up to the next integer and referenced as wavelengths (e.g., bin 2.5 is referenced as wavelength 3). The first test using this data set was to determine if there was any relationship among these 194 wavelengths. Considering the

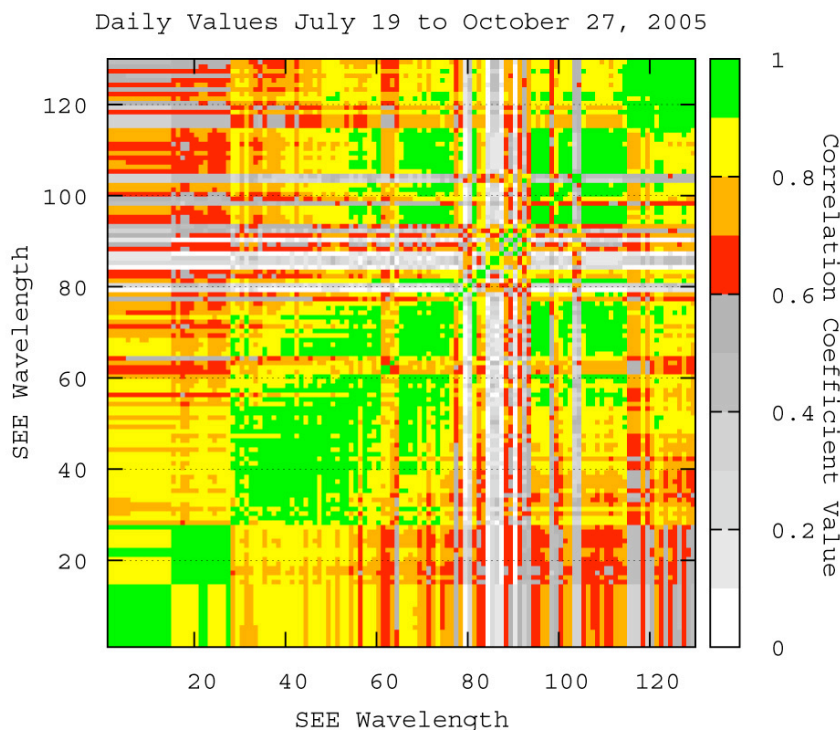


Figure 4.20: TIMED-SEE daily value correlation results. Green represents a correlation coefficient between 0.90 and 1.00, yellow is between 0.80 and 0.90, and orange is between 0.70 and 0.80.

results from the radio correlation studies, it was expected that some sort of correlation would exist between adjacent wavelengths. This correlation study focused on wavelengths of interest pertaining to the ionosphere, so only wavelengths below 130 nm were considered. Figure 4.20 shows the results of this study. Of the 8385 different correlations, 65% had a correlation coefficient greater than 0.70; 21% between 0.70 and 0.80, 26% between 0.80 and 0.90, and 17% greater than 0.90. Correlations with values greater than 0.90 occurred in groups: 1-14 nm, 15-27 nm, 28-60 nm, 65-75 nm, 94-114 nm, and 115-128 nm. Some wavelengths correlated poorly with the rest of the observations ($\rho < 0.30$): 79-80 nm, 84-87 nm, 90 nm, 92-93 nm, 98 nm, and 103-104 nm.

4.5 Correlations Between EUV, Radio Data, and Other Indices

The last of the correlation studies was between the TIMED-SEE data and the other solar indices. Table 4.6 shows the results binned according to the SEE autocorrelation results discussed in the previous section, while Figures 4.21 and 4.22 show the correlation results for each SEE bin and observatory frequency. Of the four indices (F10, sunspot number, sunspot area, and GOES soft x-ray background), the F10 had better results for more SEE wavelengths. This reaffirms the use of F10.7 as a proxy for solar UV. The GOES x-ray background correlates well with the first 27 wavelengths, the daily sunspot number with the first 60 wavelengths, and the sunspot area with the first 75 wavelengths. However, the correlations were not as good as those of F10.7. The correlation results for the RSTN data were similar or better than the correlations for F10.7. Also, the higher correlation values shifted toward lower radio frequencies as the SEE wavelengths increased. F10.7 and RSTN data are very similar for 1-75 nm, 94-114 nm, and 115-129 nm. The similarities between F10.7 (2800 MHz) and 2695 MHz are not surprising. Considering the close proximity of the frequencies one would expect the sources of these emissions to be close to one another. The similarities between F10.7, 1415, 4995 and to some extent 8800 MHz were not expected. Another unexpected result was that the correlations between 1415 MHz were more similar to F10.7 than 2695 MHz. The problem already mentioned in the TIMED-SEE correlations is again apparent in this set of correlations. There is a correlation gap between 84 and 98 nm where none of the other solar measurements correlate to the EUV data. Finally, Figure 4.21 shows that the correlations between the radio frequencies and SEE wavelengths were similar among the four solar observatories.

Table 4.6: Correlations between binned TIMED-SEE data and RSTN data.

SEE	245 MHz	410 MHz	610 MHz	1415 MHz	2695 MHz	4995 MHz	8800 MHz	15.4 GHz	F10	SSN	SXR bkg
1-14	0.70	0.55	0.65	0.88	0.93	0.92	0.86	0.60	0.89	0.76	0.86
15-27	0.73	0.63	0.72	0.91	0.91	0.84	0.82	0.59	0.91	0.71	0.86
28-60	0.41	0.44	0.65	0.79	0.74	0.72	0.66	0.36	0.76	0.65	0.68
65-75	0.49	0.55	0.72	0.86	0.80	0.77	0.70	0.45	0.83	0.69	0.69
76	0.42	0.45	0.59	0.77	0.72	0.66	0.59	0.41	0.73	0.66	0.56
77	0.36	0.40	0.39	0.61	0.60	0.54	0.48	0.37	0.60	0.59	0.41
78	0.41	0.48	0.56	0.73	0.70	0.66	0.60	0.38	0.72	0.61	0.58
79	0.34	0.33	0.15	0.23	0.21	0.15	0.10	0.17	0.26	0.30	0.11
80	0.41	0.37	0.35	0.41	0.38	0.31	0.25	0.24	0.43	0.41	0.24
81	0.40	0.45	0.63	0.77	0.71	0.66	0.59	0.41	0.74	0.65	0.56
82	0.42	0.43	0.52	0.68	0.64	0.58	0.52	0.39	0.66	0.64	0.41
83	0.42	0.43	0.58	0.73	0.68	0.63	0.56	0.34	0.70	0.68	0.45
84-87	0.24	0.10	0.11	0.12	0.10	0.05	0.00	0.01	0.12	0.24	0.03
97-114	0.45	0.49	0.68	0.81	0.72	0.67	0.60	0.34	0.77	0.66	0.57

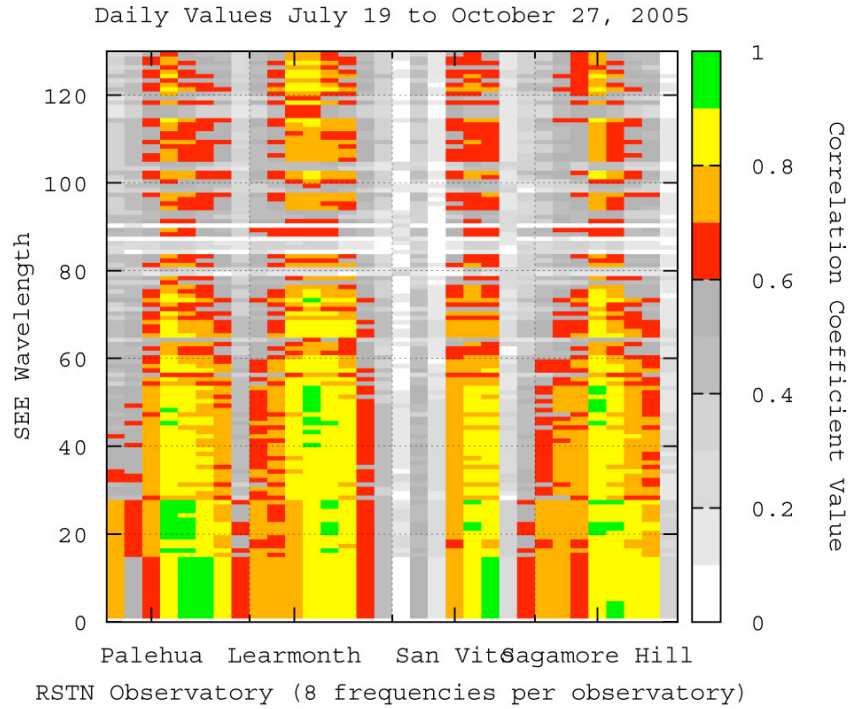


Figure 4.21: Correlation results between all RSTN observatories and SEE wavelengths.

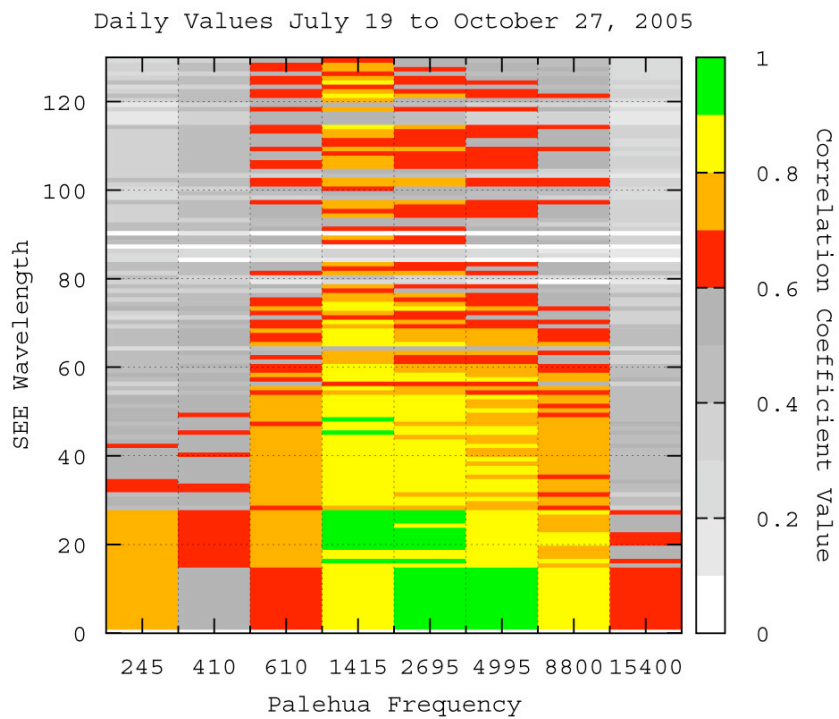


Figure 4.22: Correlation results between SEE wavelengths and Palehua radio frequencies.

CHAPTER 5

SUB-DAILY PROXIES

In the previous chapter, it was shown that there is a high correlation ($\rho = 0.8$ or better) between the daily EUV values measured by the SEE instrument and the different EUV solar daily proxies commonly used in space weather. These solar proxies include the Pencticton F10.7 index, USAF RSTN daily radio values, and GOES background x-ray daily values. However, the daily values exclude the effects of solar flares. This chapter examines the solar variability in soft x-rays, EUV, and radio using higher time resolution ranging from one second to hourly observations and including flares. The purpose of this chapter is to determine if solar radio data can be used to determine the solar EUV output that occurs throughout a day and during flares. The first part of this chapter is a review of solar flares theory and is followed by an examination of flares using soft x-ray, EUV, and radio data. Then TIMED-SEE EUV, soft x-rays, and radio observations are analyzed to determine similarities and correlations among the different data sets.

5.1 Solar Flares

Solar flares are sudden energy releases over a wide range of the electromagnetic spectrum. They come in many different sizes and behave differently depending on the spectrum being observed. Large flares significantly increase the solar output in the x-ray, UV, and radio range, but the variation in the infrared and visible spectrum is less than 0.01% [Foukal, 2004]. Flares take place predominately in active regions as they are rapidly growing and changing in complexity [Phillips, 1995]. They can also take place during the decay phase of the active region. There are many models and theories used to explore solar flares; however, flares are generally divided into two types: simple or compact, and two-ribbon flares. Simple flares usually take

place in pre-existing loops; there is usually little structural change to the loops, they involve smaller energy amounts ($\sim 10^{23}$ J), and have shorter duration times ($\sim 10^3$ seconds) [*Garcia Alvarez, 2000*]. The two-ribbon flares involve new loops emerging and large scale re-arrangement of active regions, involve energy amounts up to 10^{25} joules, and are of longer duration ($\sim 10^4$ seconds) [*Foukal, 2004*]. Most flares have three stages: precursor, impulsive, and main. However, some researchers include a separate late stage [*Garcia Alvarez, 2000*]. The precursor, or “preflare” brightening phase usually lasts a few minutes. This brightening can usually be detected in soft x-ray and EUV emissions and is associated with the rising of a filament. The impulsive stage is where all emissions reach their peak and is believed to be initiated by the reconnection of magnetic loops. This phase usually lasts from seconds to minutes. The energy from the reconnection accelerates the particles within the loops. These accelerated particles form beams that travel down through the solar atmosphere. As the solar atmosphere’s density increases (transition region and chromosphere) the beam interacts with more particles producing bremsstrahlung emissions in the x-ray regime. These areas, on either side of the loop, are seen as the “footpoints” of the flaring loop. The beams also excite the transition region ions through collisions. The increase in UV emissions during a flare is believed to be in part due to an increase in chromospheric emission from ions due to photo-ionization of the “hard x-ray producing electrons” [*Aschwanden, 2004*]. Furthermore, the heating of the plasma in the footpoints expands the plasma, resulting in an upward motion in the loop. As the plasma moves from the chromosphere to the corona (chromospheric evaporation), it increases the temperature and density of the loop. This further enhances the UV emissions during the main phase of the flare [*Aschwanden, 2004*]. In the microwave region, the mechanisms responsible for the enhanced emissions are

bremstrahlung and gyro resonance. It is believed that the same relativistic beam responsible for the x-rays is responsible for the microwave emissions as the electrons spiral downward (see Chapter 2) [Foukal, 2004; Haisch and Strong, 1991; White, 1999].

5.2 Flare Characteristics

The first goal of this chapter is to determine similarities and differences between flares measured in the different wavelength spectrums by analyzing large flares observed in 2005. The selection criteria for these large flares were M-class as measured by GOES 12. In order to simplify the description of the analysis and results, the GOES 1-8 angstrom channel is referred to as the GOES main channel, GOES .5-4 angstrom channel as the GOES secondary channel, SEM 26-34 nm channel as the SEM main channel, and the SEM .1-50 nm channel as the SEM secondary channel. If no reference is made to either channel, then the main channel is implied. Table 5.1 shows the number of flares that were used in this analysis according to their wavelength and Table 5.2 shows the distribution based on GOES magnitude, as well as latitude and longitude of the flare.

Each flare was then analyzed to compute the following parameters:

1. peak magnitude,
2. net increase (value at peak minus value before flare start),
3. time from start to peak,
4. time from peak to end (return to baseline),
5. time from peak to half power,
6. total duration,
7. total integrated value,
8. front slope (peak magnitude/time from start to peak), and

9. back slope (peak magnitude/time from peak to end).

For the radio flares, there were two additional parameters: frequency with the maximum peak for a given flare and frequency with the maximum integrated power for a given flare. This is because the radio frequency response for each flare could be different from one flare to another. Also, unlike the majority of the flares observed in GOES and SEM, the radio flares often had multiple peaks (Figure 5.1).

Table 5.1: Number of M-class flares observed in 2005 by GOES, SEM, and RSTN.

GOES	SEM	Radio							
		245	410	610	1415	2695	4995	8800	15400
103	74	66	65	67	79	79	71	68	66

Table 5.2: Breakdown of M-class flares observed by GOES, SEM, and radio based on magnitude, latitude, and longitude.

	GOES	SEM	245	410	610	1415	2695	4995	8800	15400
Magnitude										
1	58	47	37	37	37	42	44	39	35	35
2	12	7	7	7	7	8	7	9	8	7
3	11	9	8	8	8	9	9	8	7	6
4	8	6	5	5	6	7	7	6	7	7
5	2	1	2	2	2	2	2	2	1	1
6	5	1	3	3	3	5	4	3	4	4
7	1	0	0	0	0	0	0	0	0	0
8	4	1	2	1	2	4	4	2	4	4
9	2	2	2	2	2	2	2	2	2	2
Latitude										
East	41	25	31	28	31	31	31	30	26	27
West	62	49	35	37	36	48	48	41	42	39
Longitude										
North	46	30	33	31	33	35	35	34	32	32
South	44	33	24	26	25	33	34	28	27	27

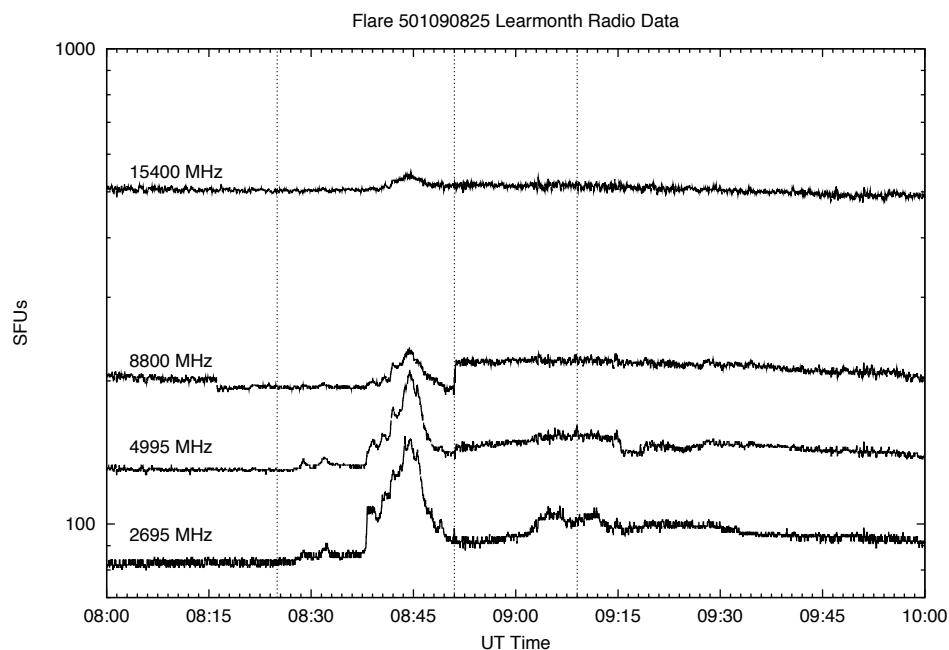


Figure 5.1: Radio flare 501090825 has multiple peaks on frequency 2695 MHz. One peak occurs at 08:45 and another one around 09:05. The dashed vertical lines are the start, peak, and half-power times for the GOES flare.

In these instances, the largest peak for each frequency was used as the peak of the flare from which the other parameters were computed. Soft x-ray flares observed by GOES presented another challenge. In many cases, the flare did not return to the pre-flare baseline before another flare started (Figure 5.2). For reasons of consistency, this parameter was not used in the analysis and was replaced with the half power point. Therefore, the total duration, total integrated value, and the back slope were computed using the half power point rather than the end point. For comparison purposes, all data was scaled by the respective average daily value from July 20, 2005. This day was chosen because it had no solar activity and there were no sunspot groups visible on the sun. The results are shown in Figures 5.3 through 5.8 and show that although there is variability in the flare response within each type of measurement (i.e., radio, EUV, and soft x-ray), there were some majority groupings

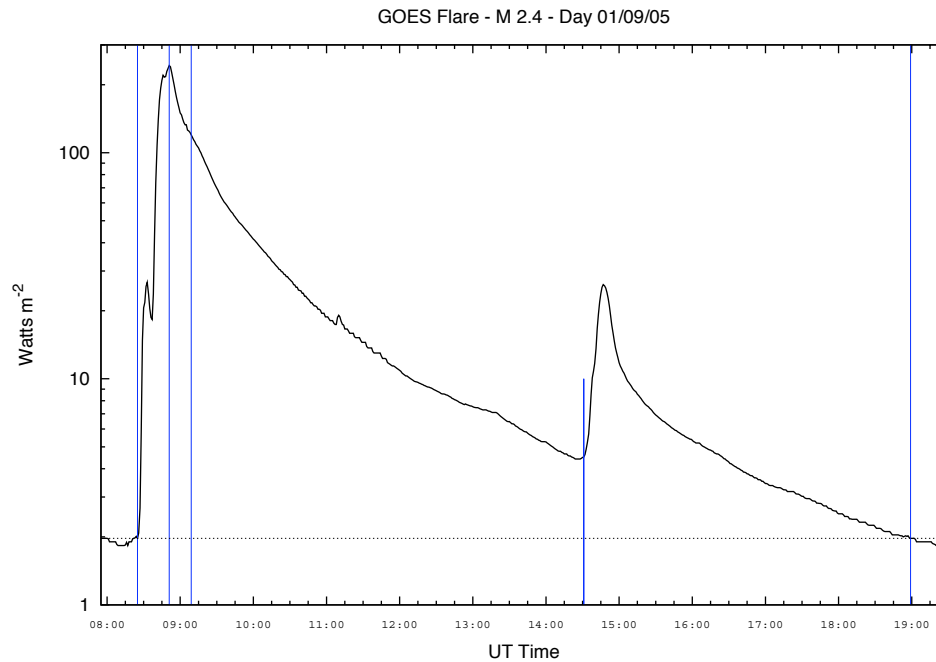


Figure 5.2: GOES flare 501090825 does not return to the pre-flare baseline before another flare takes place around 14:30.

within the flares observed by different instruments. The following comments apply to the analysis of all M-class flares observed during 2005.

1. Radio flares peaked on different frequencies and also had the largest integrated values on different frequencies (Table 5.3).
2. Radio flares reach their peak and return to the half-power point faster than GOES flares and SEM EUV flare (Figures 5.3 and 5.4).
3. SEM EUV and GOES soft x-ray flares reached their peak within 30 minutes of the start of the flare (Figure 5.3).
4. SEM EUV flares reached the half power point within 10 minutes of peaking (Figure 5.4).
5. GOES soft x-ray flares reached the half power point within 30 minutes of peaking (Figure 5.4).

6. While GOES soft x-ray flares underwent a two order of magnitude increase, radio flares generally increased by a factor of 5, SEM EUV flares increased between 10 % and 50% (Figures 5.5 and 5.6).
7. All SEM EUV flares had gradual front and back slopes, while the majority of GOES soft x-ray flares had steeper slopes than radio and SEM EUV flares (Figures 5.7 and 5.8).
8. GOES soft x-ray and radio flares had similar front and back slope distributions (Figures 5.7 and 5.8).

Table 5.3: Number of flares per frequency that had the largest intensity and largest integrated values for the 103 M-class flares in 2005.

	245	410	610	1415	2695	4995	8800	15400	None
Peak value	11	2	3	3	7	11	2	7	51
Peak integrated value	13	2	2	0	12	11	2	2	53

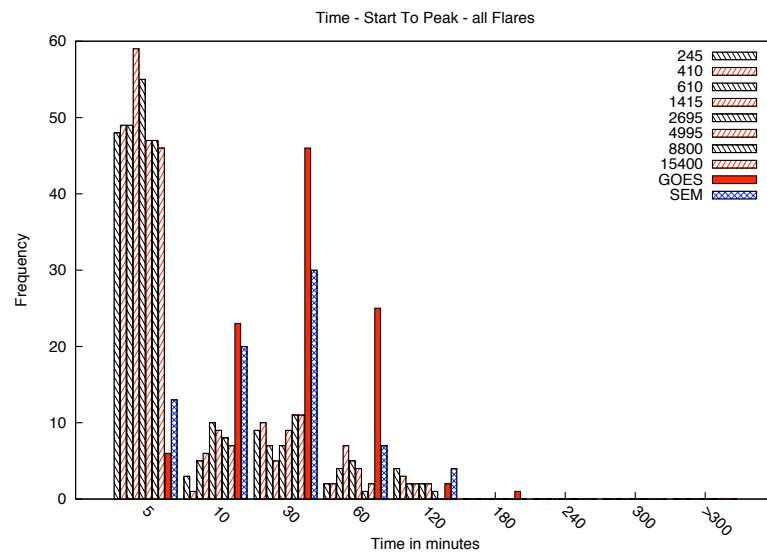


Figure 5.3: Distribution of flares according to time from start to peak of flare.

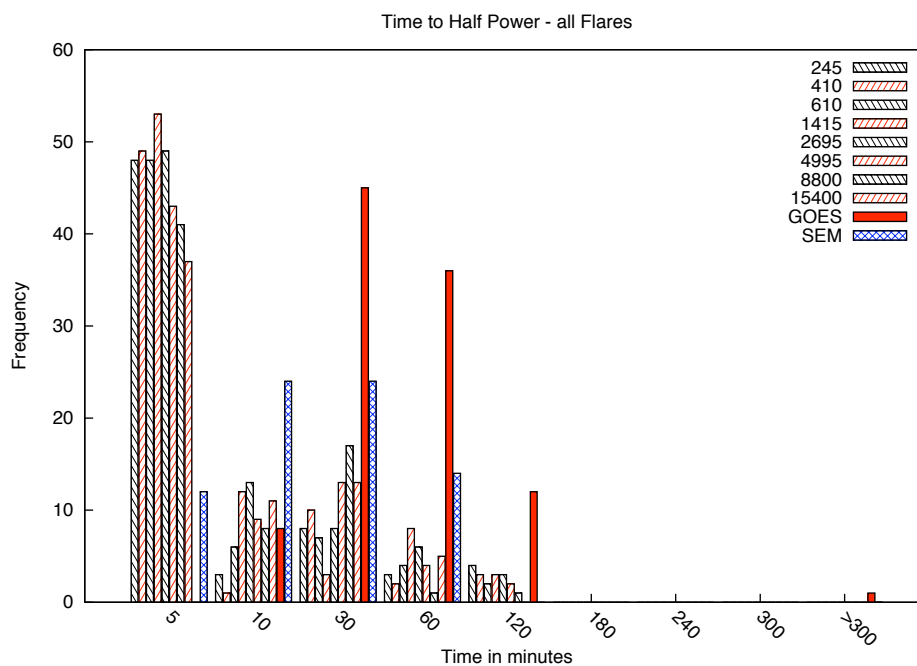


Figure 5.4: Distribution of flares according to time from peak to half power of flare.

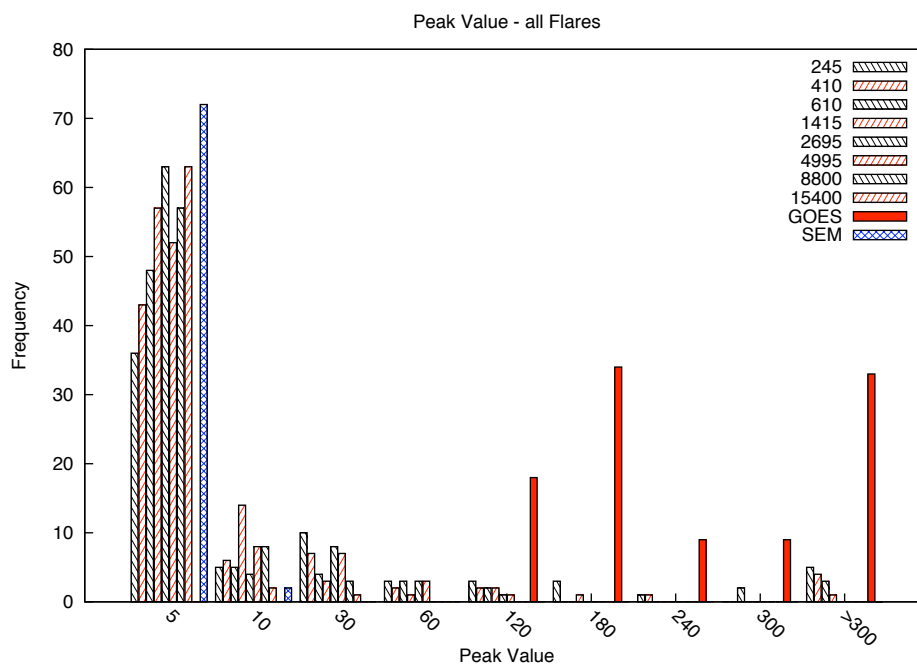


Figure 5.5: Distribution of flares according to peak intensity.

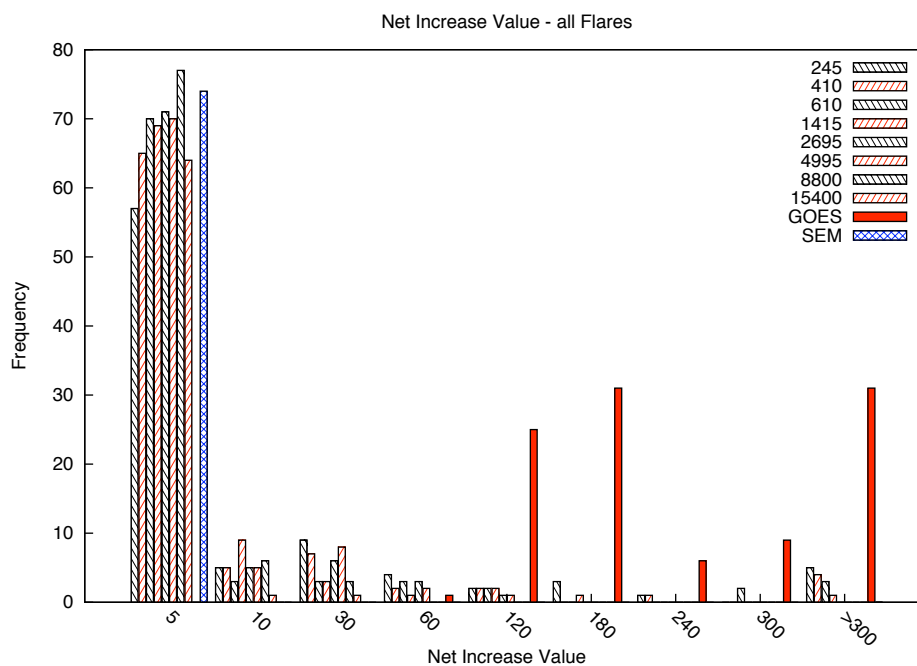


Figure 5.6: Distribution of flares according to net increase.

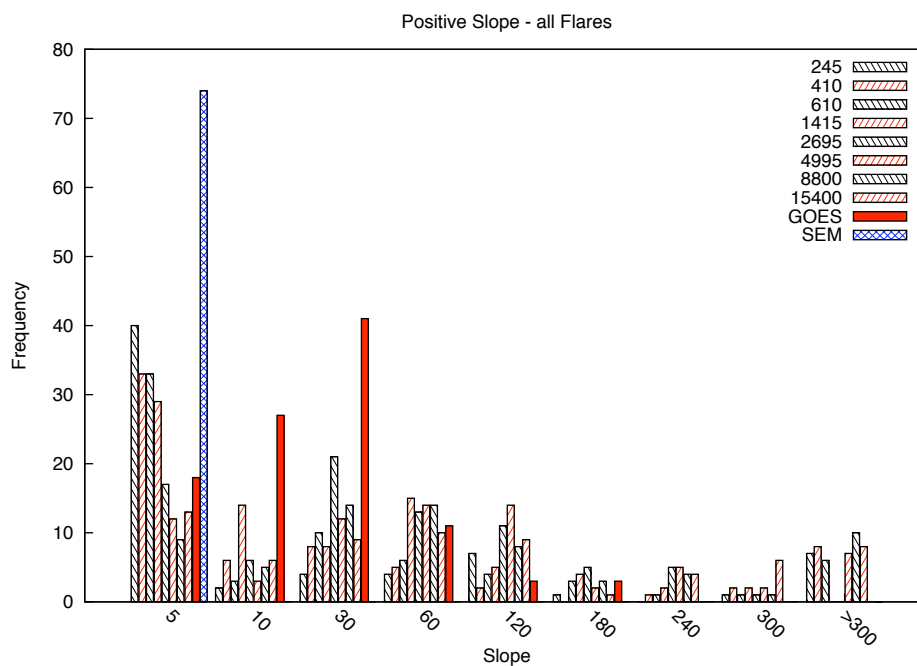


Figure 5.7: Distribution of flares according to front slope.

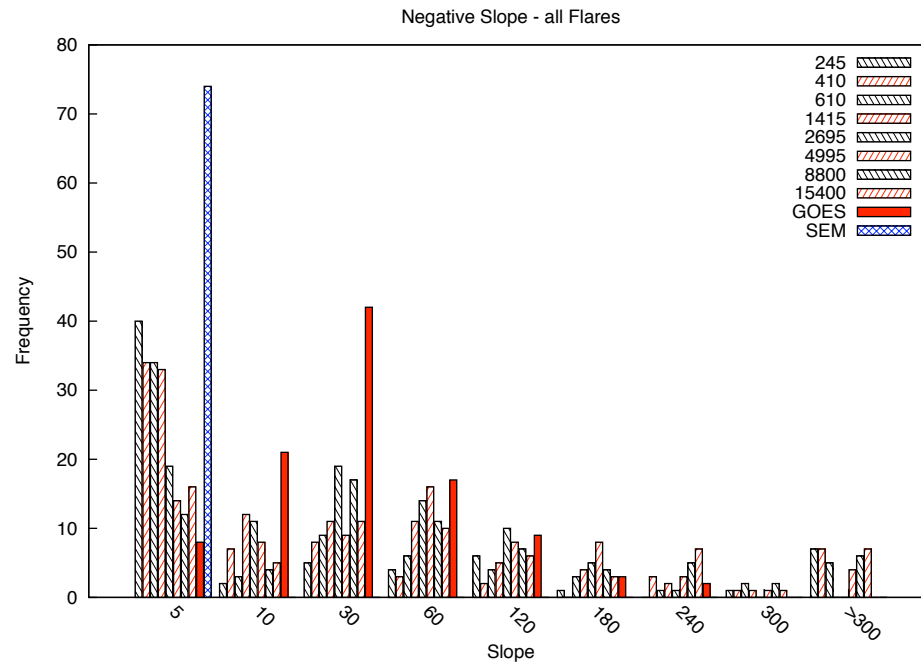


Figure 5.8: Distribution of flares according to back slope.

Figures 5.3 and 5.4 show what appears to be two distinct populations for the radio flares. One population reaches the peak and the half-power point within 5 minutes. The second population shows the same pattern as the GOES and SEM data, where the majority of the flares reach the peak and half-power point at within 30 minutes. The two radio groups were examined in greater detail to see if there were any correlations with the duration of the GOES and SEM flares. Figure 5.9 shows the results for the radio flares that reached their peak value within 5 minutes. The corresponding GOES and SEM flares for these radio flares still show the same results previously stated (i.e., majority of the GOES and SEM flares reach their peak at the 30-minute mark). Figure 5.10 shows the results for the radio flares that reached their peak values after the 5-minute mark. The results for the SEM flares showed no change. The majority of the SEM flares reached their peak at the 30-minute mark. The majority of the GOES flares reached their peak at the 60-minute mark.

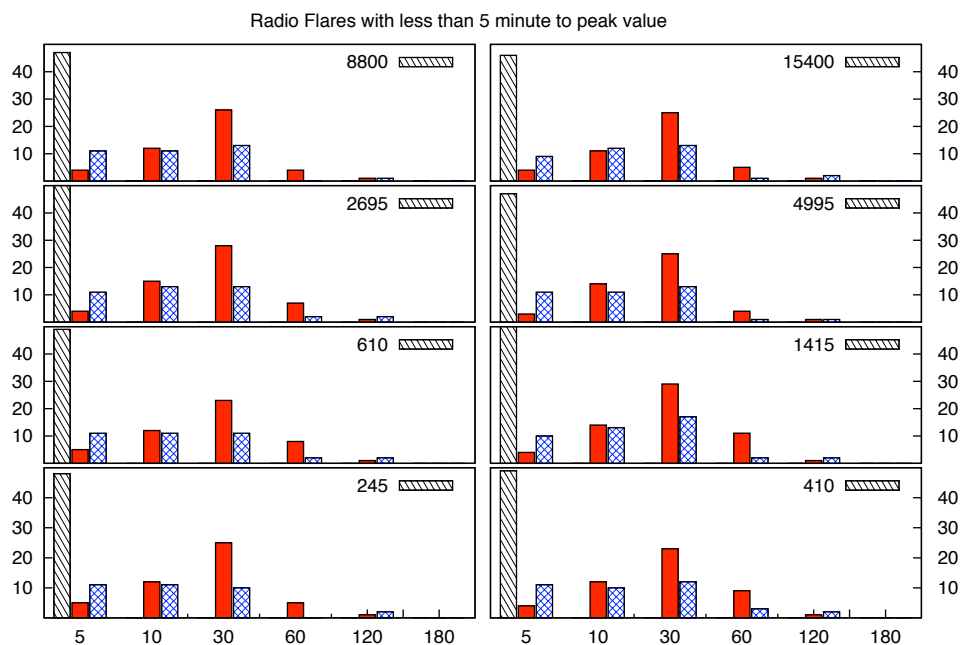


Figure 5.9: Distribution of flares observed in the western solar hemisphere according to time from peak to half-power point.

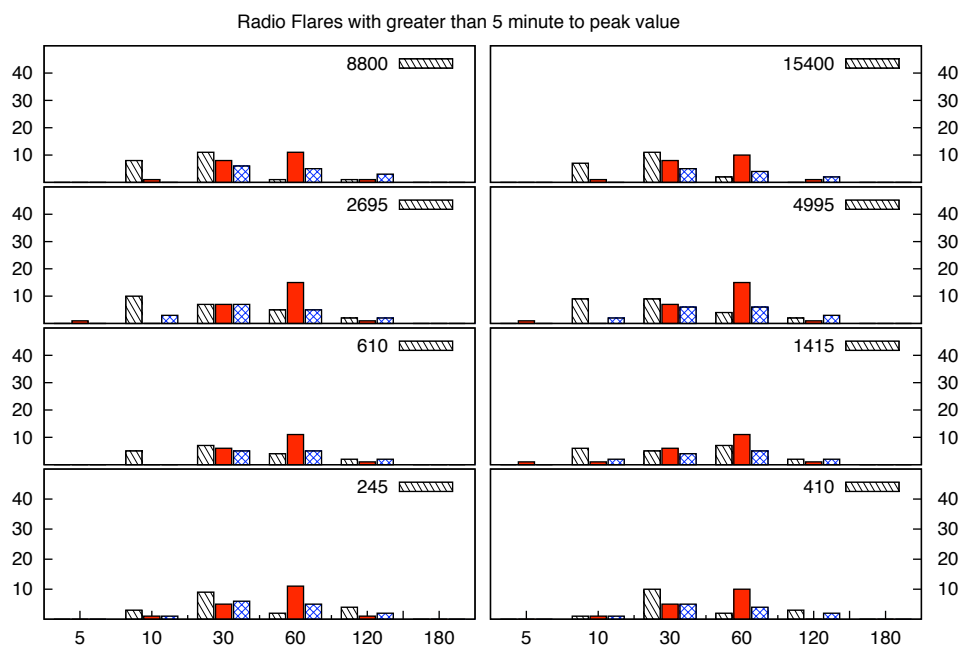


Figure 5.10: Distribution of flares observed in the western solar hemisphere according to time from peak to half-power point.

Regarding the net increase, the majority of the radio flares increased up to a factor of 5, but there were some that increased by two orders of magnitude. The increases on the SEM EUV flares were between 15% to 50%. The net increase for the GOES soft x-ray flares was biased based on the selection criteria for the flares. Since the analysis involved only M-class flares, all the soft x-ray flares increased two orders of magnitude. The breakdown of the GOES peak values are listed in Table 5.1. The analysis was repeated for flares meeting specific criteria, such as flares that occurred in the eastern (western), north (south) hemisphere, flares on the center of the solar disk (± 30 degrees), and flare magnitude. The results were consistent with the analysis of all the flares with two exceptions: the majority of the GOES soft x-ray flares originating in the North and West took longer to reach the half-power point (Figures 5.11 and 5.12).

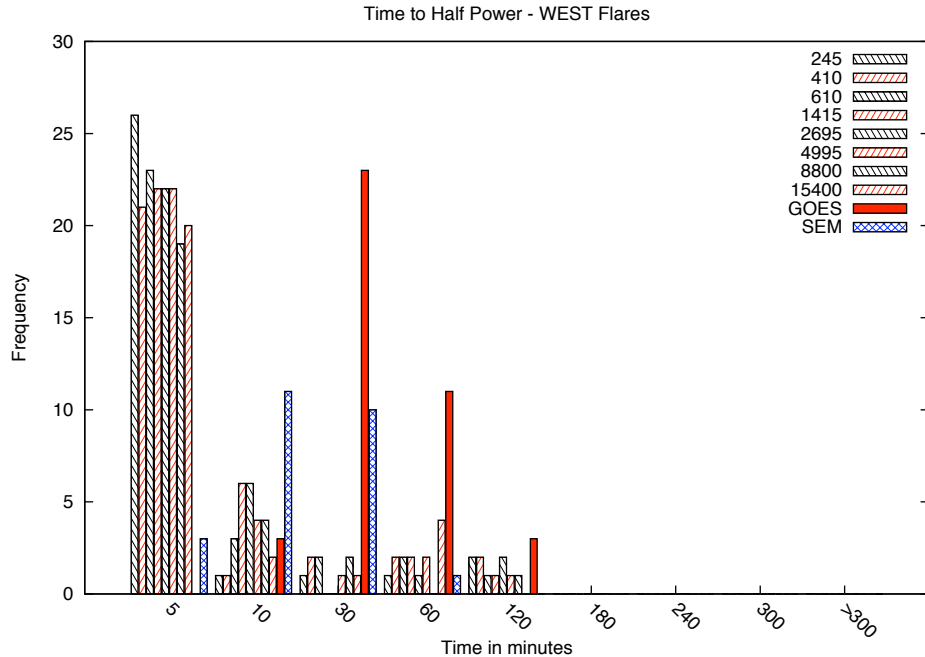


Figure 5.11: Distribution of flares observed in the western solar hemisphere according to time from peak to half-power point.

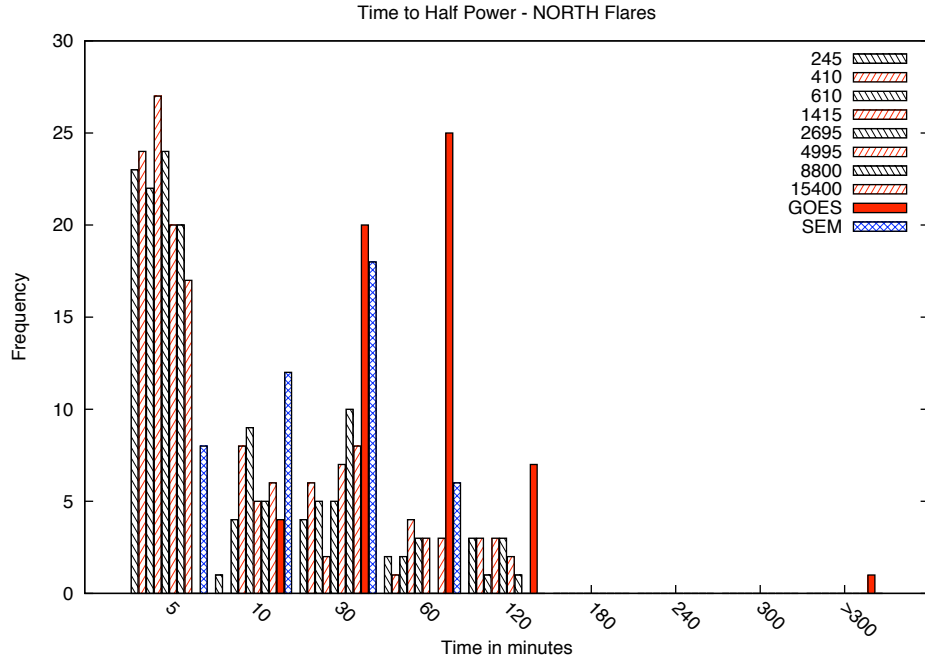


Figure 5.12: Distribution of flares observed in the northern solar hemisphere according to time from peak to half-power point.

5.3 TIMED-SEE Orbits

The TIMED-SEE instrument is able to observe the sun for 3 minutes every 97-minute orbit. During 2005, there were a total of 4860 orbits during which the instrument was able to measure the EUV spectrum. The start and end time of each orbit was cross-referenced with the start and end time of all flares detected in 2005 by the GOES satellites. Any TIMED-SEE orbit that fell within the duration of a GOES flare was flagged as a flare orbit. In some cases, several TIMED-SEE orbits took place during the duration of a flare. This was usually the case for M and X-class flares. The results are shown in Table 5.4.

The TIMED-SEE orbits were analyzed for correlations. Due to the significant difference between non-flare and flare orbits, the orbits were separated for these computations so that the results would not be dominated by the non-flare orbits.

Table 5.4: GOES flares and SEE orbits.

	No Flare	<C5 Class	>C5 Class	M Class	X Class
GOES		220	44	64	12
SEE	2288	48	8	81	34

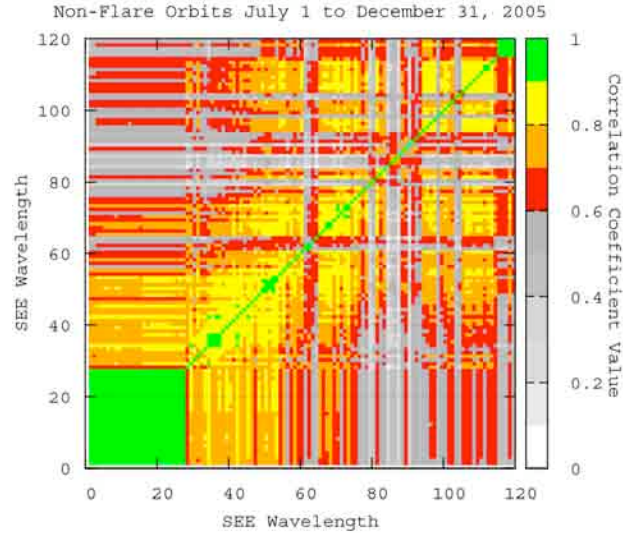


Figure 5.13: Correlations between SEE wavelengths for non-flare orbits.

The results for the non-flare orbits are shown in Figure 5.13 and are similar to the results from the daily value correlations in Chapter 4. There were three ranges of strong correlations ($\rho > 0.9$), 1-27 nm, 34-37 nm, and 115-129 nm. This indicates that the EUV response is not constant throughout the range measured by TIMED-SEE. The correlation results from the flare orbits (Figure 5.14) show even more variability and a significant decrease in the correlations indicating that the EUV response during flares varied depending on the wavelength. Finally, the correlation results for large flares (GOES M-class or larger) show a further decrease in the correlation values (Figure 5.15).

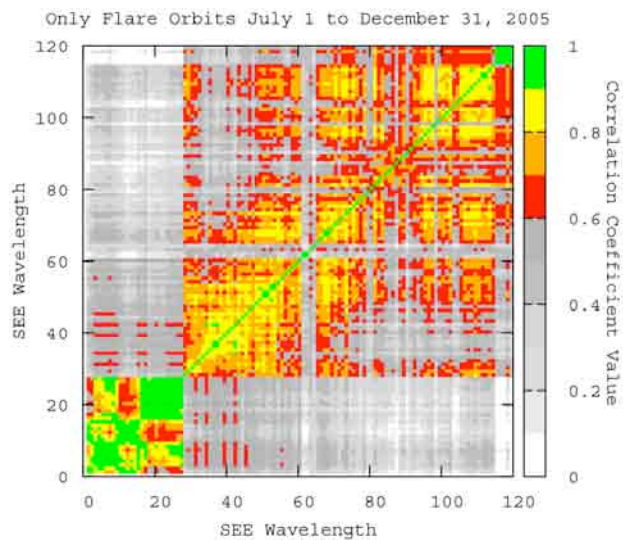


Figure 5.14: Correlations between SEE wavelengths for flare orbits.

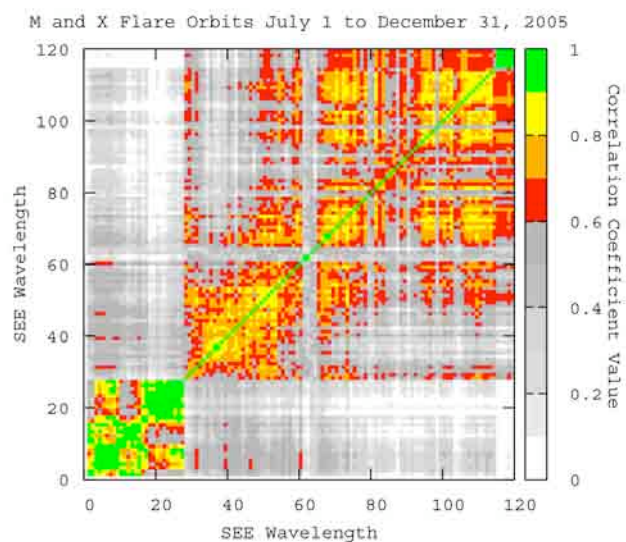


Figure 5.15: Correlations between SEE wavelengths for large flare orbits.

5.4 SEE, GOES, SEM Orbit Correlations

Next, the SEE orbits were compared to the GOES and SEM data. The start and end time of each SEE orbit was used to extract data from the GOES 1-minute data and the SEM 15-second data. The values for SEM and GOES were quality controlled for bad values and averaged to come up with a single value for each orbit. Overall, the three data sets showed similar trends and clearly tracked the solar rotations approximately every 27 days up to October 27, 2005. After that, the solar rotations are still clearly seen in GOES, but not as clearly on the SEM or SEE data. The data gap between August 22 and September 10 in the SEM data is due to sensor contamination. No data was available for SEM during this time. The smaller SEE wavelengths coincided with the GOES and SEM time series (Figure 5.16). As the wavelength increased, the SEE time series followed the GOES trend but the data became noisier (Figures 5.17 through 5.20). The same procedures used for the SEE data were used for these correlation computations: non-flare, flare, and large flares. Correlations for non-flare orbits were good ($\rho = 0.8$ or better) for both SEM channels up to a SEE wavelength of 60 nm. GOES 1-8 angstroms channel was good up to SEE wavelength of 27 nm. The GOES .5-4 angstroms channel had correlations of less than 0.6 for all wavelengths (Figure 5.21). The correlations for flares showed a decreasing trend for these three channels, but better correlations for the GOES .5-4 angstroms channel (Figure 5.22). Figure 5.24 shows these differences. The correlations for large flares were better for both GOES channels than for the SEM channels (Figures 5.23 and 5.25). This analysis shows that while SEM data correlates better to TIMED-SEE EUV data below 60 nm for non-flare orbits, GOES data correlates better to TIMED-SEE EUV data below 15 nm during flares.

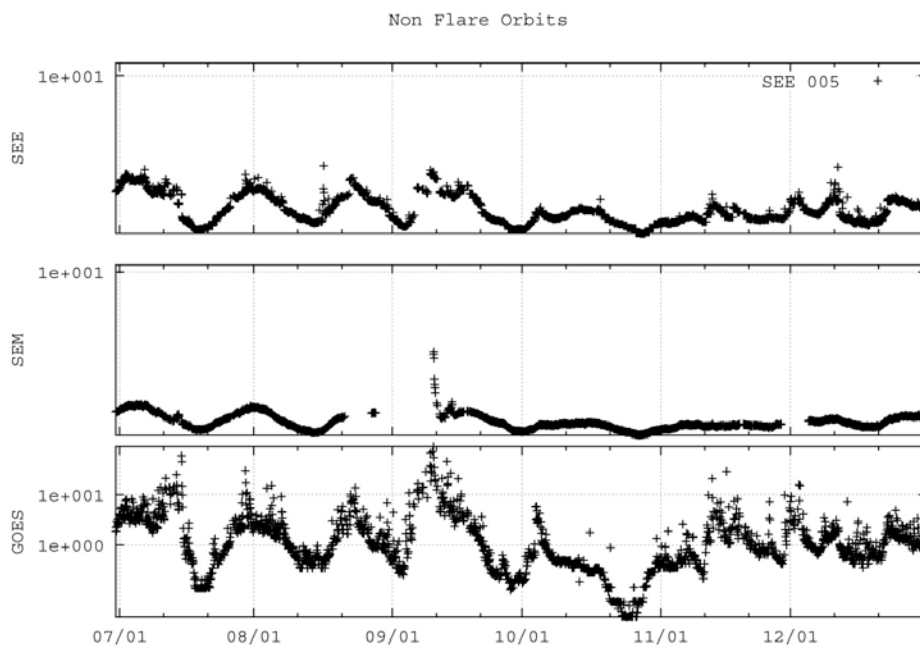


Figure 5.16: Time series of non-flare orbits for GOES, SEM, and SEE wavelength 5 from July 1 to December 31, 2005.

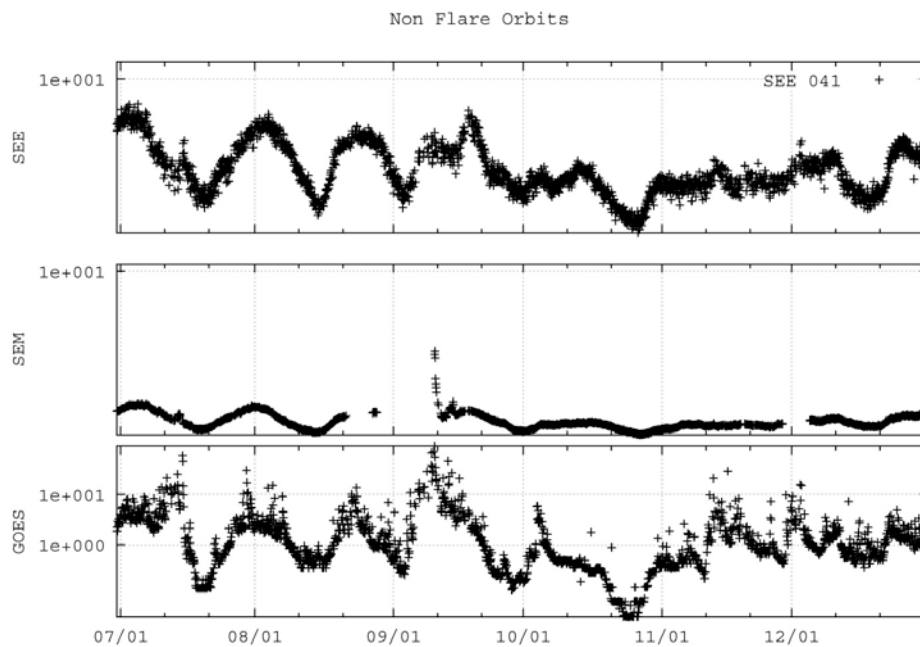


Figure 5.17: Time series of non-flare orbits for GOES, SEM, and SEE wavelength 41 from July 1 to December 31, 2005.

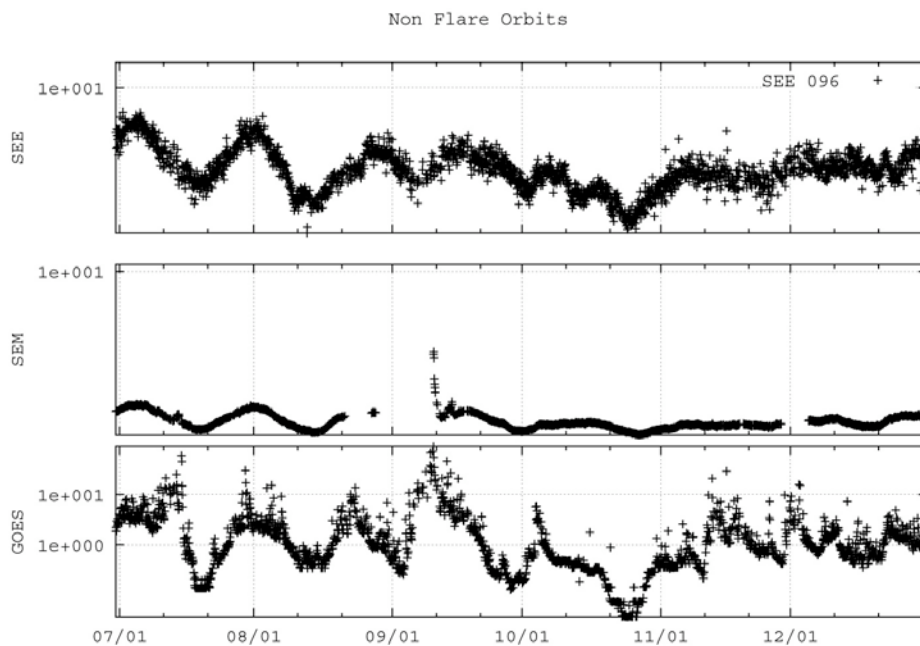


Figure 5.18: Time series of non-flare orbits for GOES, SEM, and SEE wavelength 96 from July 1 to December 31, 2005.

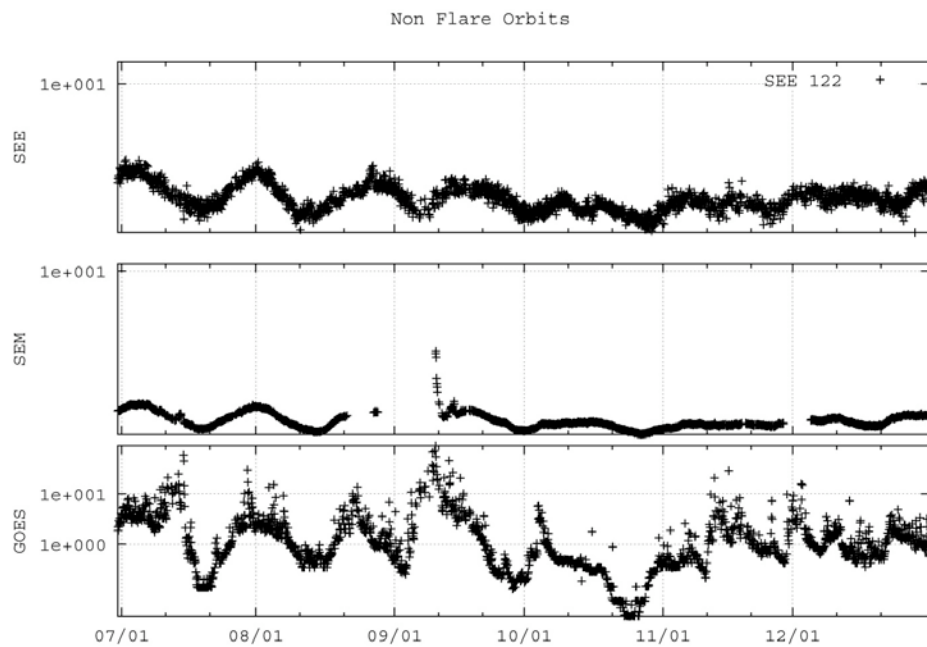


Figure 5.19: Time series of non-flare orbits for GOES, SEM, and SEE wavelength 122 from July 1 to December 31, 2005.

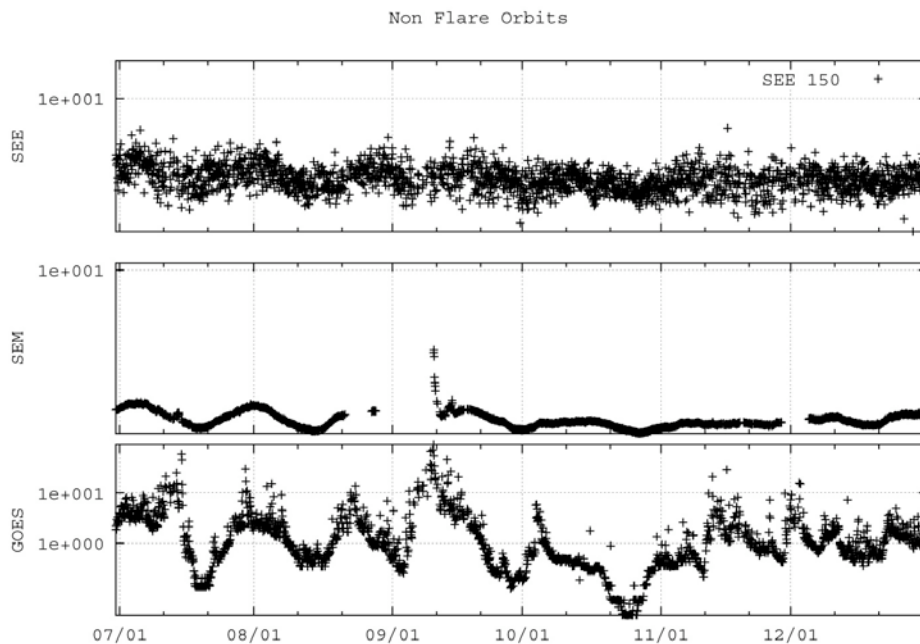


Figure 5.20: Time series of non-flare orbits for GOES, SEM, and SEE wavelength 150 from July 1 to December 31, 2005.

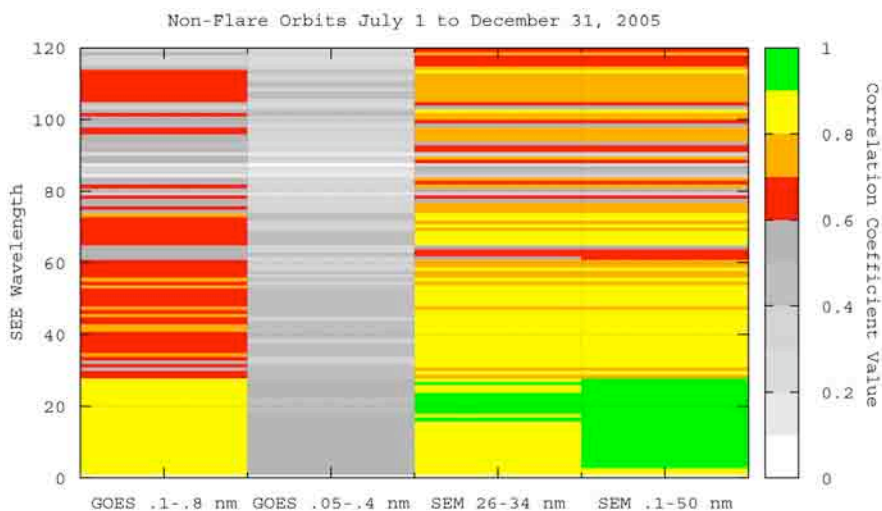


Figure 5.21: Correlations between GOES, SEM, and SEE for non-flare orbits.

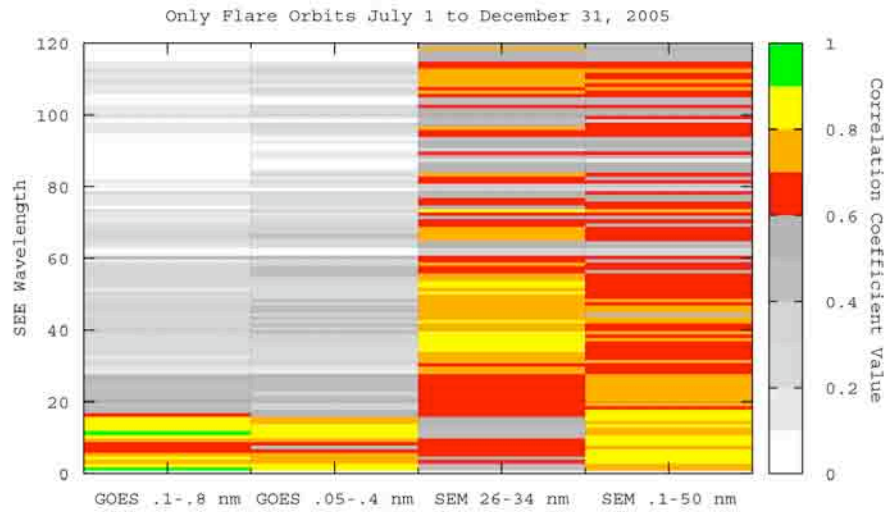


Figure 5.22: Correlations between GOES, SEM, and SEE for flare orbits.

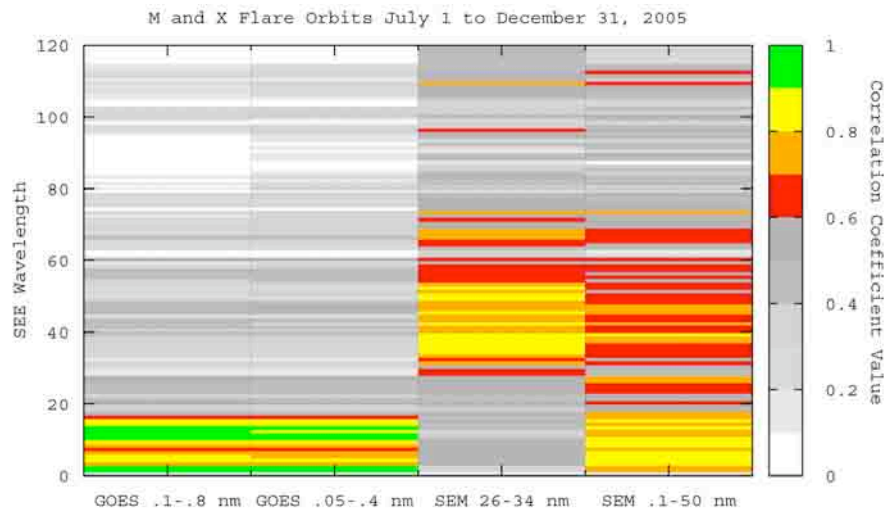


Figure 5.23: Correlations between GOES, SEM, and SEE for large flare orbits.

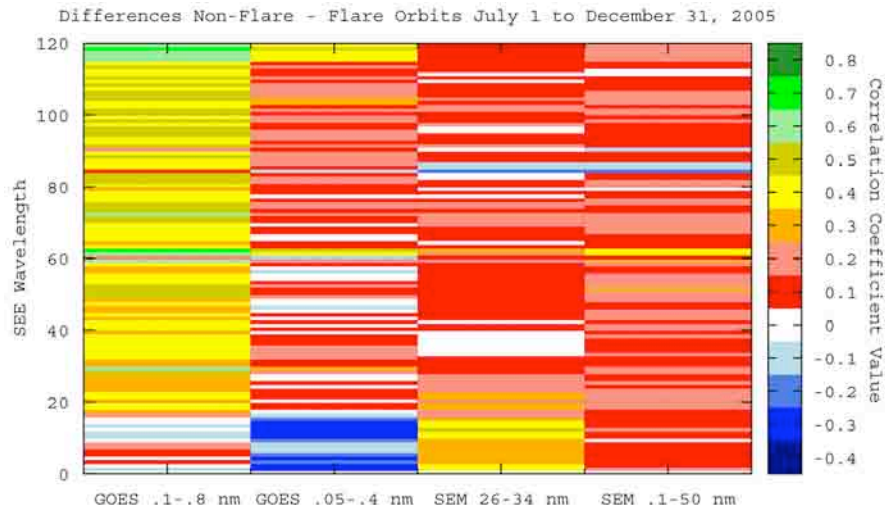


Figure 5.24: Differences between flare and non-flare orbit correlations. Negative numbers correspond to a better correlation value for the flare orbits.

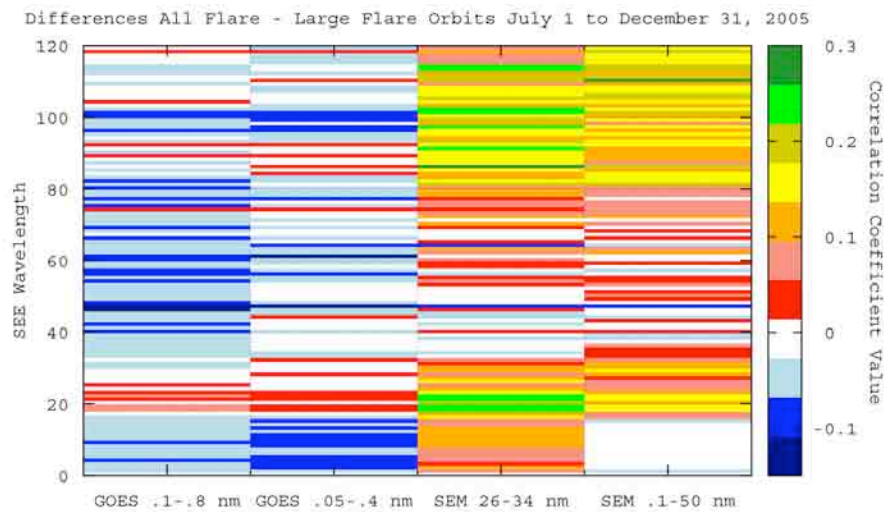


Figure 5.25: Differences between flare and non-flare orbit correlations. Negative numbers correspond to a better correlation value for the large flare orbits.

5.5 RSTN, GOES, SEM Analysis

Once again, using the start and end time for the TIMED-SEE orbits, radio data was extracted from all four observatories for each orbit. The values were quality controlled and averaged to come up with a single value for each orbit. Unlike the previous analysis using GOES and SEM data, a single observatory does not have data for each one of the SEE orbits. The approach taken was to use one observatory for the initial test, and then use the remaining three observatories as a verification of the technique. The reasoning behind this approach is that if there is a correlation between radio data and EUV data, then each observatory, although looking at different orbits within the dataset, should come up with a similar answer. Another difference between this and the previous study is the data itself. GOES data is relatively noise-free and for the most part, constant. SEM EUV data is also fairly constant and generally noise-free, unless the instrument becomes contaminated or saturated during a solar energetic proton (SEP) event. SEP events are usually associated with large flares and occur when protons emitted by the sun are accelerated to very high energies. During these events, which are easily measured by several instruments, SEM EUV data is contaminated and thus, not available. RSTN data, on the other hand, is noisy due to solar tracking issues, local radio interference, and calibration issues. Figure 5.26 is a plot of the observations from Sagamore Hill radio observatory for July 1, 2005. The eight discrete frequencies are plotted as a function of time. On the upper portion of the graph, the SEE orbits are also plotted. The numbering sequence for the SEE orbits was arbitrarily set to one for the first orbit on January 1, 2005 and then incremented by one every time there was an orbit with data. The flag on top of the orbit number indicates whether the orbit was associated with a flare (D (< C5), C, M or X) or quiet solar conditions (N). In Figure 5.26, orbits 2408 and 2416 took place at

the beginning and end of the observing day of this observatory. During these portions of the day, the data is subject to tracking, calibration, and interference issues. Orbits such as these two were removed from the time series for each observatory and not included in any of the analysis. Figure 5.27 shows the observations recorded by the San Vito radio observatory on July 4, 2005. Orbits 2447 and 2455 have similar issues already discussed regarding the start and end of the observing day. Orbit 2451 is an example of a calibration issue. As close as possible to the local noon, each observatory performs a calibration of all of its frequencies. During that time, some data may be recorded but is generally not accurate. Any orbit that coincided with any calibration activity was also excluded from the analysis. Orbit 2449 shows an example of local radio frequency interference problems. The spike on the bottom frequency (black lines) as well as the spike on the third frequency (green line) are examples of RFI. Any orbit that coincided with RFI instances were discarded. Finally, the top three frequencies show an example of tracking problems around orbit 2454. The observations exhibit a saw tooth pattern during this time. As the sun's declination angle is changing, the antenna cannot accurately track the sun, resulting in the measurement of a weaker signal. The observer will then manually adjust the antenna until the full signal from the sun is reacquired. This procedure is repeated every time the signal strength is reduced and is very common at the beginning and end of the day for each observatory. These orbits were also excluded. All observatories experienced all of the problems mentioned above. Some observatories had more problems than others. For example, the lower three frequencies (245, 410, and 610 MHz) at San Vito experienced RFI more than any other frequency bands in any other observatory. San Vito's 15400 MHz and Learmonth's 8800 MHz had tracking problems due to solar declination (sawtooth patterns). The start and end of Sagamore Hill's observing day

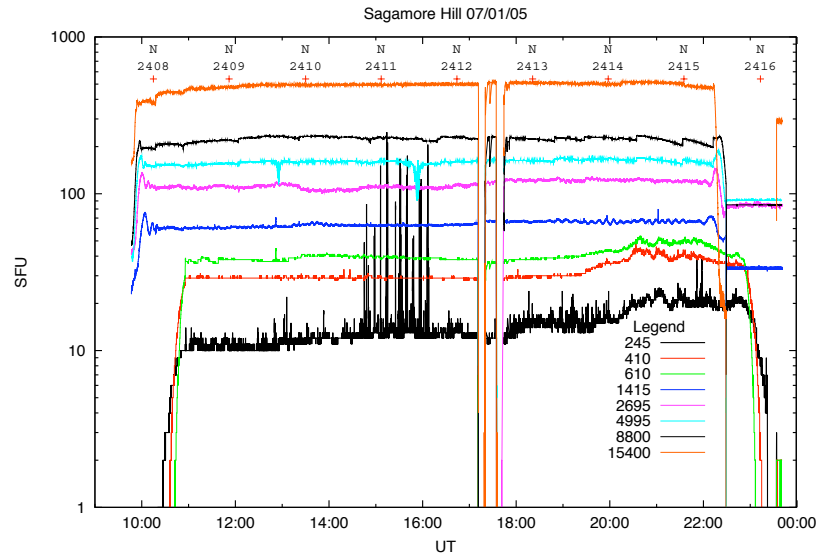


Figure 5.26: Radio plot for Sagamore Hill observatory on July 1, 2005 showing some of the SEE orbits not used due to bad radio data.

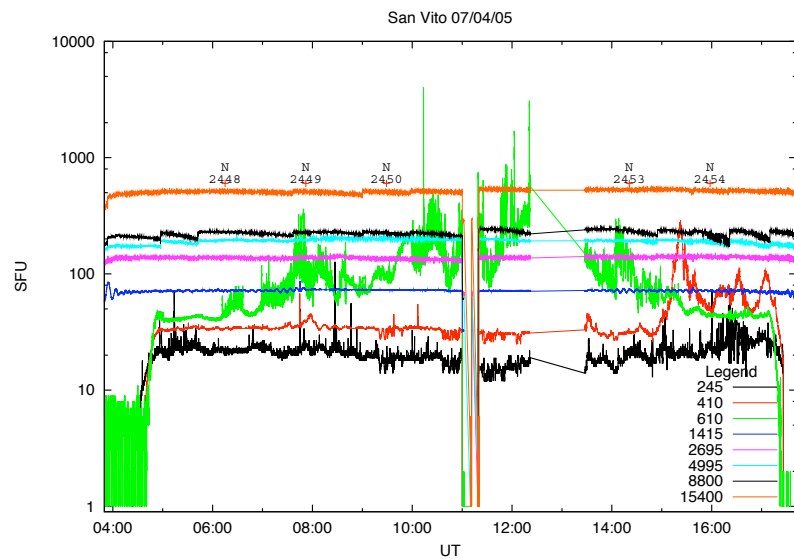


Figure 5.27: Radio plot for San Vito observatory on July 4, 2005 showing some of the SEE orbits not used due to bad radio data.

coincided with orbits almost every day during this time period.

Figures 5.28 through 5.35 (starting on page 106) show the non-flare orbits for each observatory during this time period. Despite the problems mentioned above, each observatory's frequencies show a similar pattern of activity that is comparable to what was observed by GOES, SEM, and SEE (Figures 5.16 through 5.20).

Once the "bad" orbits were removed, the radio data was compared against GOES and SEM orbits. As previously stated, one observatory was used as a test for the correlations and the other three were used as confirmation of the test. The Palehua Solar Observatory was chosen as the test observatory. Table 5.5 (on page 110) shows the number and type of orbits for each observatory used for these computations.

The first set of correlations was computed for non-flare orbits. Palehua's 1415, 2695, and 4995 MHz frequencies had ρ values greater than 0.7 for both SEM channels and GOES main channel (Figure 5.36, page 111). The correlation for the secondary GOES channel had lower values. These results were confirmed by Learmonth, San Vito, and Sagamore Hill's correlations (Figures 5.37 through 5.39, page 111). The correlations were not as good as the values for Palehua. This is due in part to the noise with the data. As more strict data quality control standards were applied to the data, the correlation values increased for these three observatories. The quality control, in this case, consisted of removing questionable orbits. Most of the orbits removed were due to wrong flux values due to tracking problems. The correlations for the flare orbits showed similar results for the SEM channels, but different for GOES. The correlations for the main GOES channel decreased and shift toward higher frequencies. The secondary GOES channel's correlations increased slightly (Figures 5.40 through 5.43, page 113). This is similar to the correlation results between GOES and SEE.

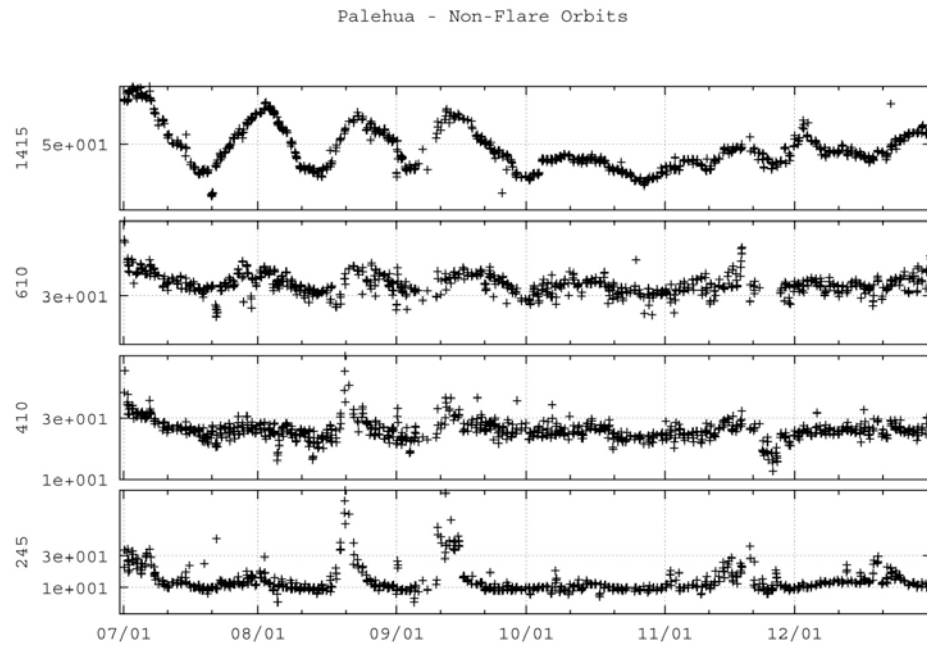


Figure 5.28: Time series of non-flare orbits for Palehua's lower four frequencies from July 1 to December 31, 2005.

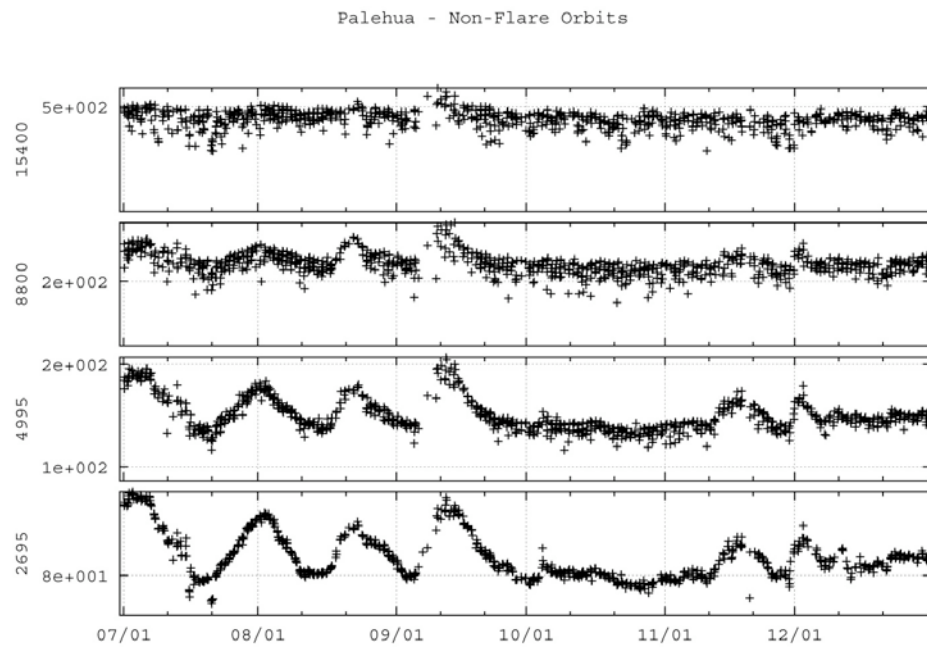


Figure 5.29: Time series of non-flare orbits for Palehua's lower four frequencies from July 1 to December 31, 2005.

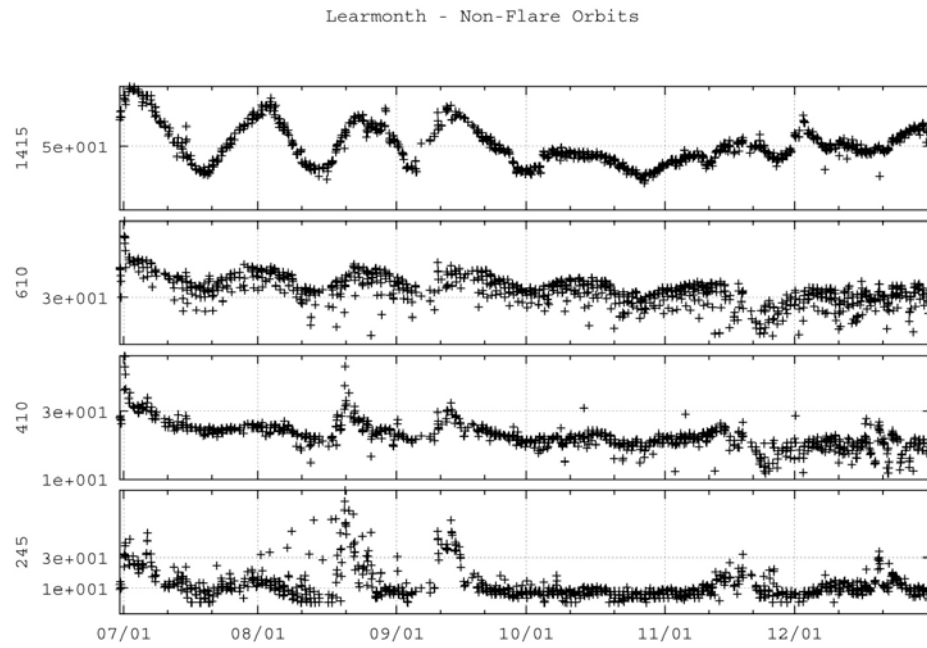


Figure 5.30: Time series of non-flare orbits for Learmonth's upper four frequencies from July 1 to December 31, 2005.

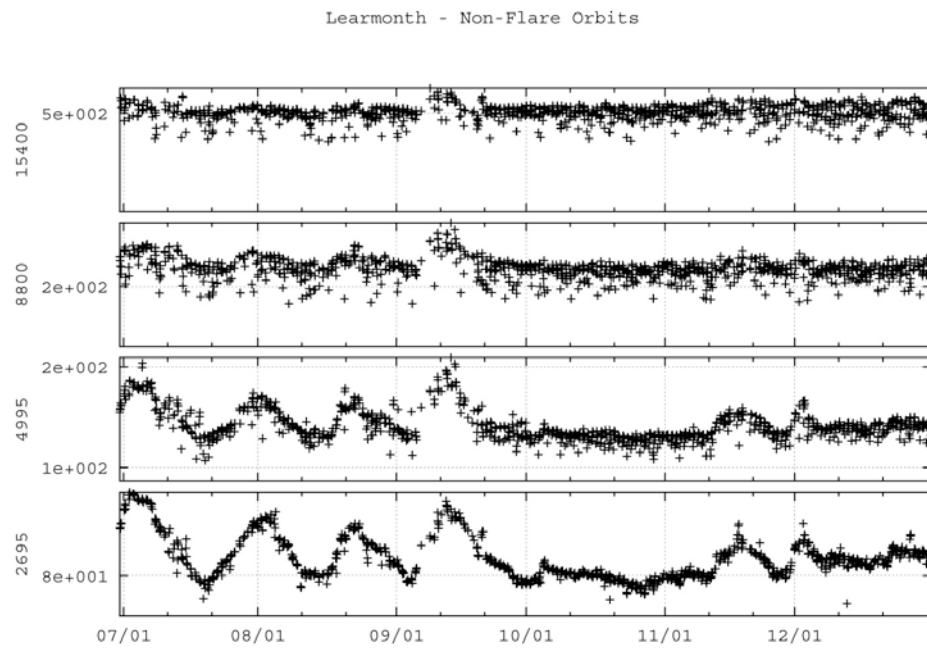


Figure 5.31: Time series of non-flare orbits for Learmonth's upper four frequencies from July 1 to December 31, 2005.

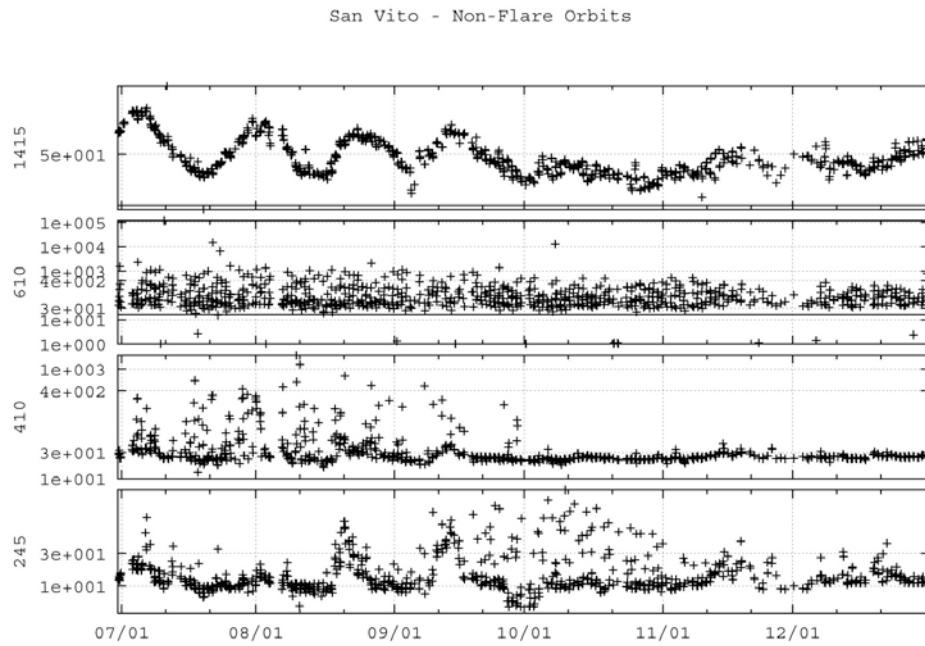


Figure 5.32: Time series of non-flare orbits for San Vito's lower four frequencies from July 1 to December 31, 2005.

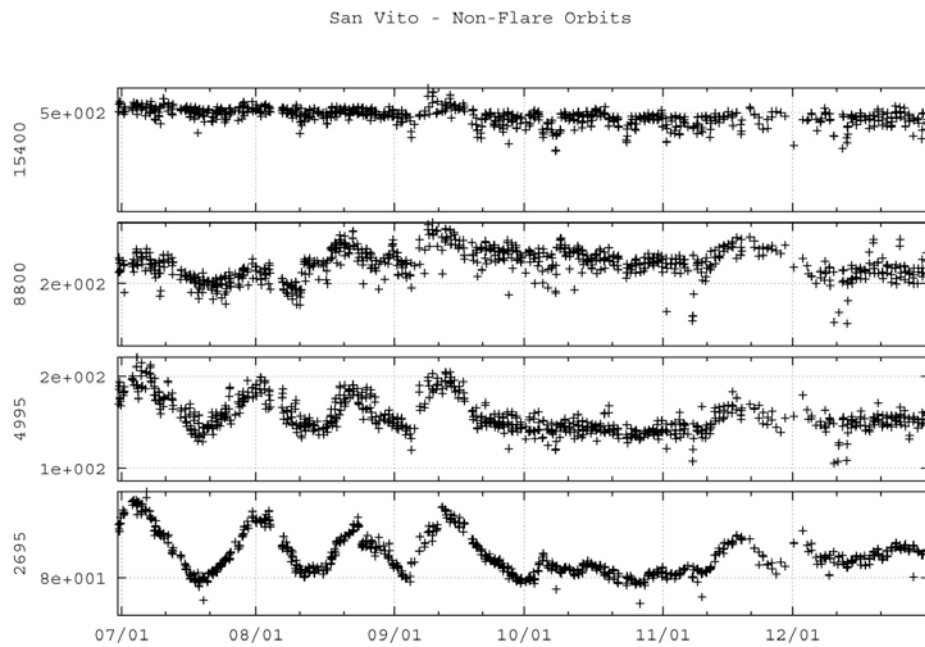


Figure 5.33: Time series of non-flare orbits for San Vito's upper four frequencies from July 1 to December 31, 2005.

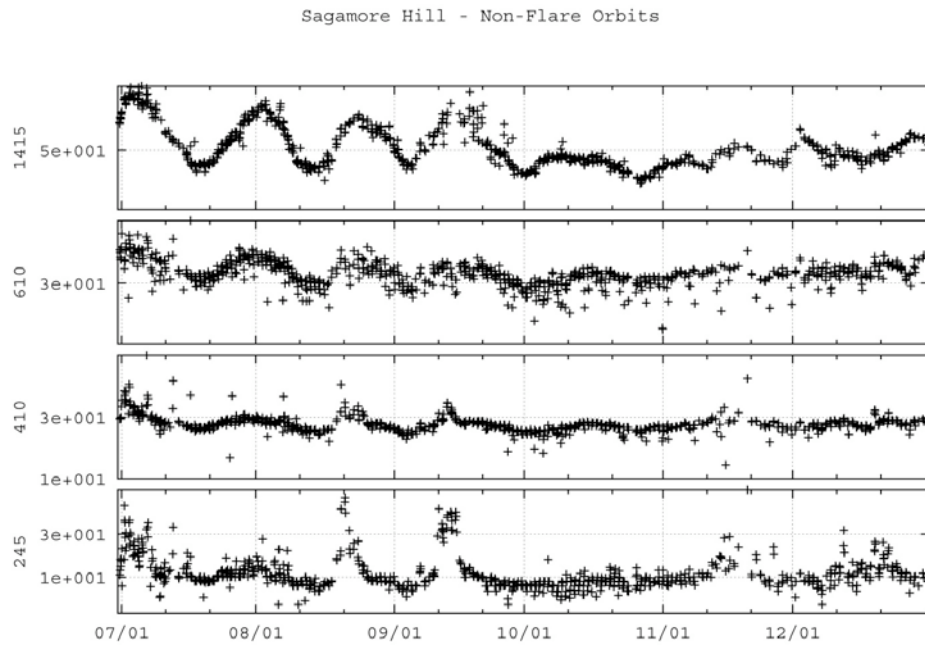


Figure 5.34: Time series of non-flare orbits for Sagamore Hill's lower four frequencies from July 1 to December 31, 2005.

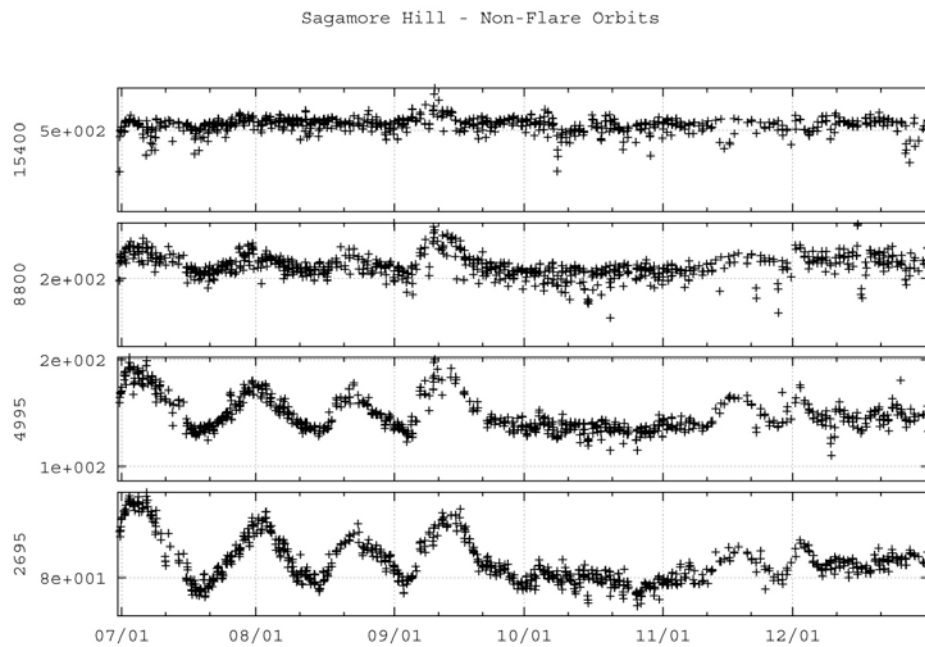


Figure 5.35: Time series of non-flare orbits for Sagamore Hill's upper four frequencies from July 1 to December 31, 2005.

Table 5.5: Number and type of orbits observed by RSTN observatories.

	245	410	610	1415	2695	4995	8800	15400
Palehua								
No Flare	919	932	922	938	917	938	941	940
<C5	11	11	11	11	11	11	11	11
>C5	3	3	3	3	3	3	3	3
M	40	40	40	40	40	40	40	40
X	18	19	19	19	19	19	19	19
Learmonth								
No Flare	1047	1042	1047	1076	1080	1072	1072	1076
<C5	18	19	18	18	19	18	19	19
>C5	5	5	5	5	5	5	5	5
M	34	34	34	34	34	34	34	34
X	19	19	19	19	19	19	19	19
San Vito								
No Flare	985	992	1037	1049	1051	1048	1043	1070
<C5	25	25	29	29	30	30	28	30
>C5	4	4	4	4	4	4	4	4
M	36	36	38	39	39	39	39	39
X	16	16	16	16	16	16	16	16
Sagamore Hill								
No Flare	961	963	955	978	984	960	980	978
<C5	25	25	24	25	25	24	25	25
>C5	3	3	3	3	3	3	3	3
M	45	44	45	44	45	43	45	45
X	15	15	15	15	15	13	15	15

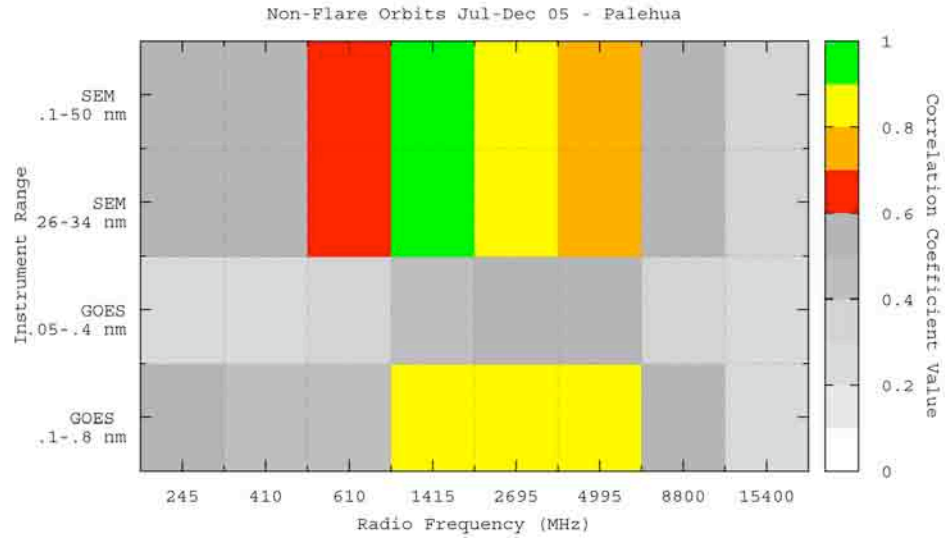


Figure 5.36: Correlations between Palehua, GOES, and SEM for non-flaring orbits.

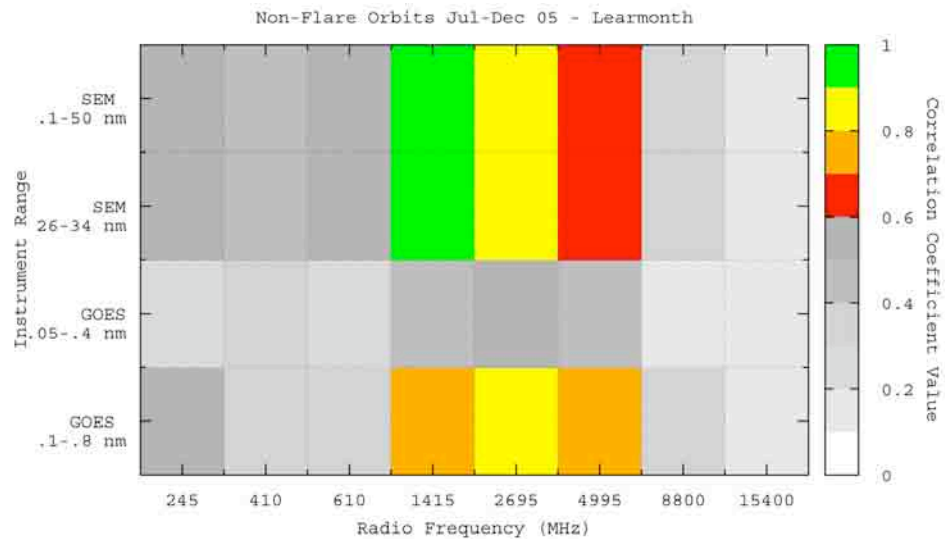


Figure 5.37: Correlations between Learmonth, GOES, and SEM for non-flaring orbits.

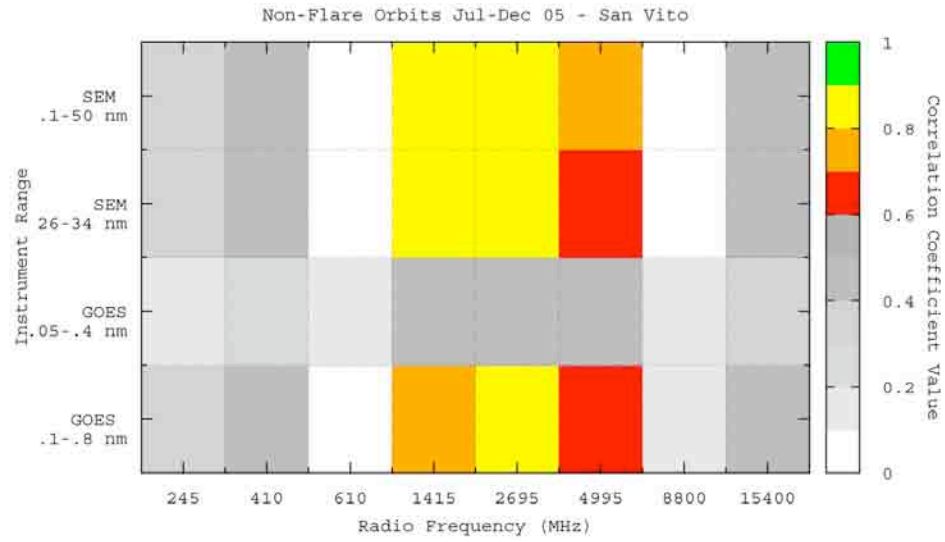


Figure 5.38: Correlations between San Vito, GOES, and SEM for non-flaring orbits.

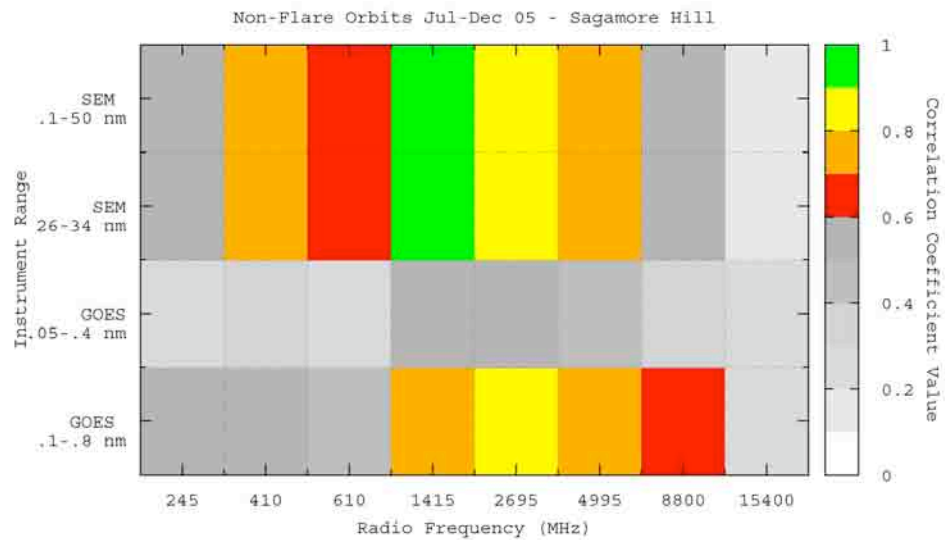


Figure 5.39: Correlations between Sagamore Hill, GOES, and SEM for non-flaring orbits.



Figure 5.40: Correlations between Palehua, GOES, and SEM for flaring orbits.

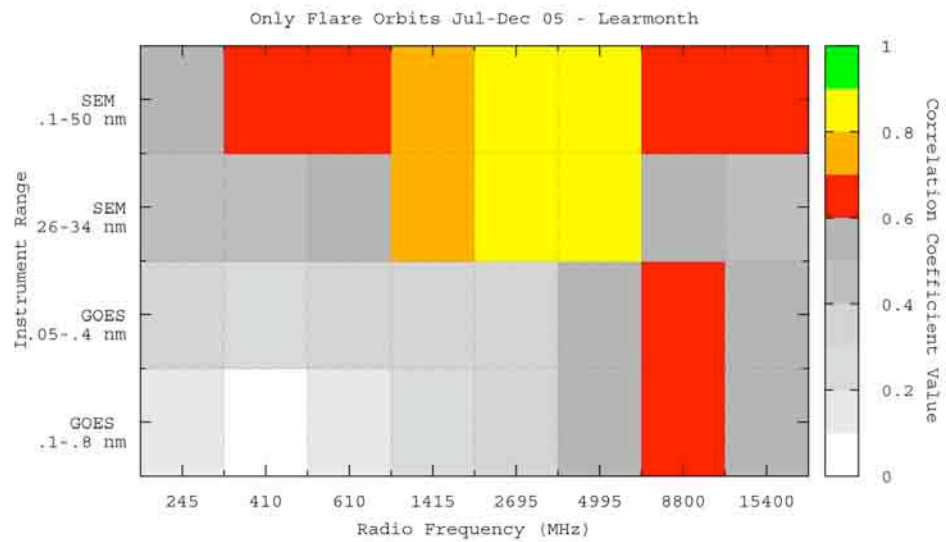


Figure 5.41: Correlations between Learmonth, GOES, and SEM for flaring orbits.

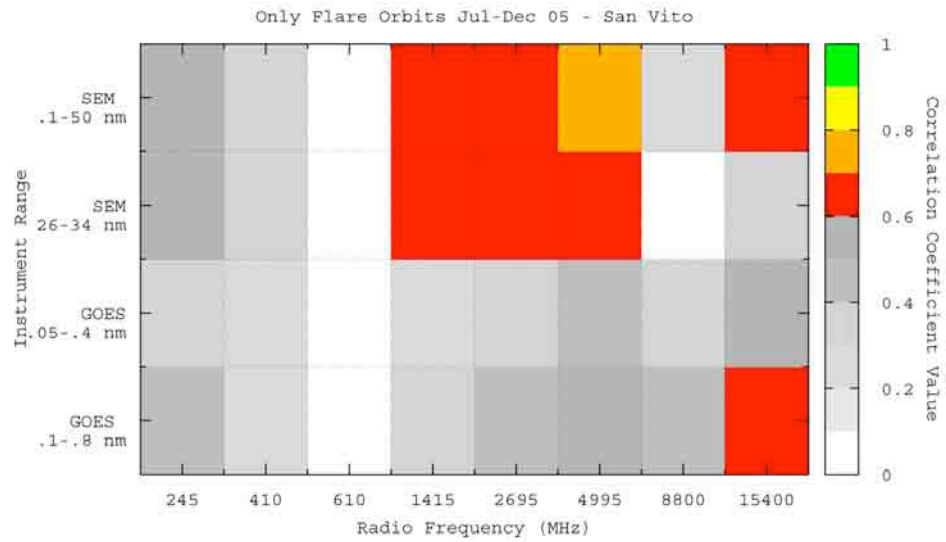


Figure 5.42: Correlations between San Vito, GOES, and SEM for flaring orbits.

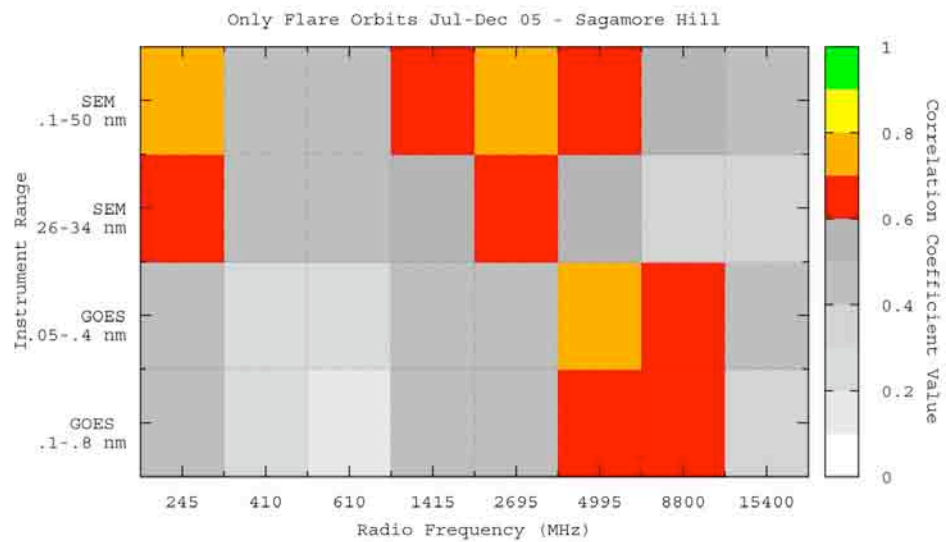


Figure 5.43: Correlations between Sagamore Hill, GOES, and SEM for flaring orbits.

5.6 RSTN-SEE Analysis

The correlations between radio and SEE for non-flare orbits had correlation coefficients greater than 0.7 for 1415, 2695, and 4995 MHz from SEE wavelength 1 to 70 and between SEE 100 to SEE 120 wavelengths (Figures 5.44 through 5.47). The results were very similar between the four observatories.

The correlations for the flaring orbits had similar results as the flaring orbit correlations between radio, GOES, and SEM. The higher correlation values moved toward higher SEE wavelengths and towards higher radio frequencies (Figures 5.48 through 5.51). Once again, the results among the observatories had similar patterns but there were some differences. Also, there was more variation among observatories for the flare orbits than for the non-flare orbits. Palehua and Learmonth had similar results for the flaring orbits with the exception of the correlations on frequencies 4995 and 8800 MHz. In this frequency range, Learmonth had tracking issues that also showed up on the results for the non-flare orbits (Figure 5.45). San Vito's results also showed the tracking problems with 8800 MHz (Figures 5.46 and 5.50).

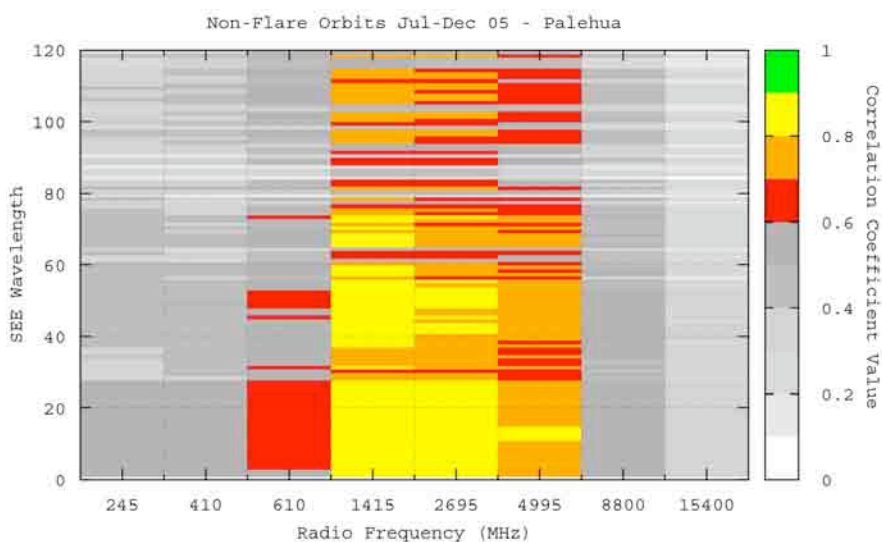


Figure 5.44: Correlations between Palehua, and SEE for non-flaring orbits.

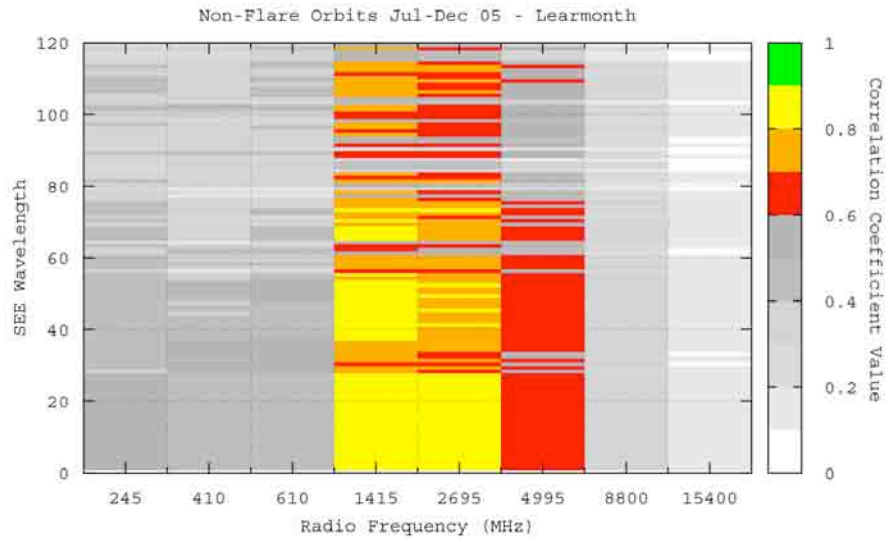


Figure 5.45: Correlations between Learmonth, and SEE for non-flaring orbits.

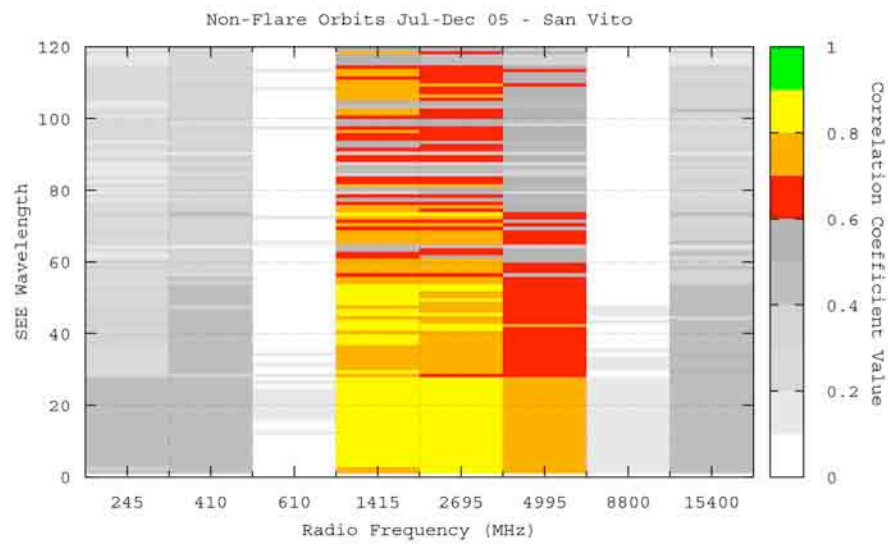


Figure 5.46: Correlations between San Vito, and SEE for non-flaring orbits.

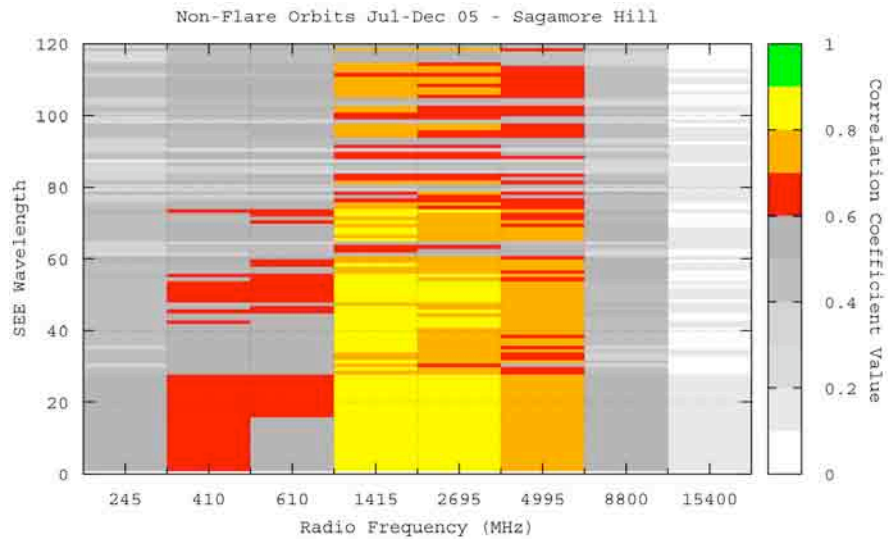


Figure 5.47: Correlations between Sagamore Hill, and SEE for non-flaring orbits.

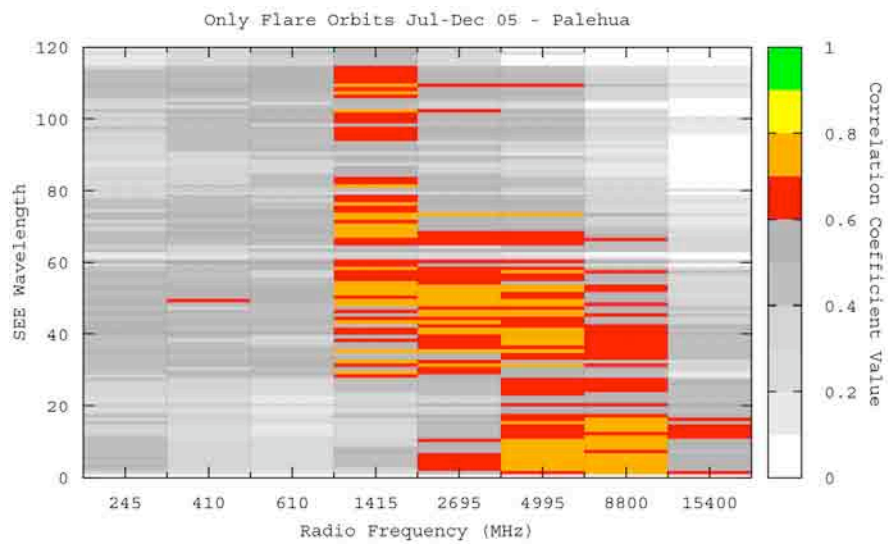


Figure 5.48: Correlations between Palehua, and SEE for flaring orbits.

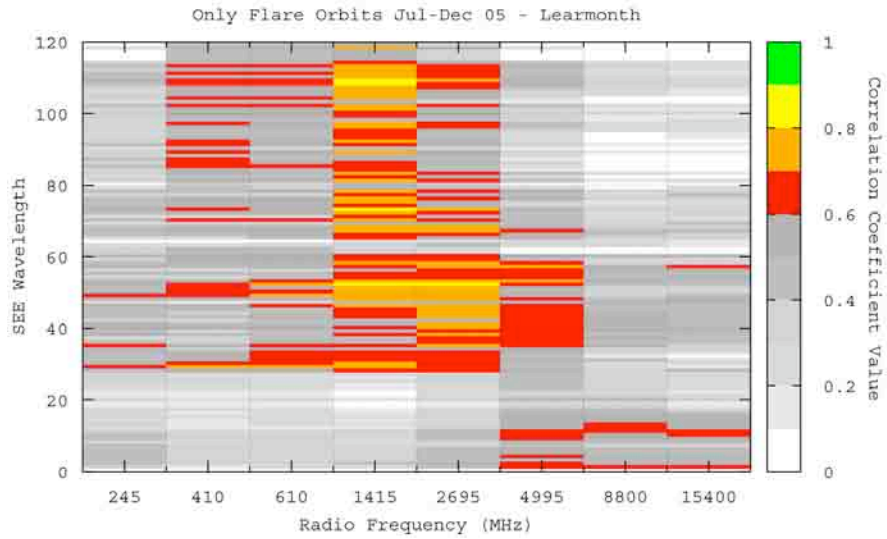


Figure 5.49: Correlations between Learmonth, and SEE for flaring orbits.

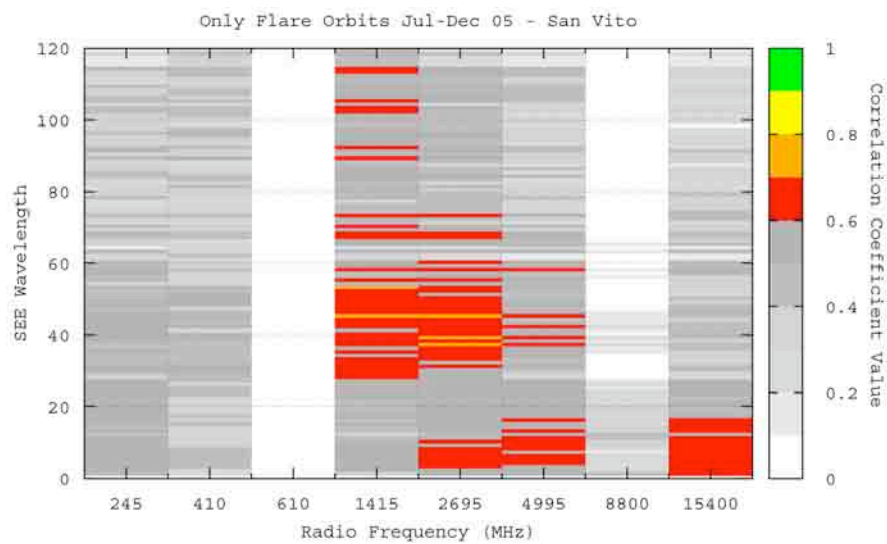


Figure 5.50: Correlations between San Vito, and SEE for flaring orbits.

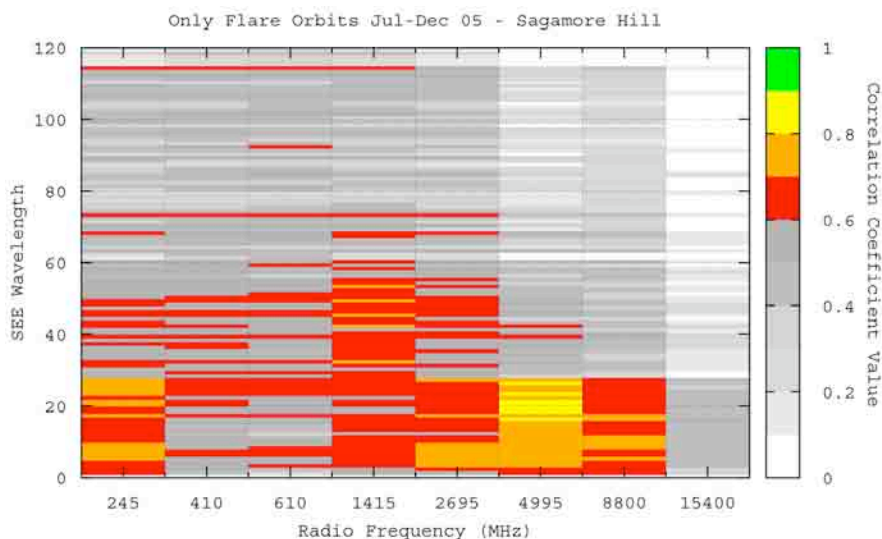


Figure 5.51: Correlations between Sagamore Hill, and SEE for flaring orbits.

Sagamore Hill's results of high correlation coefficient values on 1415 MHz did not include as many SEE wavelengths as the other observatories. The other differences in the correlation results for the different observatories could be attributed to a combination of other issues that were not possible to remove during the data quality control, issues such as tracking the sun and dealing with different baselines among observatories.

To test this idea, correlations were computed between the observatories. If the instruments were calibrated to the same values, and if there were no tracking issues, one would expect to get high correlations among each of the observatories' frequencies since they are observing the same sun. However, if there were low correlation values, the reason should be associated with the instrument. The number of non-flare orbits in common between the observatories is given in Table 5.6.

Figure 5.52 shows the results of the correlations between observatories for non-flaring orbits. This figure shows all 32 frequencies (eight for each observatory). For each observatory, the frequencies are shown in increasing order from left to right

Table 5.6: Non-flare orbits in common between RSTN observatories.

	Palehua	Learmonth	San Vito	Sagamore Hill
Palehua		427	13	400
Learmonth	427		460	3
San Vito	13	460		390
Sagamore Hill	400	3	390	

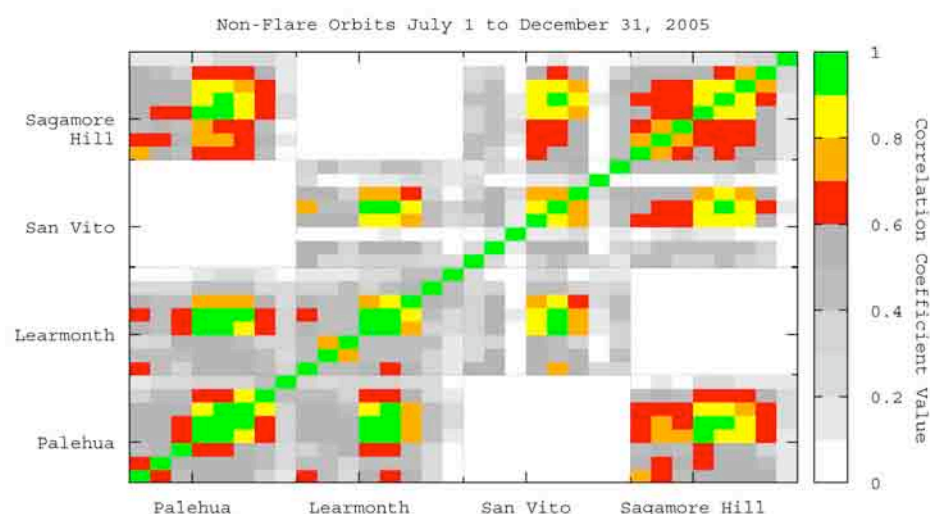


Figure 5.52: Correlations between observatories for non-flare orbits.

and bottom to top. Thus, the bottom left block is Palehua's 245 MHz frequency correlation with itself and the top right block is Sagamore Hill's 15400 MHz self-correlation. Due to the low number of orbits in common between San Vito and Learmonth, no correlations were computed between these two sites. The results show all of the observatories had correlation values greater than 0.7 for the middle three frequencies (1415, 2695, and 4995). However, some observatories had better correlations with a particular observatory than another. For example, Palehua had better results with Learmonth than with Sagamore Hill, and Sagamore Hill had better results with Palehua than with San Vito (Figure 5.52). Table 5.7 shows the number

Table 5.7: Flare orbits in common between RSTN observatories.

	Palehua	Learmonth	San Vito	Sagamore Hill
Palehua	72	29	4	40
Learmonth	29	76	33	1
San Vito	4	33	81	44
Sagamore Hill	40	1	44	88

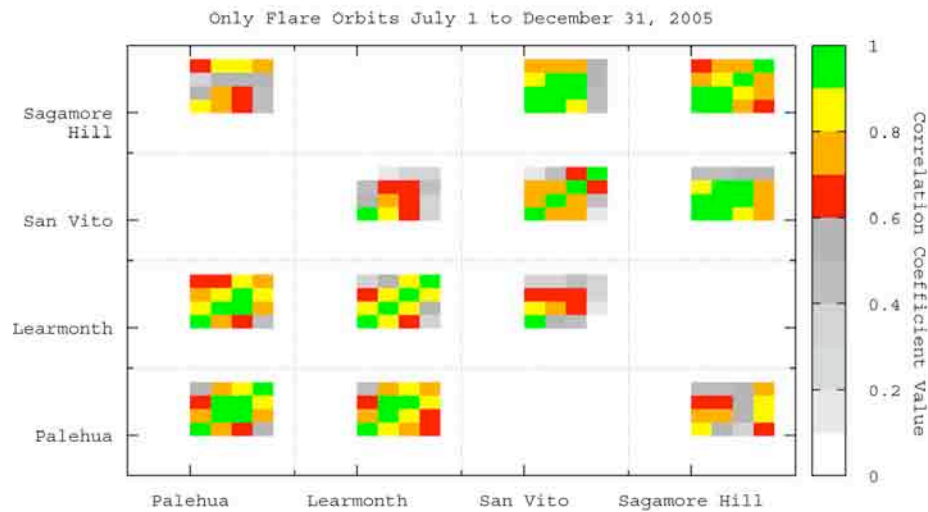


Figure 5.53: Correlations between observatories for flare orbits.

of flare orbits in common between the observatories and Figure 5.53 shows the results for frequencies 1415, 2695, 4995, and 8800 MHz.

The other frequencies are not shown due to poor results from the statistics t-value tests which indicated that similar correlation values could be attained from random values. Learmonth and Palehua show similar results while Palehua and Sagamore Hill show lower correlation values. Also, Learmonth and San Vito have lower correlation values than San Vito and Sagamore Hill. As stated at the beginning of this section, the correlations computed were measurements taken at the same time in different locations with different instruments. The source, whether changing or not,

was the same for each observation. Therefore, the variation must be attributed to either the instrument or the environment where the observation was taken. Chapter 3 already discussed calibration, tracking, and RFI issues. Any of these issues could be a factor that lowers the correlation values between similar frequencies. Weather conditions, such as rain or snow, could also affect the higher frequencies due to attenuation. These results seem to indicate that the variation in correlation values between the SEE data and the observatories could be due to different instruments or weather conditions at each observatory.

Another issue that could account for the different correlation values between observatories and the SEE data is how an observatory “sees” a flare. Figure 5.54 shows an X-class flare observed by GOES. Orbit 2594 is just before the peak of this flare, while orbits 2595 through 2598 take place during the decay phase of flare 507141016. Learmonth Solar Observatory does not see this flare (Figure 5.55). San Vito solar observatory (Figure 5.56) sees the previous flare (orbit 2593), the orbit near the flare peak (2594), another orbit with radio activity (2595), and two other orbits (2596 and 2597), which are part of the recovery phase of the flare in soft x-rays, but for which radio activity has returned to normal. Sagamore Hill Solar Observatory (Figure 5.57) sees the orbit near the peak, another orbit with radio activity, and three “flare” orbits with normal radio activity. This situation is caused by approaching the analysis from the soft x-ray flare perspective, where the flares last longer than on either the radio or EUV spectrum. An alternative method is recommended in the next chapter.

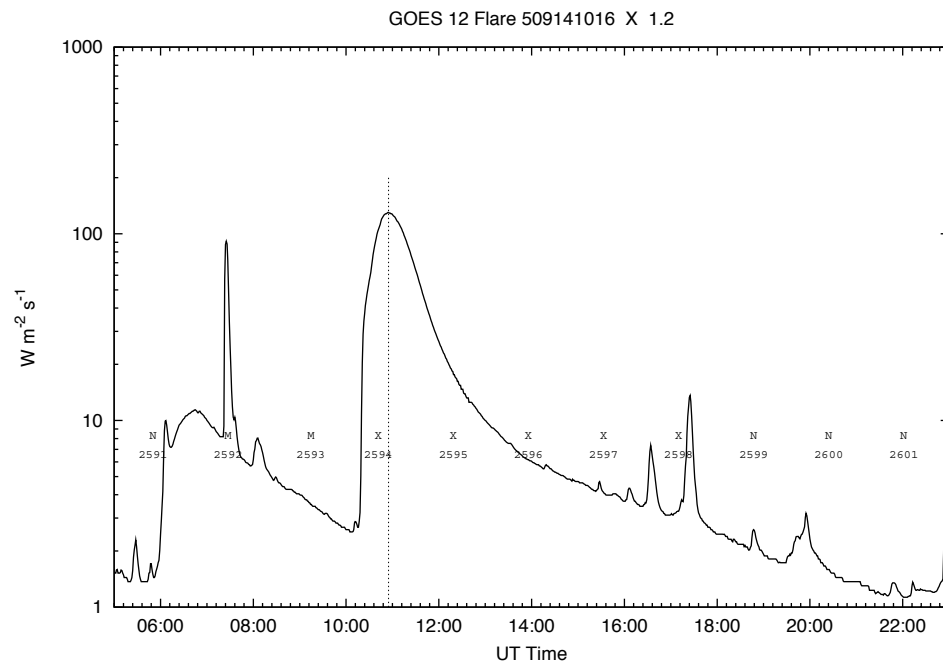


Figure 5.54: X-class flare 507141016 observed by GOES main channel.

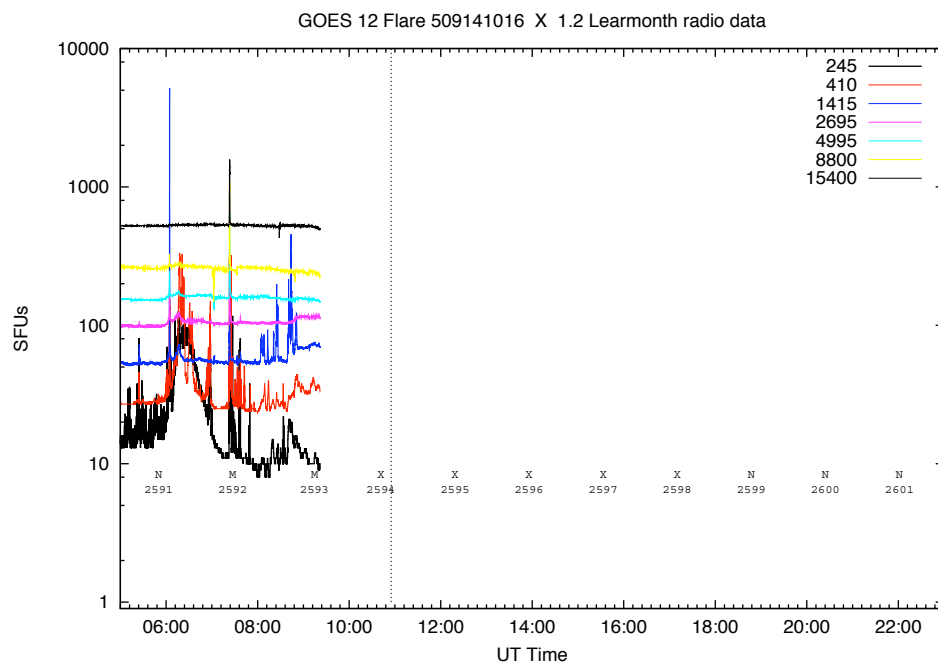


Figure 5.55: The X-class flare of Figure 5.54 observed by Learmonth Solar Observatory.

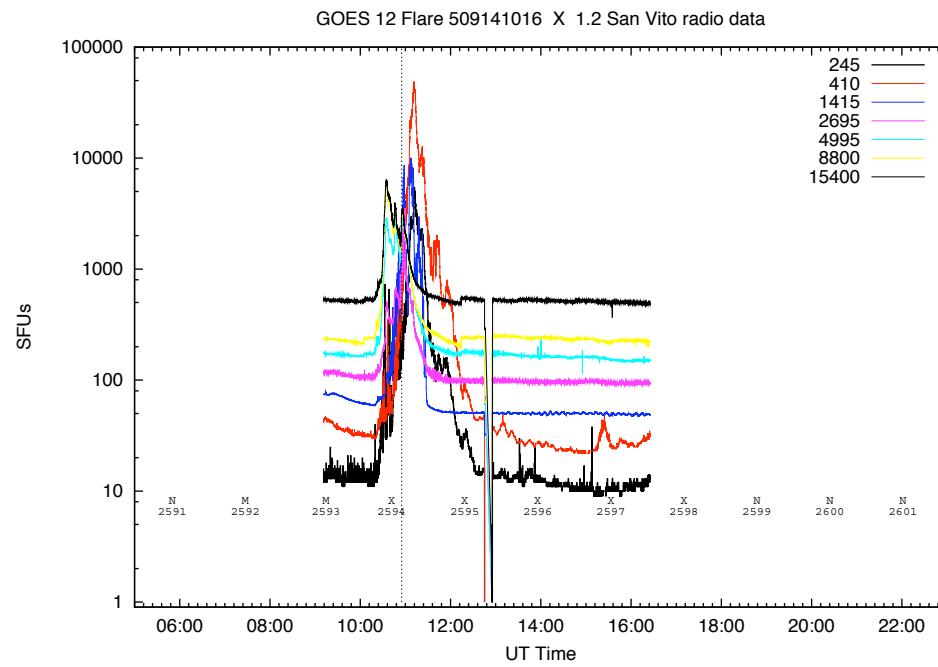


Figure 5.56: The X-class flare of Figure 5.54 observed by San Vito Solar Observatory.

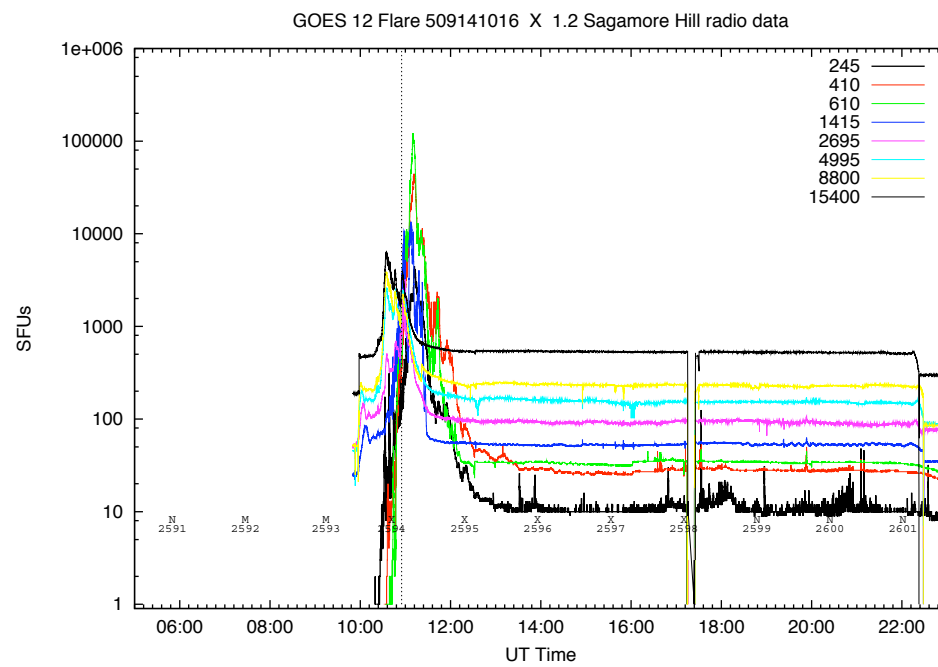


Figure 5.57: The X-class flare of Figure 5.54 observed by Sagamore Hill Solar Observatory.

CHAPTER 6

INTERPRETATION OF RESULTS

Chapter 5 showed correlations between some EUV wavelengths and RSTN radio frequencies for flare orbits. This chapter takes a detailed look at two flares from this study in an attempt to discuss what is taking place during the flares.

6.1 Typical Flare

Figure 6.1 shows a digram of a typical flare. The reconnection area is the location for the flare energy release. This accelerates electron beams in the upward and downward directions. Upward moving beams become Type III or V radio bursts (see Appendix A). The mechanism for these radio emissions is the plasma emission. Downward directed beams precipitate into the chromosphere or remain trapped in the loop. They emit radiation through the gyro synchrotron mechanism. The precipitating beam produces x-ray radiation and chromospheric evaporation. The chromospheric evaporation is due to the heating of the chromospheric material to coronal and flare temperatures. This causes the material to expand into the coronal flare loop. These loops then emit soft x-ray and EUV radiation. Additionally, the higher density of the loops permits the radiation of higher frequency radio emissions in the corona [Aschwanden, 2004].

This is a very simple description of a flare using a single loop. In reality, single loops are very rare. Most loops consist of loop arcades, loops of different scales and angles, or complex loop structures [Bastian *et al.*, 1998]. Additionally, the density of the loops does not have to vary smoothly, causing emissions at different frequencies. Furthermore, the loops are evolving with time. Lastly, there may be more than one emission mechanism involved in the process.

Figure 6.2 from Bastian *et al.* [1998] shows the evolution of a radio flare at

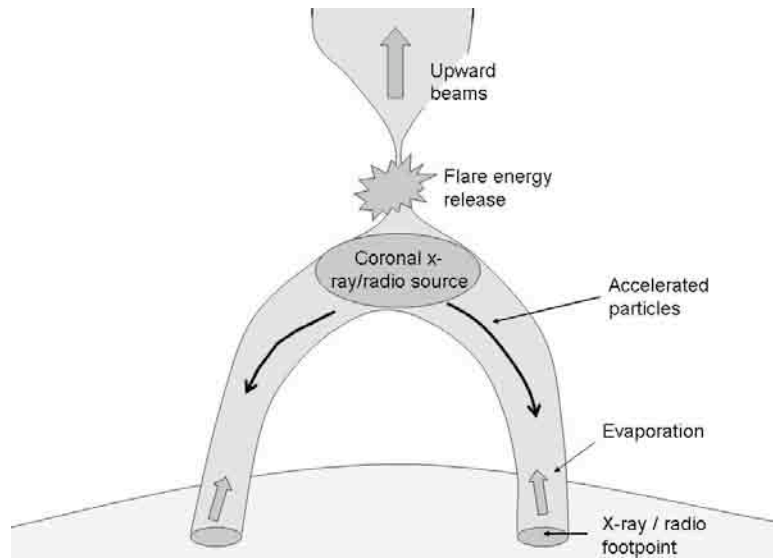


Figure 6.1: Standard model of a solar flare modified from *Benz* [2008].

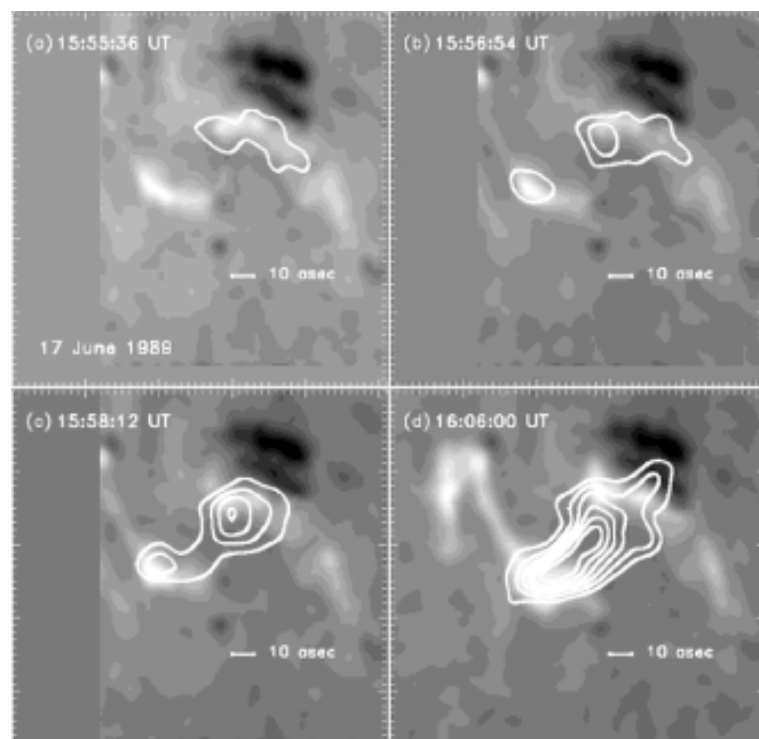


Figure 6.2: Time evolution of a radio flare as shown in *Bastian et al.* [1998].

4900 MHz observed by the National Radio Astronomy Observatory's Very Large Array. This time sequence shows the basics of the typical flare model discussed above as well as the complexity of the coronal loops and their time evolution. The gray images on the background are the $H\alpha$ emissions. The white contours are the radio emissions. Panel (a) shows the early phase of the flare where the emissions come from the strongest footpoint. Panel (b) shows emissions from the conjugate footpoint. Panel (c) shows the emissions coming from the loop as its density begins to increase from the heated chromospheric material. The last panel, panel (d) is around the flare maximum and shows that the maximum emission lies between the footpoints.

Figure 6.3 shows the radio spectrum of a flare on October 19, 2001.

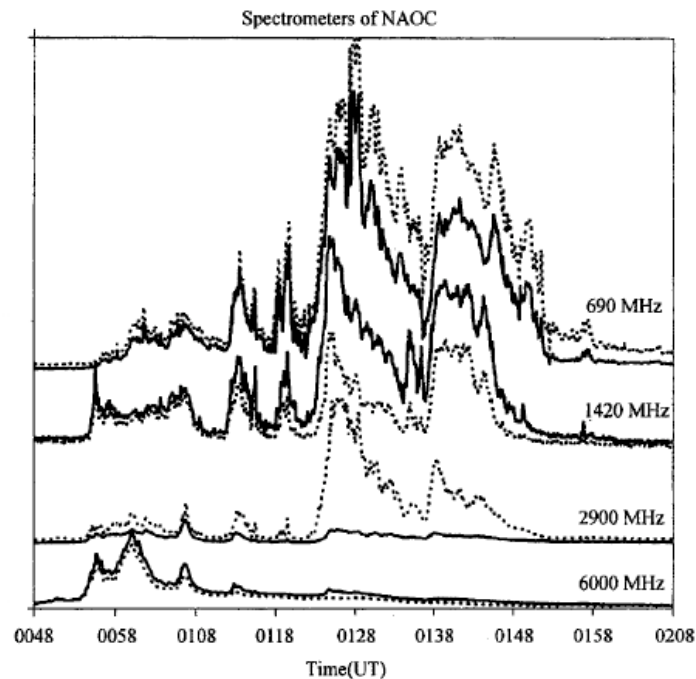


Figure 6.3: Example of two different radio emission mechanisms as shown in *Lin et al.* [2005].

Figure 6.3 is part of study conducted by *Lin et al.* [2005] using radio spectrometers and radio heliographs. The solid lines represent the left-handed polarization and the dotted lines are the right-handed polarization for each frequency. They concluded that the early portion of the burst (0048 to 0113UT) was due to gyro synchrotron emissions. The second part of the burst (0113 to 0200UT) were due to plasma emissions.

6.2 Flare 509111244

On September 11, 2005 around 1244 UT, active region AR808 produced a flare that was observed in soft x-rays by GOES 12, in EUV by TIMED-SEE, and in radio by RSTN's Sagamore Hill Observatory (Figure 6.4).

As measured by GOES 12, the flare started at 1244UT (Figure 6.5). The

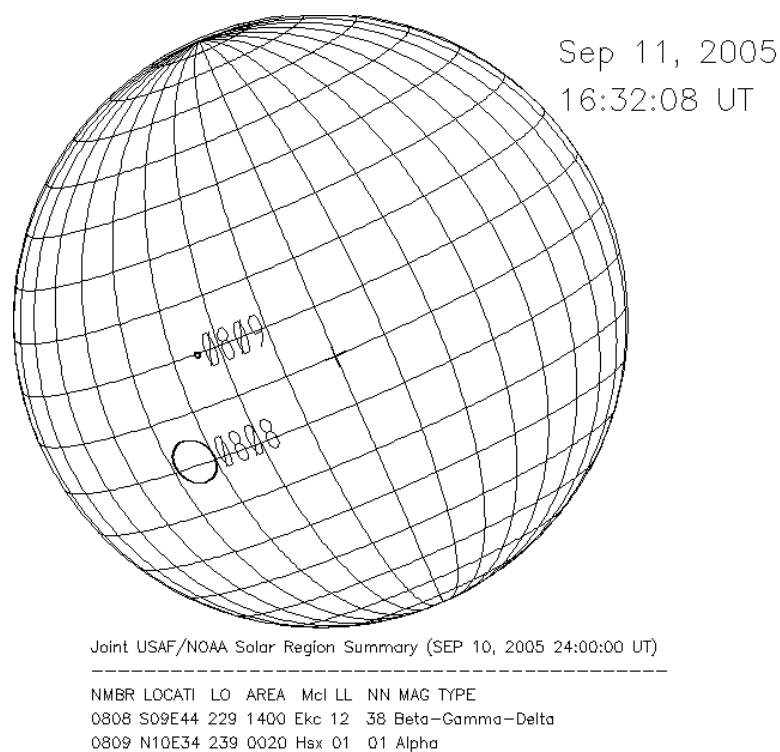


Figure 6.4: Location of active region AR808.

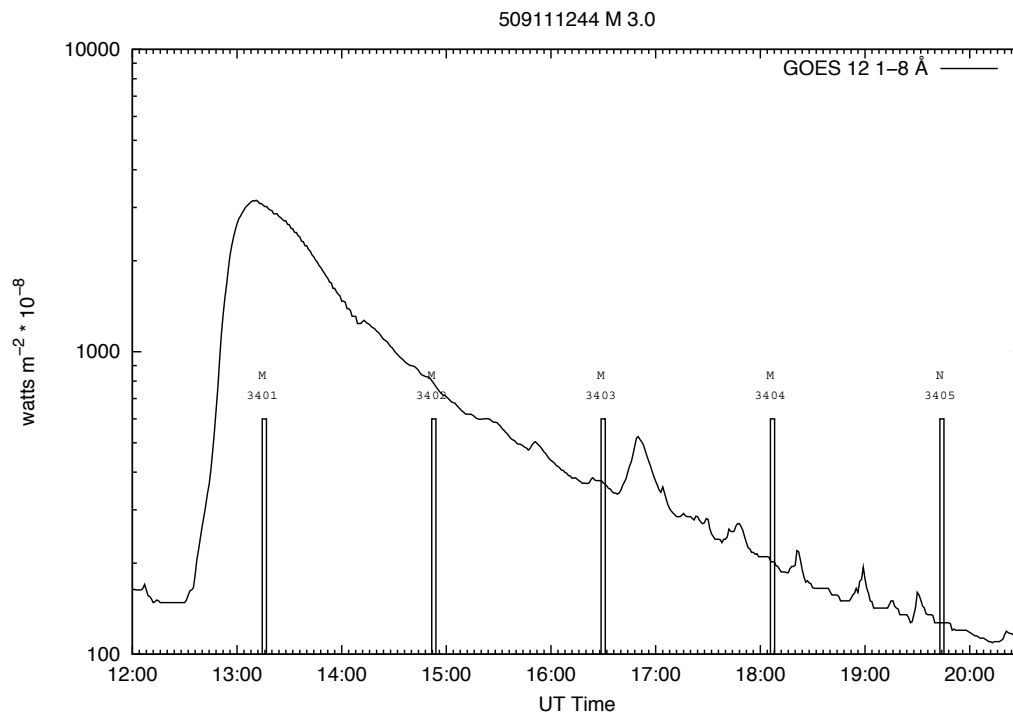


Figure 6.5: Flare 509111244 as seen by GOES 12.

M 3.0 flare reached its peak value at 1312UT and its half-power point at 1353UT. The flare had a sharp increase until it reached its peak increasing over an order of magnitude in 28 minutes. The flare had a gradual decrease, taking over six hours before returning to pre-flare values. This was a typical soft x-ray flare. Figure 6.5 also shows the TIMED-SEE orbits in relation to the flare. Orbit 3400 was considered the pre-flare orbit (i.e., non-flare orbit), orbit 3401 through 3405 were considered flare orbits.

Figure 6.6 shows the flare in the radio spectrum as measured by the Sagamore Hill observatory as well as the time and duration of the TIMED-SEE orbits. The radio spectrum shows two distinct peaks, one starting at 1238UT and the other one starting at 1330UT. The first peak is first seen in the middle frequencies (1415 through 4995 MHz) beginning at 1238UT. At 1244UT the disturbance is seen on

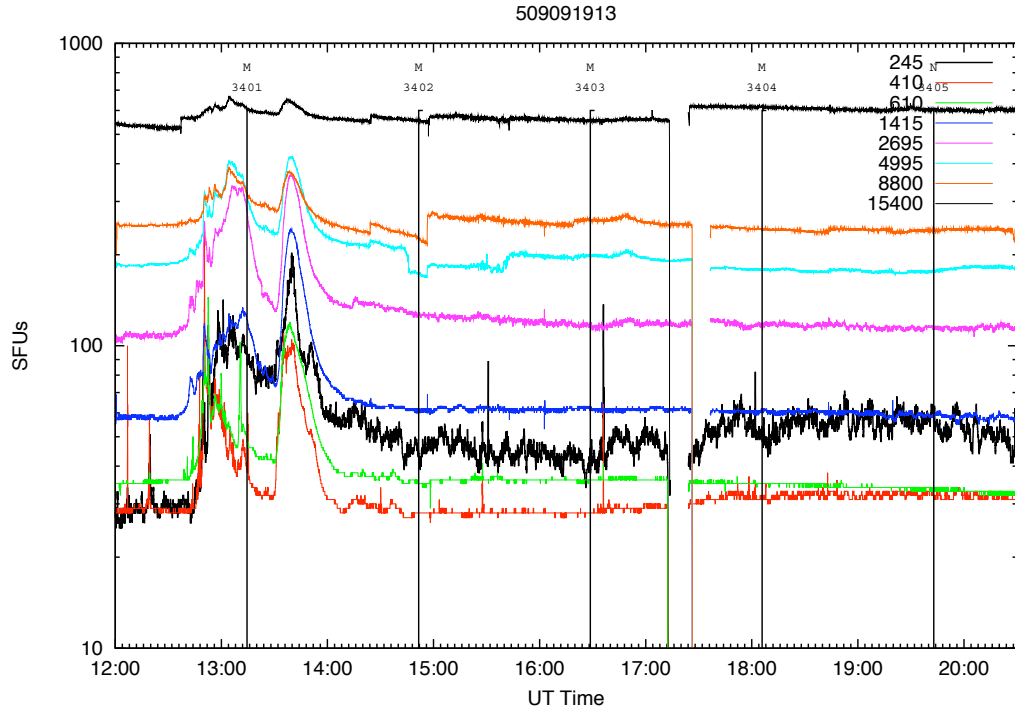


Figure 6.6: Flare 50911244 as seen by RSTN.

the lower frequencies (245 through 610 MHz) and at 1246UT it can be seen on the upper frequencies 8800 and 15400 MHz (Figure 6.7). Assuming the standard solar atmosphere model where electron densities decrease with height, this would indicate that once the event that led to the radio burst started, the disturbance propagated up into the solar corona (lower radio frequencies, lower electron densities) and then down into the denser solar atmosphere (higher radio frequencies). This is consistent with the solar flare model discussed earlier in this chapter and in Chapter 5. The broad peak around 1300-1310 UT drifts to later times with decreasing frequency (down to 1415 MHz). This feature does not appear on the lower three frequencies. The second radio peak started around 1330UT higher up in the solar atmosphere (245 MHz lowest frequency), and moved down in the solar atmosphere toward higher frequencies (Figure 6.8). It is very likely that the differences between the three lower

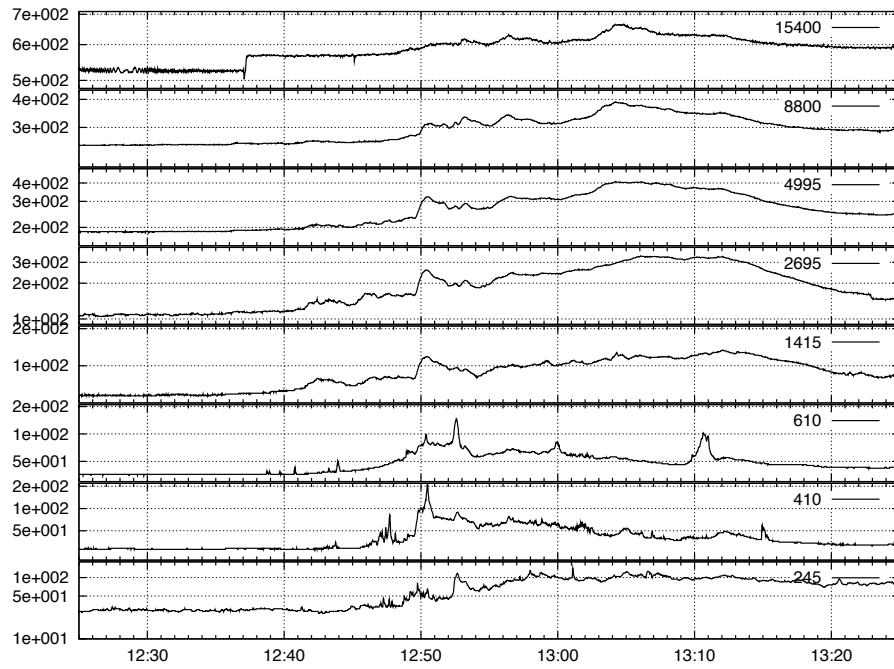


Figure 6.7: The first radio peak in Flare 50911244.

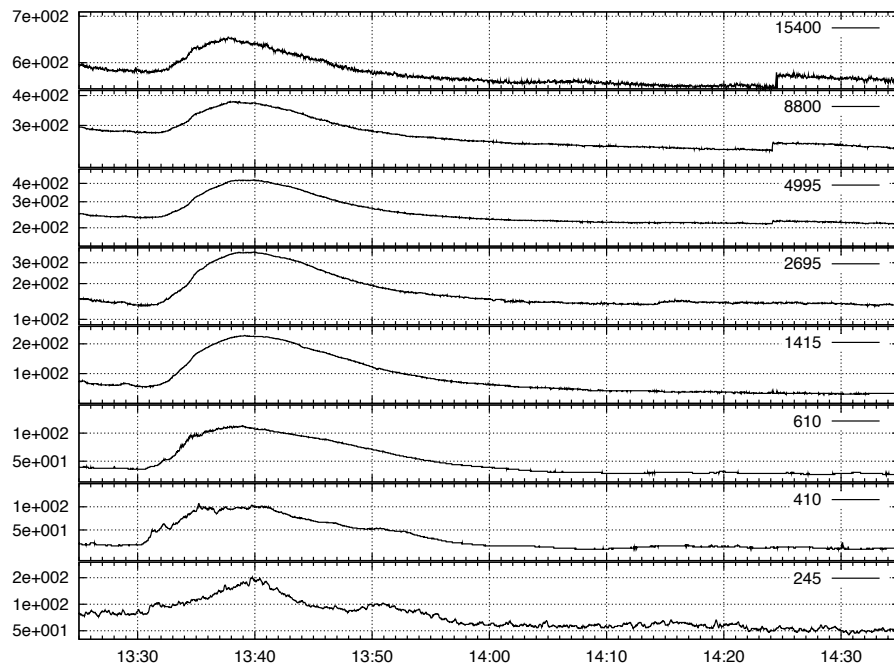


Figure 6.8: The second radio peak in Flare 50911244.

frequencies and the other five frequencies in the first burst are due to two different radio mechanisms (similar to Figure 6.3). The two main bursts are probably due to the time evolution of the radio flare (similar to Figure 6.2). Unfortunately, those details cannot be resolved with the RSTN data set.

The EUV response for wavelengths from 1 to 120 nm for this flare is shown in Figure 6.9. The largest changes were between orbit 3400 and 3401 in the 1 to 15 nm range (Figure 6.10). This wavelength range consistently decreased in the following orbits (3402 to 3405) until reaching pre-flare values. The 16 to 60 nm range showed a smaller increase between the first two orbits (Figure 6.11). The response on the following orbits was varied. Some wavelengths continued a gradual decrease to pre-flare values, while others dropped below pre-flare values on orbit 3402 and continued to decrease on the following orbits. Figure 6.12 shows wavelengths 60 to 120 nm. This range showed the smallest changes and most wavelengths decreased between the pre-flare orbit (3400) and the orbit after the GOES peak (3401). This indicates that the EUV spectrum does not have a consistent response during flares. However, this cannot be answered with the TIMED-SEE data set due to the data cadence. It is impossible to determine what is happening between TIMED-SEE orbits in the EUV spectrum. This is addressed in the next chapter as a future research interest once data from NASA's Solar Dynamic Observatory is available. Table 6.1 shows the changes between the orbits relative to the pre-flare orbit. The middle RSTN frequencies are consistent with the changes on the 1-15 nm SEE EUV wavelengths. Orbit 3404 shows a decrease in frequencies 4995 and 8800 MHz. This is due to a lower baseline due to the tracking problem already mentioned (Figure 6.6).

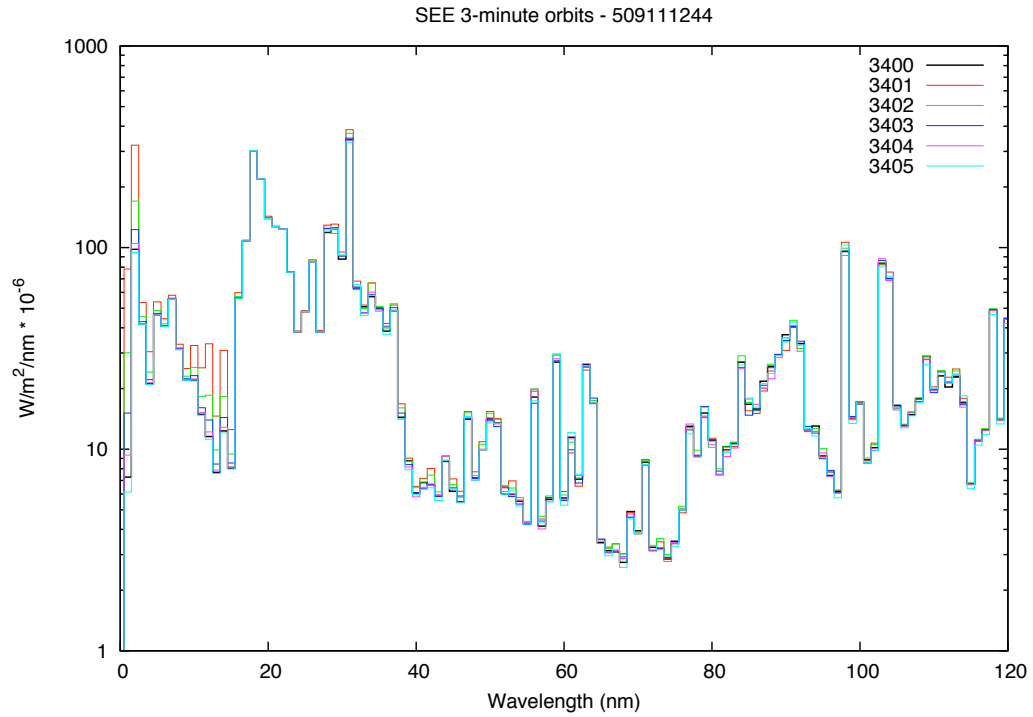


Figure 6.9: Flare 509111244 as observed by TIMED-SEE.

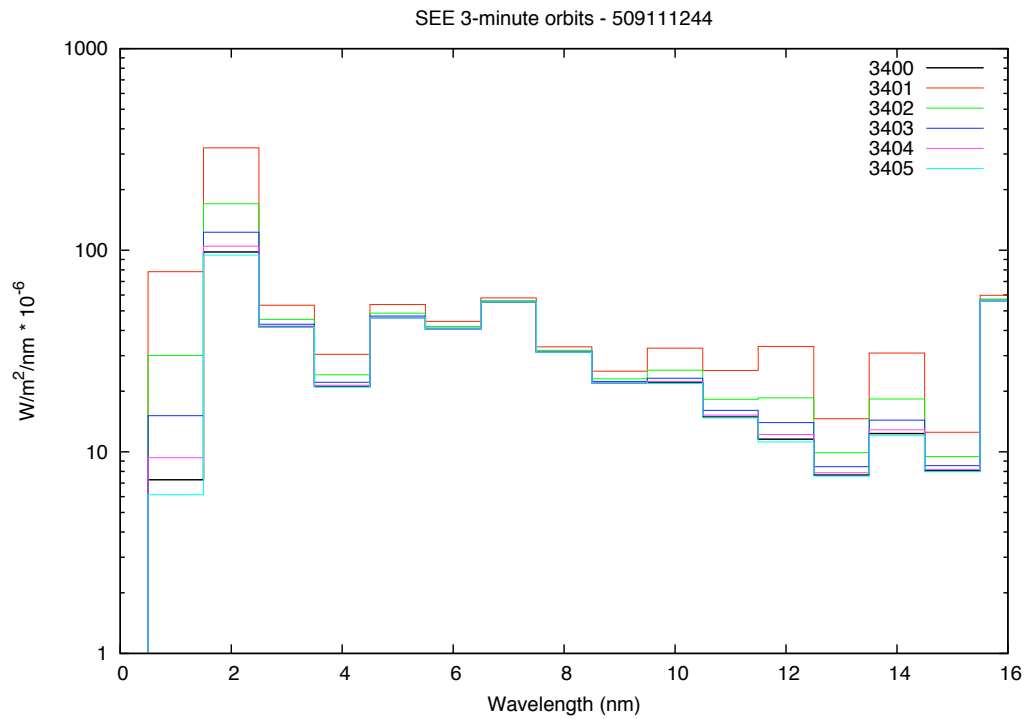


Figure 6.10: Flare 509111244 as observed by TIMED-SEE (1 to 15 nm).

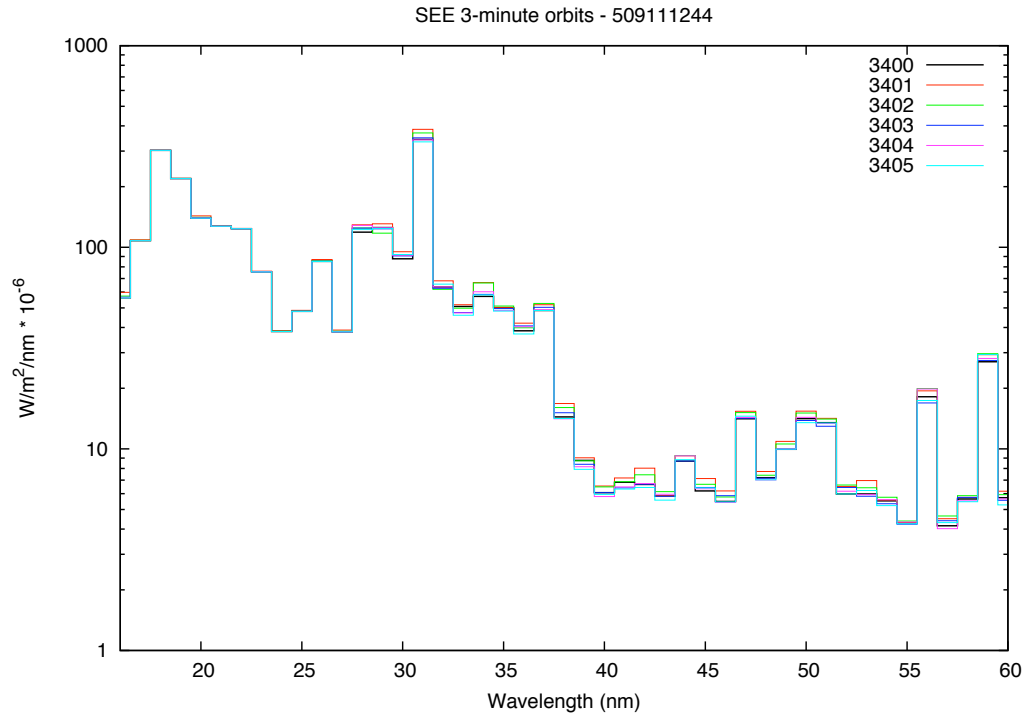


Figure 6.11: Flare 509111244 as observed by TIMED-SEE (16 to 60 nm).

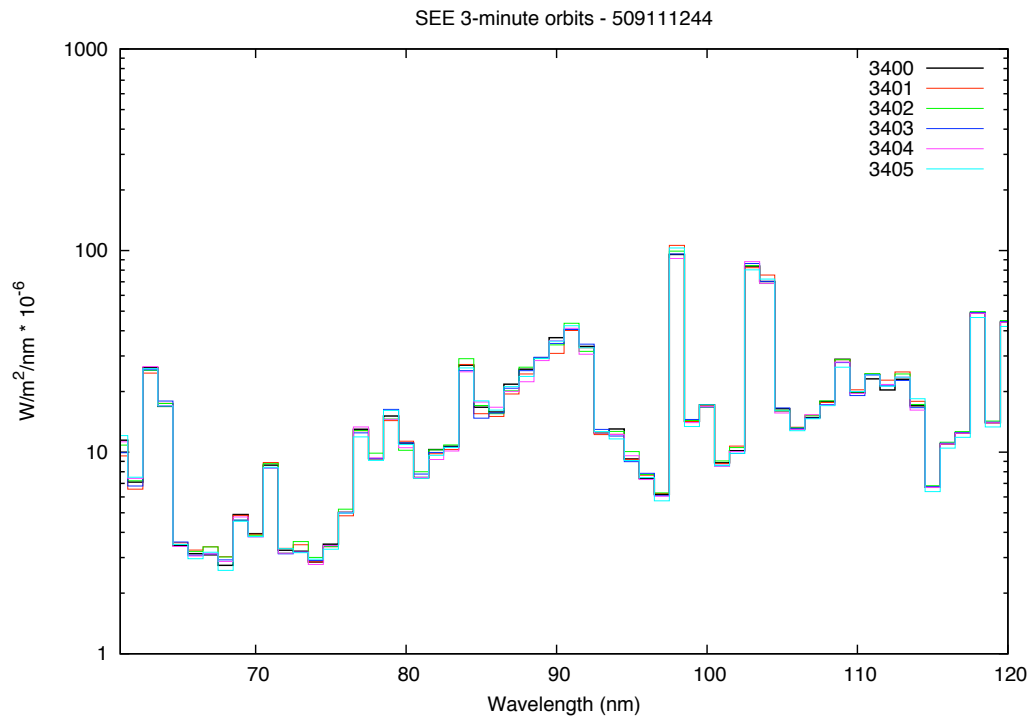


Figure 6.12: Flare 509111244 as observed by TIMED-SEE (61 to 120 nm).

Table 6.1: Changes from pre-flare orbit for flare 509111244.

SEE	3401	3402	3403	3404
1	977.9	313.7	108.1	28.7
2	228.5	73.3	25.3	6.7
3	28.0	9.0	3.1	0.8
4	44.2	14.2	4.9	1.3
5	16.2	5.2	1.8	0.5
6	9.0	2.9	1.0	0.3
7	4.6	1.5	0.5	0.1
8	6.2	2.0	0.7	0.2
9	14.2	4.6	1.6	0.4
10	48.8	15.7	5.4	1.4
11	69.9	22.4	7.7	2.1
12	188.3	60.4	20.8	5.5
13	90.1	28.9	10.0	2.7
14	150.9	48.4	16.7	4.4
15	55.4	17.8	6.1	1.6
16	6.5	2.1	0.7	0.2
17	0.9	0.3	0.1	0.0
18	0.2	0.1	0.0	0.0
19	0.2	0.1	0.0	0.0
20	2.7	0.9	0.3	0.1
RSTN	3401	3402	3403	3404
245 MHz	230.2	57.7	43.9	76.0
410 MHz	46.2	-1.1	-1.2	9.9
610 MHz	40.8	-0.3	1.6	-1.4
1415 MHz	110.7	6.3	8.0	5.6
2695 MHz	157.9	18.1	8.3	9.0
4995 MHz	68.9	6.3	5.9	-4.9
8800 MHz	28.1	7.9	3.7	-3.6
15400 MHz	12.3	1.9	2.0	12.8
GOES	3401	3402	3403	3404
1-8 Å	1483.0	310.6	91.1	6.6

6.3 Flare 509071717

The fourth largest flare measured since GOES started providing soft x-ray measurements in 1986 took place on September 7, 2005 around 1717 UT. This X 17.0 flare came out of active region AR808 and was observed in soft x-rays by GOES 12, in EUV by TIMED-SEE, and in radio by RSTN's Palehua Solar Observatory (Figures 6.13 through 6.15). Additionally, this flare was observed in $H\alpha$ (importance 3B) and in white light. GOES 12 measured the start of the flare at 1717UT (Figure 6.14). The flare reached its peak value at 1740UT and its half-power point at 1803UT. The flare was very impulsive, increasing three orders of magnitude in 23 minutes. The flare had a very gradual decrease, taking over 20 hours before returning to pre-flare values. Figure 6.14 also shows the TIMED-SEE orbits in relation to the flare. Orbit 3344 was considered the pre-flare orbit (i.e., non-flare orbit), orbit

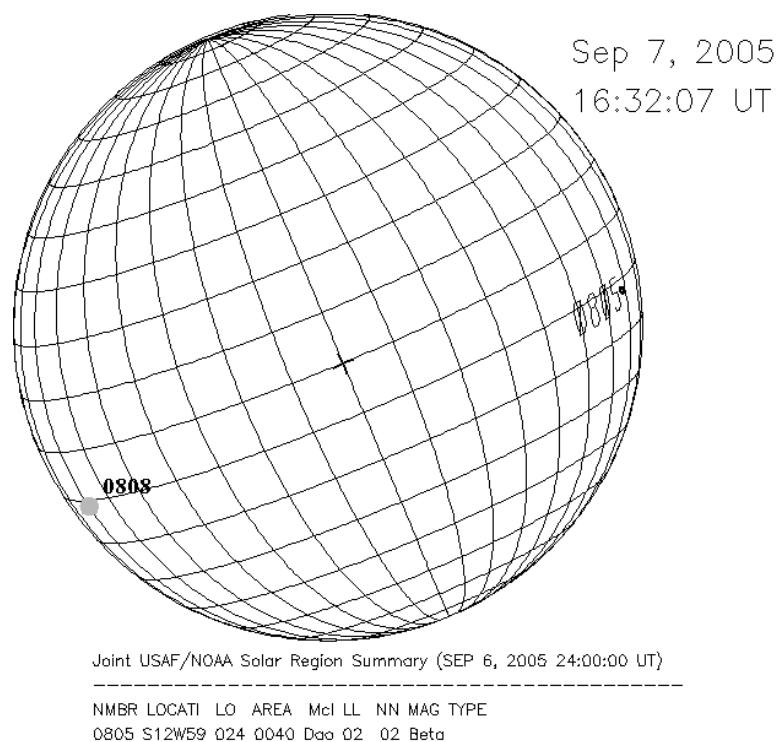


Figure 6.13: Location of active region AR808 on September 9, 2005.

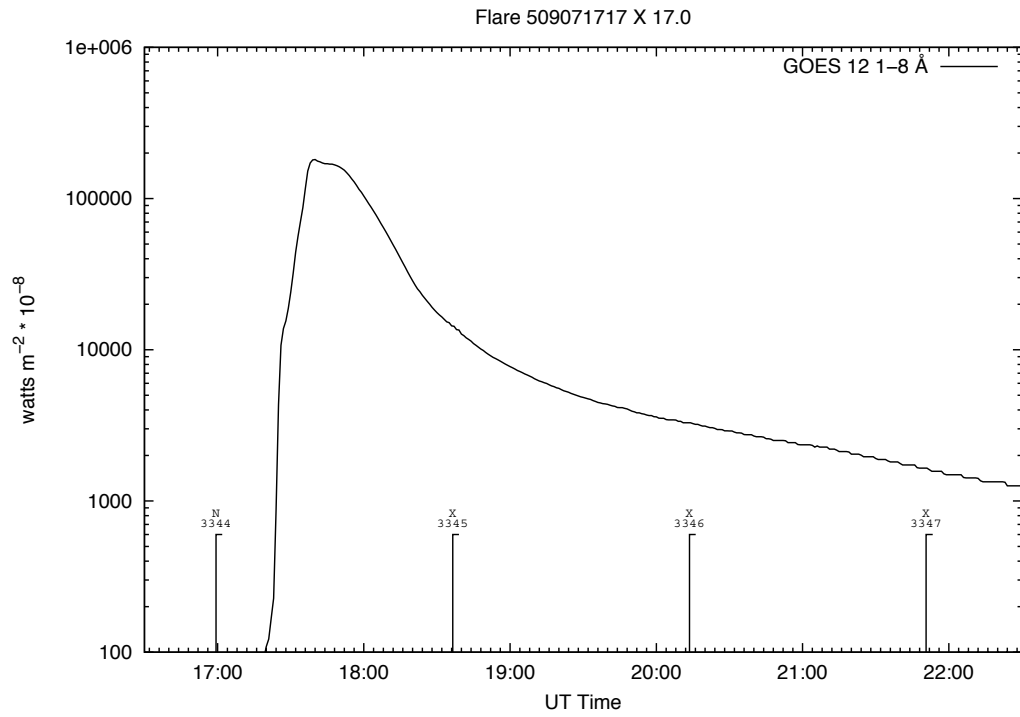


Figure 6.14: Flare 509071717 as observed by GOES.

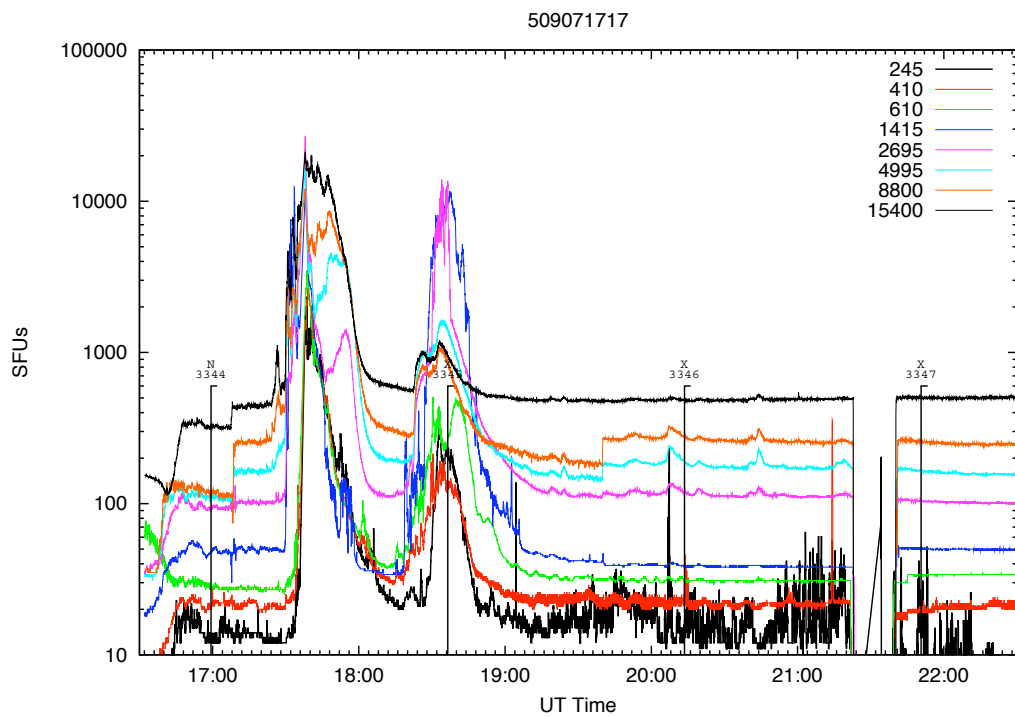


Figure 6.15: Flare 509071717 as seen by RSTN.

3445 through 3447 were considered flare orbits.

Figure 6.15 shows the flare in the radio spectrum as measured by the Palehua Solar Observatory as well as the time and duration of the TIMED-SEE orbits. The radio spectrum shows two distinct peaks, one starting at 1724UT and the other one starting at 1818UT. The first peak begins on 15400 MHz and moves to later times with decreasing frequency (Figure 6.16). There are features at the beginning of the burst that do not appear on the upper three frequencies. Also the beginning and end of the burst on 1415 MHz is different than the other frequencies. The second radio peak started around 1818UT on 2695 through 245 MHz before it appears on the upper three frequencies (Figure 6.17). The shape on the upper three frequencies is different than the other five frequencies. Furthermore, the burst on 2695 MHz shows a similar pattern than that of 4995 through 15400 MHz with a superimposed burst between 1830 to 1840 UT. Again, this seems to indicate that different mechanisms are responsible for these emissions.

The EUV response for this flare is similar to the response for flare 509111244 (Figure 6.18). The largest changes were between orbit 3344 and 3345 in the 1 to 15 nm range (Figure 6.19). This wavelength range consistently decreased in the following orbits until reaching pre-flare values. The 16 to 60 nm range showed a smaller increase between the first two orbits (Figure 6.20). The response on the following orbits was more consistent than in the previous flares. Most wavelengths continued to decrease on the following orbits. Figure 6.21 shows wavelengths 60 to 120 nm. This range again showed the smallest changes and most wavelengths decreased between the pre-flare orbit (3344) and the orbit after the GOES peak (3345). Table 6.2 shows the changes between the orbits relative to the pre-flare orbit. The middle RSTN frequencies are consistent with the changes on the 1-15 nm SEE EUV wavelengths.

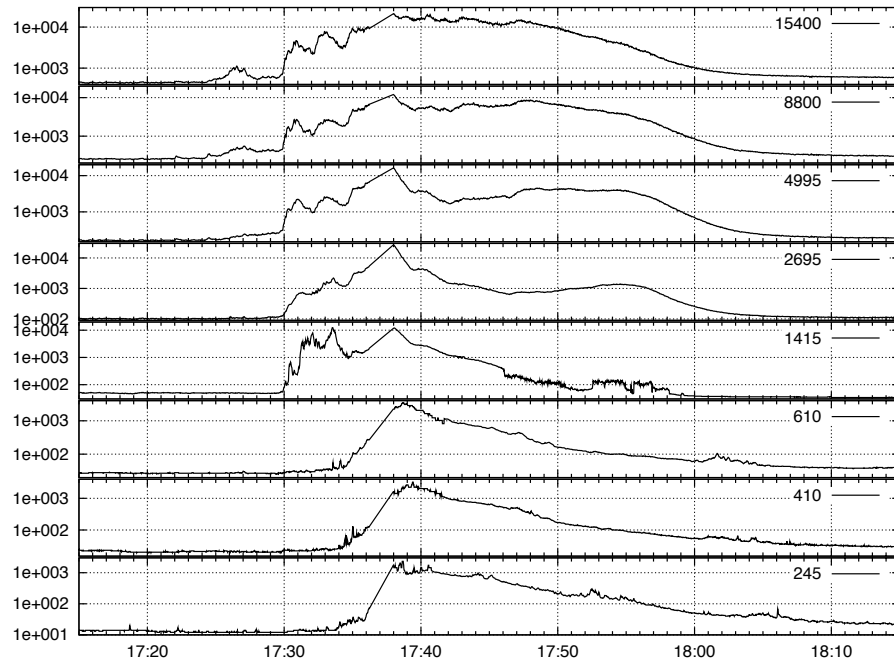


Figure 6.16: The first radio peak in Flare 509071717.

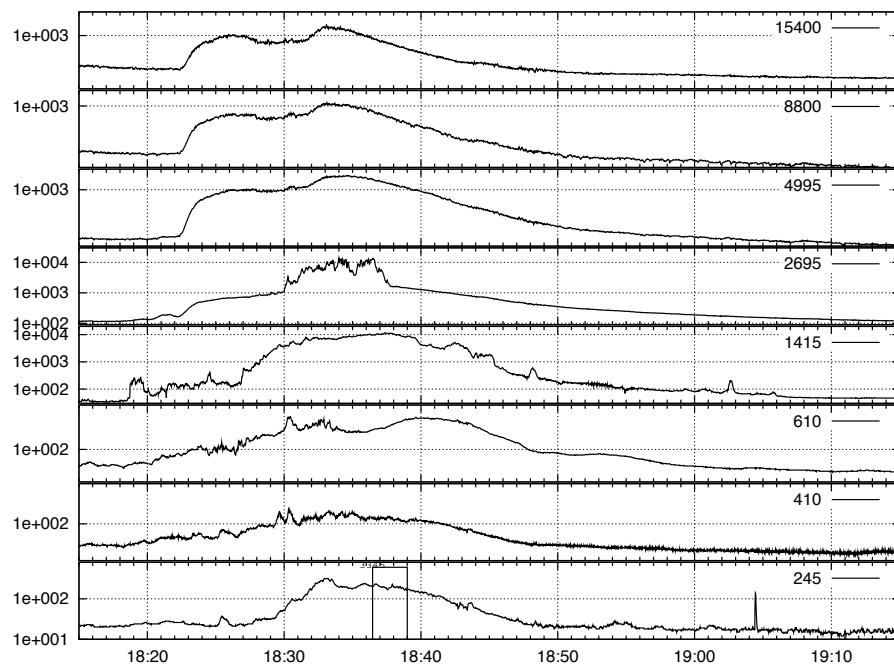


Figure 6.17: The second radio peak in Flare 509071717.

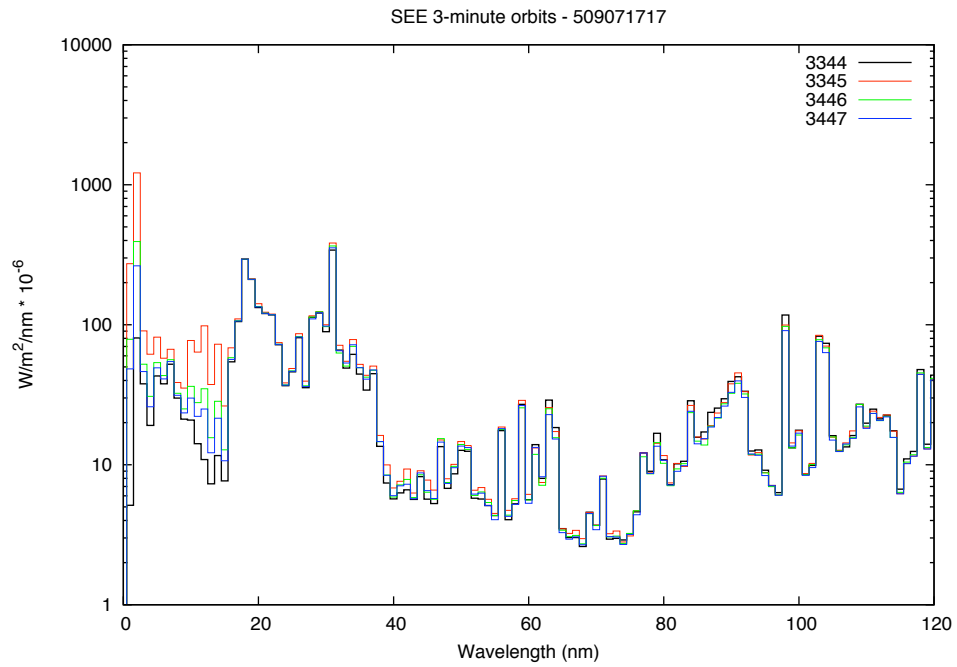


Figure 6.18: Flare 509071717 as observed by TIMED-SEE.

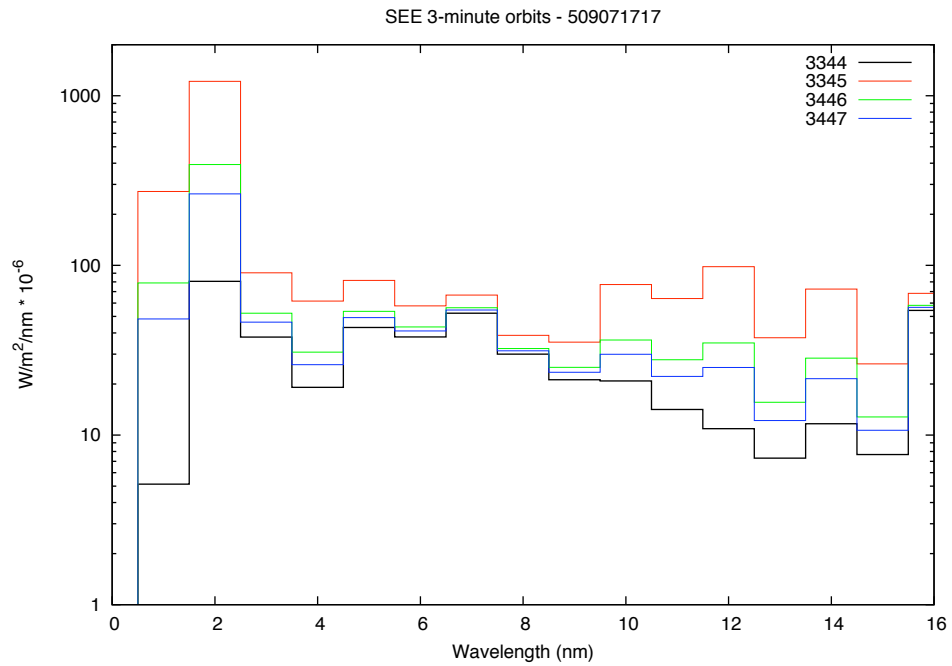


Figure 6.19: Flare 509071717 as observed by TIMED-SEE (1-15 nm).

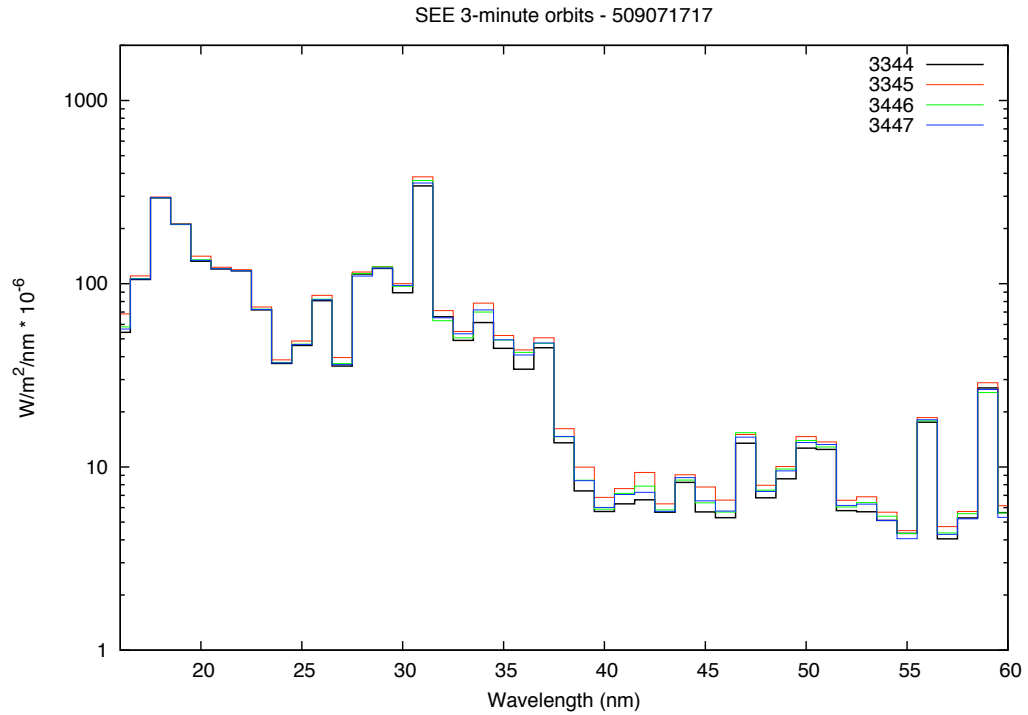


Figure 6.20: Flare 509071717 as observed by TIMED-SEE (16-60 nm).

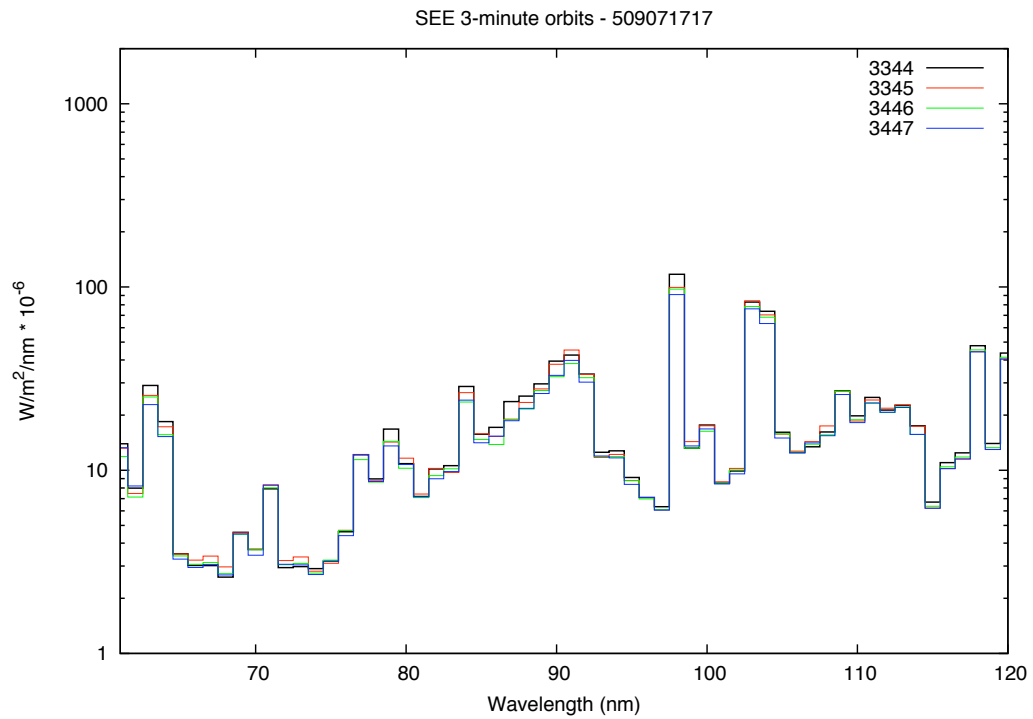


Figure 6.21: Flare 509071717 as observed by TIMED-SEE (61-120 nm).

Table 6.2: Changes from pre-flare orbit for flare 509071717.

SEE	3345	3346	3347
1	5213.6	1433.4	841.3
2	1409.5	387.5	227.4
3	139.1	38.3	22.5
4	222.7	61.2	35.9
5	89.4	24.6	14.4
6	52.4	14.4	8.5
7	28.0	7.7	4.5
8	29.2	8.0	4.7
9	66.5	18.3	10.7
10	270.0	74.2	43.6
11	350.6	96.4	56.6
12	800.8	220.2	129.2
13	412.6	113.4	66.6
14	523.0	143.8	84.4
15	242.6	66.7	39.2
16	25.9	7.1	4.2
17	4.5	1.3	0.7
18	1.1	0.3	0.2
19	1.1	0.3	0.2
20	6.6	1.8	1.1
RSTN	3345	3346	3347
245 MHz	1462.9	25.9	16.1
410 MHz	549.8	5.6	-7.5
610 MHz	932.3	11.4	20.3
1415 MHz	19602.9	-19.6	4.5
2695 MHz	6394.3	26.6	11.0
4995 MHz	1147.3	71.5	49.2
8800 MHz	227.6	6.1	-1.1
15400 MHz	112.4	7.5	12.0
GOES	3345	3346	3347
1-8 Å	16666.8	3746.2	1851.9

Orbit 3344 shows a tracking adjustment made on the upper three frequencies around 1710UT (Figure 6.15). The values on Table 6.2 are adjusted to account for this issue. The decrease on 1415 MHz for orbit 3346 is due to a calibration issue. Notice on Figure 6.15 how the baseline for this frequency is higher after the noon calibration (around 2130UT). The value for this frequency for this orbit was not used on the correlation computation.

6.4 Summary

The flares captured by the SOHO SEM instrument as well as other works cited in this document indicate that the EUV response during flares fall between the soft x-ray response measured by GOES and the radio response measured by RSTN. Also, some of the details from the TIMED-SEE data indicate that the response across the EUV spectrum during flares is probably as varied, if not more so, as the radio response. In order to resolve this question, a much higher cadence in the EUV spectrum is needed. The TIMED-SEE data, due to its time cadence, cannot provide these details. Single peaks in GOES or double peaks in radio look similar in the TIMED-SEE data, but may not be similar. In order to make a final decision on whether radio signals can be used to track the EUV response during flares, a much higher cadence EUV spectrum is needed.

CHAPTER 7

CONCLUSIONS AND FUTURE WORK

7.1 Conclusions

RSTN 1-second radio data from the four observatories was used to compute daily flux values for all eight frequencies. These daily values were compared to daily F10.7 values. As expected, correlations between 2695 MHz and F10.7 had values of $\rho > 0.94$. Additionally, correlations between 1415 MHz and F10.7 had values of $\rho > 0.92$. The correlations between 4995 MHz and F10.7 were greater than 0.87. This indicates that the RSTN daily values could be used in place of F10.7 for some applications with the advantage that the RSTN values would be updated four times a day rather than once a day as in the case of F10.7. These daily values, along with the F10.7 values, were compared to daily EUV values from TIMED-SEE. These comparisons showed that F10.7 is indeed a good proxy for EUV. The correlations between F10.7 and EUV were greater than 0.80 between $\lambda = 1$ nm and $\lambda = 60$ nm. In some portions of this range ($15 \text{ nm} < \lambda < 27 \text{ nm}$) the correlation coefficients were greater than 0.90. The correlations between RSTN and EUV showed very interesting results. Three frequencies (1415, 2695, and 4995 MHz) had correlation coefficient values greater than 0.80 for the range $1 < \lambda < 60$. The correlations for 1415 MHz and EUV extended intermittently up to $\lambda = 75$. In the range of $1 \text{ nm} < \lambda < 14 \text{ nm}$, frequencies 2695 and 4995 MHz had correlation coefficients $\rho > 0.90$. These two frequencies had the highest correlation values for this range. In the range of $16 \text{ nm} < \lambda < 27 \text{ nm}$, the highest correlation values were for 1415 MHz, 2695 MHz, and F10.7. Surprisingly, the results from the F10.7 correlations with EUV were more similar to the results of 1415 MHz than to those of 2695 MHz, as expected.

The next set of results comes from the analysis of EUV data from TIMED-

SEE orbits and RSTN values for that same time period. The orbits were divided into flare and non-flare orbits based on the times for the soft x-ray flares measured by the GOES satellite. The non-flare orbits showed very similar results for all four observatories. The overall correlation values between the radio frequencies and the SEE wavelengths were slightly lower than the daily correlation values ($0.80 > \rho > 0.90$) from $\lambda = 1$ nm to $\lambda = 75$ nm for frequencies 1415, 2695, and 4995 MHz. Frequency 1415 MHz had overall better results than the other two frequencies. This is different from the daily values where the best correlations were for 2695 MHz. The results for the flare orbits showed a shift in frequency and a decrease in correlation values. The overall correlation values dropped to $0.70 < \rho < 0.80$. In the range of $1 \text{ nm} < \lambda < 20 \text{ nm}$, the frequencies with the best correlations were 4995 and 8800 MHz. From $20 \text{ nm} < \lambda < 35 \text{ nm}$, none of the frequencies had good correlations with the EUV data. From $35 \text{ nm} < \lambda < 60 \text{ nm}$, 1415, 2695, and 4995 MHz had correlation values of $\rho > 0.70$. Between $60 \text{ nm} < \lambda < 75 \text{ nm}$, only 1415 MHz had correlation values of $\rho > 0.70$.

These set of results show that 1-second RSTN observations can be used as a proxy for solar EUV emissions. The daily values from the RSTN sites could increase the daily solar EUV input to space physics models from one a day (F10.7) to four times a day (once per site). These daily values did not include solar flares. When solar flares were included, the RSTN emissions showed some correlation to the UV emissions. However, the cadence of the UV emissions in this study may have been too large to provide a clear answer to the original questions posed at the beginning of this dissertation.

7.2 Future Work

Having demonstrated that there are correlations between radio and EUV solar emissions during quiet and flaring times, there are opportunities for future research. First, it would be desirable to recreate this study using all available TIMED-SEE and radio data. Using these six years of data (2002-2008) would increase the number of flares and allow for more options during the flare analysis. One important option would be shifting the focus of the flares from the soft x-ray perspective (GOES) to the radio perspective. The radio flares are, for the most part, shorter in duration from start time to full recovery than the soft x-ray flares. Another benefit of a longer time period analysis would be the explorations of the longitude dependence of radio and EUV emissions. Neither of the two aforementioned issues could have been addressed during this dissertation due to the low number of observations for either case.

Another area of research involving these sub-daily correlations is the sensitivity of ionospheric models to changes in the EUV spectrum as seen by the radio spectrum. As already mentioned, many models use the F10.7 as the solar input for a given day. Rather than vary the solar input once a day, one could vary the solar input at a faster cadence using different frequencies for different parts of the EUV spectrum. One model that could easily be adapted for these changes is the Global Average Ionosphere and Thermosphere (GAIT) model developed by Christopher Smith for his dissertation at Utah State University in 2004.

Finally, this analysis should be reaccomplished using data from the EUV Variability Experiment (EVE) once it becomes available. The EVE instrument is part of NASA's Solar Dynamic Observatory and is scheduled to launch in January 2009.

The EVE instrument will provide observations from 0.1 to 121 nm at a 10-second cadence. This data would allow a more detailed comparison of flares between the EUV and radio spectrum.

REFERENCES

- Aschwanden, M. J., Irradiance observations of the 1-8 Å solar soft X-ray flux from GOES, *Solar Physics*, 152, 53–59, 1994.
- Aschwanden, M. J., *Physics of the Solar Corona. An Introduction*, 908 pp., Springer, Berlin, 2004.
- Bastian, T. S., A. O. Benz, and D. E. Gary, Radio Emission from Solar Flares, *Annual Review of Astronomy and Astrophysics*, 36, 131–188, 1998.
- Benz, A. O., Coherent Radio Emission of Solar Flares in the Decimeter Range (0.3-3 GHz), in *Radio Emission from the Stars and the Sun, Astronomical Society of the Pacific Conference Series*, vol. 93, edited by A. R. Taylor and J. M. Paredes, pp. 347–354, 1996.
- Benz, A. O., Flare observations, *Living Reviews in Solar Physics*, 5(1), 2008.
- Bossy, L., Solar indices and solar UV-irradiances, *Planetary and Space Science*, 31, 977–985, 1983.
- Coffey, H. E., and J. A. McKinnon, Solar-geophysical data number 515, July 1987. Supplement (explanation of data reports), *Tech. rep.*, National Oceanic and Atmospheric Administration, 1987.
- Conway, A. J., and A. L. MacKinnon, The electron cyclotron maser in hot thermal plasmas, *Astronomy and Astrophysics*, 339, 298–308, 1998.
- Covington, A. E., Solar Radio Emission at 10.7 cm, 1947-1968, *Journal of the Royal Astronomical Society of Canada*, 63, 125–132, 1969.
- Das, T. K., H. Sarkar, and A. K. Sen, The Ratio of the radio and optical diameters of the sun at centimeter wavelengths, *Solar Physics*, 194, 155–163, 2000.
- Donnelly, R. F., R. N. Grubb, and F. C. Cowley, Solar X-ray measurements from SMS-1, SMS-2, and GOES-1, information for data users, *NASA STI/Recon Technical Report N*, 78, 65, 1977.
- Dulk, G. A., Radio emission from the sun and stars, *Annual Review of Astronomy and Astrophysics*, 23, 169–224, 1985.
- English, R. A., R. E. Benson, J. V. Bailey, and C. M. Barnes, Apollo experience report protection against radiation, *Technical Note NASA-TN-D-7080*, NASA/JSFC, Houston, TX, 1973.

- Floyd, L., D. McMullin, and L. Herring, Intercomparison of SEM irradiances and solar indices, in *From Solar Min to Max: Half a Solar Cycle with SOHO*, *ESA Special Publication*, vol. 508, edited by A. Wilson, pp. 197–200, Davos, Switzerland, 2002.
- Floyd, L., J. Newmark, J. Cook, L. Herring, and D. McMullin, Solar EUV and UV spectral irradiances and solar indices, *Journal of Atmospheric and Solar-Terrestrial Physics*, *67*, 3–15, 2005.
- Foukal, P. V., *Solar Astrophysics, 2nd, Revised Edition*, 480 pp., Wiley-VHC, Chichester, UK, 2004.
- Garcia Alvarez, D., Modelling of flares on late-type stars, *Irish Astronomical Journal*, *27*, 117–136, 2000.
- Golightly, M. J., oh! i slipped the surly bonds of earth . . . and ran into space weather!, in *Symposium on Space Weather, AMS 84th meeting*, NASA/JSFC, Houston, TX, 2004.
- Grubb, R. N., The SMS/GOES space environment monitor subsystem, *NASA STI/Recon Technical Report N*, *76*, 28,260, 1975.
- Güdel, M., and A. O. Benz, A catalogue of decimetric solar flare radio emission, *Astronomy and Astrophysics Supplement*, *75*, 243–259, 1988.
- Haisch, B., and K. T. Strong, Flares on the sun and other stars, *Annual Review of Astronomy and Astrophysics*, *29*, 275–324, 1991.
- Hedin, A. E., Correlations between thermospheric density and temperature, solar EUV flux, and 10.7-cm flux variations, *Journal of Geophysical Research*, *89*, 9828–9834, 1984.
- Hovestadt, D., M. Hilchenbach, A. Bürgi, B. Klecker, P. Laeverenz, M. Scholer, H. Grünwaldt, W. I. Axford, S. Livi, E. Marsch, B. Wilken, H. P. Winterhoff, F. M. Ipavich, P. Bedini, M. A. Coplan, A. B. Galvin, G. Gloeckler, P. Bochsler, H. Balsiger, J. Fischer, J. Geiss, R. Kallenbach, P. Wurz, K.-U. Reiche, F. Gliem, D. L. Judge, H. S. Ogawa, K. C. Hsieh, E. Möbius, M. A. Lee, G. G. Managadze, M. I. Verigin, and M. Neugebauer, CELIAS - Charge, Element and Isotope Analysis System for SOHO, *Solar Physics*, *162*, 441–481, 1995.
- Isliker, H., and A. O. Benz, Catalogue of 1-3 GHz solar flare radio emission, *Astronomy and Astrophysics Supplement*, *104*, 145–160, 1994.
- Jiříčka, K., M. Karlický, and H. Mészárosová, Occurrences of different types of 0.8–2.0 GHz solar radio bursts and fine structures during the solar cycle, in *ESA SP-477: Solspa 2001, Proceedings of the Second Solar Cycle and Space Weather Euroconference*, edited by H. Sawaya-Lacoste, pp. 351–354, 2002.

- Judge, D. L., D. R. McMullin, H. S. Ogawa, D. Hovestadt, B. Klecker, M. Hilchenbach, E. Mobius, L. R. Canfield, R. E. Vest, R. Watts, C. Tarrío, M. Kuehne, and P. Wurz, First solar EUV irradiances obtained from SOHO by the CELIAS/SEM, *Solar Physics*, 177, 161–173, 1998.
- Kane, R. P., Correlation of solar indices with solar EUV fluxes, *Solar Physics*, 207, 17–40, 2002.
- Kaufmann, P., On the activity of solar coronal condensations discussed after long-enduring microwave events., *Revista Brasileira de Fisica*, 1, 289–295, 1971.
- Kendall, M., *Rank Correlation Methods*, 260 pp., Charles Griffin and Co., London, 1975.
- Kraus, J. D., *Radio Astronomy*, 481 pp., McGraw-Hill Book Company, New York, 1966.
- Kundu, M. R., *Solar Radio Astronomy*, 660 pp., Interscience Publication, New York, 1965.
- Lee, J., and D. E. Gary, Solar microwave bursts and injection pitch-angle distribution of flare electrons, *Astrophysical Journal*, 543, 457–471, 2000.
- Lin, W., X. Rui-Xiang, W. Min, X. Chun, and L. Yu-Ying, A complex solar radio burst and the characteristics of its related microwave sources and EUV coronal loops, *Chinese Astronomy and Astrophysics*, 29, 189–202, 2005.
- Markus, R. M., N. F. Halbeisen, and J. F. Fuller, *Air Weather Service: Our Heritage 1937-1987*, Military Airlift Command, United States Air Force, Scott Air Force Base, Illinois, 1987.
- McLean, D. J., and N. R. Labrum, *Solar Radiophysics: Studies of Emission from the Sun at Metre Wavelengths*, 540 pp., Cambridge University Press, New York, 1985.
- Pacholczyk, A. G., *Radio Astrophysics. Nonthermal Processes in Galactic and Extragalactic Sources*, Freeman, San Francisco, 1970.
- Phillips, K. J. H., *Guide to the Sun*, 400 pp., Cambridge University Press, Cambridge, UK, 1995.
- Press, W., B. Flannery, S. Teukolsky, and W. Vetterling, *Numerical Recipes in FORTRAN: The Art of Scientific Computing*, 588 pp., Cambridge University Press, New York, 1992.
- Ramsey, P. H., Critical values for Spearman's rank order correlation, *Journal of Educational Statistics*, 14, 245–253, 1989.

- Raulin, J.-P., and A. A. Pacini, Solar radio emissions, *Advances in Space Research*, *35*, 739–754, 2005.
- Rybicki, G. B., and A. P. Lightman, *Radiative Processes in Astrophysics*, 400 pp., Wiley-Interscience, New York, 1979.
- Schamhl, E. J., and M. R. Kundu, Microwave proxies for sunspot blocking and total irradiance, *Journal of Geophysical Research*, *100*, 19,851–19,864, 1995.
- Tanaka, H., J. P. Castelli, A. E. Covington, A. Kruger, T. L. Landecker, and A. Tlamicha, Absolute calibration of solar radio flux density in the microwave region, *Solar Physics*, *29*, 243, 1973.
- Tapping, K. F., and D. P. Charrois, Limits to the accuracy of the 10.7 cm flux, *Solar Physics*, *150*, 305–315, 1994.
- Tobiska, W. K., Current status of solar EUV measurements and modeling, *Advances in Space Research*, *18*, 3–10, 1996.
- Treumann, R. A., The electron cyclotron maser for astrophysical application, *Astronomy and Astrophysics Review*, *13*, 229–315, 2006.
- White, S. M., Radio versus EUV/X-Ray observations of the solar atmosphere, *Solar Physics*, *190*, 309–330, 1999.
- Wilks, D. S., *Statistical Methods in the Atmospheric Sciences*, 467 pp., Academic Press, San Diego, CA, 1995.
- Woods, T. N., S. M. Bailey, F. G. Eparvier, G. M. Lawrence, J. Lean, W. E. McClintock, R. G. Roble, G. J. Rottman, S. C. Solomon, W. K. Tobiska, G. J. Ucker, and O. R. White, TIMED solar EUV experiment, *SPIE*, *3442*, 180–191, 1998.
- Woods, T. N., F. G. Eparvier, S. M. Bailey, P. C. Chamberlin, J. Lean, G. J. Rottman, S. C. Solomon, W. K. Tobiska, and D. L. Woodraska, Solar EUV Experiment (SEE): Mission overview and first results, *Journal of Geophysical Research (Space Physics)*, *110*, 1312, 2005.
- Zar, J. H., Significance testing of the Spearman rank correlation coefficient, *Journal of American Statistical Association*, *67*, 578–580, 1972.
- Zar, J. H., *Biostatistical Analysis*, 4th Ed., 929 pp., Prentice Hall, Englewood Cliffs, NJ, 1999.

APPENDICES

APPENDIX A

RADIO EMISSIONS

This appendix deals with the morphology of radio emissions. It is intended to describe in broad terms the radio emissions often associated with flares. As mentioned in Chapter 3, radio emissions span over five orders of magnitude in frequency. Figure A.1 shows an idealized solar radio burst spectrum. All of these emissions are possible during a flare; however, most of them are not always seen on an individual flare.

The meter wavelength range is one of the most explored ranges in solar radio. Terminology that originated in this range has been applied to other radio ranges. Many references are available regarding radio meter wavelength emissions, among them *Kundu* [1965], *Dulk* [1985], *McLean and Labrum* [1985], and *Aschwanden*

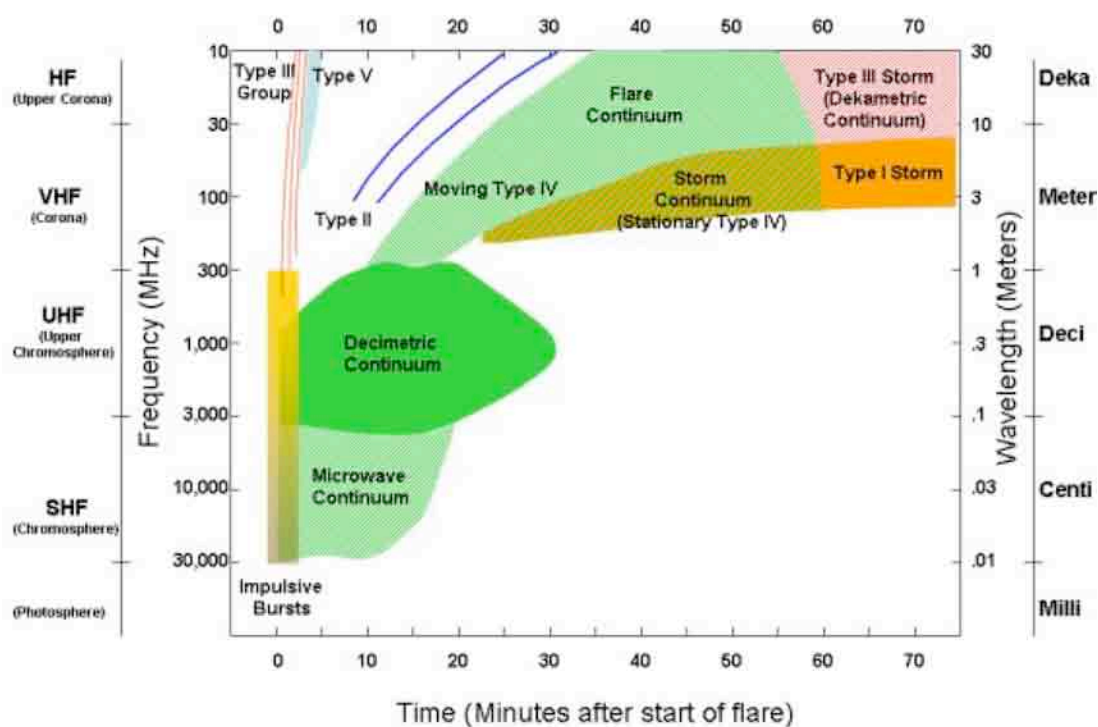


Figure A.1: Typical radio burst spectrum.

[2004]. The frequency range for meter wavelengths is 300 MHz or less. Radio emissions in this range have been classified into five different type of radio sweeps:

1. Type I
2. Type II
3. Type III
4. Type IV
5. Type V

The Air Force RSTN sites use a solar radio spectrograph (SRS) to observed the sweeps. This instrument measures that radio spectrum from 25 to 180 MHz. Figure A.2 show some of the common radio frequency interference measured by this instrument. This particular plot is from the Learmonth Solar Observatory, which has the “cleanest” radio environment out of all the RSTN sites. Type I bursts are the most common of the radio bursts. They last around one second and are superimposed on a continuum that may last a few hours to several days. If the continuum lasts a few hours, then it is associated with a flare and it is called a storm continuum. Continua that last several days to a week are associated with active regions and are called “Type I Storms.”

The next type is the Type II sweep. These sweeps usually last ten minutes or more and have a frequency range from 200 to 10 MHz. This burst is characterized as a slow drifting burst with time from high to low frequencies. It is associated with shocks traveling out from the corona into space and is often an indication of coronal mass ejections. These sweeps are generated by plasma emissions at the fundamental and second harmonic. Figure A.3 shows the fundamental and harmonic emission of

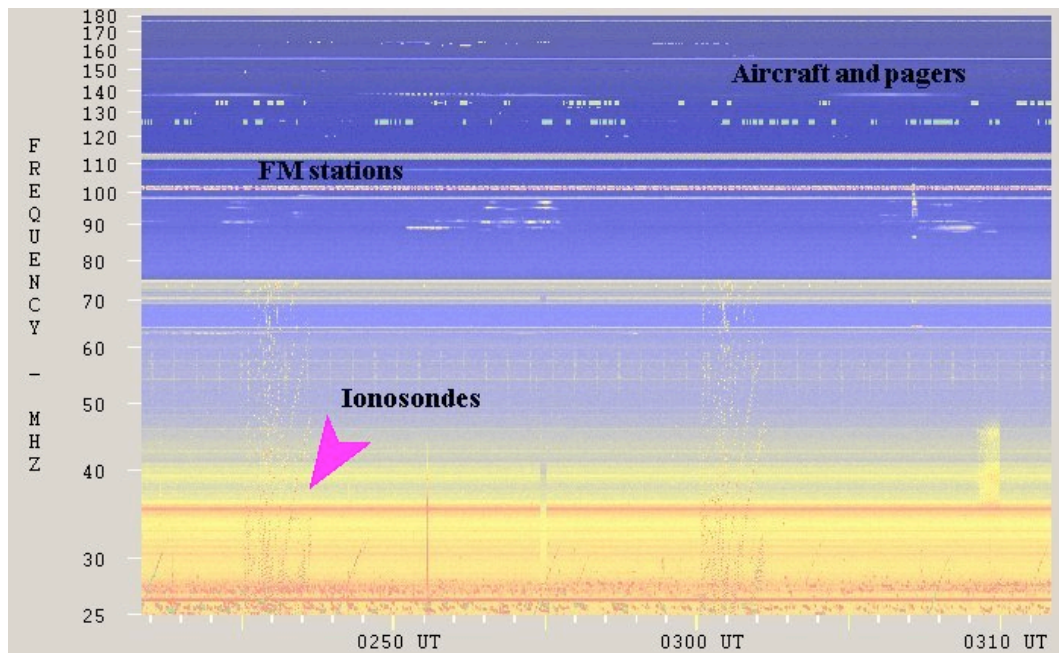


Figure A.2: Plot of RFI commonly measured by RSTN's SRS.

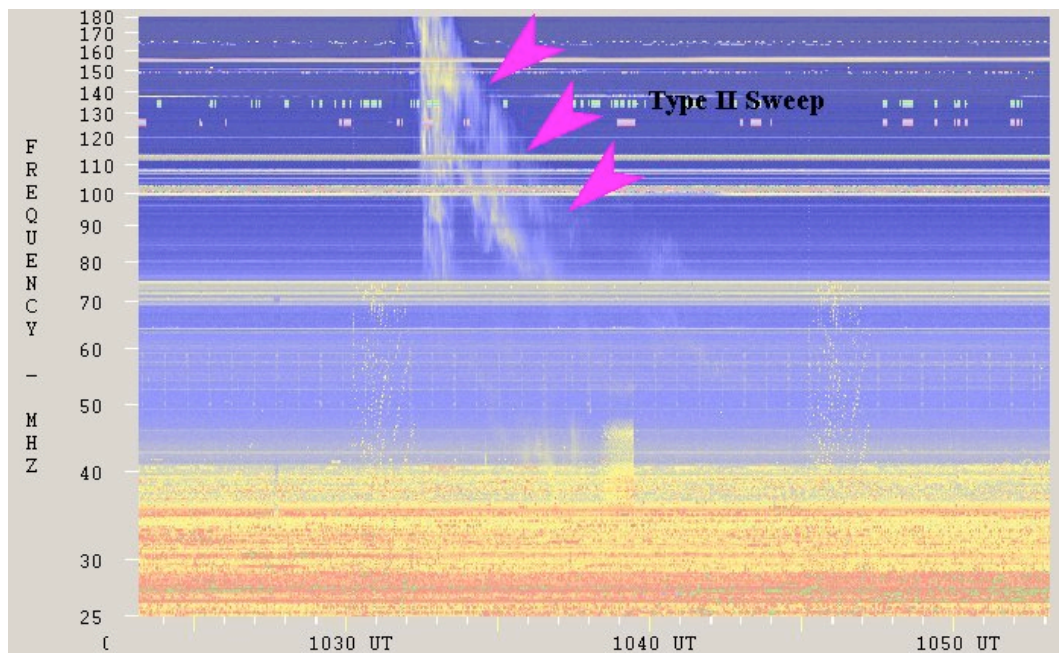


Figure A.3: Type II radio sweep observed by the Learmonth Solar Observatory on February 1, 2005 at 10:32 UT.

a Type II sweep. These plots are used to calculate the shock propagation speed and are used to forecast the onset of geomagnetic storms.

Type III radio sweeps are the second most common kind of radio sweep [*McLean and Labrum*, 1985]. These sweeps usually occur in groups, last only a few seconds, and range from 200 MHz down to 1 MHz. These bursts are caused by subrelativistic electron beams traveling out from the sun. The classic Type III sweep is characterized by a fast drift from high to low frequencies. Other variations of these bursts include the U-type (travels up on one side of a loop and down the other side), the J-type (travels up on side and starts coming down the other side of a loop and then stops). A classic Type III is shown in Figure A.4.

Type IV radio sweeps usually last between twenty minutes and several hours. These sweeps are observed in three different varieties:

1. Moving Type IV
2. Flare Continuum
3. Storm Continuum

According to *Dulk* [1985], the moving Type IV sweep is very rare. It is believed that is produced by a self-contained, moving magnetic structure. Trapped fast electrons in this structure emit either plasma or gyro synchrotron radiation. The flare continuum Type IV usually starts at the same time as a Type II sweep, but can start earlier, and has the same frequency range (Figure A.5). These sweeps are most likely created by plasma emissions from trapped electrons in the coronal loops. The storm continuum Type IV sweep is associated with large flares. It usually starts around 10 minutes after the onset of the flare at around 300 MHz and then slowly drifts down to lower frequencies.

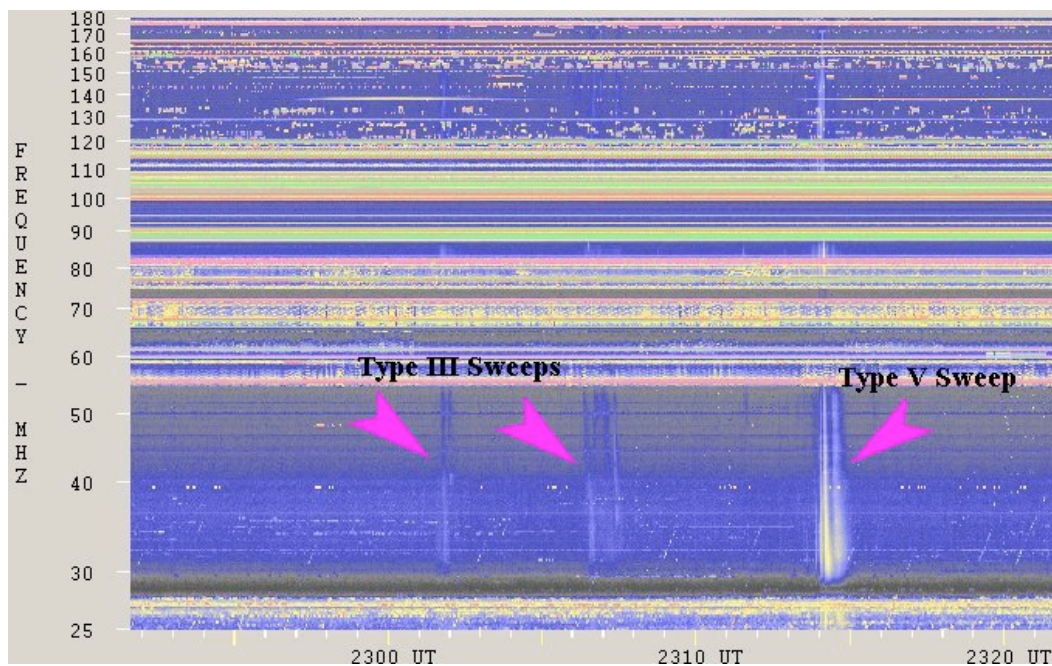


Figure A.4: Type III radio sweep observed by the Palehua Solar Observatory on March 16, 2005 at 23:02 UT. This image also shows a Type V sweep around 23:13 UT.

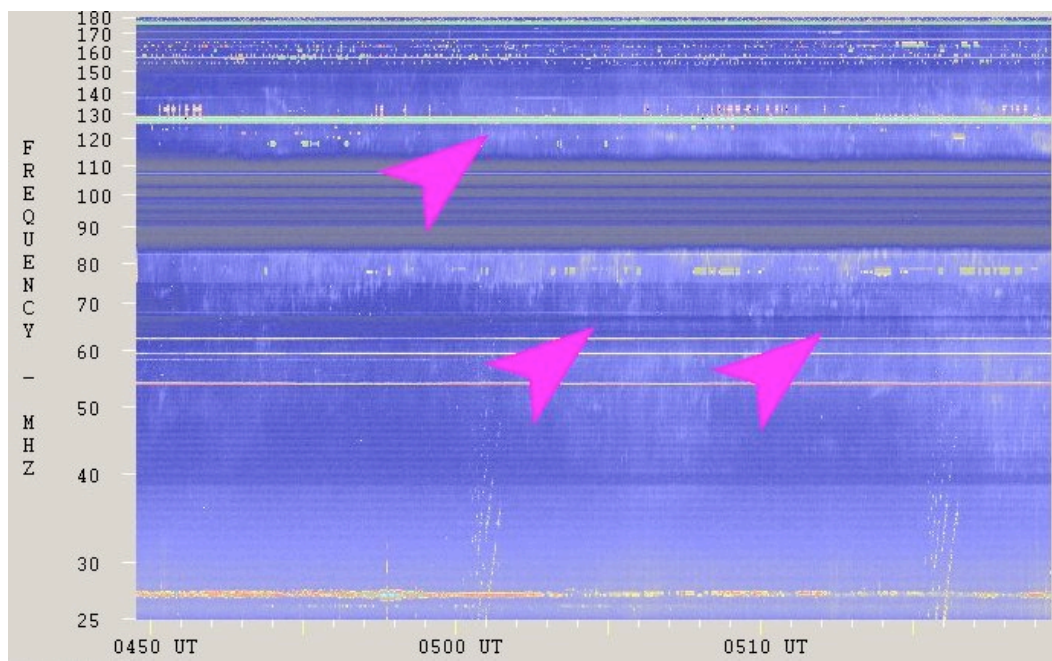


Figure A.5: Type IV radio sweep observed by the San Vito Solar Observatory on September 14, 2005 starting at around 04:50 UT. The Type IV is the diffuse-looking pattern marked by the arrows.

The last sweep in the meter wavelength range is the Type V (Figure A.4). These sweeps last a few minutes and follow some Type III sweeps. They are most likely due to plasma radiation produced by slower electrons in the electron stream responsible for the Type III that precedes the Type V sweep.

These meter wavelength plots were created using the SRS Data Viewer software created by Graham Steward from the IPS Radio and Space Services at the Learmonth Solar Observatory. This free software is available through the National Geophysical Data Center.

The decimeter wavelengths range from 300 to 3000 MHz. The discrete bursts are very similar to the centimeter bursts described in Chapter 3. The radio sweeps use the similar terminology as the meter wavelengths. Reviews of these sweeps can be found in *Güdel and Benz* [1988], *Islaker and Benz* [1994], *Benz* [1996], and *Jiříčka et al.* [2002]. Overall, these bursts are much smaller in intensity and duration than their meter counterparts. There are four main categories:

1. Type III-like bursts
2. Spike (or narrow-band spikes)
3. Diffuse continua
4. Pulsations

Type III-like bursts last from 0.2 to 1.0 seconds and occur in groups of 10 to 1000 individual bursts. They drift in frequency opposite to the classic Type III sweep at a rate of ~ 1 GHz/s. Individual spikes last a few tens of milliseconds and occur in groups of tens to ten thousand. Diffuse continua last a few seconds to minutes and are usually broadband (100 MHz). These emissions are similar to the metric Type IV. Pulsations are almost periodic short pulses with a separation of 0.1 to 1.0

seconds. They occur in groups of some ten thousands and usually last a few minutes. The mechanisms for these bursts are coherent, but the specific details are still being researched.

APPENDIX B

ADDITIONAL DATA SOURCES

The first geostationary operational environmental satellite (GOES) was launched in 1974. These satellites usually operate in pairs: one over the eastern coast of the United States and one over the western coast. The satellites spin on an axis perpendicular to the equatorial plane at the rate of 100 rpm. Their main purpose is to monitor different aspects of the environment by using a combination of different instruments suites. One instrument suite is the Space Environment Monitoring System (SEMS). The SEMS consists of different instruments that measure the energetic particles, magnetic field, and solar x-rays [Donnelly *et al.*, 1977].

The soft x-rays are measured by the soft x-ray sensor. The soft x-ray sensor was first flown on the Solar Radiation satellite and then on NASAs Synchronous Meteorological Satellite (SMS) series [Aschwanden, 1994]. The version flown on the GOES satellites has provided continuous data since 1974. The x-ray detector scans the sun once per satellite rotation. However, a sample of the data measured is transmitted to the ground once every three seconds. The elevation angle of the x-ray detectors is adjusted through the use of stepping motors to correct for seasonal variations. The detectors measure two wavelength bands: .5-4 Å and 1-8 Å using gas ion chambers. The ion chambers convert the solar energy into low voltages. The voltages are then amplified using four overlapping gain ranges. Some details of the sensors are listed in Table B.1. A detailed description of the detector is provided by Grubb [1975].

The x-ray measurements made by GOES are available through the Space Weather Prediction Center website in almost real time. The data is available in either one-minute or five-minute averages (see Figure B.1). The 3-second data used

Table B.1: Soft x-ray sensor characteristics.

	Wavelength Band	
	.5-4 Å	1-8 Å
Beryllium Filter Window		
Thickness	5×10^{-4}	5×10^{-5}
Area	5.8×10^{-4}	1.9×10^{-4}
Weight	0.952	0.108
Filler Gas	Xenon	Argon
Gas Pressure, mm Hg	180	800
Intensity Resolution	0.2% to 0.3% of the maximum flux of the range	
Spatial Resolution	none, collimated to view full disk	
Sample Rate	every 3 seconds	
Wavelength Resolution	none within the wavelength bands	

in this dissertation was generously provided by Rodney Viereck (SWPC/NOAA). The soft x-ray data is available more than 99.9% of the time. The only times data may not be available is during: eclipses of the sun by the earth (near equinox), calibrations, eclipses of the sun by the moon, and telemetry problems. Impacts from eclipses only impact one satellite at a time since there is a large longitudinal separation between the pair of operational satellites. Calibrations are not performed on both satellites at the same time. This ensures at least one set of x-ray measurements during calibrations.

GOES x-ray data is one of the primary tools used to monitor and describe solar activity. Solar flares are commonly referred to by the magnitude of the soft x-rays measured by GOES (e.g. C-class, M-class, X-class). Unfortunately, using only the soft x-ray data during a flare could lead to incorrect assumptions regarding the flare's energy in the radio and EUV/UV energy bands.

Another data set used in this dissertation is the TIMED-SEE EUV irradiance measurements. NASA's Thermosphere Ionosphere Mesosphere Energetics Dynamics (TIMED) satellite was launched on December 7, 2001. The TIMED spacecraft's mission is to measure basic parameters in the mesosphere, lower thermosphere, and

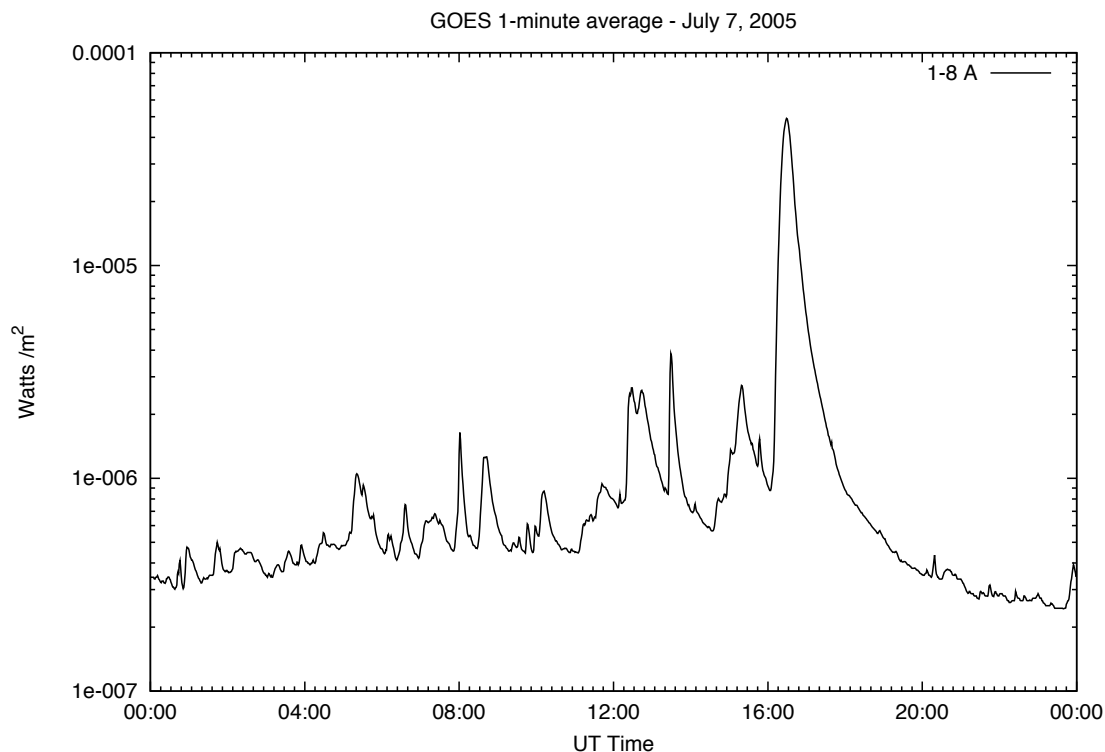


Figure B.1: GOES measurements on July 7, 2005.

ionosphere (MLTI). The spacecraft is on a 388-mile (625-km) circular orbit around the Earth inclined 74.1 degrees from the equator. There are four main instruments on board: the Global Ultraviolet Imager (GUVI), the Solar Extreme Ultraviolet Experiment (SEE), the Doppler Interferometer (TIDI), and SABER (Sounding of the Atmosphere using Broadband Emission Radiometry). GUVI is a far-ultraviolet spectrograph used to measure the global composition and temperature profiles of the MLTI region and auroral energy inputs. The TIDI measures wind and temperature profiles of the MLTI. SABER measures heat emitted by the atmosphere over a wide altitude and spectral range. The SEE instrument measures solar spectral irradiances from 0.1 nm to 194 nm using two instruments. The EUV grating spectrograph (EGS) measures the 27 to 194 nm range with a 0.4 nm resolution. The XUV photometer system (XPS) measures the 0.1 to 27 nm range using nine photodiodes with built-in

Table B.2: Available TIME-SEE data sets.

Data Type	Time Resolution	Corrections
EGS Level 1 XPS Level 1	Irradiances of each 10-second measurement during each orbit	No corrections
EGS Level 2 XPS Level 2	Irradiances averages over one day	South Atlantic Anomaly Edge of field of view Flares are removed Corrected to 1 AU
EGS Level 2A XPS Level 2A	Irradiances averaged over one orbit	South Atlantic Anomaly Edge of field of view Flares are not removed Corrected to 1 AU
SEE Level 3	Daily average. Combination of EGS and XPS Level 2	Flares are removed Adjusted to 1 AU Atmospheric Absorption
SEE Level 3A	Single orbit average. Combination of EGS and XPS Level 2A	Same as Level 3 except flares are not removed

filters. These two instruments are mounted on a one-axis gimbal platform called the SEE solar pointing platform. Since there is only one axis to point the instrument, the sun drifts through the 11° field of view for about three minutes during each orbit. The period of the orbit is around 97 minutes. Thus, there is around 15 observations periods per day. During each three-minute window, SEE obtains twenty ten-second integrations as the sun drifts through the field of view. The raw data are counts per second which are converted to irradiances using straightforward convection formulas [Woods *et al.*, 2005]. The converted data is processed into eight different data types listed in Table B.2. A complete description of the SEE instrument is given by Woods *et al.* [1998], and calibration and algorithm information can be found in Woods *et al.* [2005]. Figure B.2 is an example of the Level 3A data.

A fourth dataset used in this dissertation is the solar EUV measurements taken by the Solar EUV Monitor (SEM) on board the Solar Heliospheric Observatory (SOHO). The SOHO satellite was launched on December 2, 1995. Its mission is

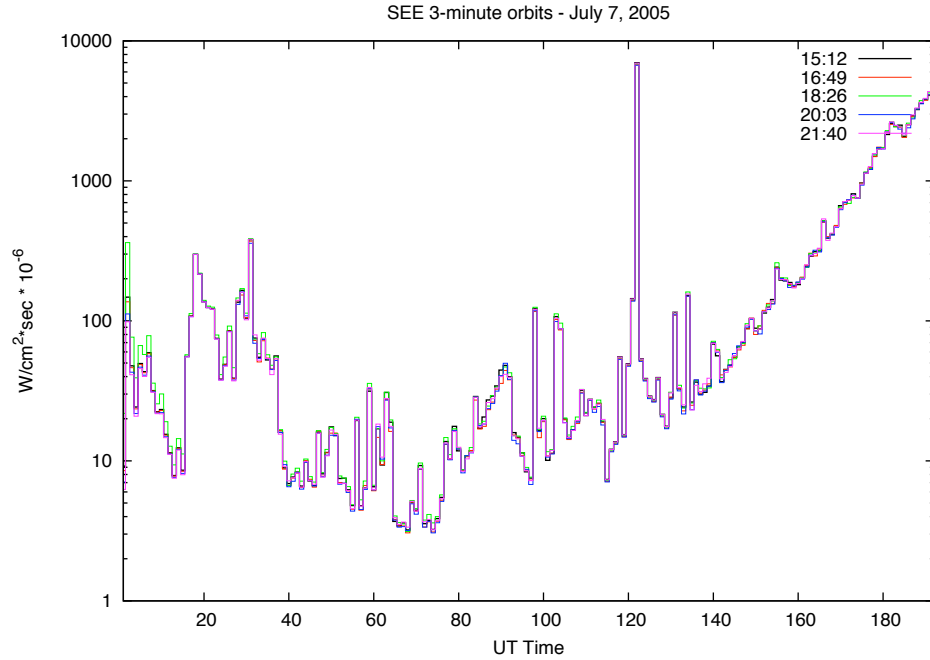


Figure B.2: SEE measurements on July 7, 2005. Each orbit is shown as a different color. There is an enhancement on the lower wavelengths on the 18:26 orbit.

to study the internal structure of the sun, its atmosphere, and the solar wind. SOHO is on a halo orbit around the Lagrangian point L1, 1.5 million kilometers sunward of the Earth. The spacecraft consists of two parts. The service module provides power, control, communications to the scientific instruments, and support for the solar panels. The payload module houses twelve different instrument packages. One of those instrument packages is the Charge, Element, and Isotope Analysis System (CELIAS). CELIAS is designed to measure the composition of the solar wind. Attached to CELIAS is SEM. SEM's purpose is to measure the absolute EUV flux of the sun. This instrument is a photodiode spectrometer that continuously measures the absolute solar flux at 30.4 nm and the absolute integral flux between 17 and 70 nm. A detailed description of the instrument is given by *Hovestadt et al.* [1995], and details on the calibration of the instrument can be found in *Judge et al.* [1998]. The

data available for SEM are photon counts for the 26-34 nm flux and 0.1 to 50 nm flux, both corrected to 1 AU. The data is provided in 15-second averages. Figure B.3 shows the SEM measurements taken on 9 January, 2005.

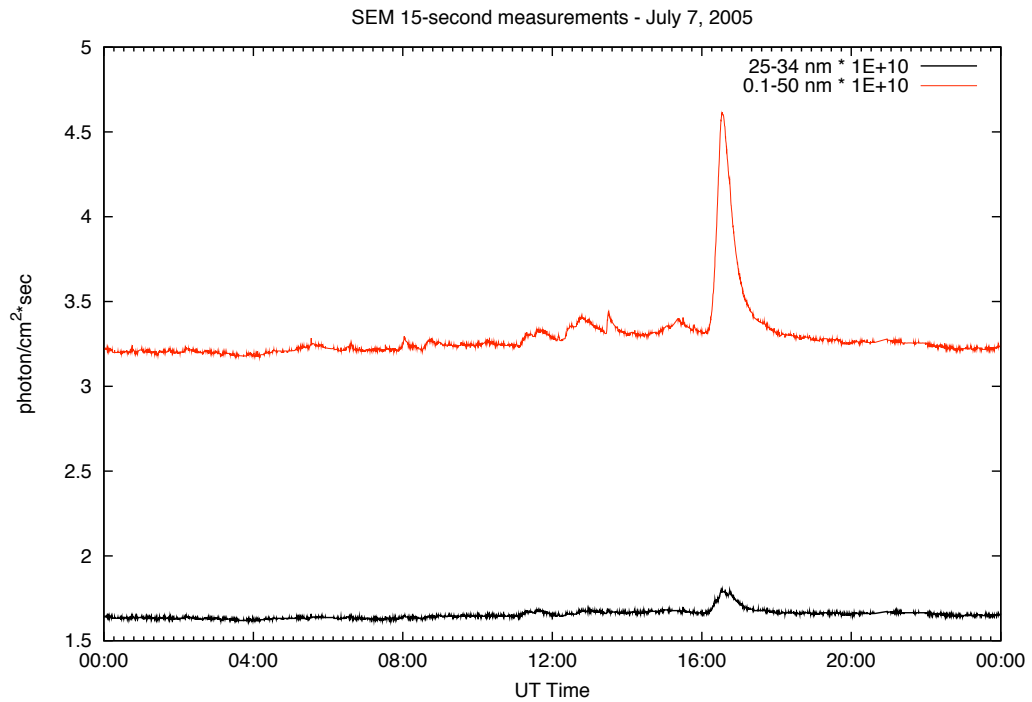


Figure B.3: SEM measurements on July 7, 2005.

APPENDIX C

RANK CORRELATIONS

Correlation coefficients are a simple way to show association between two datasets using a single number. This number, the correlation coefficient, has a value ranging from -1 to 1 . If the coefficient is equal to -1 , then there is a perfect negative association between variables. A coefficient of 1 indicates that there is a perfect positive association between the variables. The correlation coefficient provides no physical explanation regarding the relationship between the two variables, i.e., there is no implication of cause and effect.

The most common correlation computation is the Pearson correlation coefficient (r). According to [Wilks, 1995] it is often misused, due to a lack of understanding of some of its potential shortcomings. One of these shortcomings is the assumption that must be made in order to properly use this computation. That assumption is that the two variables have normal distributions. If this is not the case, the results will not be accurate. Another issue is that r tests for linear relationships between the variables. If the relation is non-linear, r will underestimate the correlation. Additionally, the Pearson correlation coefficient is very sensitive to outlying points. Large value outlying points will cause r to overestimate the correlation.

Fortunately, the Spearman rank correlation coefficient (ρ) resolves some of these issues. The Spearman rank correlation coefficient is similar to the Pearson correlation coefficient. However, the Spearman rank correlation uses the ranks of the data rather than the values of the data. The data are ordered according to their values. The lowest value is assigned a rank of 1 , and so on until the M^{th} data point is assigned the largest rank of M . If two or more data points have the same value, then the rank for the repeated data points is the average rank of those values. Table C.1

Table C.1: Example of ranked data. This is similar to example shown on Zar [1999].

X	Rank X	Y	Rank Y	d_i	d_i^2
10.4	4	7.4	5	-1	1
10.8	8.5	7.6	7	1.5	2.25
11.1	10	7.9	11	-1	1
10.2	1.5	7.2	2.5	-1	1
10.3	3	7.4	5	-2	4
10.2	1.5	7.1	1	0.5	0.25
10.7	7	7.4	5	2	4
10.5	5	7.2	2.5	2.5	6.25
10.8	8.5	7.8	9.5	-1	1
11.2	11	7.7	8	3	9
10.6	6	7.8	9.5	3.5	12.25
11.4	12	8.3	12	0	0

shows an example of a data set and how it is ranked.

The benefits of the Spearman rank correlation over the Pearson rank correlation come at a cost. There is some information lost in replacing the data values with their ranks [Press et al., 1992]. In cases where the both correlation coefficients apply, the Spearman rank correlation coefficient is 0.91 as powerful as the Pearson correlation coefficient [Zar, 1999].

A full derivation of the Spearman rank correlation coefficient is give by [Kendall, 1975]. The results of this derivation give the correlation coefficient as

$$\rho = \frac{1 - \frac{6}{N^3 - N} \left[D + \frac{1}{12} \sum_k (f_k^3 - f_k) + \frac{1}{12} \sum_m (g_m^3 - g_m) \right]}{\left[1 - \frac{\sum (f_k^3 - f_k)}{N^3 - N} \right]^{1/2} \left[1 - \frac{\sum (g_m^3 - g_m)}{N^3 - N} \right]^{1/2}} \quad (\text{C.1})$$

$$D = \sum_{i=1}^N (R_i - S_i)^2 \quad (\text{C.2})$$

where R_i is the rank of x_i among all the x values, S_i is the rank of y_i among all the y values, f_k are the number of ties in the k^{th} group of ties among the R_i s, g_m are the number of ties in the m^{th} group of ties among the S_i s, and N is the number of data points.

Using Table C.1 and equations C.1 and C.2 and $N = 12$, then $D = 42$, $\sum f_k^3 - f = (2^3 - 2) + (2^3 - 2) = 12$ since among the x 's there are two ties of two measurements each (10.2 and 10.8); $\sum g_m^3 - g = (2^3 - 2) + (3^3 - 3) + (2^3 - 2) = 36$ since among the y 's there are two ties of two measurements each (7.2 and 7.8), and one tie of three measurements (7.4), yields $\rho = 0.85108$.

Once ρ is computed, it is necessary to test the significance of this value. This evaluation depends on the number of data points used and how certain one wants to be of the results. The first step in testing this significance is to establish a hypothesis:

H_o : The x_i and y_i are mutually independent.

H_a : The x_i and y_i are correlated.

The next step is to compute a test value for the correlation and compare it to a critical value based on a specific distribution. A recommended test [Zar, 1972] is the t-test where the test value is

$$t = \rho \frac{\sqrt{N-2}}{\sqrt{1-\rho^2}} \quad (\text{C.3})$$

and the distribution is the student's t distribution with $N-2$ degrees of freedom [Ramsey, 1989].

Most often, the t -value from equation C.3 is computed and then the critical value is found by looking it up on a statistical table after deciding on a confidence level α . This confidence level, in conjunction with the critical value, states that there

is a $1 - \alpha\%$ assurance that any value of t greater than the critical value cannot happen by chance. In the above example, the critical value for $\alpha = 0.05$ is given as 2.228 while equation C.3 evaluated to 5.120. Since $t > t_c$, the H_o hypothesis is rejected at a 95% confidence level. In other words, it is 95% certain that ρ would not have that value unless X and Y were correlated.

Press et al. [1992] suggests a direct way of computing the significance on ρ . Rather than computing a t -value, choosing a confidence level (α), and then comparing the t -value to the critical value, this method computes α for which $t > t_c$. This method uses the t -distribution function

$$A(t|\nu) = 1 - I_{\frac{\nu}{\nu+t^2}}\left(\frac{\nu}{2}, \frac{1}{2}\right) \quad (\text{C.4})$$

where $I_{\frac{\nu}{\nu+t^2}}$ is the incomplete beta function. The limiting values for this equation are $A(0|\nu) = 0$ and $A(\infty|\nu) = 1$. Using this method, the result of equation C.4 will give the confidence level at which the resulting ρ will have a $t > t_c$. In other words, there is a $1 - \alpha\%$ chance that two data sets which are mutually independent will have that same value of ρ . For this example, the α value for which $t > t_c$ is 0.0447. In this case, there is a 99.9553% that the x_i 's and the y_i 's are correlated.

APPENDIX D
COPYRIGHT PERMISSIONS

Two figures in this dissertation required copyright permissions from their respective sources. I have submitted the permission requests as outlined in the “Publication Guide for Graduate Students.” The following figures are copies of the permission letters.

I hereby give permission to Ariel Acebal to reprint the following material in his dissertation:

Figure 2, page 143 from Bastian, T. S., A. O. Benz, and D. E. Gary (1998), Radio Emission from Solar Flares, *Annual Reviews of Astronomy and Astrophysics.*, 36, 131-188, doi: 10.1146/annurev.astro.36.1.131.

Fee -0-

Signed Laura Folkner, Permissions Department, Annual Reviews 5-14-08

Figure D.1: Copyright permission submitted to the Annual Reviews of Astronomy and Astrophysics Journal.

**ELSEVIER LIMITED LICENSE
TERMS AND CONDITIONS**

May 14, 2008

This is a License Agreement between ariel o acebal ("You") and Elsevier Limited ("Elsevier Limited"). The license consists of your order details, the terms and conditions provided by Elsevier Limited, and the payment terms and conditions.

Supplier	Elsevier Limited The Boulevard, Langford Lane Kidlington, Oxford, OX5 1GB, UK
Registered Company Number	1982084
Customer name	ariel o acebal
Customer address	335 Park Meadow Circle Hyde Park, UT 84318
License Number	1947681362469
License date	May 14, 2008
Licensed content publisher	Elsevier Limited
Licensed content publication	Chinese Astronomy and Astrophysics
Licensed content title	A complex solar radio burst and the characteristics of its related microwave sources and EUV coronal loops
Licensed content author	Lin Wang, Rui-xiang Xie, Min Wang, Chun Xu and Yu-ying Liu
Licensed content date	April-June 2005
Volume number	29
Issue number	2
Pages	14
Type of Use	Thesis / Dissertation
Portion	Figures/table/illustration/abstracts
Portion Quantity	1
Format	Print
You are an author of the Elsevier article	No
Are you translating?	No
Purchase order number	
Expected publication date	Jul 2008
Elsevier VAT number	GB 494 6272 12
Permissions price	0.00 USD
Value added tax 0.0%	0.0 USD
Total	0.00 USD

Figure D.2: Copyright permission received from the Chinese Astronomy and Astrophysics Journal.

CURRICULUM VITAE

Ariel O. Acebal

(May 2008)

EDUCATION:

Ph.D. in Physics, Utah State University, Logan, Utah (expected 2008).
M.S. in Applied Physics, Air Force Institute of Technology, Wright-Patterson
Air Force Base, Ohio (2000).
B.S. in Meteorology, Florida State University, Tallahassee, Florida (1993).

EXPERIENCE:

Palehua Solar Observatory Commander, Palehua, Hawai'i (2003-2005).
Space Weather Branch Chief, Air Force Weather Agency, Offutt Air Force Base,
Nebraska (2000-2003).
Wing Weather Officer, Ramstein Air Base, Germany (1995-1998).
Staff Weather Officer, Osan Air Base, Republic of Korea (1994-1995).

ACADEMIC HONORS:

Sigma Pi Sigma Physics National Honor Society, 2007
Chi Epsilon Pi Meteorology National Honor Society, 1993
Golden Key National Honor Society, 1993
Phi Beta Kappa National Honor Society, 1993